


Doctoral Dissertation
Doctoral Program in Electrical, Electronics and Communications Engineering (32.th cycle)

GNSS-only Collaborative Positioning Methods for Networked Receivers

Alex Minetto
* * * * * *

Supervisors
Prof. Fabio Dovis

Doctoral Examination Committee:
Prof. G. Seco-Granados, *Referee*, Universitat Autònoma de Barcelona (UAB)
Dr. M.A. Caceres, *Referee*, Deutsches Zentrum für Luft- und Raumfahrt (DLR)
Prof. J. Vilà-Valls, Institut Supérieur de l'Aéronautique et de l'Espace (ISAE-SUPAERO)
Dr. S. Bartoletti, University of Ferrara
Prof. C. F. Chiasserini, Politecnico di Torino

Politecnico di Torino
March, 2020

I hereby declare that, the contents and organisation of this dissertation constitute my own original work and does not compromise in any way the rights of third parties, including those relating to the security of personal data.

Alex Minetto
Turin, March, 2020

Summary

The Global Navigation Satellite System (GNSS) has been mostly considered as an ubiquitous and reliable positioning and navigation technology characterized nowadays by considerable precision and accuracy but weakened by critical limitations due to the intrinsic nature of radio navigation systems. Indeed, GNSS positioning in harsh environment has been intended as one of the major challenges in the field of Positioning and Navigation Technologies (PNT) due to several impairments affecting the quality of the received signals, thus the positioning estimation performed by the receivers. The quality of GNSS absolute positioning can be enhanced through the integration of further information about the state of a given agent (i.e. position, velocity, heading) or exploiting additional data from the surrounding environment, which can be directly obtained through sensors (i.e. UWB, Lidar, Sonar), or through the network connectivity. In parallel with the advances in satellite-based and network-based augmentation systems, sensor fusion and complementary positioning systems, in the last decades, Cooperative Positioning (CP) has been addressed as a further paradigm for improving localization of networked users relying on the exchange of independent information. The basic approach has leveraged the estimation of relative measurements and the sharing of these data through ad-hoc communication channels or permanent network infrastructures. In light of this, this work considers the exploitation of redundant visible satellites among interconnected users (i.e. generic agents equipped with networked Global Navigation Satellite System (GNSS) receivers) as a powerful resource for the improvement of GNSS-based solutions. Such a redundancy can be effectively exploited to determine relative distances between receivers through opportunistic usage of the network connectivity, thus leading to the *collaborative estimation of the baseline length*.

The discussed approach has been indeed investigated to overcome the Line-of-Sight (LoS) limitation in the sensing of the surrounding environment through direct measurements among GNSS users. In the proposed framework the focus is on collaborative techniques, which uniquely exploit the exchange of data typically used for GNSS-based positioning, without the need of additional sensors. The problem of a profitable usage and integration of redundant and correlated inter-agent information exchanged within a network of GNSS receiver has been named GNSS-based Cooperative Positioning (CP).

Within such a context, this thesis aims at investigating the paradigm of GNSS-based CP according to a bottom-up approach: from the theoretical bounds of a hybridized tight integration of collaborative measurements up to the development of a real-time Proof of Concept (PoC) for networked mobile devices. First a proper framework will be defined for the analysis and investigation of GNSS-based ranging among networked receivers. Then the paradigm of GNSS-based CP is explored through numerical and controlled-environment simulations, and eventually, the PoC is presented along with an on-field analysis of feasibility and a performance assessment of the technology.

Acknowledgements

I would express my sincere gratitude to my advisor, prof. Fabio Dovis, for his continuous support along the last three years. I thank him for his passion towards the topic and for his endless scientific knowledge and tutoring. Thanks for believing in me and in my ideas and let me growing professionally and scientifically towards any goals of this Ph.D. Thanks to my mom, Nicoletta, because she has never stopped supporting me in all my choices even crossing the saddest period of our life. Thank you for your patience and your lovely, unconditioned kindness. Thanks also to my dad, Valter, for being so enthusiast about all my achievements and experiences. For both of them I can proudly say that the apple has not fallen far from the tree. Thanks to Calogero and Nicola for their precious know-how and for the time spent in shaping my mind as a "GNSS scientist". Thank you for your friendship, passion and time spent together. Thanks to all the new friends and colleagues, Andrea, Neil, Caner, Wenjian, Rayan and Akmal for their tireless desire of innovating, researching, and above all to share some pieces of our lives in motivating relationships at the workplace. Sincere thanks to Marco and all the researchers of the Space and Navigation Division at LINKS foundation (ex ISMB) for their technical, scientific and human support in this research. Thanks to Gianluca, Mario, Gianluca, Matteo, Davide, Emanuela, Micaela, Beatrice and Gabriella for sharing their expertises about GNSS and for their hard work spent during the crazy journeys of SVN 49 in 2017 and of Galileo Satellites during the system outage occurred in 2019. I will remember such moments as the funniest and most exciting investigations of the last years. Many thanks to the HANSEL consortium and to Rui Sarnadas, ESA officer and contact point for the project, to have strongly encouraged the development of our proof of concept within the HANSEL testbed an to have supported us in all the phases of this challenging task. A special thanks goes to Andrea to have worked with passion on the early stages of this research, and to Maria Chiara for her hard work on the development side of our cooperative positioning proof of concept, thank you for your effort and for turning this paradigm into an effective application. I would thank the whole CAPS.loc team, Neil, Giampaolo and Maria Chiara for their effort in the study of applied cooperative positioning. Thanks to Vincenzo and Umberto, friends and colleagues who invited me to contribute to the PitchD talk in April 2019, and thanks to evaluation committee of the Tiziana Vitrano Competition, "My reseearch in three minutes" for the chance to present my research to other Ph.D. students. Thanks to the staff of TEDx Talk Politecnico di Torino for the amazing opportunity they gave me to participate as a speaker in the TEDx Talk "Sound and Safe" in November 2019. Thanks to all the people who supported me and the most unforgettable journey of my life in Longyearbyen (Svalbard). Thanks to the INGV team (Vincenzo Romano , Lucilla Alfonsi and Luca Spogli) for their kind availability and thanks to Stefano Poli for the training against polar bears. Last but definitely not least, thanks to my love, Denise, for her patience and support during these three years, thank you for being the perfect partner in such a crazy journey. Thank you for your limitless understanding and for being always by my side during the nights, weekends and summer holidays spent working hard on my research.

Dedicato a Claudio

alla persona che, più di chiunque altro, mi ha insegnato a ricercare attraverso le proprie passioni una soluzione ad ogni problema.

Contents

List of Tables

List of Figures

Chapter 1

Introduction

Up to 10 billions of electronic devices with localization capabilities will populate the world by 2025 to satisfy the booming request for Location-Based Service (LBS)[75]. While professional GNSS receivers will keep dominating the market of highly-precise, accurate and reliable positioning and navigation, mass market products will demand for smart solutions to obtain the best performance at the minimum cost. A considerable number of LBS such as vehicle pooling, vehicle sharing and remote control of Unmanned Aerial Vehicle (UAV)s are mostly based on the positiong solution provided by mobile mass market devices (e.g. smartphones) [209].

In the last decades a remarkable research effort has been broadly spent in the field of navigation and positioning by mostly addressing sensor integration to GNSS [72, 174]. As depicted in Figure 1.1, a growing set of subsystems is nowadays responsible of the provisioning of localization and navigation data. As an example, modern vehicular navigation systems can exploit proprioceptive sensors such as Inertial Navigation System (INS) to improve the quality of absolute positioning solutions [88, 138]. These components are devoted to the measure of values internal to the system (e.g. angular rate, wheel rotations, accelerations). GNSS/INS integration schemes benefit from the accurate measurements provided by INS and periodically compensate for their typical drifts through GNSS solutions. Such an approach, known as *dead reckoning* is conceived on top of absolute positioning, thus position estimation based on loose sensors integration can always benefits from improved GNSS performance [187]. Advanced integration schemes such as tight and ultra-tight GNSS/INS offer promising performance in harsh environment where standalone GNSS is typically weak [52, 27, 210, 26] but they require reliable sensors and challanging implementations such as in mobile devices where they still show relevant issues [211, 173]. In fact, in many devices such as smartphones and smartwatches or in limiting conditions (e.g. off-road driving, urban canyon, forest), the integration of INS can be challenging due to the uncorrect modelling of the dynamics of the object itself [157, 22].

In parallel, the sensing of the surrounding environment has become a relevant aid to the navigation and it can be accomplished through cameras ot through several exteroceptive sensors such as Ultra Wide Band (UWB), LiDAR and many others. Indeed, when inertial sensing is not available or sufficiently reliable, other kinds of measurements can be used to retrieve information about the surrounding environment such as the distances from anchor points whose position is known a-priori [167, 93, 207] or by considering peers as anchors of opportunity relying on their position estimates [158]. Therefore, the contribution of exteroceptive sensors to improve absolute and relative localization has been deeply explored in literature [73].For instance, Charge-Coupled Device (CCD)/complementary metal-oxide semiconductor (CMOS) camera can be used as a complementary heading sensor through the computation of vanishing points [26].

Although GNSS is a fundamental source for geolocalization, the applications related to relative positioning were typically referred in literature and real implementations to carrier-phase ambiguity resolution [11, 86] for Real Time Kinematic (RTK) and Differential GNSS (DGNSS) applications.

Hovewer, recent advances in communication networks are going to enable the integration of such relative measurements among connected GNSS receivers thus addressing the field of CP. CP gathers several techniques through wich a set of agents (also referred as nodes in network domain) requiring for a positioning solution collaborate with others to determine their own location. The paradigm of CP also known in literature as *network localization*, *cooperative localization* or *collaborative localization* has been hence addressed to guarantee positioning capabilities to specific nodes which may be not equipped with positioning systems or connectivity to other nodes within the same network [17]. Furthermore most of the early contributions addressed CP to provide positioning and navigation in GNSS-denied environment and they were mostly focused on sensor networks. A misleading classification was attributed in the field of GNSS to peer-to-peer Assisted GNSS (AGNSS) solutions.

A deep investigation on the optimality of CP for network applications has been also provided in [172, 122]. The interest in CP strategies was first raised in the field of robotics by several contributions [133, 134, 161],then leading to Simultaneous Localization and Mapping [95, 168]. Later, other works faced the problem of localization in wireless sensor networks [170] and afterwards towards vehicular navigation [116, 28, 3]. A novel approach to range-only localization has been also proposed in [191] where terrestrial range measurements retrieved from occasional anchors allow to approximate the position estimate. The most of the contributions related to these fields concerned Maximum Likelihood Estimation (MLE) approaches which is not suitable to exploit prior knowledge about the dynamics of the receivers effectively. Differently, another approach named *belief propagation* has been deeply explored in the field of indoor positioning contemplating mostly static or low dynamic agents [97, 19].

As an example, interesting results about the superiority of collaborative strategies with respect to Differential GPS techniques [6, 4, 130, 129] have been presented. This trend justified the fusion of DGNSS and collaborative navigation techniques for a further improvement of the performance [73, 151] oriented to the future generation of GNSS receivers.

Previous works investigated the computation of distance among GNSS receivers. For example in [203], the authors presented a technique to compute inter-vehicular range measurements through weighted GNSS double differences. .

Pioneering works on the tight integration of DGPS and INS in an Extended Kalman Filter (EKF)-based positioning algorithm were proposed to improve accuracy and availability of GPS positioning [73, 151, 154]. A two-steps positioning algorithm has been proposed to refine the GNSS-only position estimates through a Maximum Likelihood (ML) approach constraining the positioning solution by means of inter-vehicle ranges obtained by weighted double differentiation of shareable pseudorange measurements [109]. The approach foresees a distributed computation of the locations of all the agents by each agent. A final estimated was then performed as a weighted mean of the different estimates provided by the collaborating agents. The scheme proposed in [109] does not exploit the dynamics of the agents, thus being suboptimal in dynamics applications. Recent works such as [103, 180] demonstrate how timely and appealing is CP in the field of GNSS.

According to the taxonomy presented in [17] the proposed architecture was developed as *distance-based*, *distributed*, *sequential* and *probabilistic* positioning estimation. First we addressed the cooperative determination of the distance among the receivers, namely inter-agent distance to provide additional information to the positioning problem. Such a computation is conceived to be carried out by each agent independently in a distributed fashion.

The collaborative position update of each receiver is not used as a reference for other receiver to avoid error propagation and the estimation is locally performed with a probabilistic Bayesian approach which guarantees also the estimation of uncertainty on the output.

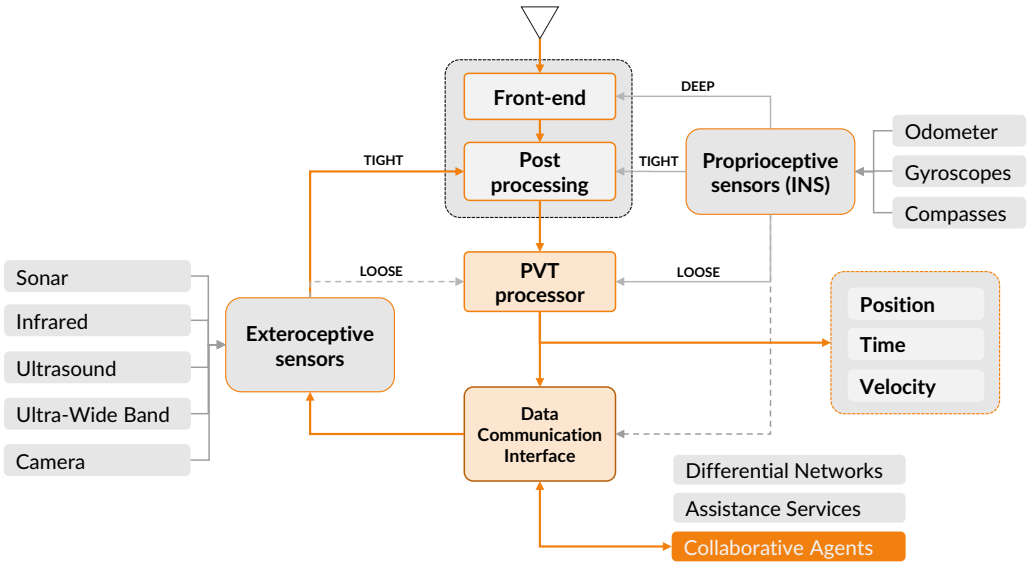

Figure 1.1: Reference architecture of a modern positioning system providing data channel for positioning applications.

1.1 Research motivation and objectives

Provided the fundamental role of positioning and navigation technologies and the growing attention to the new generation of telecommunication networks, this thesis aim at developing an innovative framework for the cooperation of networked GNSS receiver for the improvement of positioning and navigation performance. The algorithms which will be presented in the context of the proposed GNSS-based CP, are conceived to exploit GNSS measurements as they are provided by professional as well as by Ultra-low Cost receivers GNSS. It comes out that the proposed framework can be intended as an auxiliary layer which can be implemented in any receivers architecture and it can be adapted to different grades of Positioning and Navigation Technologies (PNT), from high-end products to smartphones. Although the aforementioned works has brought significant contribution to the integration of auxiliary measurements, they were conceived in more general frameworks. The proposed study is tightly linked to GNSS and it exploits natively both satellite-to-user range and Doppler measurements for the improvement of the positioning in kinematics systems.

Therefore, this thesis aims in parallel at defying theoretical aspects about the use of non independent measurements in the positioning estimation. The identification of a theoretical background is addressed to the cooperation of GNSS receiver sharing GNSS measurements for the improvement of their positioning estimation. Provided that the proposed paradigm is conceived on top of GNSS as a refinement of GNSS-only positioning solutions, sensor fusion will as well as network differential corrections will not be investigated in this work. This work addresses the computation and the analysis of distance measurements among peer receivers and their integration in the computation of the receiver status and the position, specifically.

1.2 Main Contributions

The main contributions of this thesis can be summarized as follows:

- Definition of the problem of GNSS-based cooperative positioning according to the hybridized architecture present in literature.
- Analysis, development and performance assessment of state-of-the art differential ranging algorithms for the collaborative estimation of the inter-agent distances.
- Definition and development of a theoretical framework for of a novel method for the estimation of the baseline length in limited visibility conditions.
- Study and design of a tight-integration scheme for Bayesian estimation integrating correlated measurements.
- Definition, study and implementation of the concept of GNSS networked receiver through asynchronous instances of a GNSS software receiver.
- Real-signal simulation test campaigns through professional signal generator
- Design and development of a smartphone-based mass-market PoC of GNSS-based CP.
- Analysis of the feasibility and effectiveness of the framework through 4G network carried out through on-field test campaigns of the proof-of-concept.

Part of the work included in this thesis was presented through several contributions in international conferences renown in GNSS community [125, 123, 130, 126, 129, 67, 124] and peer-reviewed journal [127, 68]. A side work concerning positioning investigation under geomagnetic storm was also published in further peer-reviewed journal [135]. Some contribution were instead part of the HANSEL European Space Agency (ESA) project deliverables and technical reports [60, 24, 25]. Eventually, further side contributions were published about GNSS anomalies in magazines [45, 44].

Some research contributions included in this work were acknowledged by the international GNSS community with a Best Student Paper Award at the 32nd Internation Technical Meeting of the Satellite Navigation Division of the Institute of Navigation (ION GNSS+ 2019)[123] and with the Francesco Carassa Award 2018 by Gruppo Telecomunicazione e Tecnologie dell'Informazione (GTTI). Furthermore, the innovative cooperative framework developed within the HANSEL project won the Italian Prize of the Galileo Master sponsored by the Italian Space Agency, was selected among the finalists of the University Challenge and reached the top ten of the Galileo Masters 2019 in Helsinki.

1.3 Outline of the thesis

Chapter 2 first provides an overview on radio-positioning systems among which GNSS is described in detail. It describes the overall system architecture and the basic theoretical principles which allow positioning solutions and navigation.

Chapter 3 describes the architecture of a GNSS receiver by providing the fundamental knowledge and definitions for the computation of GNSS raw measurements. Eventually, the concept architecture of a networked GNSS receiver for the implementation of CP is discussed as a guideline of the proposed research.

Chapter 4 presents the differential techniques at the state of the art for the estimation of the distance among two receivers through GNSS measurements, namely GNSS-based ranging methods. It also introduces a novel method, named IAR to determine the same measurements in non-ideal satellite visibility conditions.

Chapter 5 presents a detailed investigation about the methods presented in Chapter 4. A formal assessment of the proposed IAR is discussed through a proper theoretical framework and experimental results are presented to assess the theoretical behaviour. A comparison of the different GNSS-based ranging techniques is eventually provided by means of simulated GNSS signal.

Chapter 6 first recalls a set of popular navigation filters conceived for linearized and approximated Bayesian positioning estimation. The hybridization of the filters is proposed proposed and eventually the analysis of theoretical bounds are investigated for the exploitation of collaborative measurements.

Chapter 7 gives a detailed discussion about implementation aspects related to GNSS-based CP. Different application are presented and the benefits of the approach are discussed in terms of accuracy and precision of the positioning solution. Eventually a trade-off analysis is also provided by comparing the computational complexity and accuracy of two Bayesian filters.

Chapter 8 presents a PoC of GNSS-based cooperative positioning implemented on Android Smartphones. The context of the project which funded the research is first introduced. Afterwards, a background on hardware and software is reported. Eventually the system architecture is explained in detail and feasibility and effectiveness of the proposed paradigm are discussed through on-field tests. Selected results are discussed in details while the whole test campaign is commented according to a given set of performance metrics.

Chapter 9 aim at summarizing the research presented in this thesis and it provides a discussion about future activities about the topic.

Appendixes recall a set of theoretical aspects fundamental to the complete understanding of the proposed approach.

Chapter 2

Global Navigation Satellite Systems and Cooperative Positioning

GNSS is nowadays a consolidated technology to determine positioning and timing information of a receiver w.r.t. an absolute reference frame with good accuracy, precision and availability [90]. The space segment of each system is based on a set of spacecrafts, namely a satellite *constellation*, orbiting the Earth at a distance of more than 20 000 km and continuously broadcasting a set of RF electro-magnetic signals. Despite of the popularity of such a paradigm, the use of satellites can be considered a relatively recent achievement in the history of navigation. In light of this it is worthy to recap the relevant milestones of radio navigation within this chapter. It is remarkable that the age of GNSS started a massive revolution of our daily habits after 30 years from the birth of the first Satellite Navigation System, the GPS. About 20 years later the availability of inexpensive microelectronics led to miniaturized receivers, thus moving GNSS into highly-integrated devices and getting closer to other ground-breaking technologies such as the broadband cellular networks. The synergy of these technologies is going to naturally enable new paradigms such as the GNSS-based CP proposed in this thesis. In order to provide a proper timeline of the history of radionavigation, a brief summary of the techniques developed for positioning and navigation is given in Section 2.1. A brief summary of the current Global and regional Navigation Satellite System is then provided in Section 2.2 highlighting focus to GPS and Galileo systems. The fundamentals of GNSS PVT computation are eventually recalled in Section 2.1.1 to describe the mathematical background on top of which this thesis has been conceived.

2.1 From the Observation of the Stars to Radio Navigation

In this section, the main milestones of the navigation technologies are introduced to provide an historical overview about radio navigation and satellite navigation systems. First, some historical details are given about the evolution of navigation technologies and an overview of current satellite navigation systems is then presented. Accurate historical detail and extended technical data about these system are our of the scope of this work and they can be retrieved by the reader through introductory chapters of [141, 90, 131, 17], to which this content is inspired.

2.1.1 Brief history of navigation technologies

With the term PNT we collect findings and technologies which supported the mankind by providing the answer to an age-old need: the *orientation*. The need of reliable reference markers and landmarks guided the whole history of navigation starting from the observation

of the sky up to the design of modern satellite navigation systems. The *orientation* entails two fundamental aspects which can be identified as *positioning* and *navigation*. The first is defined as the ability of determining the location of an object w.r.t. to a conventional reference system while the latter implies the capacity to describe the motion (speed, direction) of an object along a path.

Geodesy, timekeeping and astronomy

The need of estimating position and travel directions led first to an accurate mapping of the stars, used as celestial markers by Phoenicians to cross the Mediterranean sea and by Polynesians to navigate across the Pacific Ocean for thousands of kilometres. In parallel, the interest towards the study of the size and shape of the earth grew rapidly along with the mapping of its surface. However the position and dynamics of the stars remained for a long time the most reliable tool draw accurate maps. Early navigators were able to determine both time and position on the earth surface by relying on celestial observations and exploiting relative angular measurements. The accuracy of such estimations was remarkably poor thus turning long travels into dangerous challenges. To support these activities, a conventional reference frame was conceived by Greeks more than two thousands years ago w.r.t. to the equator; the latitude was hence defined and measured according to the elevation of the Pole star w.r.t. to the point of observation. Despite the advances in the field, early explorers navigated by keeping track of direction and distance travelled w.r.t. a reference point.

After more than 2 thousands years of star-based navigation, the intrinsic limitation of this methods such as the unavailability due to non favourable weather conditions were overtaken by the technological findings of the 13th century. *Astrolabes* and *sextants* allowed to easily identify latitude thus enabling and supporting maritime treading over the centuries. Compass was then introduced for the first time in Europe in the 12nd century.

In 1519, Magellan tried the circumnavigation of the globe estimating the speed, direction and latitude of the ship but he was still not able to determine the longitude. The relationships between *longitude* and difference in local times was in fact known by navigators but errors of few minutes in the evaluation of local time w.r.t. to the reference clock lead to several degrees in longitude. In light of this, in the seventeenth and eighteenth indeed, maritime trading and the consequent need of accurate navigation pushed the development of accurate clocks. Key advances in time measurements were provided by Christiaan Huygens around 1657, and John Harrison who built in 1726 a pendulum clock having an error of about 1 second a month. The *Harrison no. 4*, also known as H-4, was awarded with £20.000 according to the *Longitude Act of the British Parliament* for discovering the longitude at sea [176]. The innovation introduced by Harrison's first *sea watch* enabled secure navigation in open see and turning navigation from being an art into a scientific and technological discipline.

Terrestrial Radionavigation System

The advent of radionavigation was fuelled by military needs during and after the World War II, provided the consolidated knowledge on radio-wave propagation already used in communications. The radionavigation relies generally on a set of different techniques all based on distances, angle or Doppler measurements w.r.t. known reference landmarks. Such quantities are measured through electro-magnetic RF signals lying in the range from 10 KHz up to 300 GHz.

A set of one-way techniques have been exploited in the last century to passively determine the position of a receiver according to different geometrical solutions. Provided that navigation was initially related mostly to maritime applications, the following techniques were used mainly for 2-D estimation. However, further advances in following decades required

extended solutions to provide 3-D positioning and navigation capabilities to avionics and aerospace systems. An exhaustive analyses of radionavigation and GNSSs is out of the scope of this thesis, therefore the content of this list aim at summarizing the main aspects of each of them.

TDoA - The first radio positioning and navigation systems were based on the TDoA, a hyperbolic determination of the position exploiting the ranging signals broadcasted by three transmitting stations, as shown in Figure 2.1. The computation of the position is based on the *difference* in the ToA of the signals, thus implying synchronous transmitters but not-necessarily synchronous receivers. As an example, LOng-range Aid to Navigation (LORAN) and Omega were extensively used during the Wolrd War II, especially for maritime applications [90].

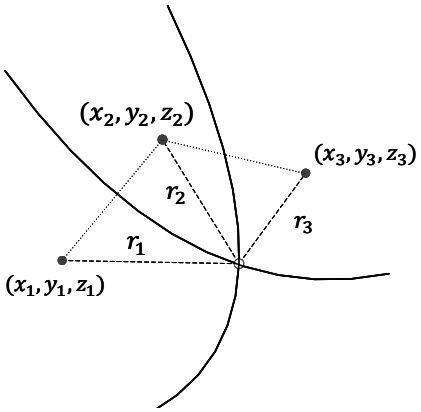

Figure 2.1: Hyperbolic positioning solution using three transmitter and TDoA measurements.

DoA - A further technique is known as DoA or Angle of Arrival (AoA) and foresee the use of antenna arrays to determine the direction of the incoming signals. Besides a DoA system does not necessarily require clocks synchronization among transmitters and receivers, it implies higher costs, computational complexity and power consumption w.r.t. other techniques [17]. Given the dependency of technique on the measurements of angles, DoA localization is often referred in literature to as *triangulation*, as shown in Figure 2.2.

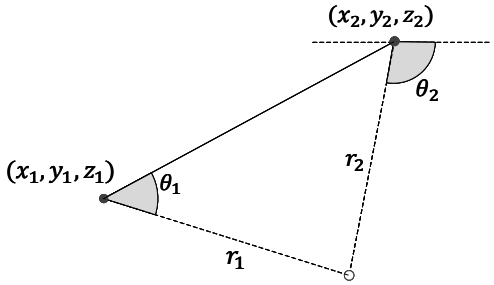

Figure 2.2: Triangulated positioning solution using two asynchronous transmitter and DoA measurements.

Doppler Navigation . A different approach in radionavigation foresees the observation of the *Doppler effect* which turns in an apparent change of the frequency of the received signal. Doppler positioning was considered less intuitive despite it provided the baseline for the development of modern satellite navigations systems in the early 1960s.

ToA - Differently from the previous approaches, current GNSSs are based on a measurements paradigm named ToA also known in literature as Time of Flight (ToF). As for the other techniques, the early adoption of ToA positioning system were addressed to 2-D positioning. In 2-D, the position of a ToA receiver can be hence obtained unambiguously as the intersection of a minimum of three circumferences as shown in Figure 2.3, namely *trilateration*. As far as it was conceived, ToA positioning required accurate synchronization of transmitter and receiver clocks which turned to be feasible only in GNSS with an additional computational cost. Time misalignment of the receiving clock was hence considered as a further unknown in the positioning problem, thus increasing the number of minimum transmitter to four, as it is foreseen by modern GNSS.

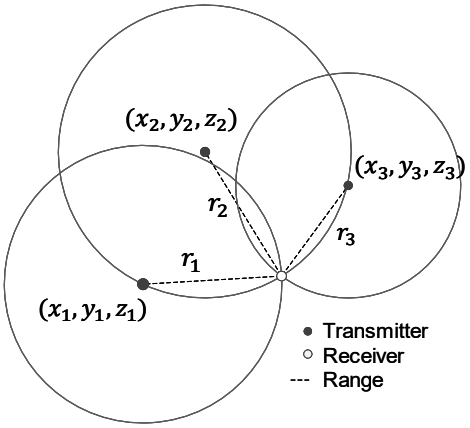

Figure 2.3: Trilaterated positioning solution using three transmitters and ToA measurements with synchronous transmitters and receivers.

Early Satellite Navigation Systems

The early intuition about satellite-based positioning came through a non-trivial observation: it appeared evident that the Doppler shift affecting the signals transmitted by *Sputnik I* was enough to determine its orbit when it was observed from a known location. The reversed problem led to the born of Satellite Navigation Systems [131]. The first operational satellite navigation system was developed by Defense Advanced Research Projects Agency (DARPA) and the Johns Hopkins Applied Physics Laboratory in 1959 and named *Transit* (a.k.a. NAVSAT or Navy Navigation Satellite System (NNSS)). It was designed to be used by U.S. Navy to provide accurate location information to UGM-27 Polaris missiles. The system provided continuous navigation service from 1964 to 1996 employing overall 41 satellites and becoming obsolete with the advent of modern GPS. Few years later URSS developed a system transmitting on the same carrier frequencies and known as Tsikada, which was operational from 1978 to 2008. These systems can be considered the ancestors of modern GNSSs such as GPS and GLobal NAvigation Satellite System (GLONASS) although they allowed two-dimensional positioning computation (at the see-level) with severe limitation due to satellites visibility and complexity of the position estimation algorithm.

Differently from modern ToA navigation systems, these previous ones provided positioning and navigation capabilities relying on Doppler measurements.

2.2 Navigation Satellite Systems

The active satellite-based navigation systems are listed along with a summary of their main features in Table 2.1. They are distinguished according to their coverage in *global* and *regional* systems. The evolution of such systems has been conditioned by a certain degree of interoperability (i.e. GPS+Galileo multiconstellation approach) therefore navigation signals are all transmitted in the same bands for all the systems [80]. In the following, a short description of each system is provided.

2.2.1 GPS

The knowledge acquired with Transit pushed U.S. Navy and the Air Force to the development of a modernized space-based navigation system in the late 1960s. The Department of Defense (DoD) approved the basic system architecture in 1973: It was the birth of GPS. Initially it included a constellation 24 Medium Earth Orbit (MEO) satellites, named Navigation System with Time and Ranging (NAVSTAR) to provide a passive positioning system based on trilateration. The MEO orbit was chosen to achieve the best compromise in terms of satellite design, global coverage and lunching costs. L-band ($1 - 2$ GHz) was selected within Ultra High Frequency (UHF) for the carrier frequency of the transmitted signals and a bandwidth of 20 MHz was designed to host the Code Division Multiple Access (CDMA) spreading codes implemented to allow simultaneous transmission and discrimination of the satellites [90]. Satellites payloads were hence capable to transmit two L-band navigation signals at 1575.42 MHz (L1) and 1227.60 MHz (L2). With the launch of first spacecraft, *Navstar 1*, the first generation (Block I) of GPS satellite was completed in October 1985. The full operational status of GPS was declared in 1995 [136]. The third generation of GPS satellites is expected to be fully operational in 2023 [159, 121] with substantial updates. Satellites belonging to Block III are designed to broadcast modernized L1 and L2 navigation signals named L1C and L2C, respectively [65]. The military code, known as P(Y) in the previous generations, will be replaced with a modernized M-code. A further signal referred to as L5 1176.45 MHz, already available on all the satellites launched from 2010 (Block IIF) is expected to be declared fully operational by 2024 [80]. At the time of writing a total of 31 operational satellites in the GPS constellation, not including the decommissioned, on-orbit spares.

System	BeiDou	Galileo	GLONASS	GPS	NAVIC	QZSS
Owner	China	European Union	Russia	United States	India	Japan
Coverage	Global	Global	Global	Global	Regional	Regional
Coding	CDMA	CDMA	FDMA & CDMA	CDMA	CDMA	CDMA
Altitude	21,150 km	23,222 km	19,130 km	20,180 km	36,000 km	32,600 km 39,000 km
Period	12.63 h (12 h 38 min)	14.08 h (14 h 5 min)	11.26 h (11 h 16 min)	11.97 h (11 h 58 min)	23.93 h (23 h 56 min)	23.93 h (23 h 56 min)
Rev./S. day	17/9 (1.888...)	17/10 (1.7)	17/8 (2.125)	2	1	1
Satellites	23 in orbit (Oct 2018) 35 by 2020	26 in orbit 22 operational 6 to be launched	24 by design 24 operational 1 commissioning 1 in flight tests[34]	31,[35] 24 by design	3 GEO, 5 GSO MEO	4 operational (3 GSO, 1 GEO) 7 in the future
Frequency	1.561098 GHz (B1) 1.589742 GHz (B1-2) 1.20714 GHz (B2) 1.26852 GHz (B3)	1.559–1.592 GHz (E1) 1.164–1.215 GHz (E5a/b) 1.260–1.300 GHz (E6)	1.593–1.610 GHz (G1) 1.237–1.254 GHz (G2) 1.189–1.214 GHz (G3)	1.563–1.587 GHz (L1) 1.215–1.2396 GHz (L2) 1.164–1.189 GHz (L5)	1176.45 MHz (L5) 2492.028 MHz (S)	1575.42MHz (L1C/A,L1C,L1S) 1227.60MHz (L2C) 1176.45MHz (L5,L5S) 1278.75MHz (L6)
Status	Basic nav. service by 2018 end to be completed by H1 2020	Operating since 2016 2020 completion	Operational	Operational	7 operational	Operational
Precision	10m (Public) 0.1m (Encrypted)	1m (Public) 0.01m (Encrypted)	4.5m – 7.4m	5m (no augmentation)	10m (Public) 0.1m (Encrypted)	1m (Public) 0.1m (Encrypted)
System	BeiDou	Galileo	GLONASS	GPS	NAVIC	QZSS

Table 2.1: Current Global Navigation Satellite Systems.

2.2.2 Galileo

Galileo is a GNSS developed by the ESA by means of the Global Navigation Satellite Systems Agency (GSA). The early development stage of Galileo can be identified in the 1990s when the European Union discussed the need for an independent satellite navigation system mostly conceived for civilian use. The first operational satellite, GIOVE-A, was launched in 2011 and in 2016, 26 of the 30 satellites foreseen for the system were actively in orbit. In october 2012 four Initial Operational Capability (IOC) satellites were availbale by transmitting L1 ranging signal allowing our Research group, NavSAS, to perform one of the first Galileo fixes worldwide [119]. Starting from December 2016, Galileo provides its Early Operational Capability (EOC) and its full operational Capability is expected by 2019 [54]. A total of 26 first-generation Galileo satellites have been deployed to date, including In-Orbit Validation (IOV) units. In 2025-2026 is expected the beginning of the transition between first and second generation of Galileo satellites. According to the European Radio Navigation Plan (ERNP) the system transmits three signals: E1 (1575.42 MHz), E5 (1191.795 MHz) consisting of E5a (1176.45 MHz) and E5b (1207.14 MHz), and E6 (1278.75 MHz), as documented in Table 2.1. According to the agreement with U.S. in 2004, European Union designed the payload using Binary Offset Carrier (BOC) modulated-signal allowing both an easier coehexistence with GPS signals and future interoperability.

2.2.3 Other global and regional systems

Although this thesis mainly addresses GPS and Galileo signals, the proposed methodology can be generalized to other systems and potentially extended to a multi-constellation approach. Therefore, it is worth mentioning other important GNSSs and regional satellite systems.

The **Globalnaya navigatsionnaya sputnikovaya sistema (GLONASS)** is the second satellite navigation system being able to provide global navigation capabilities. Its development was pushed by the Soviet Union in 1976 up to the complention of the first operational constellation in 1995. Differently from GPS, the initial architecture provided Frequency Division Multiple Access (FDMA) signals but new CDMA signal have been designed (e.g. L1OC, L1SC, L2OC, L2SC) both for restricted and civil services. The new CDMA signals uses L1 and L2 frequencies to be interoperable with legacy GPS and Galileo signals.

The **BeiDou Navigation Satellite System (BDS)**, also known as Beidou-2 or COMPASS is a global evolution of the previous system Beidou-1 (decommissioned at the end of 2012) which was conceived as a regional system. BeiDou-2 was designed to be an independent satellite navigation system owned by Chinese government and it became operational in China in 2011 with an initial constellation of 10 satellites.

The **Quasi-Zenith Satellite System (QZSS)** is an integrated Japanese regional satellite system based on 1 geostationary satellite and 3 satellites travelling on geosynchronous orbits. It was conceived to provide augmentation to GPS but it will be updated as an independent satellite navigation system by 2023 [98].

The **Indian Regional Navigational Satellite System (IRNSS)**, a.k.a. NAVIC is a regional satellite navigation system developed by the Indian Research Organization (ISRO) and owned by the Indian Government. The constellation consists of 7 satellites among which 3 satellites are located in geostationary orbit. At the time of writing, IRNSS only provides a restricted service conceived for military purposed but the system is expected to be available for civilian use by 2020 [**ganeshan2005indian**, 162].

2.2.4 Augmentation Systems and DGPS

At the early development stages, GNSS offered a positioning accuracy which is suitable for navigation in wide-open space [131] such as maritime applications in open sea and aircraft navigation in open sky. GPS did not meet the requirements for the precision landing of aircraft thus not representing a valuable alternative to the consolidated Instrument Landing System (ILS). However, the nominal accuracy guaranteed by GNSS could be insufficient for vehicular applications [145] as well as for precise surveying activities. A set of ground infrastructures were designed for providing Differential corrections supporting first GPS and afterwards new GNSSs, namely DGNSS.

Similarly to terrestrial DGNSS, new satellites systems has been conceived to support GNSS positioning and navigation by providing additional integrity data and differential corrections over defined service areas. Such augmentation systems are indeed referred to Satellite-based Augementation System (SBAS) and, starting from the 1990s, they provided a complementary infrastructure to support improved accuracy in GNSS.

- **European Geostationary Navigation Overlay System (EGNOS)** was designed to support GPS and it reached its operational capabilities in 2005, thus guaranteeing an accuracy within 2 m and an availability greater than 99%. The third version of the system was natively capable to supplement Galileo. It is composed by 3 geostationary satellites and a ground-segment of 40 Ranging and Integrity Monitoring Stations (RIMSs) stations [61] to serve a wide area including Europe and the northern coastal region of Africa. Additional ground stations are operational in Kourou (KOU), Montreal (MON), Hartebeesthoek (HBK).

- **Wide Area Augmentation System (WAAS)** was developed by the Federal Aviation Administration to support aircraft navigation, thus enabling the use of GPS for precise approaches to airports [REF]. The current constellation is composed by 3 geostationary satellites but additional satellites will be lunched in 2020 [192]. Satellites included in WAAS are designed to provide legacy GPS signals to improve the geometry of the standalone GPS constellation [113].

- **Multi-functional Satellite Augmentation System**(MSAS) is a Japanese SBAS operated by Japan's Ministry of Land, Infrastructure and Transport and Civil Aviation Bureau (JCAB). By exploiting two geostationary satellites launched in 2005 and 2006, MSAS provides supplement to GPS to achieve better accuracy.

- **GPS Aided Geo Augmented Navigation** (GAGAN) is the implementation of a civil SBAS by the Indian in 2008 government[148]. It foresees a set of 3 geostationary satellites and more than 15 ground stations to provide an improved accuracy of GPS up to 3 m.

Errors in satellite clocks, inaccurate orbit determination, ionospheric and tropospheric impairments and other sources of uncertainties contribute to the inaccuracy of the positioning solutions. In the field of precise surveying, most of the applications rely on differential positioning to effectively compensate for such biases, namely DGNSS. The principle of DGNSS foresees a base receiver located at a known location which is capable to receive GNSS signals similarly to a further receiver whose location is unknown. Post processing of the data such as Precise Point Positioning (PPP) [13] allows to determine accurate coordinates of the unknown location. Nowadays the most common approach utilizes receivers installed on reference stations providing correction signals to the GNSS users by means of data link (i.e. over internet, radio signal, cell-phone) and they are often suitable in real time.

2.3 Fundamental of PVT computation in GNSS

By assuming ideal synchronization of the clocks carried by GNSS satellites, ToA measurements can be performed locally by each receiver. The whole process for the construction of satellite-to-receiver pseudorange measurements will be provided in Chapter 3, while at the moment let us consider the availability of unbiased measurements.

In order to determine the positioning solution in the ECEF three-dimensional reference frame (see Appendix A for details) and the clock bias $b_u(t_k)$ w.r.t. to GNSS time scale, a minimum set of four pseudorange measurements is needed. Despite the four unknowns of the receiver position and time state vector the need of four satellites is justified by a simple geometrical assumption: differently from the 2-D trilateration which relies on the intersection of 3 coplanar circumferences, 3-D trilateration (or multilateration) deals with the intersection of a set of spheres. Once the receiver knows the distance from s_1, its location is assumed to lie on a sphere with radius ρ_1. When a further distance is measured,

The first satellite locates the receiver on a sphere. The second satellite narrows the receiver position to a circumference created by the intersection of the two spheres. The third satellite reduces the choice to two possible points. Finally, the fourth satellite uniquely identifies the location of the receiver.

Neglecting all additional error affecting the measurements, a pseudorange measurement retrieved by the receiver can be modelled as

$$\rho_u^s(t_k) = ||\mathbf{x}_s(t_k) - \mathbf{x}_u(t_k)|| + b_u(t_k)c \tag{2.1}$$

where $\mathbf{x}_s(t_k)$ and $\mathbf{x}_u(t_k)$are the receiver and satellite positions, respectively. Equation (2.1) can be expanded in a minimum set of four equations which model the trilateration problem shown in Figure 2.4.

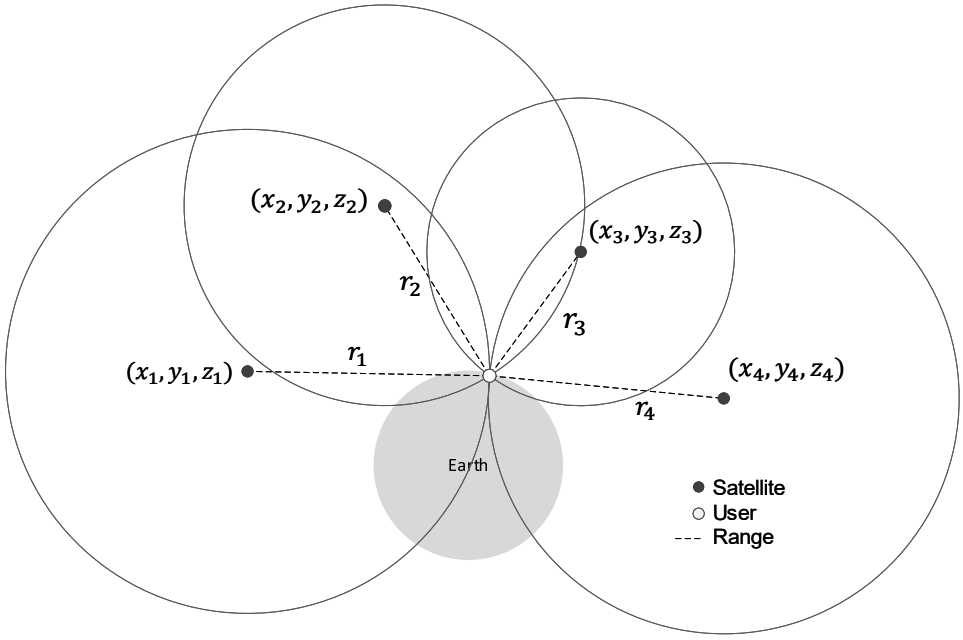

Figure 2.4: Trilateration in GNSS position and time solution based on pseudorange measurements. Size and distances are not scaled to real ratio.

$$\begin{aligned}
\rho_1(t_k) &= \sqrt{(x_1 - x_u)^2 + (y_1 - y_u)^2 + (z_1 - z_u)^2} + c \cdot b_u(t_k) \\
\rho_2(t_k) &= \sqrt{(x_2 - x_u)^2 + (y_2 - y_u)^2 + (z_2 - z_u)^2} + c \cdot b_u(t_k) \\
\rho_3(t_k) &= \sqrt{(x_3 - x_u)^2 + (y_3 - y_u)^2 + (z_3 - z_u)^2} + c \cdot b_u(t_k) \\
\rho_4(t_k) &= \sqrt{(x_4 - x_u)^2 + (y_4 - y_u)^2 + (z_4 - z_u)^2} + c \cdot b_u(t_k)
\end{aligned} \tag{2.2}$$

where x_s,y_s and z_s denotes the position of the satellites in ECEF reference frame. The non-linear equations in (2.2) can be solved for the position state by implementing approximated closed algebraic solutions [90], iterative methods operating through linearization or by means of classic optimal Bayesian filtering such as for example KF or Particle Filter (PF).

According to the linearized methods, the solution can be solved iteratively by determining the offset $\Delta\mathbf{x}_u = (\Delta x_u, \Delta y_u, \Delta z_u, \Delta b_u)$ of the positioning solution w.r.t. an approximated state $\hat{\mathbf{x}}_u = (\hat{x}_u, \hat{y}_u, \hat{z}_u, \hat{b}_u)$, each pseudorange equation can be formally expressed as a function of the user position as $\rho_s(t_k) = f(x_u, y_u, z_u, b_u)$. Assuming a known position and bias state, an approximation of the pseudorange equation can be rewritten as

$$\rho_s(t_k) \simeq \sqrt{(x_s - \hat{x}_u)^2 + (y_s - \hat{y}_u)^2 + (z_s - \hat{z}_u)^2} + c \cdot b_u(t_k) = f(\hat{x}_u, \hat{y}_u, \hat{z}_u, \hat{b}_u) \tag{2.3}$$

The positioning problem can hence be represented according to

$$f(x_u, y_u, z_u, b_u) \simeq f(\hat{x}_u + \Delta x_u, \hat{y}_u + \Delta y_u, \hat{z}_u + \Delta z_u, \hat{b}_u + \Delta b_u). \tag{2.4}$$

Equation (2.4) can be then expanded through the Taylor expansion w.r.t. the approximation point as

$$\begin{aligned}
f(\hat{x}_u, \hat{y}_u, \hat{z}_u, \hat{b}_u) \simeq\ & f(\hat{x}_u + \Delta x_u, \hat{y}_u + \Delta y_u, \hat{z}_u + \Delta z_u, \hat{b}_u + \Delta b_u) \\
& + \frac{\partial f(\hat{x}_u, \hat{y}_u, \hat{z}_u, \hat{b}_u)}{\partial \hat{x}_u} \Delta x_u + \frac{\partial f(\hat{x}_u, \hat{y}_u, \hat{z}_u, \hat{b}_u)}{\partial \hat{y}_u} \Delta y_u \\
& + \frac{\partial f(\hat{x}_u, \hat{y}_u, \hat{z}_u, \hat{b}_u)}{\partial \hat{z}_u} \Delta z_u + \frac{\partial f(\hat{x}_u, \hat{y}_u, \hat{z}_u, \hat{b}_u)}{\partial \hat{b}_u} \Delta b_u
\end{aligned} \tag{2.5}$$

The truncation of the Taylor expansion at the first order of the partial derivatives corresponds to a planar approximation of the spherical intersection expected for the multilateration. The partial derivatives are computed as

$$\frac{\partial f(\hat{x}_u, \hat{y}_u, \hat{z}_u, \hat{b}_u)}{\partial \hat{x}_u} = \frac{x_s - x_u}{||\mathbf{x}_s - \hat{\mathbf{x}}_u||} \tag{2.6}$$

substituting the partial derivative in (2.5), the following holds

$$\rho_s \simeq \hat{\rho}_s - \frac{x_s - \hat{x}_u}{||\mathbf{x}_s - \hat{\mathbf{x}}_u||} \Delta x_u - \frac{y_s - \hat{y}_u}{||\mathbf{x}_s - \hat{\mathbf{x}}_u||} \Delta y_u - \frac{z_s - \hat{z}_u}{||\mathbf{x}_s - \hat{\mathbf{x}}_u||} \Delta z_u + c\Delta b_u \tag{2.7}$$

Equation (2.7) can be rearranged as

$$\hat{\rho}_s - \rho_s \simeq \frac{x_s - \hat{x}_u}{||\mathbf{x}_s - \hat{\mathbf{x}}_u||} \Delta x_u + \frac{y_s - \hat{y}_u}{||\mathbf{x}_s - \hat{\mathbf{x}}_u||} \Delta y_u + \frac{z_s - \hat{z}_u}{||\mathbf{x}_s - \hat{\mathbf{x}}_u||} \Delta z_u - c\Delta b_u \tag{2.8}$$

In order to simplify the notation, the differential terms will be referred to

$$\Delta\rho = \hat{\rho}_s - \rho_s \tag{2.9}$$

$$h_x^s = \frac{x_s - \hat{x}_u}{||\mathbf{x}_s - \hat{\mathbf{x}}_u||} \tag{2.10}$$

$$h_y^s = \frac{y_s - \hat{y}_u}{||\mathbf{x}_s - \hat{\mathbf{x}}_u||} \tag{2.11}$$

$$h_z^s = \frac{z_s - \hat{z}_u}{||\mathbf{x}_s - \hat{\mathbf{x}}_u||} \tag{2.12}$$

The coefficients h_x^s,h_y^s and h_z^s in 2.12 denote the Cartesian components of the unitary steering vector pointing towards the $s-th$ satellite. We define a *steering vector* towards the s-th satellite according to

$$\mathbf{h}^s = (h_x^s, h_y^s, h_z^s) \tag{2.13}$$

such as the (2.8) can be rewritten as $\Delta\rho = h_x^s\Delta x_u + h_y^s\Delta y_u + h_z^s\Delta z_u - c\cdot\Delta b_u$

The component of such linearized equations can be now expressed in matrix notation as

$$\Delta\boldsymbol{\rho} = \begin{bmatrix} \Delta\rho_1 \\ \Delta\rho_2 \\ \Delta\rho_3 \\ \Delta\rho_4 \end{bmatrix} \mathbf{H} = \begin{bmatrix} h_x^1 & h_y^1 & h_z^1 & 1 \\ h_x^2 & h_y^2 & h_z^2 & 1 \\ h_x^3 & h_y^3 & h_z^3 & 1 \\ h_x^4 & h_y^4 & h_z^4 & 1 \end{bmatrix} \Delta\mathbf{x}_u = \begin{bmatrix} \Delta x_u \\ \Delta y_u \\ \Delta z_u \\ \Delta b_u \end{bmatrix} \tag{2.14}$$

.

The set of pseudorange equations can be written as

$$\Delta\boldsymbol{\rho} = \mathbf{H}\Delta\mathbf{x}_u \tag{2.15}$$

and eventually the unknown vector, $\Delta\mathbf{x}_u$, can be hence computed solving for

$$\Delta\mathbf{x}_u = \mathbf{H}^{-1}\Delta\boldsymbol{\rho}. \tag{2.16}$$

By substituting the result of (2.16) in the fundamental relationship

$$\mathbf{x}_u = \hat{\mathbf{x}}_u + \Delta\mathbf{x}_u$$

and iterative solutions can be applied to improve the convergence of the algorithm according to a pre-defined threshold [79].

2.3.1 Determination of the velocity

The same approach can be implemented for the determination of the velocity of a receiver. In this case, simple pseudorange measurements do not provide a proper information about the dynamics of a receiver and their variation must be considered in form of *pseudorange change rate* or equivalently *Doppler shift*.

Every GNSS receiver estimates the Doppler shift of each received satellites signals w.r.t. the nominal carrier frequency at the acquisition stage in order to feed the tracking and to guarantee a proper data demodulation of the navigation message, as it will be clarified in Chapter 3. Furthermore, modern GNSS receivers are capable to perform carrier-phase

measurements and can produce precise Doppler shift estimation which must be compared to satellite velocity provided through ephemeris data [90].

When a GNSS receiver, u, is considered, the received signal frequency from a generic satellite s, can be modelled by

$$f_r^s = f_c \left(1 - \frac{\mathbf{v}_u^s \cdot \mathbf{h}_u^s}{c}\right) \tag{2.17}$$

where f_c is the nominal carrier frequency associated to the transmitted signal (i.e. 1575.42 MHz for GPS L1), $\mathbf{v}_u^s$ is the user-to-satellite relative velocity and $\mathbf{h}_u^s$ is the steering vector directed along the LoS, as determined previously. The dot product between the relative velocity and the steering vector provides the radial projection of the relative velocity along the LoS. By considering a common ECEF reference frame, the relative velocity, $\mathbf{v}_s^u$, is computed as

$$\mathbf{v}_u^s = \dot{\mathbf{x}}_s - \dot{\mathbf{x}}_u = \begin{bmatrix} \dot{x}_s - \dot{x}_u & \dot{y}_s - \dot{y}_u & \dot{z}_s - \dot{z}_u \end{bmatrix}^\top. \tag{2.18}$$

The Doppler shift can be hence computed as

$$\Delta f_u^s = f_r^s - f_c^s = -f_c^s \frac{(\dot{\mathbf{x}}_s - \dot{\mathbf{x}}_u)\, \mathbf{h}_u^s}{c} \tag{2.19}$$

The carrier frequency f_c^s is not stable and proper corrections are forwarded in the navigation message to compensate for satellites on-board instrumental drift of the local oscillators. These corrections can be applied to the nominal transmitting frequency as $f_c^s = f_0 + \Delta f_u^s$.

The received signal is not centred at $f_c + \Delta f$ but is affected by a bias due to the drift of the receiver clock. The received frequency, f_r^s is hence obtained as $f_r^s = f_c^s \left(1 + \dot{b}_u\right)$. For the generic s-th satellite, the following relationship can be defined for the Doppler shift

$$f_r^s = f_c^s \left\{1 - \frac{1}{c}\left[(\dot{\mathbf{x}}_s - \dot{\mathbf{x}}_u) \cdot \mathbf{h}_u^s\right]\right\} \tag{2.20}$$

By manipulating 2.20, the relationships

$$c\frac{(f_u^s - f_c^s)}{f_c^s} + \mathbf{v}_s \cdot \mathbf{h}_u^s = \dot{\mathbf{x}}_u \cdot \mathbf{h}_u^s - \frac{c f_u^s \dot{b}_u}{f_c^s} \tag{2.21}$$

can be expanded in the basic elements of each vector, leading to

$$c\frac{(f_u^s - f_c^s)}{f_c^s} + \dot{x}_s h_{ux}^s + \dot{y}_s h_{uy}^s + \dot{z}_s h_{uz}^s = \dot{x}_u h_{ux}^s + \dot{y}_u h_{uy}^s + \dot{z}_u h_{uz}^s - \frac{c f_u^s \dot{b}_u}{f_c^s} \tag{2.22}$$

where the left elements of $\mathbf{v}_s$ are obtained from the ephemeris, the elements of $\mathbf{h}_u^s$ are computed along with the positioning solutions. The right part of (2.22) can be associated to a dummy variable for the sake of simplicity which contains the derivatives of position and clock bias of the GNSS receiver

$$d_u = \frac{(f_u^s - f_c^s)}{f_c^s} + \dot{x}_s h_{ux}^s + \dot{y}_s h_{uy}^s + \dot{z}_s h_{uz}^s \tag{2.23}$$

Provided that generally $f_u^s / f_c^s \simeq 1$, a simplification on the right term can be applied to simplify the problem at the cost of small error in the computation [90]. Being d_u^s the unknown vector, the (2.23) can be solved through

$$\mathbf{d}_u = \begin{bmatrix} \dot{x}_u \\ \dot{y}_u \\ \dot{z}_u \\ \dot{b}_u \end{bmatrix} \mathbf{H} = \begin{bmatrix} h_x^1 & h_y^1 & h_z^1 & 1 \\ h_x^2 & h_y^2 & h_z^2 & 1 \\ h_x^3 & h_y^3 & h_z^3 & 1 \\ h_x^4 & h_y^4 & h_z^4 & -1 \end{bmatrix} \mathbf{g} = \begin{bmatrix} \dot{x}_u \\ \dot{y}_u \\ \dot{z}_u \\ c\dot{b}_u \end{bmatrix} \tag{2.24}$$

.

Provided that $\mathbf{H}$ is the same Direct Cosine Matrix obtained in 2.3 and that is invertible, the solution of the first order derivative terms is obtained as $\mathbf{g} = \mathbf{H}^{-1}\mathbf{d}_u$.

Position, velocity and time constitute the fundamental set of information which can be autonomously computed through GNSS only and which is included in the *receiver state vector*. Such a state vector can be arbitrarily extended with further information about the motion of the receiver such as linear and angular accelerations.

Chapter 3

Receiver architecture and satellite-to-receiver measurements

This chapter addresses the conventional architecture of a GNSS receiver which constitute the main element of the GNSS user segment. A receiver is in charge of acquiring the satellites signals crossing the atmosphere and reaching the earth with a remarkably low power level. A GNSS receiver is designed to extract the pseudorange and Doppler measurements required for the estimation of the PVT, according to the process introduced in Chapter 2.

While mass-market single frequency receivers exploit code pseudoranges, computed starting from the estimation of the signal code delay, professional multifrequency receivers make use of carrier phase measurements. Code measurements are unambiguous but noisy; on the contrary, carrier phase measurements are much more precise but inherently ambiguous, and the process to solve for the integer ambiguity is hardly affordable by mass-market receivers [131].

The chapter first introduces the structure of the navigation signal in Section 3.1. Then, the receiver architecture is presented in Section 3.2 up to the construction of the pseudorange measurements to recall the useful nomenclature used in this thesis. It is worth remarking that most of the analysis included in this work are referred to the use of Software GNSS receiver whose architecture will be briefly summarized at the end of Section 3.2. The concept of networked receiver is eventually introduced as the reference architecture of the current research.

3.1 Signal structure and frequency plans

As introduced in Chapter 2, healthy GNSS satellites continuously broadcast navigation signals from their orbits towards the earth. Before being received by the users, a navigation signal is typically referred to as Sequential Importance Sampling (SIS) and is designed to provide accurate estimation of its ToA and accordingly of the related satellite-to-receiver distance, namely the *pseudorange* measurement. The SIS is also conceived to be resilient to intentional and unintentional interferences encountered in the crossing of the atmosphere and troposphere, multipath reflection, scattering and all the potential sources of disturbance [90]. The payload of each GNSS satellite generates the components of the SIS which are mixed prior to the transmission over a selected *carrier frequency*, according to the systems signal plan[136].

A SIS transmitted over a specific carrier frequency is identified as a *channel* and is composed by two parts defined accordingly to the In-Phase (I) and Quadrature (Q) components of an original baseband complex signal, as

$$S_X = \sqrt{2}P_T \left[s_{X-I}(t)\cos(2\pi f_c t) - s_{X-Q}(t)\sin(2\pi f_c t) \right] \tag{3.1}$$

where P_T is the transmitted power associated to the given channel and f_c, the *carrier frequency*, characterizes the fundamental RF sinusoidal signal (e.g. L1=1575.42 MHz) which mostly condition the RF properties in the free-space propagation. The baseband signal s_X can be instead defined as

$$s_X = \sqrt{2}A(s_{X-I} + j s_{X-Q}). \tag{3.2}$$

I and Q components in 3.2 are typically independent real signals which can carry four main components each, as shown in Figure 3.1. Such components are multiplied as

$$s_{X-Y} = \underline{s}_Y(t) c_Y(t) \bar{c}_Y(t) d_Y(t) \tag{3.3}$$

where Y indicates I or Q components and

- c_Y, named **spreading sequence**, is the binary PRN ranging code designed both to guarantee CDMA capabilities and the spectral spreading over the specific bandwidth.
- d_Y, named **navigation message**, is a sequence of bits including information about satellites clock correction, ephemeris and health.
- $\bar{c}_Y$, named **secondary code**, has been included in modernized GNSS signals to improve acquisition performance.
- $\underline{s}$, named **subcarrier**, is a periodic sequence resulting from the combination of an arbitrary number of binary offset carriers [9].

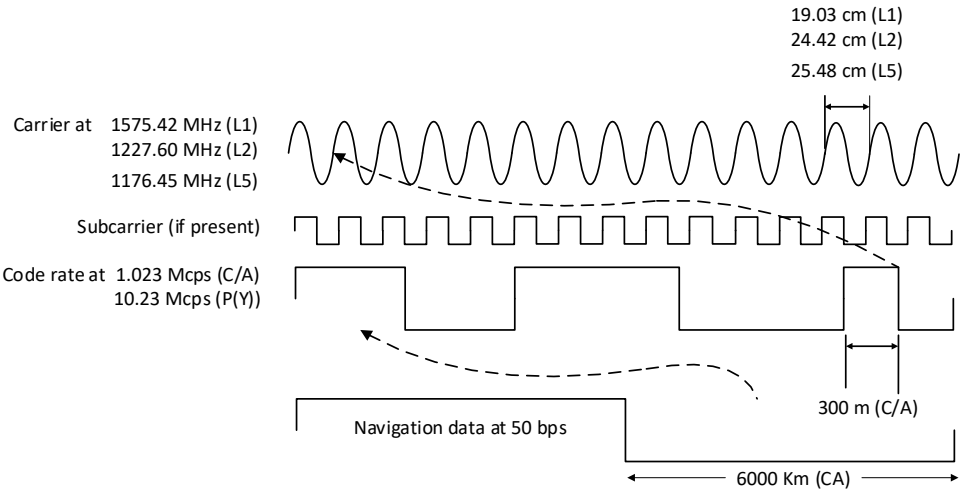

Figure 3.1: GPS navigation signal components: RF carrier signal (top), subcarrier(second), spreading code (third), navigation data (bottom). The signals are not in scale.

Sofisticaded modulation schemes, named Multilevel Coded Spreading Symbols (MCS) can be applied at the sub-carrier level to improve performance in modernized SIS such as for BOC and AltBOC schemes used in Galileo [58]. MCS sequences are indeed a promising field since well selected configurations offer clear performance advantages as well as the possibility to control spectral properties in a more efficient way. This aspect has been of

crucial importance during the design of Galileo in order to be compatible and interoperable with GPS, and could show us the way to proceed in the future when new signals are planned to be placed in the already crowded RNSS bands[9].

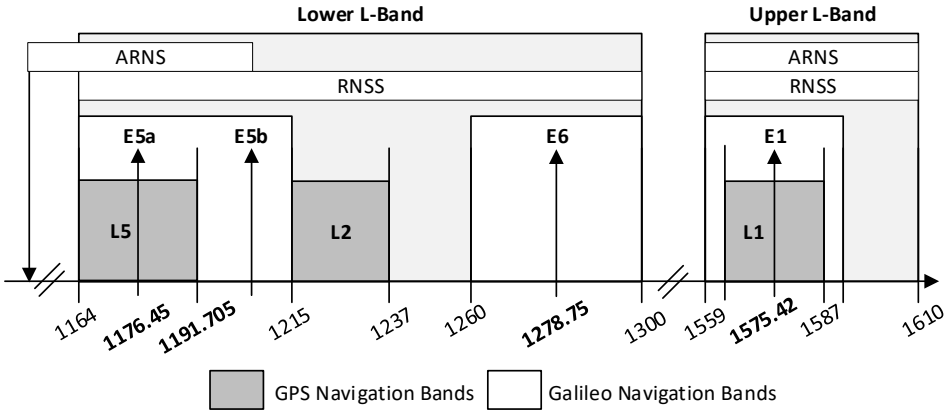

Figure 3.2: Galielo and GPS frequency plan fitting the bands reserved to RNSS. Reproduced from [58].

The accurate description of the signal plan is out of the scope of this work but further details are available about GPS and Galileo in the respective Interface Control Document (ICD)s [136, 58] and excellent references can be found in GNSS literature, as well. For the sake of completeness the updated signal plans of GPS and Galileo are summarized in Figure 3.2 and detailed in Table 3.1 and Table 3.2, respectively.

Band	**Service**	**Type (*)**	**Modulation scheme**	**Spect. occup. (**)**	**Code rate**		**Navig. data rate**	**Min. Rx Power**	**Status (***)**
				MHz	**chip/s**		**bit/s**	**dBW**	
L1	C/A	C	BPSK(1)	2.046	1.023e6		50	-158.5	T
L1/L2	P	M	BPSK(10)	20.46	10.23e6		50	-161.5	T
L1	L1C	C	TMBOC(6,1,4/33)	4.092	CP	1.023e6	no data	-158.25	F
			BOC(1,1)	4.092	CD	1.023e6	50	-163	
L2	L2C	C	BPSK(1)	2.046	CM	511.5e3	25	-158.5	P
					CL	511.5e3	no data		
L1/L2	M	M	BOC(10,5)	30.69	5.115e6		N/A	N/A	T
L5	L5	C	QPSK(10)	20.46	I5	10.23e6	50	-157	P
					Q5	10.23e6	no data	-157	

REMARKS:

(*)	C = civil signal
	M = military signal
(**)	null-to-null bandwidth
	For BOC modulations, only the two main spectral lobes are considered
(***)	T = transmitted (full operation capability);
	P = pre-operational broadcast;
	F = foreseen signal.

Table 3.1: Current (2019) and modernized GPS signals [63], [64], [62]. Taken from [41].

Band	Service	Channel	Modulation scheme	Spectral occup. (*)	Subcarrier freq.	Code rate	Sec. code rate	Nav. data	Multiplex. tech.	Min. Rx power	Status(**)
				MHz	MHz	Mchip/s	chip/s	symb/s		dBW	
E1	PRS	A	BOCcos(15,2.5)	35.805	15.345	2.5575	-	N/A	Const. env.	N/A	T
	OS	B	CBOC(6,1,1/11)	14.322	1.023 / 6.138	1.023	-	250		-157 (B+C)	T
	Pilot	C	CBOC(6,1,1/11)	14.322	1.023 / 6.138	1.023	250	no data			T
E6	PRS	A	BOCcos(10,5)	30.69	10.23	5.115	-	N/A	Const. env.	N/A	T
	HAS	B	BPSK(5)	10.23	-	5.115	-	1000		-155 (B+C)	V
	Pilot	C	BPSK(5)	10.23	-	5.115	1000	no data			V
E5a	OS	I	BPSK(10)	20.46	15.345	10.23	1000	50	AltBOC(15,10)	-155 (I+Q)	T
	Pilot	Q	BPSK(10)	20.46	15.345	10.23	1000	no data			T
E5b	OS	I	BPSK(10)	20.46	15.345	10.23	1000	250		-155 (I+Q)	T
	Pilot	Q	BPSK(10)	20.46	15.345	10.23	1000	no data			T

REMARKS:

(*) null-to-null bandwidth
For BOC modulations, only the two main spectral lobes are considered

(**) T = transmitted (initial services);
V = under test and validation.

Table 3.2: Current(2019) Galileo signals [49], [50], [51]. Taken from [41].

3.2 Receiver Architecture

In order to accomplish this core functionality, the architecture of a GNSS receiver is made of several stages concerning specific tasks: *acquisition*, *tracking*, *decoding* of the navigation message, and *post-processing*. An analog stage is typically conceived to constraint signals features (i.e. bandwidth, amplitude) fitting the input requirements of the Analog-to-Digital Converter (ADC). Once the signal is digitalized acquisition and tracking stages aim at estimating delay and Doppler shift to align the incoming signal and the local replica of the spreading code [131]. While the acquisition stage identifies the signals coming from any visible satellite by roughly estimating code delay and Doppler shift, the tracking stage is in charge to refine such estimates to provide accurate information to the post-processing stage, thus reliable pseudorange and Doppler shift measurements.

3.2.1 Received signal

An active or passive antenna is in charge of capturing the GNSS signals to feed the receiving chain of the front-end. In real scenarios, the received signal $y_{\mathrm{RF}}(t)$ is composed by the independent contributions of all the S visible satellites at a given time, t. The resulting signal is in fact the superposition of S signals, denoted as $y_{s,\mathrm{RF}}$ and an additive noise component. For the sake of simplicity, the terms related to the subcarriers are omitted hereafter. Each signals is transmitted on a independent channel which alters delay, Doppler shift and noise differently for each satellite. The overall SIS reaching the antenna is hence

$$y_{\mathrm{RF}} = \sum_{s=1}^{S} \tilde{y}_{s,\mathrm{RF}} + \eta(t) \tag{3.4}$$

where $\tilde{y}_{s,\mathrm{RF}}$ is the signal contribution provided by the s-th satellite and $\eta(t)$ is the additive noise. Such term can be due both to in-band interferences, or due to the thermal noise injected by electronics component such as Low Noise Amplifier (LNA) or power-line supplying the antenna. The noise contribution, $\eta(t)$, is typically modelled as Additive White Gaussian Noise (AWGN) and characterized by a uniform power spectral density assuming a value of $N_0/2$ W/Hz where $N_0 = kT$ and k and T are the Boltzmann constant and the temperature of the system in Kelvin, respectively.

The noise is considered as a Gaussian process which is distributed as

$$\eta(t) \sim \mathcal{N}(0, \sigma^2). \tag{3.5}$$

Considering the (3.5), the $\sigma^2 = N_0/2BT$ where B is the bandwidth of the receiving front-end.

Supposing to receive a single component transmitted from one single satellite, the received signal can be formalized as

$$y_{\mathrm{RF}}(t) = \sqrt{2P_R}c(t-\tau_s)\bar{c}(t-\tau_s)d(t-\tau_s)cos(2\pi(f_{RF}+f_{d_s})t+\phi) + \eta(t) \tag{3.6}$$

where P_R is the received power, τ is the propagation delay of the signal to reach the receiver antenna, f_{d_s} is the Doppler shift and ϕ_s is a phase shift.

3.2.2 Front-end

The architecture of usual GNSS receivers is composed by two distinct parts: analog and digital stages. We identify the analog part as the *front-end* of the system, which is in charge of filtering the received signal and provide a suitable signal to the subsequent ADC, thus the following signal processing. The first task concerns the amplification of the signal by means

of a LNA. Typically, the LNA is also the main contributor to the noise figure of the receiver [90]. The signal is then filtered via band-pass filter to exclude out-of-band contributions and is down-converted to a proper Intermediate Frequency (IF) or to baseband, according to the selected architecture.

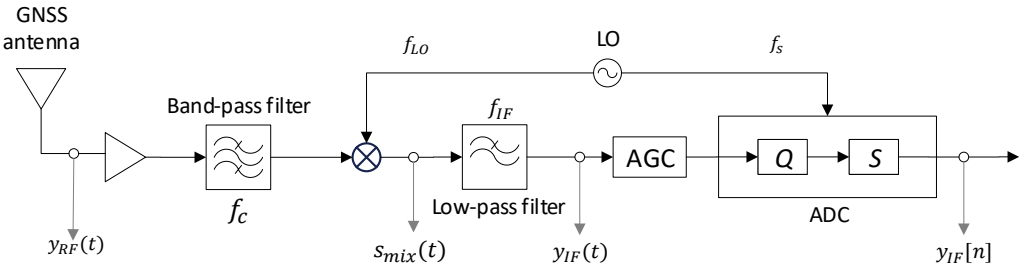

Figure 3.3: Front-end architecture for the Analog-to-digital conversion of GNSS RF signals.

Multiple Local Oscillator (LO)s can be used along with RF mixers to properly down-convert the RF signal to IF, thus optimizing harmonics suppression and amplification stages when present. The amplified and filtered signal $y_{\mathrm{RF}}(t)$ is hence down-converted to a given IF using LOs. A mixer simply multiplies the incoming signal by a sinusoidal tone locally generated by the LO. Neglecting the Doppler frequency shift f_d and the code delay τ, then the output signal $s_{mix}(t)$ can be written as

$$\begin{aligned} s_{mix}(t) &= \underbrace{y_{RF}(t)}_{\text{RF signal}} \cdot \underbrace{2\cos(2\pi f_{LO} t)}_{\text{LO}} \\ &= \sqrt{2P_R}c(t)\bar{c}(t)d(t)\cos\left(2\pi \underbrace{(f_{RF} - f_{LO})}_{\text{IF}} t + \varphi\right) + \\ &\quad \sqrt{2P_R}c(t)\bar{c}(t)d(t)\cos(2\pi(f_{RF} + f_{LO})t + \varphi) + \eta(t) \end{aligned} \tag{3.7}$$

where f_{LO} term is the local oscillator frequency, which depends on the overall frequency plan and on the desired IF. It is chosen to obtain $(f_{IF} = f_{RF} - f_{LO})$. The signal $s_{mix}(t)$ (3.7) is made by two terms: one with frequency centered at $(f_{RF} - f_{LO} = f_{IF})$ and the other one with frequency centered at $(f_{RF} + f_{LO})$. Since only the term at IF is desired, the higher order harmonics are filtered out. At the end of the filtering process, the component $y_{IF}(t)$ can be written as:

$$y_{IF}(t) = \sqrt{2P_R}c^{(b)}(t)\bar{c}^{(b)}(t)d(t)\cos(2\pi f_{IF} t + \varphi) + \eta_{IF}(t) \tag{3.8}$$

where $c^{(b)}(t)$ represent the filtered version of the in-phase transmitted PRN code, $\bar{c}^{(b)}(t)$ represent the filtered version of the subcarrier, η_{IF} is the filtered noise at the output of the IF filter which is still a white Gaussian noise with the same variance. The subscript (b) on the code and the subcarrier denote the fact that the pulses could be actually be modified by the IF filtering. On the other hand, the data are almost unaffected by the filtering effect due to their very low rate in GNSS systems.

Finally, the frequency down-conversion allows the ADC, which is the last component of the front-end chain, shown in Figure 3.3, to digitalize the signal at a suitable sampling frequency and quantization depth. ADC conversion indeed allows to transform the analog signal to a digital format and it is made of two steps: the discrete time conversion of the

signal (sampling) and the quantization. An Automatic Gain Control (AGC) can be used to automatically adjust the signal dynamics to fit the input requirements of the ADC.

The digital signal $y_{IF}(nT_s)$ after the ADC converter can be written as

$$y_{IF}(nT_s) = \sqrt{2P_R}c^{(b)}(nT_s)\bar{c}^{(b)}(nT_s)d(nT_s)\cos(2\pi f_{IF}(nT_s) + \varphi) + \eta_{IF}(nT_s) \tag{3.9}$$

Note that, in the following, the notation $y[n] = y(nT_s)$ will indicate a discrete-time sequence $y[n]$, obtained by sampling a continuous-time signal $y(t)$ with a sampling frequency $f_s = 1/T_s$. The digital signal $y_{IF}[n]$ finally becomes:

$$y_{IF}[n] = \sqrt{2P_R}c^{(b)}[n]\bar{c}^{(b)}[n]d[n]\cos(2\pi f_{IF}[n] + \varphi) + \eta_{IF}[n] \tag{3.10}$$

3.2.3 Acquisition

The acquisition strategy is adopted by GNSS receivers to estimate the ToA, τ, (which contains the information required for computing pseudorange measurements, thus user position and clock offset) and the Doppler frequency f_d (which contains the information required for computing the user velocity and the clock drift). Therefore, acquisition is exploited, after signal conditioning, to first detect which satellites are in view and estimate approximate value of τ and f_d. These values are therefore passed to the tracking block, that performs a local search for their accurate estimates. In this stage also the estimation of the carrier phase may be included. The acquisition system is made of a number of functional blocks that conceptually operate independently.

According to the estimation theory, it is possible to show that the ML estimate of the vector $p = (\tau, f_d)$, whose elements are two unknowns of $y_{IF}[n]$, is obtained by maximizing the function

$$\hat{\mathbf{p}}_{ML} = \arg\ \max_{\bar{\mathbf{p}}} \left| \frac{1}{L} \sum_{n=0}^{L-1} y_{IF}[n]\hat{r}_{IF}[n] \right|^2 \tag{3.11}$$

where L is the number of samples representing the incoming signal $y_{IF}[n]$, $\hat{\mathbf{p}} = (\hat{\tau}, \hat{f}_d)$ is a vector of test variables $\hat{\tau}$, and $\hat{f}_d = f_c + \hat{f}_{d,v}$ is the estimate of the true Doppler $\hat{f}_{d,v}$ plus the frequency shift f_c, defined in a proper support D_p which contains all the possible values which can be assumed by the elements of $p = (\tau, f_d)$. $\hat{r}_{IF}[n]$ is a locally generated signal

$$\hat{r}_{IF}[n] = c[n - \hat{\tau}]\ \exp(j2\pi(f_{IF} + \hat{f}_d)n) \tag{3.12}$$

where $c[n - \tau]$ is the local replica producing the PRN code, the subcarrier and potentially the secondary code.

The inner product of (3.11) is the CAF which is a two-dimensional cross-correlation function between the incoming code and a local replica of the desired signal to acquire. Therefore the CAF can be defined in the discrete time as

$$R(\hat{\tau}, \hat{f}_d) = \sum_{n=0}^{N-1} y_{IF}[n]\ c[n - \hat{\tau}]\ \exp(j2\pi(f_{IF} + \hat{f}_d)n) \tag{3.13}$$

where $y_{IF}[n]$ (3.10) is the received signal and $\hat{r}_{IF}[n]$ (3.12) is the local generated signal.

In order to decide whether a specific satellite is in view or not, detection is usually performed on the squared envelop of the CAF. This choice is adopted in order to be insensitive to the phase of the incoming signal and also to the sign of the bits in case a data channel is acquired

$$S(\hat{\tau}, \hat{f}_d) = |R(\hat{\tau}, \hat{f}_d)|^2. \tag{3.14}$$

According to a Pearson's hypothesis problem, S is compared with a predetermined threshold (V) in order to decide which hypothesis between H_0 ($S < V$) and H_1 ($S > V$) is true,

where H_0 and H_1 respectively represent the absence or presence of the desired peak. Once the decision is taken, the parameters $\hat{\tau}$ and $\hat{f}_d$ are taken. Such parameters are estimated within a lattice (or discrete mesh grid) named *search space*, as shown in Figure 3.4. The resolution of the code delay is usually a fraction of the code chip (i.e. $0.5 \cdot T_c$). On the other hand, the Doppler frequency typically ranges from 5 to 10 kHz. As an example, in GPS receivers, the Doppler shift range is estimated in the range ± 5 kHz, with respect to the carrier L1, according to the orbital period of GPS satellites [90].

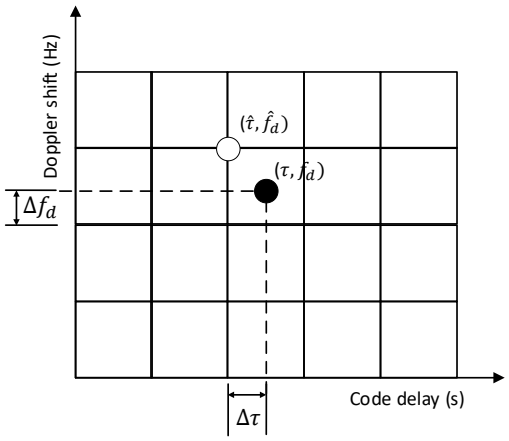

Figure 3.4: Simplistic scheme of search space for the rough estimation of Doppler shift and code delay in the acquisition stage.

In order to keep values like a 0.5 chip delay range, it is possible to compute the frequency step, as suggested in [89], as

$$\Delta f_0 = \frac{2}{3T} \tag{3.15}$$

where Δf_0 is the frequency bin width, expressed in Hz, and T coherent integration time, expressed in seconds. As an example, the CAFs evaluated over the search space on a Galileo PRN12 and PRN21 real signal are reported in Figure 3.5. The figure shows how the signal was acquired for PRN12 (left) and not acquired for PRN21 (right) as only noise was present.

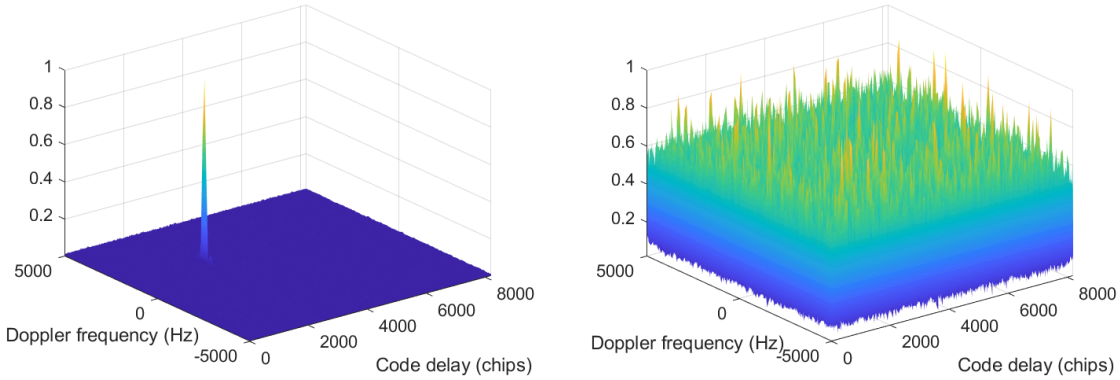

Figure 3.5: Example of CAF over the search space evaluated on a Galileo PRN12 (left) and for PRN21 (right) realistic signal. Image taken from [26].

There are several acquisition techniques reported in literature, that implement different types of searches which are characterized by a trade-off between computational complexity

(number of operations) and detection probability: two examples are the *serial search* and the *parallel search*. More details about these acquisition strategies can be found in [15] as well as in many books such as [89] and [131].

3.2.4 Tracking

The tracking stage is responsible for the refinement of the code delay, $\hat{\tau}$ and Doppler shift $\hat{f}_d$ estimated through the CAF. It has to continuously maintain and correct the best possible alignment between the two codes by means of closed loop operations.

The coupled loops required to maintain the best possible alignment between the two codes, are DLL for the code and a PLL for the carrier. The DLL continuously adjusts the local code replica to keep it aligned with the code of the incoming signal. When the two codes are perfectly aligned, the PRN code is removed from the signal (*code wipe-off*), leaving just the carrier modulated by the navigation messages. This signal is the input of the PLL, which estimates the carrier frequency (*carrier wipe-off*). After *carrier wipe-off* the DLL can synchronize the local carrier and the incoming carrier. This process continuously goes on during the receiver operations [89]. The generic tracking loop (DLL/PLL) architecture is shown in Figure 3.6. The two loops are initialized by the outputs of the acquisition phase ($\hat{\tau}^A$, $\hat{f}_d{}^A$).

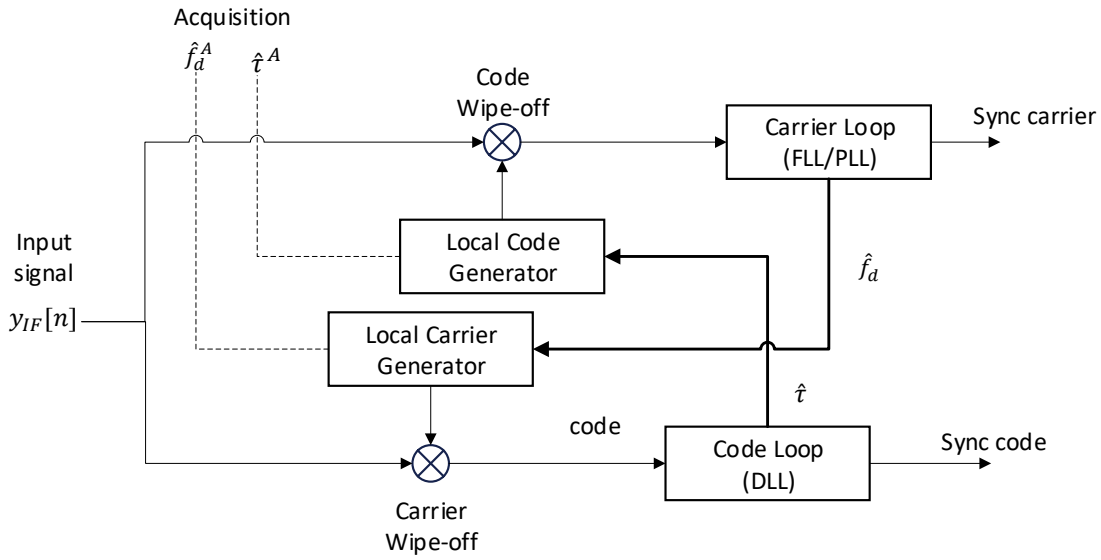

Figure 3.6: Generic tracking loop (DLL/PLL) architecture.

Code tracking loops

The code tracking loop is a feedback loop able to finely estimate the residual code delay by means of a DLL. Since the information about the relative delay between the incoming and the local code is contained in the correlation peak, the goal of DLL is to finely estimate the correlation value. However, GNSS receivers do not search the maximum of the correlation peak since it is not an effective approach and it would be dependent on the absolute peak value. They adopt a strategy insensitive to the absolute peak value, based of a discrimination function that is null only when the incoming and the local codes are synchronized (*null-seeker*).

Figure 3.7 shows the block diagram of a tracking system commonly used in digital GNSS receivers. It is possible to distinguish the code and the carrier tracking loops. Focusing for the moment on the code tracking loop, it is characterized by the design of the components of the loop, such as predetection integrators, code loop discriminator and code loop filter [89]. The first operation to be performed is the correlation between the incoming signal and different local code replicas, each characterized by a different delay. They are denoted as prompt (P), early (E) and late (L) versions. These correlation values are integrated to produce an output which is subsequently used by the discriminator function, denoted also *S-curve*. This discrimination function is unambiguous with respect to the delay, contrary to the normal correlation function. It is proportional to the difference of the values of the early and late correlators. A comprehensive description about the most common discriminator functions can be found in [89]. The output of the discriminator is given to the code loop filter, which combines the present and past values of the error signal. It generates corrections to the locally generated code in order to maintain the discriminator function output around zero, according to the null seeker principle. The E, P and L replica codes can be synthesized by the code generator, a shift register and the code Numerical Controlled Oscillator (NCO) which generates an accurate code replica of the incoming signal.

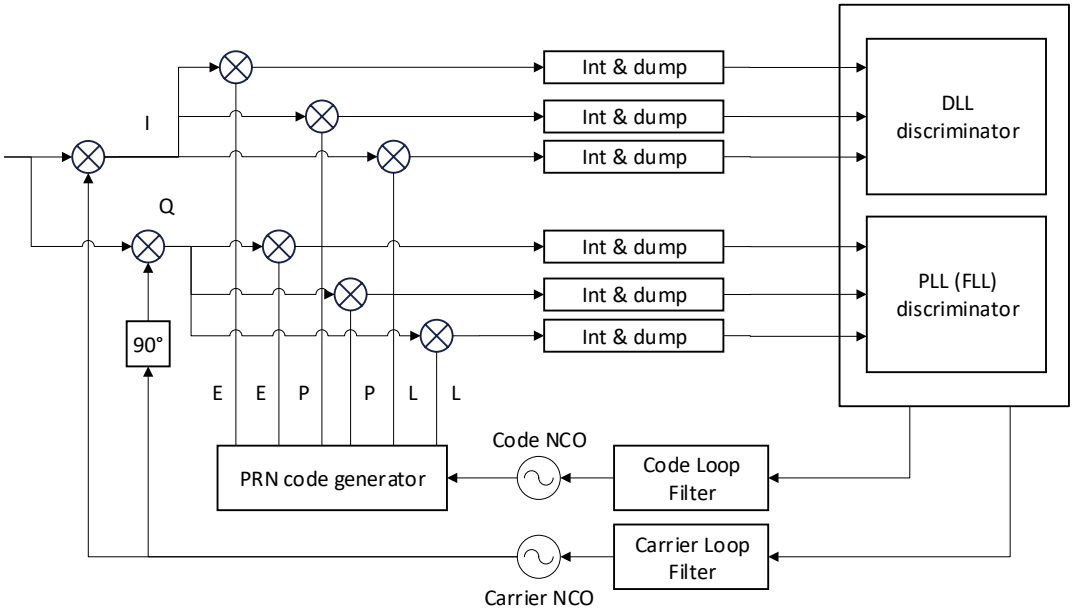

Figure 3.7: Block diagram describing the architecture of a generic code and carrier tracking loop for GNSS receivers.

The process performed by the DLL can be seen in Figure 3.8 where the incoming signal is correlated with the three replicas of the locally generated signal. When the replica code is aligned, the discriminator does not generate any error since early and late envelopes are equal in amplitude. On the other hand, if the replica code is misaligned, the early and late envelopes are unequal by an amount that is proportional to the amount of code phase error between the replica and the incoming signal [89].

Carrier tracking loops

The carrier tracking loop is a feedback loop able to finely estimate the frequency of a noisy sinusoidal wave and to track the frequency changes while the satellite is moving. In the GNSS community, one of the most used scheme is the PLL. It is capable to adjust the

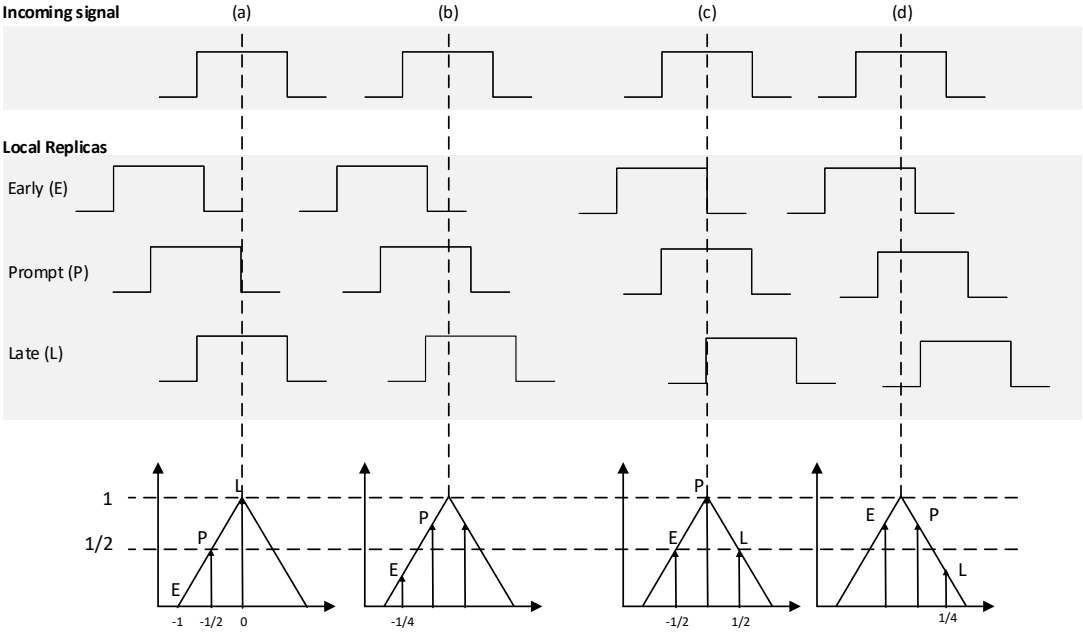

Figure 3.8: Example of code correlation phases: (a) replica code 1/2-chip early, (b) replica code 1/4-chip early, (c) replica code aligned, and (d) replica code 1/4-chip late. Figure taken from [89].

frequency of a local oscillator to match the frequency of the input signal. Also the phase of the received signal is estimated. It is worth noticing that, if the receiver is tracking a data channel, after the code wipe-off has been performed, the PLL would receive a continuous wave signal still modulated by the navigation data. Therefore, a PLL insensitive to phase transitions has to be adopted. Costas loop is one of the most used in the GNSS community. It tolerates the presence of data modulation on the received signal and then provides a carrier phase reference. Note that if data is not present in the signal, a pure PLL could be used. Another carrier tracking loop is the Frequency Lock Loop (FLL) which is able to track the frequency of the signal, ignoring the phase. In this case, PLL could be used to refine the value of the frequency provided by the FLL. Excellent references about the theory of PLL, FLL and Costas loops, that can be used in GNSS receives, is provided in many textbooks [89], [141] and [131].

The block diagram of a generic carrier tracking loop is shown in Figure 3.7. The principle of PLL is similar as the one of DLL. The local generator generates two sinusoidal signals, a sine and a cosine, in the two branches of the loop, called In-Phase (I) and Quadrature (Q) components. The role of the PLL is to align the instantaneous phase of the I component with the phase of the incoming signal. After the effect of the noise is mitigated by the integrators, the discriminator extracts the phase difference between the incoming signal and the local one. A loop filter can be included to further reduce the effect of noise. Once the phase difference is approximately zero, the PLL reaches a steady-state condition and the local waveform results aligned with the incoming carrier which is needed for the recovery of the code delay by the DLL.

After code wipe-off has been performed, assuming an unitary amplitude, the incoming signal is

$$y(t) = d(t-\tau)\cos(2\pi(f_{IF}+f_d)t+\varphi)+\tilde{\eta}(t) \tag{3.16}$$

where $\tilde{\eta}$ is the amplitude noise altered by non-linear trasformations applied during the tracking stage. Costas loop contains two multiplications. The input signal is multiplied by the local carrier wave as well as by its phase-shifted version by 90°, obtaining two different expressions for I and Q. After low-pass filtering, the two terms with the double intermediate frequency are eliminated and the following two signals remain

$$I = \frac{1}{2} d(t-\tau)\cos(\varphi) + \tilde{\eta}(t-\tau) \tag{3.17}$$

$$Q = \frac{1}{2} d(t-\tau)\sin(\varphi) + \tilde{\eta}(t-\tau) \tag{3.18}$$

The phase error of the local carrier phase replica can be found as

$$\frac{Q}{I} = \tan(\varphi) \tag{3.19}$$

By using this discriminator, it can be seen how the phase error is minimized when the correlation in the quadrature-phase arm is zero and the correlation value in the in-phase arm is maximum. Therefore, it is clear that the goal of the Costas loop is to try to keep all energy in the I (in-phase) arm. According to [89], which also describes other possible Costas discriminators the, the *arctan* discriminator in (3.19) is the most precise of the Costas discriminators, but it is also the most time-consuming.

The characteristics of a PLL can be seen in Figure 3.9. The phasor A is represented by the vector sum of I_P and Q_P. It tends to remain aligned with the I-axis. If a navigation bit transition occurs, it switches 180°. Costas loop is therefore capable to detect the bits in the data message, despite there is a phase ambiguity of 180°.

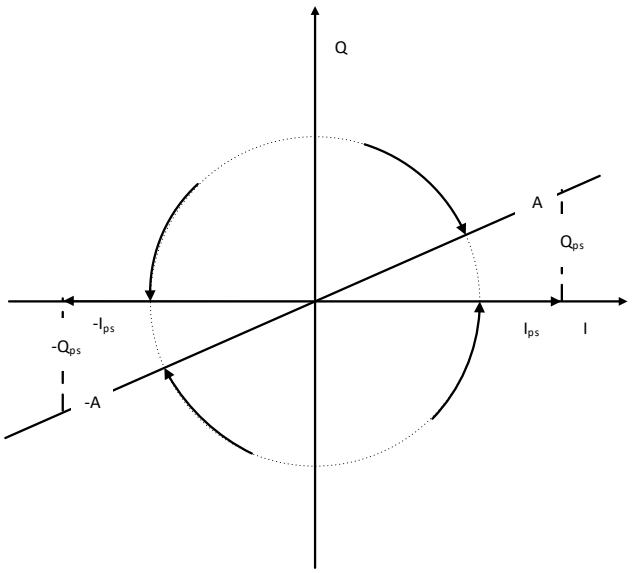

Figure 3.9: I, Q phasor diagram[89].

3.2.5 Navigation Message demodulation

Once the tracking loops are locked (i.e. the local code keeps the alignment with the incoming code and the local carrier is exactly a replica of the received one), the navigation data bits appear at the output of the Prompt correlator, on the in-phase branch of the

tracking loops. Considering the GPS L1 C/A code, using an integration time equal to the code period, we obtain a bit value every ms. However, due to the low signal power, real receivers usually set the integration time to 20 ms, which is the inverse of the navigation data rate (i.e. 50 Hz). The same example could be repeated considering the Galileo E1-B signal: in this case, a proper value of integration time is 4 ms, that corresponds to either the code period and the inverse of the navigation data rate.

The stream of data bits must be decoded to recover the message broadcast by the satellite. The navigation data follow the scheme defined in the GPS ICD in case of GPS [136], while all the information regarding the navigation message of the Galileo Open Service (OS) can be found in [58]. Since the navigation format is out of scope of this chapter an introduction is provided by showing the general structure of the GPS message. In Figure 3.10 the overall navigation data carried by GPS L1 C/A channel is depicted.

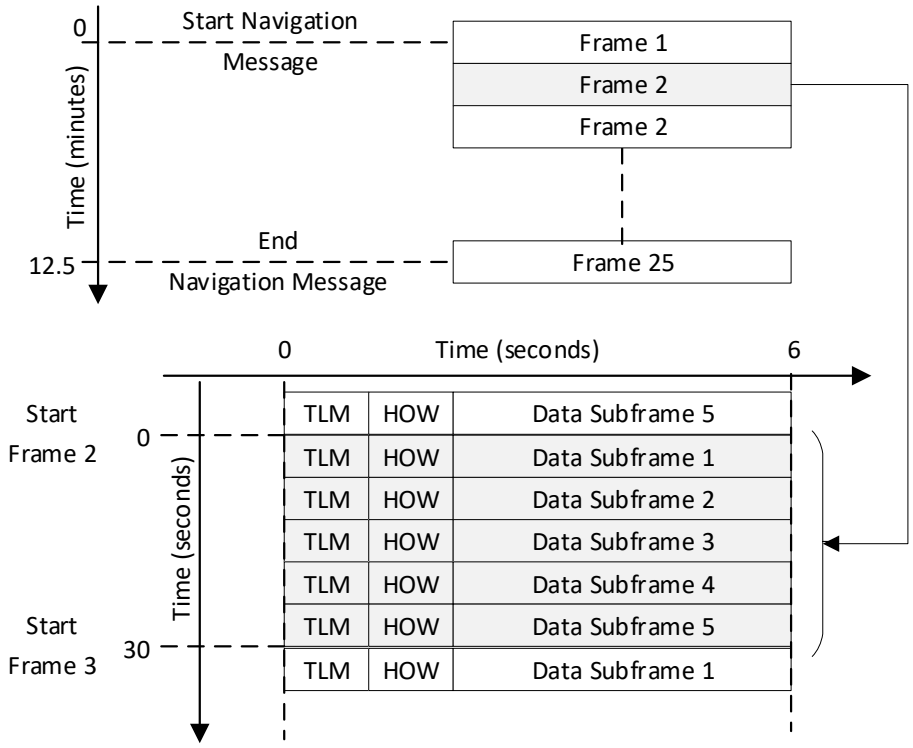

Figure 3.10: Structure of the navigation message included in the GPS civil signal, transmitted on L1 frequency.

The rate of the navigation data bits is 50 bits per second. The whole message is 12.5 minutes long and is divided in 25 frames. Each frame lasts 30 seconds and is further divided in 5 subframes, six seconds long. Each subframe of the navigation message always starts with two special words, the Telemetry (TLM) and the Handover word (HOW). In case of the Galileo E1 signal, the complete navigation message is transmitted on the data channel (E1-B) as a sequence of frames. A frame is composed of several sub-frames, and a sub-frame, in turn, is composed of several pages. The page is the basic structure to build the navigation message. Fig. 6 shows the structure of the Galileo data and an example of page for the E1-B message. Prior to the navigation data decoding, the receiver seeks for the preamble, a defined sequence of n bits, that marks the beginning of a subframe for the GPS L1 C/A, a page for the Galileo E1-B. A simple, but efficient, way to detect the preamble is to correlate the navigation data

stream with a local binary sequence equal to the preamble. A maximum is detected when such a local sequence is aligned with the preamble. Naturally, the bit pattern used for the preamble can occur anywhere in the received data stream, thus an additional check must be carried out to authenticate the real preamble (e.g. in case of GPS, only when the maximum of correlation is found exactly every 6 seconds). When the beginning of the subframe is identified, the content of the subframe can be decoded. The receiver retrieves all the orbital parameters (i.e. ephemeris) necessary to compute the satellite position corresponding to the transmission of the subframe. Through the process used for navigation data decoding, the receiver is able to understand which subframe and word a certain bit belongs to. In this way, the receiver can have an exact, precise and real-time understanding of each sample/bit broadcast by the satellite.

3.3 Pseudorange Measurements

In this thesis, pseudorange measurements will be distinguished according to the level of correction (i.e. error compensation) which is applied. For the sake of clarity we will refer to the following three classes:

- **raw pseudorange measurements** are obtained as a difference between the transmission and the reception time of a navigation signal, obtained with misaligned clocks. Such a class of measurements is provided by high-end receiver and it has recently become available in Android devices [75].
- **corrected pseudorange measurements** are obtained applying error corrections to compensate for unwanted biases affecting the propagation time of the signal. Corrected pseudoranges are the input data of the PVT computation.
- **smoothed pseudorange measurements** are code pseudorange measurements refined through Doppler or carrier phase measurements in order to reduce the variance of the estimation [135]. They are extensively used in professional receivers and their analysis within specific application was included in [135]

3.3.1 Raw measurements computation

Even assuming a perfectly synchronous transmission time among the satellite payloads, the reception time of the preambles will result different due to the different propagation paths. In order to estimate the pseudoranges, this time misalignment has to be compensated according to one of the paradigms known as *Common Transmission Time* and *Common Reception Time*. According to the first approach, since the satellites are assumed to be synchronous, the same preamble is assumed being broadcast at the same time instant, t_{TX} . The signal is then received by the user at different time due to the propagation delays, as shown in Figure 3.11. Such time instant is set as common reference time for all the received signals. Thus, the first received signal will belong to the nearest satellite and the beginning of its first subframe will be set as reference. For each channel, the receiver has to count the amount of time elapsed from the reception of the reference subframe and the reception of the same subframe of each tracked signal. By knowing the relative time difference, the receiver is able to evaluate the pseudoranges [143].
In the Common Reception Time, instead, the time instant corresponding to the reception of the first Telemetry word (TLM) is set as common receiving time t_u^R over all the channels. Moreover, the corresponding satellite is set as reference. For each channel, the receiver

computes elapsed time $\delta t_{rx,i}$ between frame reception time $t^R_{rx,i}$ and reference t^R_u, as expressed in (3.20).

$$\delta t_{rx,i} = t^R_u - t^R_{rx,i} \tag{3.20}$$

For the reference satellite, the receiver reads in the previous subframe the Hand-over word (HOW), which contains the transmission time $t^{GNSS}_{tx,i}$ in the GNSS reference time. Due to the misalignment between the GNSS time scale and the receiver time scale, the difference between the reception time in the two scales is an unknown bias b_u.

$$t^R_{rx,i} = t^{GNSS}_{rx,i} - b_u \tag{3.21}$$

At first computation, b_u cannot be estimated, so the propagation time τ_1 is set to a nominal expected value between 65 ms and 85 ms and the reference pseudorange is computed as 3.23.

$$\tau_1 = t^{GNSS}_{rx,1} - t^{GNSS}_{tx,1} \tag{3.22}$$

$$\rho_1 = \tau_1 \cdot c \tag{3.23}$$

After this step, the difference between each satellite and the reference one is calculated as in (3.24) and each pseudorange is written in relation to the first one (3.25). Since the propagation time at first time is not estimated but only fixed, all the pseudoranges will have an additional error $c \cdot b_u$ due to the time misalignment.

$$\Delta t_i = \delta t_{rx,i} - \delta t_{rx,1} \tag{3.24}$$

$$\rho_i = \rho_1 + + c \cdot b_u + c \cdot \Delta t_{rx,i} \tag{3.25}$$

In the Figure 3.11, a scheme is proposed to understand how a common reception time is fixed for all the tracking channels.

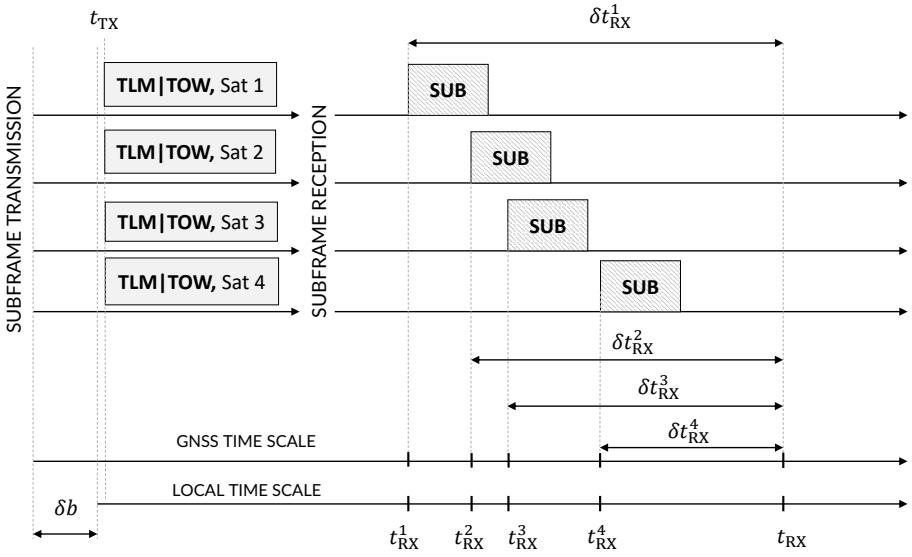

Figure 3.11: Common reception time diagram.

What is obtained at the end of this process is a measure of the distance between the satellite and the receiver, still affected by several errors and by the receiver clock bias, b_u, namely a *raw pseudorange*.

3.3.2 Pseudorange correction and PVT

Pseudoranges are obtained by means of time measurements which can be severely affected by errors. An overview of such errors and a brief description of the correction process carried out by the GNSS receiver are contextually explained hereafter.

GNSS satellites are all equipped with atomic clocks which stably discipline timing operations such as signal generation and broadcast [90]. Although their well-known stability, ground segments of each system are responsible to monitor the offset of on-board clocks w.r.t. a reference time-scale and to update the clock correction field carried by the navigation message. The satellite clock correction is hence independently updated for each satellite. Such a correction also takes into account the relativistic effect and is computed by the receiver by means of a second order polynomial including satellite clock bias, clock drift and frequency drift of the on-board clock [136].

Despite these deterministic biases which are effectively compensated through navigation data, the signal components are further delayed as they propagates trough the atmosphere [90] by stochastic quantities. A set of additional delays are then responsible for an overall time shift, δt_D, of the expected reception time, according to

$$\delta t_D = \delta t_{atm} + \delta t_r + \delta t_{mp} + \delta t_{hw} \tag{3.26}$$

where:

- δt_{atm} delays due to the atmosphere. The propagation velocity of the signal through this mean changes accordingly to the refraction indexes of the different layers. Indeed, free electrons released by ionized molecules in the ionosphere influence the refractive index of this upper layer. Also in the troposphere the refractive index alters phase and group delays of RF signal with frequency lower than 15 GHz.
- δt_r errors due to additive noise and additional, intentional or unintentional interferences.
- δt_{mp} multipath offset (if only reflected signal is received). Multipath reflections due to multiple scattering significantly induce highly stochastic errors in the pseudorange measurements. The unpredictability of multipath phenomena makes such impairments usually hard to be detected and compensated.
- δt_{hw} delay induced by receiver hardware. These errors are typically ignored due to their smaller impact w.r.t. other contributions. However, electronics components such as RF and IF filters, LNA, mixers, splitter and other RF interfaces are typically responsible for huge biases (higher than 1μs). Although this error cannot be neglected for timing application, it is irrelevant in terms of positioning computation cause it will be included in the user clock bias obtained as output from the PVT.

Raw pseudorange measurements are always corrected prior to be used within the PVT according to the scheme in Figure 3.12. It can be noticed that the computation of the PVT is essential to the effective exploitation of ionospheric and tropospheric error models, thus to a higher accuracy in the positioning computation [90]. Further details on the pseudorange error correction and the respective atmospheric models can be found in the ICDs.

3.3.3 GNSS software receivers

In the last decades the increasing interest in satellite navigation fuelled the research towards the development of high-performance GNSS receivers. Provided the lower data rates

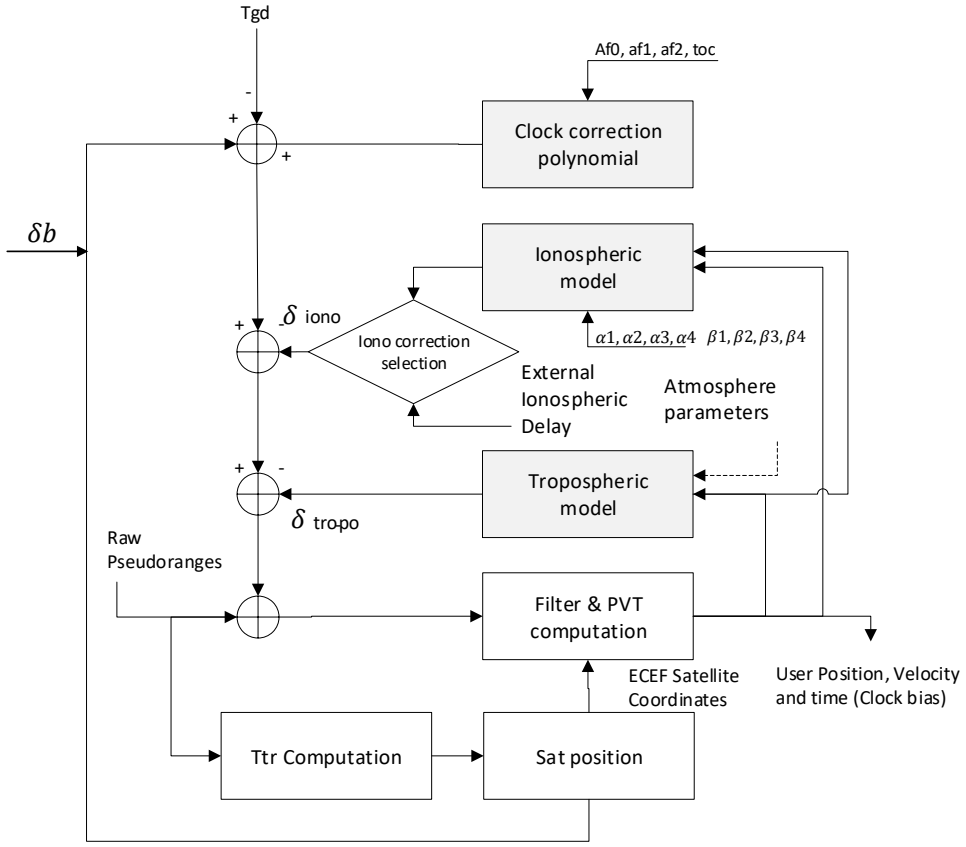

Figure 3.12: Pseudorange correction scheme reproduced from the GPS ICD [136].

involved in GNSS w.r.t. the ones which can be encountered in modern communication technologies, GNSS receivers can be effectively emulated through Software Defined Radio (SDR) implementation. An analysis of the SDR approach oriented to GNSS was presented in [112]. A brief recap of the evolution of the GNSS software receiver is instead presented in [201] in which the main challenges are described along with the technical solutions exploited to cope with hardware and software limitations. Valuable SDR tools for research and development in GNSS were designed according to Hardware (HW)/Software (SW) mixed architectures or *fully-software* architecture. In the context of this research, a wide usage of SDR-based fully-software receiver was done to analyse ad-hoc scenarios, thus allowing reproducibility of the scenario in laboratory and in parallel the access to data at any level of the processing chain. When used, the fully-software chain was fed by a general purpose front-end, namely Ettus Research Universal Software Radio Peripheral (USRP) N-210 or B-210 providing digitalized signals in form of binary files (.bin). The digitalized signal, $y_{IF}[n]$, was represented through digital samples with a quantization depth from 2-to-8 bits and a sampling frequency, f_s of 16 Msps within a bandwidth of 5 MHz. The use of a software receiver allowed to access all acquisition, tracking and post-processing data, thus providing natively pseudorange measurements belonging to all the three classes described in Section 3.3

Details about the implementation of the NavSAS MATLAB-based fully-software receiver and the modifications to its architecture will be discussed accordingly to the content of the chapters.

3.4 Networked GNSS Mass-market receiver: a concept

As discussed in Chapter 2, network connectivity has been exploited in GNSS to provide differential corrections, or alternatively to reduce the Time-to-First-Fix (TTF) by providing aiding information in peer-to-peer receiver [110, 46, 118, 91, 111, 149]. Differently from these early approaches, this thesis is focused on a different usage of the network connectivity which aim at extending the available information to the positioning problem including collaborative ranging measurements. In order to accomplish this task, GNSS receivers are expected to provide a network interface enabling the inter-agent communication, as shown in Figure 3.13 which extends the general architecture shown in Figure 1.1. This functional block is in charge to provide raw pseudorange measurements coming from networked receivers to the Collaborative Ranging Unit (CRU). The CRU is then responsible of combining *local* and *external* measurements into inter-vehicle ranging measurements to be further integrated in a hybrid PVT processor.

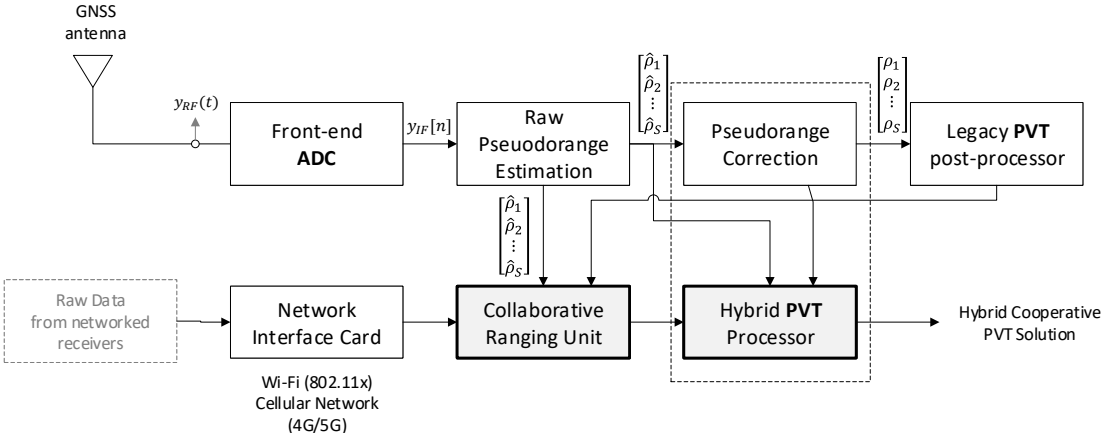

Figure 3.13: High-level scheme of the concept of a networked GNSS receiver with a PVT stage aided by auxiliary measurements retrieved from collaborating receivers.

The high-level scheme shown in Figure 3.13 describes the architecture of a networked GNSS positioning system designed to implement the proposed hybridization scheme. As emphasized by the gray boxes in Figure 3.13, the following chapters of this thesis will address both numerical and experimental analysis of the algorithms suitable for the implementation in the *Collaborative Ranging Unit* and in the *Hybrid PVT Processor*. The proposed approach foresees a refinement of the PVT solution originally performed by a single agent (referred hereafter as target , named *target agent* which acts according to the following work-flow:

- *Coarse Position and Time estimation.* The target agent iteratively computes a coarse Position-Time estimation at a given time instant, thus estimating an absolute timestamp of the correspondent positioning solution and measurements set. This task was explored in its basic shape in Chapter 2 discussing about fundamentals on GNSS PVT solution.

- *Measurements synchronization* or *epochs misalignment compensation.* The task is performed by the CRU prior to combine the local and external measurements. In fact, according to the scheme depicted in Figure 3.14, asynchronous receivers retrieves measurements set and positioning solutions independently.and according to the established reception time.

The time-compensation is hence fundamental to ensure the time-consistency of the heterogeneous pseudorange and Doppler measurements w.r.t. the satellites and receivers positions. Being a pre-requisite for the combination of heterogeneous GNSS measurements, this task will be treated accordingly to the baseline computation method.

- *Collaborative inter-agent ranging.* The target agent retrieves the available observables from the agents and computes collaborative range contributions after the time-alignment of the measurements. The algorithms of interest to perform the task will be discussed in detail in Chapter 4. The *collaborative ranging unit* exploits external GNSS measurements provided by the collaborating agents through a network link.

- *Fine PVT estimation.* The target agent integrates the inter-agent information along with the coarse estimate of the available agents through a hybrid navigation filters. Details about the hybrid solution investigated within this thesis will be provided in Chapter 6.

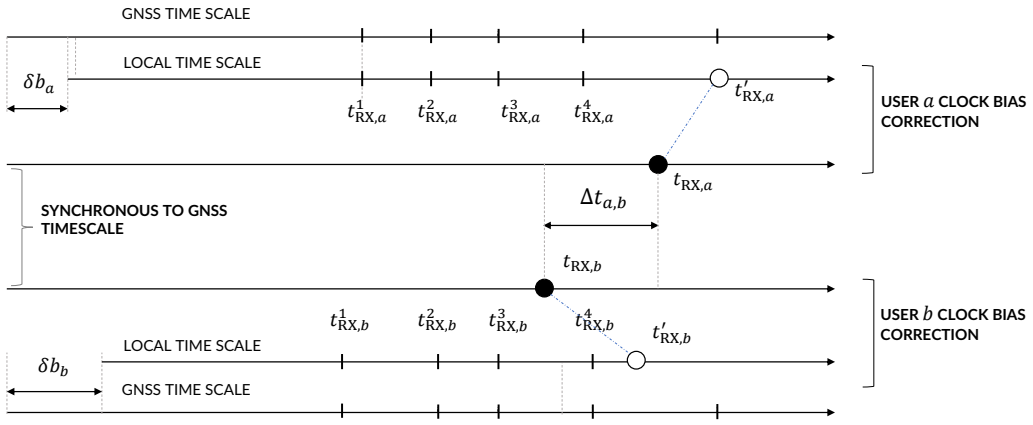

Figure 3.14: Asynchronous measurements and PVT epochs in GNSS independent receivers.

Nowadays several mobile devices integrate a considerable number of modules devoted to both RF transmission and reception. Among these, Wi-Fi™ IEEE® 802.11, Bluetooth®, GNSS, and cellular modules are all aggregated in portable electronic devices such as smartphones and tablet, thus enabling a number of additional, complementary positioning solutions.

Chapter 4

GNSS-based collaborative ranging algorithms

As discussed in the introductory chapters of this thesis, the CP algorithms rely on the exchange of information among networked users with the aim of exploiting such additional information locally. The estimation of the reciprocal distance among navigating agents is one of the most relevant information to be carried out by CP algorithms. In GNSS literature, the problem is typically referred as *baseline estimation* [90, 83], while it is known as *inter-agent distance estimation* [87, 139, 33] or simply *ranging* in other domains such as in automatic control, mechanics and robotics [133, 161]. The scope of this chapter is to recall the state-of-the art of GNSS-based ranging methods which will be analysed and implemented in the following chapters.

A set of fundamental definitions concerning agent-to-agent distance estimation is provided in Section 4.1 to define the needed nomenclature. A description about LoS ranging sensors and GNSS differential methods is discussed to contextualize the research and to define the gap w.r.t. different sources of ranging information in Section 4.1.1 and Section 4.3.1, respectively. GNSS-based baseline estimation methods inherited from DGNSS are then presented in detail through their analytical definitions. Eventually the IAR is presented as an extent of the state-of-the art of the GNSS-based baseline computation solution.

4.1 Baseline: Fundamental Definitions

This section provides a set of general definitions and a background about state-of-the art techniques for the estimation of the *baseline*.

In conformity to the GNSS literature, the term *baseline* will refer to the *distance vector* or *displacement vector* between the estimated positions of two independent agents.

Let us suppose to know the true locations $\mathbf{x}_A(t_k) = [x_A(t_k) \quad y_A(t_k) \quad z_A(t_k)]^\top$ and $\mathbf{x}_B(t_k) = [x_B(t_k) \quad y_B(t_k) \quad z_B(t_k)]^\top$ of two agents at a given discrete time instant, t_k, referred to a common time scale and a common reference frame. Their true *baseline vector* at t_k can be expressed through its orthogonal components in a Cartesian frame, as

$$\mathbf{d}_{AB}(t_k) = \begin{bmatrix} x_A(t_k) - x_B(t_k) \\ y_A(t_k) - y_B(t_k) \\ z_A(t_k) - z_B(t_k) \end{bmatrix} = \begin{bmatrix} \Delta x_{AB}(t_k) \\ \Delta y_{AB}(t_k) \\ \Delta z_{AB}(t_k) \end{bmatrix} \tag{4.1}$$

and their true *baseline length* is hence defined through

$$d_{AB}(t_k) \triangleq ||\mathbf{d}_{AB}(t_k)|| = \sqrt{(\Delta x_{AB}(t_k))^2 + (\Delta y_{AB}(t_k))^2 + (\Delta z_{AB}(t_k))^2} \tag{4.2}$$

which is, by definition, the norm of $\mathbf{d}_{AB}(t_k)$, obtained by means of the Euclidean distance between $\mathbf{x}_A(t_k)$ and $\mathbf{x}_B(t_k)$.

While the *baseline length*, (4.2), is a scalar quantity which is not necessarily defined for a specific reference frame, the orthogonal components of a *baseline vector*, (4.1), can vary according to the selected reference frame, as depicted in 2D in Figure 4.1. The quantity $d_{AB}(t_k)$ is indeed invariant w.r.t. isometric transformations (i.e. translations and rotations) of any Euclidean reference frames. Therefore, by considering a local frame centred in $\mathbf{x}_A(t_k)$ and oriented according the heading of agent A, the *baseline vector* shows a different set of orthogonal components w.r.t. the one obtained in an absolute reference frame (4.1b).

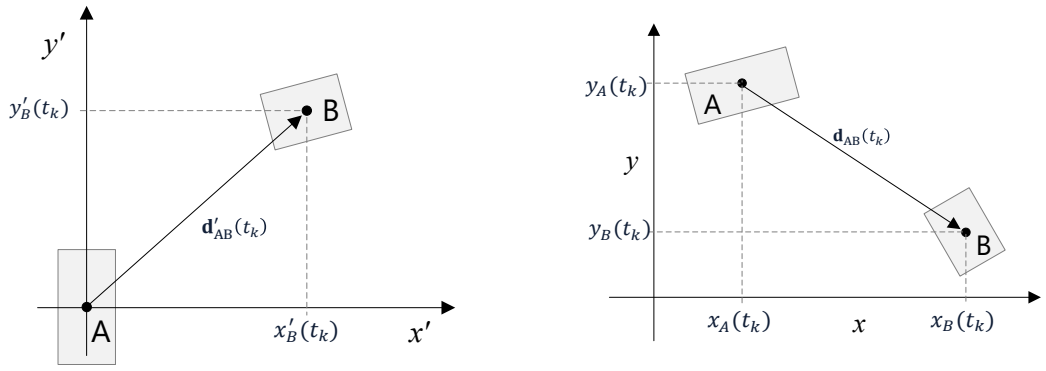

(a) Relative Cartesian reference frame

(b) Absolute Cartesian reference frame

Figure 4.1: Baseline vectors shown in different 2D Cartesian reference frames.

However, if the local reference frame in Figure 4.1a is obtained by means of isometric transformations of the absolute frame in Figure 4.1b, the equivalence $d_{AB}(t_k) = d'_{AB}(t_k)$ holds besides $\boldsymbol{d}'_{AB}(t_k) = \boldsymbol{d}_{AB}(t_k)\mathbf{R}$, where $\mathbf{R}$ is the rotational matrix used to define the local frame (further details about reference frames are recalled in Appendix A. Despite of the specific reference frame, it is trivial noticing that knowing the orthogonal components of $\boldsymbol{d}_{AB}$, the computation of d is performed through (4.2). However it is worthy to remark that sensor-based ranging mostly addresses direct estimation of d_{AB}.

4.1.1 Sensor-based baseline estimation

In the last decades, exteroceptive sensors such as UWB, Light Detection and Ranging System (LiDAR) and ultrasonic (i.e. Sound Navigation and Ranging (SONAR)), have been extensively employed in robotics and vehicular applications for the estimation of (4.2), providing high accuracy, precision and availability rate of the measurements [34]. These approaches are based on a ToA estimation, namely on the principles of monostatic and bistatic RAdio Detection And Ranging (RADAR), thus relying on the sensing of scattered RF signals. Therefore, several works addressed the ranging problem in many application fields by exploiting such LoS technologies [137, 198, 195]. A remarkable number of contributions in robotics and vehicular applications addressed the enhancement of CP by means of such sensor-based *inter-agent measurements* [59, 39]. Unfortunately, the operational capabilities of RF sensors are typically limited by LoS constraint, so that they are mostly implemented for close objects localization (e.g. pedestrian detection) and for short-range relative positioning applications addressing proximity awareness (e.g. automatic cruise control, collision avoidance, park assistance). Furthermore, sensor-based ranging is typically affected by a degradation of the performance as the magnitude of the measurement increases [34]. In ideal

conditions in fact, many of these devices can indeeed determine range measurements with a centemeter-level accuracy [34], [199], thus providing useful additional navigation data to multi-agent navigation and positioning systems. Single or fixed RF ranging sensors cannot easily provide information in form of range vector, therefore synchronized arrays (e.g. SONAR and UWB) or rotating sensors (e.g. LiDAR) are typically implemented in several fields for proximity awareness as well as for indoor navigation. Similarly, vision-based systems such as monocular and binocular digital cameras, have been extensively implemented to the estimation of both *baseline length* and *baseline vector* [23, 21, 87]. Besides a less accurate estimation, these systems enable a further processing stage devoted to object recognition, which is not negligible in LiDAR and UWB in terms of computational complexity (see for example [96, 184]). As, shown in 4.1, the orientation estimation is fundamental for the usage of such relative information within absolute positioning framework. To this goal, the attitude information provided through the integration of INS is essential as well as the introduction of proper *mechanization equations* to reliably convert the ranging information to an absolute frame. It is worth mentioning thath sensor-based ranging typically suffers of negligible delays in the determination of the *baseline length*, mainly due to the ToF of the RF signals and to the processing time of the retrieved measurements. Besides the extensive literature about sensor-based CP, many theoretical investigations have assumed high availability of such inter-agent measurements, often over-simplifying their statistical models and neglecting the cross-correlation among such data [178, 19, 142].

4.2 Absolute Positions Distance (APD)

GNSS receivers are often considered as sensors. Despite of this misleading but frequent definition, we could state that two GNSS receivers can be used as a passive distance sensor. As anticipated indeed, the most intuitive way to obtain an estimate of (4.2) is referred to APD, which needs to consider the fact that the positions $\mathbf{x}_i(t_k)$ and $\mathbf{x}_j(t_k)$ are the solutions of two disjoint estimation processes such as the multi-lateration foreseen in GNSS. The *baseline length* is hence estimated through

$$\hat{d}_{ij}^{(APD)}(t_k) = ||\hat{\mathbf{x}}_i(t_k) - \hat{\mathbf{x}}_j(t_k)||. \tag{4.3}$$

Equation (4.3) is the *baseline length* estimated by computing the Euclidean distance between the estimated positions $\hat{\mathbf{x}}_i(t_k)$ and $\hat{\mathbf{x}}_j(t_k)$ as

$$\hat{d}_{ij}^{(APD)}(t_k) = \sqrt{(\hat{x}_i - \hat{x}_j)^2 + \left(\hat{y}_i - \hat{y}_j\right)^2 + (\hat{z}_i - \hat{z}_j)^2}. \tag{4.4}$$

$\hat{d}_{ij}^{(APD)}(t_k)$ is affected by the overall uncertainty of the positioning solutions (i.e. GDOP and potential biases according to the position error model in Chapter 2). The estimation error affecting $\hat{d}_{ij}^{(APD)}(t_k)$ can be caused by different unexpected effects in the positioning computation but the specific error contribution cannot be easily discriminated as for other techniques.

By generalizing the problem according to the retrieval of asynchronous positioning solutions

$$\hat{d}_{ij}^{(APD)}(t_k) \simeq ||\hat{\mathbf{x}}_i(t_i) - \hat{\mathbf{x}}_j(t_j)||. \tag{4.5}$$

where t_i and t_j are two different discrete time instants referred to a common time scale. This time misalignment causes a major issue in the determination of a reliable baseline length measurement, turning the estimation in non-real-time process. A possible way to compensate

for this time-inconsistency could be the extrapolation of the positioning solution of the local receiver i at the time t_j but this will provide an outdated solution w.r.t. the actual agents' positions.

Assuming the mitigation of the time offset, let suppose that agent B transmits to the agent A its own position estimate at time t_k, namely $\mathbf{x}_B(t_k)$. Due to the network delay, δt, the information is received by A at time $t_k+\delta t$ when the two agents are located at $\mathbf{x}_A(t_k+\delta t)$ and $\mathbf{x}_B(t_k+\delta t)$, respectively. The true baseline vector $\mathbf{d}_{AB}(t_k+\delta t)$ cannot be computed and two approximated distances can be computed:

$$d_{AB}(t_k) = ||\mathbf{x}_A(t_k) - \mathbf{x}_B(t_k)|| \tag{4.6}$$

$$d'_{AB}(t_k) = ||\mathbf{x}_A(t_k + \delta t) - \mathbf{x}_B(t_k)|| \tag{4.7}$$

Equation (4.6) refers to outdated information while (4.7) is a time-inconsistent solution. The two solutions can approximate the true baseline length depending on the dynamic of the systems.

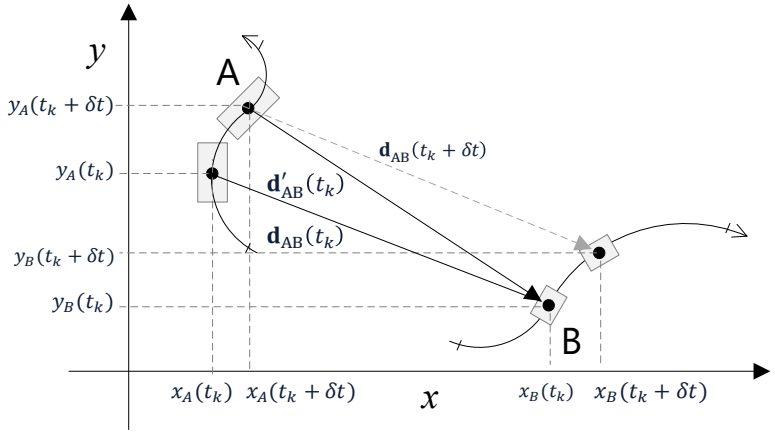

Figure 4.2: Geometrical effect of the network delay on the baseline estimation in dynamic scenario.

As shown in Figure 4.2, depending on the dynamics of the agents the actual delay in the computation of the baseline length can lead to misleading information.

Intuitively, the APD cannot be used to improve the positioning estimation because it is directly computed through the estimate itself. Although the method is ineffective for the enhancement of positioning and navigation solutions, its error model involves multivariate statistics and it is useful for more advanced GNSS-based solutions such as Single Difference (SD) and DD, as detailed hereafter.

4.2.1 Error modelling of Euclidean distance in GNSS positioning solutions

The following analysis has been presented in [124] to provide a reference statistical distributions of the distance between two independent GNSS fixes.

Distribution of GNSS positioning solutions

Considering a scenario not affected by multipath, the independence of the elements of the position vector estimated by an agent is not verified due to their dependency of the satellite geometry [193, 100].

An example of distributions of two static GNSS solutions is shown in the two-dimensional example of Figure 4.3 along with the visualization of their covariance through error ellipses. They are obtained by simulating the positioning problem with different sets of satellites and *corrected pseudorange* measurements. The measurements are created through true range values affected by independently generated White Gaussian Noise (WGN) samples. It can be noticed that X_j presents an evident correlation of its components thus, showing a non-diagonal error covariance matrix, $\sigma_{xy,i} \neq 0$. On the opposite, X_i is characterized by a quasi-diagonal covariance matrix ($\sigma_{xy,i} \simeq 0$) but the errors affecting its components are not identically distributed, formally $\sigma_{x_i} > \sigma_{y_i}$.

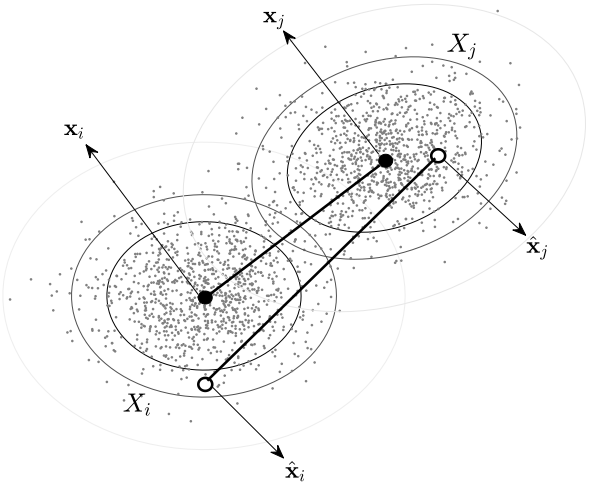

Figure 4.3: Example of bivariate Gaussian distributed PVT solutions (Horizontal positioning solution) with a graphical visualization of the error covariance matrices in terms of 95% and 99% confidence intervals.

According to error model defined in Chapter 2, the elements of the positioning solutions of two GNSS receivers can be considered pairwise-independent assuming independent residual noise components on the respective pseudorange measurements. With this in mind, each differential term in the *baseline vector* is still a Gaussian random variable resulting from the difference of independent Gaussian variables.

In a realistic scenario the elements of the *baseline vector* obtained through the APD are strongly cross-correlated. Therefore the distribution of $d_{ij}^{(APD)}$ in a bi-dimensional frame follows a generalized Nagakami distribution considering non null covariances of the elements or a generalized Rice distribution considering correlated non-identically distributed elements. In the following we aim at inspecting the approximation of this general distribution with a Gaussian distribution by identifying the validity conditions through the Batthacharyya distance.

On the generalization of APD error distribution

For readability reasons, the time dependency indicated in the variables will be dropped without any loss of generality.

By recalling fundamental probability theory, let us consider X_i and X_j as generic random variables modelling GNSS positioning solutions of two receivers. By assuming potential

dependency between the distributions, it can be shown that the distribution of the difference is defined as

$$Y_{ij} = X_i - X_j \sim \mathcal{N}(\mathbf{x}_{ij}, \mathbf{P}_i + \mathbf{P}_j + 2\mathbf{P}_{ij}) \tag{4.8}$$

where $\mathbf{x}_{ij} = \mathbf{x}_i - \mathbf{x}_j$ is the difference of the mean vectors and $\mathbf{P}_{ij}$ is the cross-covariance matrix of the two distributions. By assuming pairwise-independent positioning solutions, the (4.8) can be approximated by neglecting the cross-covariance terms. Let us remark that the set of satellites used to compute the PVT solution only affects the Dilution Of Precision (DOP), thus close receivers could easily experience similar covariance matrices but this does not imply dependency between pairs of coordinates.

The random variable $W = ||Y_{ij}(t_k)||$ models the distribution of the norm of a vector of correlated Gaussian random variables w.r.t. the selected reference frame. Let us recall indeed that according to the definition of the baseline vector as in (4.1), given a non diagonal covariance matrix, the correlation among the elements cannot be neglected.

The purpose of this analysis is to understant the behaviour of W and the conditions that allow to approximate it to a Gaussian distribution fitting its real counterpart and being suitable for GNSS applications. The Bhattacharyya distance [12], D_B, for multivariate normal distributions has been observed to provide a heuristic for the validity of such a Gaussian approximation. It represents a measure of the distance of the two distributions by considering both the difference between the mean values, and the combined covariance matrix, thus being independent from the simulated or experimental scenarios.

The Bhattacharyya distance is computed as

$$D_B(\mathbf{X}_i, \mathbf{X}_j) = \frac{1}{8} (\bar{\mu})^T \mathbf{P}^{-1} (\bar{\mu}) + \frac{1}{2} \ln \left(\frac{\det \mathbf{P}}{\sqrt{\det \mathbf{P}_i \det \mathbf{P}_j}} \right) \tag{4.9}$$

where

$$\bar{\mu} = \mathbf{x}_i - \mathbf{x}_j, \boldsymbol{P} = \frac{\boldsymbol{P}_i + \mathbf{P}_j}{2} \tag{4.10}$$

A comparison between real and modelled Gaussian distributions was performed by letting the (4.9) increase. The increment of D_B was ensured by increasing the distance between the mean values of the two distributions or alternatively, by reducing the magnitude of their covariance matrices.

Figure 4.4a shows the results of Monte Carlo simulations performed to verify the bin-by-bin matching accuracy of the approximated Normal distribution with respect to the real one in terms of Mean Square Error (MSE) [14]. The decreasing trend, shown in Figure 4.4b, allows to conclude that the PDF of the APD between two multivariate Gaussian distributed random variables is a general distribution which approximates the behaviour of Gaussian distribution with the increasing of the Bhattacharyya distance.

It can be shown that in case of bivariate variable, a Kolmogorov-Smirnov Goodness of Fit (GoF) test failed to reject the null hypothesis (baseline length distributed accordingly to a Gaussian distribution) for $D_B > 5$ at 5% of confidence level.

We found that such a Gaussian approximation is reasonable for the APD computed for two general positioning solutions when their Bhattacharyya distance grows, in practice when the magnitude of the elements of the covariance matrix are small, or the distance between their mean assumes high values.

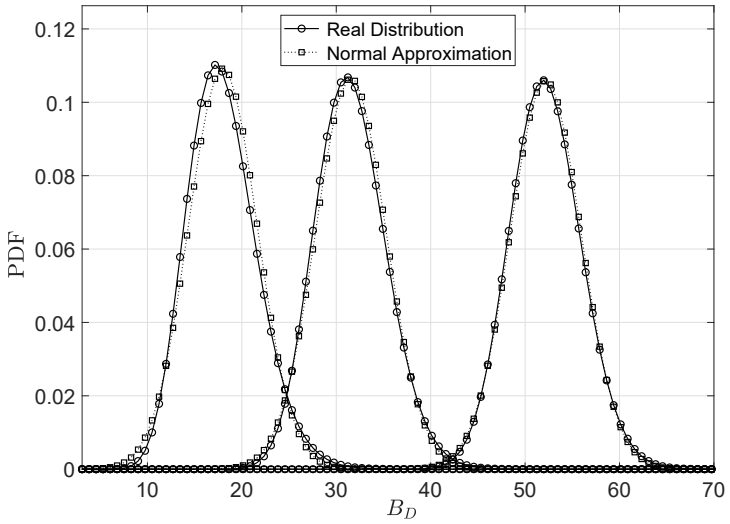

(a) Qualitative comparison between real and approximated probability distributions

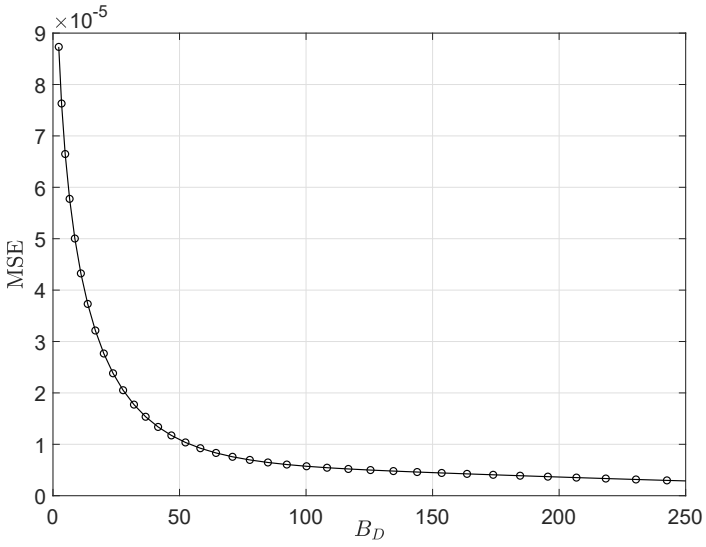

(b) Sample-based MSE reduction by increasing D_B

Figure 4.4: APD distribution approaching Gaussian distribution with the same mean and variance with the increase of D_B.

4.3 GNSS-based differential baseline computation

Despite GNSS fixes are largely employed in determining the distance among receivers through APD [140, 200], this solution does not guarantee the best practice to solve for this unknown. In the following, GNSS differential solutions are presented as methods capable to provide baseline computation typically relaying on *raw pseudorange* measurements instead of the receiver's positions.

4.3.1 GNSS-based baseline estimation

To cope with the limitations of sensor-based ranging and to provide a measurements which is less-dependent on the estimated positions, recent works have investigated a set of popular algorithms in the field as DGPS/DGNSS methods, addressing the estimation of (4.1) to improve the quality of the position estimation within a GNSS cooperative framework [183, 109, 144, 125].

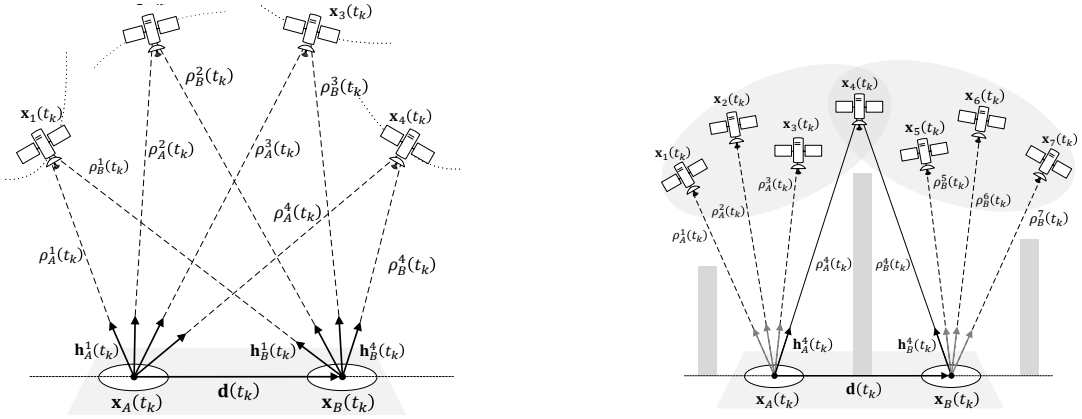

(a) (b)

Figure 4.5: GNSS-based ranging: open sky scenarios characterized by the full common visibility of the satellites (4.5a) and urban scenario with a single satellite in common view (4.5b).

These sensor-less methods rely on the availability of network connectivity and of a number of GNSS satellites in common view, hereafter referred as *shareable satellites*.

According to Figure 4.1, the *baseline vector* (4.1), can be treated as the unknown of the problem, as it holds for the position vector in the positioning estimation. Besides the direct use of the position estimates, presented in 4.2 as APD and widely adopted in several LBS, raw pseudorange measurements provided by the collaborating GNSS receivers can be combined in a number of fashions to effectively retrieve $\mathbf{d}_{AB}(t_k)$. The computation can be pursued according to DGPS observables and the number of shareable satellites, as depicted in Figure 4.5. Multiple raw pseudorange measurements can be integrated within an iterative algorithm Pseudorange Ranging (PR) [183] or similarly, combined as single or double differences in SD and DD, respectivelty [153]. Also single shareable satellites can be exploited by a networked GNSS receiver for a novel geometrical solution named IAR. Differently from ranging sensors, collaborative GNSS-based techniques, which foreseen a network-based exchange of information, can suffers of poorly predictable delays due to the network infrastructure (e.g. latency, network congestion, etc.). Furthermore, while the first are performed passively by a single agent relying on its on-board local clock, the latter requires additional adjustments to mitigate time issues enabling consistent merge of the measurements obtained by other asynchronous receivers, as discussed in Chapter 3.

As introduced in Chapter 3, the following differential techniques have been deeply investigated in GNSS since the early phases of the development of this technology. The theoretical approach reported in the next sections has been inspired replacedinto the literature on DGPS [83] but it will be extended in this thesis to a more general framework. Differently from this consolidated solutions indeed, in the context of multi-agent CP, it is not assumed to deal with a static reference base station and the observables from the receivers are not assumed to be synchronized neither augmented through precise corrections. This aspect differentiates the approach from RTK and DGPS relative positioning, in which reference stations with

precisely known positions are used to provide differential corrections or relative positioning data. The benefits introduced by the use of collaborating agents as *anchors of opportunities* has been assessed theoretically and experimentally in set of previous research contributions [123, 117, 86, 73] and it has recently become appealing in novel transportation paradigms such as Intelligent Transport System (ITS) [3].

Prior to the description of differential techniques, the section recall a solution to compensate for the time-misalignment of the pseudorange measurements exploiting the pseudorange rate or Doppler shift [35], thus enabling the whole set of algorithms within a network of asynchronous GNSS receivers, as presented in the general scheme of Chapter 3.

The performance of the baseline estimation can be improved through a weighting strategy at the cost of an a-priori knowledge of the error covariance matrices of such differential measurements. Therefore, a formal derivation of this statistical property is provided for each technique. It is worth recalling that all the measurements used in this research are code-based pseudorange measurements but the same approaches can be applied to carrier-phase measurements with specific solutions to solve for the integer ambiguity [83].

4.3.2 Time-compensation of asynchronous observables (Doppler-based)

When two independent GNSS receivers are considered to retrieve pseudorange measurements, the offset between their reception times induces a partial uncorrelation of the correlated errors [35]. This issue limits the effectiveness of differential methods in cancelling correlated errors. To compensate for this, the two receivers have to share the timestamps of their pseudorange measurements and the target should be able to measure the Doppler shift or the pseudorange rate relative to the common satellites. It is fundamental to recall that the accuracy of the time-stamps also depends on the quality of the clock bias estimation of previous PVT computation. Knowing the last two estimated timestamps t_{jk} and t_{ik}, referred to the common GNSS time scale, an estimated time offset, $\Delta t_{ij,k} = t_{ik} - t_{jk}$ is obtained. By exploiting the Doppler measurements collected by one of the receiver it is possible to compensate for asynchronous pseudorange measurements through the following

$$\hat{\rho}_i^s(t_{jk}) = \rho_i^s(t_{ik} + \Delta t_{ij}) = \rho_i^s(t_{ik}) + \Delta t_{ij,k} \cdot \lambda \cdot \phi_i^s(t_{ik}) \tag{4.11}$$

where λ is the wavelength of the carrier frequency of the transmitted signal according to the GNSS constellation (e.g. $\lambda \approx 0.190293$ m for GPS L1 signals) and $\phi_i^s(t_k)$ is the estimate of the Doppler frequency shift at t_k for the s-th satellite. The Doppler estimate is hence converted to a *pseudorange change rate* that can be used to predict the measurements at a given time via linear regression. This synchronization solution holds well for static receivers but it can lose accuracy in case of high relative dynamics between satellites and receivers. Sudden changes in speed such as receiver acceleration could lead to wrong compensation, but the resulting error has been shown to be negligible for vehicular applications [35].

In the following, the measurements obtained by two cooperating agents are considered synchronized through the presented strategy.

4.3.3 Raw Pseudorange Ranging (PR)

This technique has been introduced in [183] in the framework of vehicular relative positioning. The idea relies on the exploitation of raw pseudorange measurements to jointly solve for the baseline vector contextually to the positioning solutions.

At each time instant, t_k, the position of the agent i is expressed as the true position of the agent j and the baseline vector $\mathbf{d}_{ij}(t_k)$, as

$$\mathbf{x}_i(t_k) = \mathbf{x}_j(t_k) + \mathbf{d}_{ij}(t_k). \tag{4.12}$$

The PR algorithm computes the baseline vector by means of the linearization of the pseudorange equations (as modelled in Chapter 2).

$$\rho_j^s(t_k) = ||\mathbf{x}_s(t_k) - \mathbf{x}_j(t_k)|| + \delta b_j + \epsilon_c^s + \epsilon_{j,u}^s \tag{4.13}$$
$$\rho_i^s(t_k) = ||\mathbf{x}_s(t_k) - \mathbf{x}_j(t_k) - \mathbf{d}_{ij}(t_k)|| + \delta b_i + \epsilon_c^s + \epsilon_{i,u}^s. \tag{4.14}$$

Given a set of S shareable satellites between the two agents and defining a linearization point, a WLS approach can be used to solve for the following equation

$$\Delta\boldsymbol{\rho}_{ij}(t_k) = \begin{bmatrix} \mathbf{H}_j & \mathbf{0}_{N\times 4} \\ \mathbf{0}_{N\times 4} & \mathbf{H}_j \end{bmatrix} \begin{bmatrix} \Delta\mathbf{x}_j \\ \Delta b_j \\ \Delta\mathbf{x}_i \\ \Delta b_i \end{bmatrix} \tag{4.15}$$

where $\Delta\boldsymbol{\rho}_{ij}(t_k) = [\boldsymbol{\rho}_i - \boldsymbol{\rho}_j]$ for the same satellites and $\mathbf{H}_j$ is defined as the Direction Cosine Matrix computed at t_k by the agent j, as for the PVT algorithm described in Chapter 2. By inverting the relationship between the two locations (4.12), the (4.15) can be solved iteratively to estimate the baseline vector

$$\hat{\mathbf{d}}_{ij}(t_k) = \hat{\mathbf{x}}_i(t_k) - \hat{\mathbf{x}}_j(t_k) \tag{4.16}$$

According to (4.15), the error covariance matrix on the baseline vector is derived similarly as for Section 4.2.1. The difference is that the baseline vector is obtained with a high redundancy of measurements which typically increases the precision of the solution, thus reducing the covariance elements.

4.3.4 Single Difference Ranging (SD)

This method computes the *baseline vector* by exploiting a set of differential observable known as single differences.

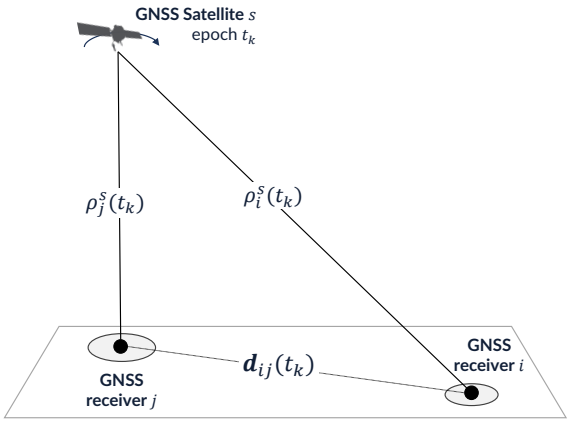

Figure 4.6: Single Difference principle applied to two GPS receivers. Image taken from [194].

A generic single difference can be defined between two GNSS receivers i, j tracking a common satellite s as the difference between synchronous pseudorange measurements [83].

$$\begin{aligned} S_{ij}^{s}(t_k) &= \rho_i^s(t_k) - \rho_j^s(t_k) \\ &= \Delta r_{ij}(t_k) + \Delta b_{ij}(t_k) + \Delta \epsilon_{ij}(t_k) \end{aligned} \tag{4.17}$$

where $\Delta b_{ij}(t_k)$ is difference between the clock biases of the two agents and the $\Delta\epsilon_{ij}$ is a noise term which aggregates all the non-correlated errors. In fact, provided that all the measurements are synchronous as expected from (4.11), single differences allow to cancel the satellite clock bias and correlated bias terms affecting pseudorange measurements. Under the assumption of close proximity of the receivers, ionospheric and tropospheric delay are also effectively removed due to their high spatial correlation [90]. Besides the cancellation of correlated error terms, the variance of the uncorrelated errors, such as multipath, is increased due to the typical low spatial and temporal correlation. This noise contributions are hence aggregated in $\Delta\epsilon_{ij}(t_k)$. The behaviour of multipath errors are indeed caused by satellite, receiver, reflector or scatter movement which are mainly responsible for its high time variability [190, 105].

A useful notation for the computation of a set of single differences can be derived in matrix form, as

$$\begin{bmatrix} S_{ij}^{1}(t_k) \\ S_{ij}^{2}(t_k) \\ \vdots \\ S_{ij}^{S}(t_k) \end{bmatrix} = \begin{bmatrix} -1 & 1 & 0 & 0 & \cdots & \dots & 0 & 0 \\ 0 & 0 & -1 & 1 & \vdots & \vdots & 0 & 0 \\ \vdots & \vdots & \cdots & \dots & \ddots & \ddots & \vdots & \vdots \\ 0 & 0 & 0 & 0 & \cdots & \cdots & -1 & 1 \end{bmatrix} \begin{bmatrix} \rho_i^1(t_k) \\ \rho_j^1(t_k) \\ \rho_i^2(t_k) \\ \rho_j^2(t_k) \\ \vdots \\ \vdots \\ \rho_i^S(t_k) \\ \rho_i^S(t_k) \end{bmatrix}. \tag{4.18}$$

The computation of the baseline vector based on SD is performed through

$$\begin{bmatrix} S_{ij}^{1}(t_k) \\ S_{ij}^{2}(t_k) \\ \vdots \\ S_{ij}^{S}(t_k) \end{bmatrix} \simeq \begin{bmatrix} \mathbf{h}_j^1(t_k) & 1 \\ \mathbf{h}_j^2(t_k) & 1 \\ \vdots & \vdots \\ \mathbf{h}_j^S(t_k) & 1 \end{bmatrix} \begin{bmatrix} \mathbf{d}_{ij}(t_k) \\ \Delta b_{ij}(t_k) \end{bmatrix} \tag{4.19}$$

In order to compute the covariance matrix of the SD ranging, the following relationship holds

$$\mathbf{R}_d^{(SD)} = \left(\mathbf{H}^\top \mathbf{H}\right)^{-1} \mathbf{H}^\top \mathbf{R}_{SD} \mathbf{H} \left(\mathbf{H}^\top \mathbf{H}\right)^{-1} \tag{4.20}$$

where $\mathbf{R}_{SD}$ is the error covariance matrix of the single differences and $\mathbf{H}$ is the second term in (4.19). $\mathbf{R}_{SD}$ can be a diagonal matrix if the satellites are not repeated among the pairs (i.e. each difference is independent) [83]. A generic element of the diagonal of $\mathbf{R}_{SD}$ is hence defined as $[R_{SD}]_{ss} = (\sigma_i^s)^2 + \left(\sigma_j^s\right)^2$.

4.3.5 Double Difference Ranging (DD)

When the same pair of satellites r and s is visible to both the receivers, a double difference measurement can be obtained as difference of two single differences

$$D_{ij}^{sr}(t_k) = S_{ij}^{s}(t_k) - S_{ij}^{r}(t_k) = \Delta R_{ij}^{sr} + \Sigma_{ij} \tag{4.21}$$

where S_{ij}^s is a single difference computed according to (4.17) while Σ_{ij} is a random variable collecting residual error contributions that cannot be cancelled due to the non-correlation

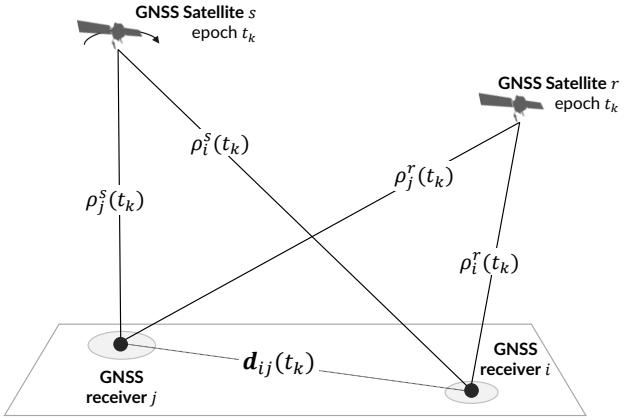

Figure 4.7: Single Difference principle applied between two GPS receivers.

between the measurements such as multipath, second-order noise components of the receiver front-ends and additional non-modelled noise contributions [90].

The term ΔR^{sr} can be expressed highlighting the dependency from the baseline vector as

$$\Delta R^{sr}(t_k) = \left[\mathbf{h}_i^s(t_k) - \mathbf{h}_j^s(t_k)\right]^T \mathbf{d}_{ij}(t_k) \tag{4.22}$$

where $\mathbf{h}_m^s$ is a *unitary steering vector* defined as in Chapter 2.

The computation of DD measurements can be expanded from the linear relationship $\mathbf{D}_{ij}(t_k) = \mathbf{L}_{DD}\mathbf{S}_{ij}(t_k)$, as

$$\underbrace{\begin{bmatrix} D_{ij}^{12}(t_k) \\ D_{ij}^{13}(t_k) \\ \vdots \\ D_{ij}^{1S}(t_k) \end{bmatrix}}_{\mathbf{D}_{ij}} = \underbrace{\begin{bmatrix} -1 & 1 & 0 & \cdots & 0 \\ -1 & 0 & 1 & \ddots & 0 \\ \vdots & \vdots & \ddots & \ddots & \vdots \\ -1 & 0 & \cdots & \cdots & 1 \end{bmatrix}}_{\mathbf{L}_{DD}} = \underbrace{\begin{bmatrix} S_{ij}^1(t_k) \\ S_{ij}^2(t_k) \\ S_{ij}^3(t_k) \\ \vdots \\ S_{ij}^S(t_k) \end{bmatrix}}_{\mathbf{S}_{ij}}. \tag{4.23}$$

Equation (4.22) can be then expanded, neglecting the noise contribution in (4.21), in

$$\underbrace{\begin{bmatrix} D_{ij}^{12}(t_k) \\ D_{ij}^{13}(t_k) \\ \cdots \\ D_{ij}^{1S}(t_k) \end{bmatrix}}_{\mathbf{D}_{ij}} \simeq \underbrace{\begin{bmatrix} \left[\mathbf{h}_i^2(t_k) - \mathbf{h}_i^1(t_k)\right] \\ \left[\mathbf{h}_i^3(t_k) - \mathbf{h}_i^1(t_k)\right] \\ \cdots \\ \left[\mathbf{h}_i^S(t_k) - \mathbf{h}_i^1(t_k)\right] \end{bmatrix}}_{\mathbf{H}_D} \mathbf{d}_{ij}(t_k) \tag{4.24}$$

collecting $S-1$ double difference measurements from a set of S satellites simultaneously visible to i and j. This set of equations can be exploited to estimate $\mathbf{d}_{ij}(t_k)$ through a Least Square (LS) algorithm in the form of

$$\hat{\mathbf{d}}_{ij}(t_k) \simeq (\mathbf{H}_D(t_k)^\top \mathbf{H}_D(t_k))^{-1} \mathbf{H}_D(t_k)^\top \mathbf{D}_{ij}(t_k) \tag{4.25}$$

where $\mathbf{D}_{ij}(t_k)$ and $\mathbf{H}_D(t_k)$ are respectively the first and the second term in (4.1).

In order to determine the steering vectors, an approximation of the two positions is needed. A GNSS receiver can solve for the aiding position by using the external pseudorange

measurements. By means of this approach the exchange of the estimated position is not necessary since it can be computed autonomously by the target.

As for the previous methods, uncorrelated errors such as multipath, are increased by differentiation. Furthermore, according to what demonstrated in [35], statistical assumption of mutual independence can be made on different pseudorange measurements but it cannot be assessed for the resulting double difference measurement.

In addition, the variance for such a kind of measurements is four times the variance of each involved pseudorange (assuming i.i.d. pseudorange measurements).

A general algebraic equation can be used to evaluate the covariance of inter-agent collaborative measurements relying on the covariance of the LMS estimator in (4.25). It is hence sufficient to compute

$$\mathbf{R}_d^{(DD)}(t_k) = \left(\mathbf{H}_D^\top(t_k)\mathbf{H}_D(t_k)\right)^{-1}\mathbf{H}_D^\top(t_k)\mathbf{R}_{DD}(t_k)\mathbf{H}_D(t_k)\left(\mathbf{H}_D^\top(t_k)\mathbf{H}_D(t_k)\right)^{-1} \tag{4.26}$$

where $\mathbf{R}_{DD}$ is the covariance matrix of the vector $\mathbf{D}_{ij}(t_k)$ which is in turn computed from the SD covariance (4.20), as

$$\mathbf{R}_{DD}(t_k) = \mathbf{L}_{DD}(t_k)\mathbf{R}_{SD}(t_k)\mathbf{L}_{DD}^\top(t_k) \tag{4.27}$$

where $\mathbf{L}_{DD}$ is the linear relationship between single differences and double difference measurements, whose errors are still assumed independent for the two receivers. The use of a reference satellite for the construction of the double differences implies that $\mathbf{R}_{DD}$ is non-diagonal, cross-correlation terms among these measurements cannot be neglected.

Timing of observables exchange through packet network

The timing of the data transmission could represent a bottleneck in the actual implementation of the GNSS collaborative approaches. This aspect affects both static and dynamic applications in terms of time-consistency of the exchanged data but it can induce dramatic biases in kinematic scenarios when the relative positions of satellites and users change over the time. However, the feasibility of a GNSS-based time synchronization has been considered plausible in high-dynamic multi-agent systems such as vehicular networks[78]. A GNSS time scale can be indeed considered as a reference for the agents, whenever they are capable to solve for their location and time. Although network-based syncrhonization strategies fall outside the scope of this research, we remind to the reader that a set of network protocols have been conceived to the purpose for the synchronization of connected vehicles [78], thus supporting modern ITS paradigm. The effect of the epoch offset between the agents returns a time-inconsistency in the measurements in all of the listed cooperative methods.

Despite the misalignment among the measurements epochs of the agents, it is worth recalling that such a kind of network connectivity adds a transmission delay according to the throughput and the latency of the network infrastructure as exemplified in Figure 4.8.

Figure 4.8 describes the exchange of GNSS data on a temporal axis, assuming that the agents A and B are aligned to the GNSS time scale but providing asynchronous positioning solutions, thus inconsistent set of observables.

Blue dots and orange dots show the *measurements epochs* for agent A and agent B respectively, in which each receiver estimates the position and updates the set the pseudoranges measurements. The variable Δt is the time difference between agents' measurements epochs, while $RTT = \tau_1 + \tau_2$ is the Round Trip Time, which is mainly determined by the communication network. The term τ_1 is relevant for actual collaborative strategies in which an aiding request is foreseen. On the contrary, it can be neglected if raw data are available independently from an active requests.

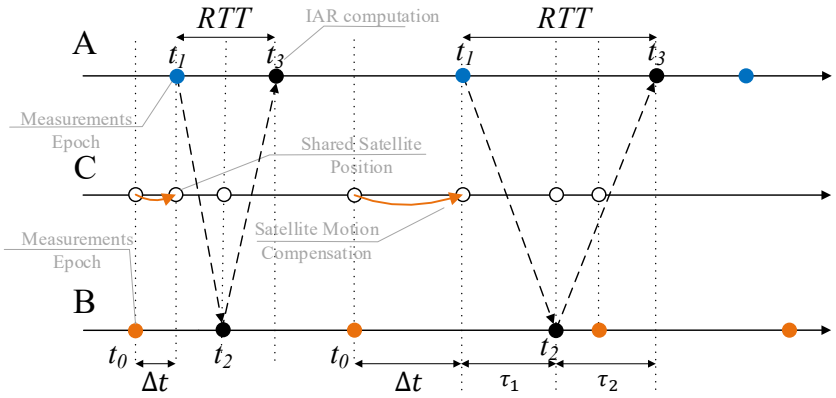

Figure 4.8: Timing of the exchange of navigation data for the computation of collaborative measurements between agents retrieving asynchronous measurements and PVT solutions.

In the following, a set of relevant GNSS-based methods addressing the *baseline estimation* are described in detail according to their input requirements and their computational complexity. A preliminary discussion is also provided concerning the synchronization issues of the measurements coming from asynchronous receivers, according to what has been discussed so far. Eventually the analysis of the uncertainties on the estimation is provided for each method. A more compact notation will be adopted to distinguish the roles of each agent within a cooperative framework. For an improved readability indeed, A and B subscripts will be replaced by i and j to identify generic *aiding agent* and *aided agent* in a multi-agent scenario.

4.4 Inter-agent Ranging (IAR)

This section provides a description of an original technique for the computation of the *baseline length* among connected GNSS receivers presented in [124, 126]. The IAR method exploits the *steering vectors* computed contextually in the PVT algorithm and the current pseudorange measurements for the computation of pairwise baseline lengths between two agents. This method differs from other solutions because the *baseline vector* is not computed and the baseline length is the only information provided. The method is based on the exchange of a part of the Direction Cosine Matrix (i.e. steering vector) and the corresponding pseudorange measurement to obtain $\hat{d}_{ij}^{s}(t_k)$, where s identifies the satellite shared for the computation.

4.4.1 Theoretical Inter Agent Range

A scenario in which the agents i and j observe a common satellite in LoS is addressed in the following, according to Figure 4.9. The scheme depicts a static scenario or equivalently the snapshot of a kinematic scenario at a given time instant t_k.

In order to discuss the theoretical framework of the IAR, the basic geometry is hereafter defined with exact distances and positions, assumed as sides and vertices of the aforementioned geometrical arrangement. The location of the satellite, $\mathbf{x}_s(t_k)$, is obtained from the computation of the orbit equation at time t_k, defined by the ephemeris carried by the broadcasted navigation message [136].

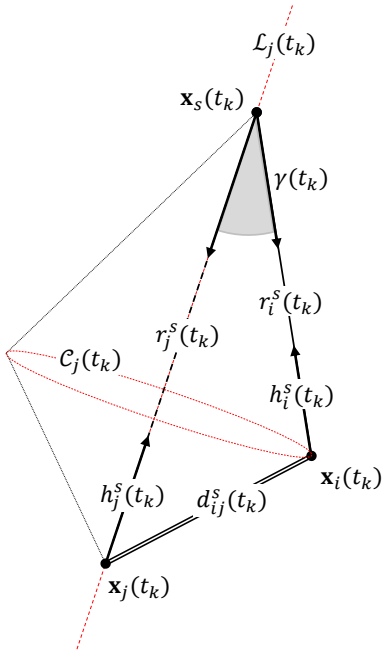

Figure 4.9: IAR geometrical scenario. Ranging description with highlighted *ambiguity circumference* and *ambiguity line*.

Given the true satellite-to-user ranges $r_i^s(t_k)$ and $r_j^s(t_k)$ and the respective steering vectors $\mathbf{h}_i^s(t_k)$ and $\mathbf{h}_j^s(t_k)$, the IAR can be computed by solving for the unknown of interest, $d_{ij}^s(t_k)$, by means of the Carnot theorem (or law of cosines). The resulting computation is

$$d_{ij}^s(t_k) = \sqrt{r_i^s(t_k)^2 + r_j^s(t_k)^2 - 2\, r_i^s(t_k)\, r_j^s(t_k)\, \cos\gamma(t_k)} \tag{4.28}$$

where $\gamma(t_k)$ is the angle included between the two steering vectors w.r.t. the shared-satellite C and can be computed by means of a dot product as

$$\begin{aligned} \gamma(t_k) &= \cos^{-1}\left(\mathbf{h}_i^s(t_k) \cdot \mathbf{h}_j^s(t_k)\right) \\ &= \cos^{-1}\left(\mathbf{h}_i^s(t_k)\mathbf{h}_j^s(t_k)^T\right) \ . \end{aligned} \tag{4.29}$$

The equivalence in (4.29) is due to the unitary norm of the steering vectors, by definition.

In real case the joint effect of incorrect satellite-to-user range measurements and the geometry of the observed constellation characterizes the distribution of the positioning solution, thus the computation of (4.29). Input uncertainties must be discussed according to GNSS literature, to evaluate the error propagation through the IAR computation steps. The inputs of (4.28) are hence replaced by the corresponding random variables according to

$$\hat{d}_{ij}^s(t_k) = \sqrt{\hat{r}_i^s(t_k)^2 + \hat{r}_j^s(t_k)^2 - 2\, \hat{r}_i^s(t_k)\, \hat{r}_j^s(t_k)\, \cos\hat{\gamma}(t_k)} \tag{4.30}$$

The notation $\hat{d}_{ij}^s(t_k)$ allows to highlight the dependency from the involved agents and satellite as shown in Figure 4.9. To compute (4.30), a user needs first to establish the cooperation with an available aiding agent in order to retrieve the quantities involved in the IAR computation.

It worth mentioning that when the magnitudes of the range measurements are similar, the (4.28) implemented in floating point can lead to numerical cancellation, therefore a stable solution for the IAR is provided in the following.

4.4.2 Numerically-stable Law of Cosines for GNSS applications

The popular law of cosines, a.k.a. Carnot Theorem of triangles, relates the values of the three side lengths and one angle in a triangle ABC, as

$$c^2 = a^2 + b^2 - 2ab\cos\gamma \tag{4.31}$$

where a,b and c are the lengths of the sides and γ is the angle included between the sides a and b.

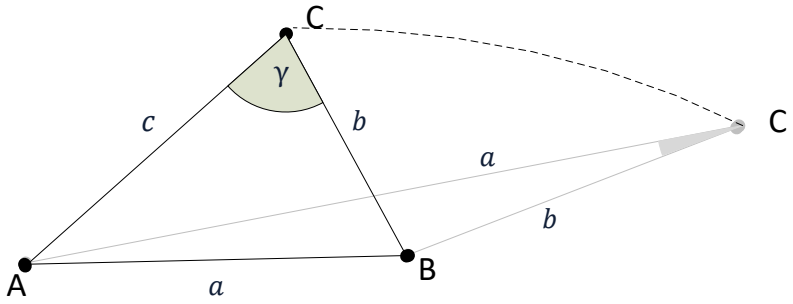

Figure 4.10: Triangular geometry emphasizing the limiting conditions of IAR implementation: $a \simeq b$ and $\gamma \simeq 0$.

According to the knowledge of three of the aforementioned elements, the equation for a side or an angle can be solved. Equation (4.31) can be straightforwardly implemented in floating-point arithmetic but it can produce very inaccurate results whether is used under certain conditions. If the investigated triangle is highly acute, numerical results show high relative errors due to dramatic numerical cancellation in the subtraction of very similar quantities. This issue, known as *loss of significance* is highly impacting when large distance measurements are involved in (4.31). By rearranging (4.31) it is possible to compute the value of c according to

$$c = \sqrt{a^2 + b^2 - 2ab\cos\gamma} \tag{4.32}$$

given that $a \approx b$ have comparable magnitudes and angle γ is severely close to zero, then $\gamma \approx 1$ [152].

This is the case of terrestrial IAR computation based on satellites-to-receivers range measurements, whose order of magnitude can easily reach 6 times the one assumed by the baseline length. In practical terms

$$a^2 + b^2 - 2ab\cos\gamma \simeq a^2 + a^2 - 2a^2\cos(0) \simeq 2a^2 - 2a^2 \simeq 0 \tag{4.33}$$

even if $c = 10^{-20}$ can be still represented in floating points arithmetic. A possible solution to the numerical cancellation is to exploit the Taylor expansion of the cosine for angle γ approaching $\gamma \simeq 0$, as

$$c^2 = a^2 + b^2 - 2ab\cos\gamma = a^2 + b^2 - 2ab(1 + cos\gamma - 1) \tag{4.34}$$
$$= \left(a^2 + b^2 - 2ab\right) - 2ab(cosC - 1) \tag{4.35}$$
$$= \left(a^2 - 2ab + b^2\right) - 2ab\left(-\frac{\gamma^2}{2!} + \frac{\gamma^4}{4!} + o(\gamma^4)\right) \tag{4.36}$$
$$\simeq (a-b)^2 + 2ab\left(\frac{\gamma^2}{2!} + \frac{\gamma^4}{4!}\right) \tag{4.37}$$
$$\tag{4.38}$$

which gives a stable formula to prevent numerical cancellation is then

$$c = \sqrt{(a-b)^2 + ab\gamma\left(1 - \frac{\gamma^2}{12}\right)} \tag{4.39}$$

In (4.39), both the terms of the sum are positive and error cancellation is only possible for the squared term $(a-b)^2$, which turns to be critical only in case of zero-baseline tests. It has been shown that in general, the noise affecting the code-based pseudorange measurements mitigates cancellation phenomena when (4.39) is used.

4.4.3 Time-compensation of asynchronous observables (orbit-based)

As a first step for IAR estimation, a shareable satellite s, has to be jointly identified by agents i and j.

Let suppose that the agent i sends a request, at time t_1. At such a time epoch, i retrieves the range, $r_i^s(t_1)$ and computes the steering vector $\hat{\mathbf{h}}_i^s(t_1)$. Agent i is able to send the timestamped steering vector to agent j. Such a request is received by an aiding agent at time $t_2 = t_1 + \tau_1$, which can fall randomly between two measurements epochs of the aiding receiver. The misalignment between the measurement epochs of the agents must be taken into account to manage the time-inconsistency of the measurements coming from each receiver. For the aforementioned state-of-the-art methods, this compensation is provided by means of an estimate of the changing rate of the satellite-to-user range which is typically measured by the receiver itself relying on doppler measurements [36]. Unfortunately, this approach does not provide sufficient information to properly predict the associated steering vector for the IAR computation. However, by knowing the ephemeris and timestamps of the received data, the aiding agent can compensate for satellite motion properly through (4.40). The closest measurements in time that j is able to use are the measurements taken at time t_0, that are then compensated for $\Delta t = t_1 - t_0$ seconds by linear regression to make them as consistent as possible with the information provided by i. The evaluation of

$$\hat{\mathbf{r}}_j^{s*}(t_1) = \hat{r}_j^s(t_0)\hat{\mathbf{h}}_j^s(t_0) + [\mathbf{x}_s(t_1) - \mathbf{x}_s(t_0)] \tag{4.40}$$
$$\hat{r}_j^{s*}(t_1) = ||\hat{\mathbf{r}}_j^{s*}(t_1)|| \tag{4.41}$$
$$\hat{\mathbf{h}}_j^{s*}(t_1) = \frac{\hat{\mathbf{r}}_j^{s*}(t_1)}{\hat{r}_j^{s*}(t_1)} \tag{4.42}$$

allows agent j to compute an estimate of the angle $\gamma(t_1)$ in (4.29) using the predicted $\hat{\mathbf{h}}_j^{s*}(t_1)$ and the received $\hat{\mathbf{h}}_i^s(t_1)$.

At time $t_3 = t_1 + RTT$, agent i receives $\hat{\gamma}(t_1)$ and $\hat{r}_j^{s*}(t_1)$ and determines $\hat{d}_{ij}^s(t_1)$ through (4.30).

Notice that the communication latency affects the ageing of the estimated IAR, which is computed RTT seconds after agent i measurement epoch t_1. The network latency cannot be bypassed in a cooperative ranging framework, and the value of RTT may limit the set of possible applications of this paradigm, even for a low-latency DSRC communication link.

In summary, agent j must share partial information on its position, communicating $\hat{\gamma}(t_k)$ and $\hat{r}_j^{s*}(t_k)$ to the aided agent to allow the latter to retrieve the baseline length estimation $\hat{d}_{ij}^{s}(t_k)$. However, even considering the ideal IAR computation (4.28), the position of the aiding agent j at t_k cannot be retrieved by i because the direction information is not exchanged. Indeed, the dot product shown in (4.29) is not invertible such that agent i has only a partial knowledge of the position of j. It can only assume that its position lies on the circumference $\mathcal{C}_j$ shown in Figure 4.9, which is the locus of the points at distance $d_{ij}^s(t_k)$ from the receiver i and $r_j^s(t_k)$ from the satellite s. By the aiding side, the only knowledge of the steering vector $\mathbf{h}_i^s(t_k)$ bounds the uncertainty on the location of agent i to a straight line, $\mathcal{L}_i$, which passes the through points $\mathbf{x}_i(t_k)$, $\mathbf{x}_s(t_k)$ and the center of $\mathcal{C}_j$. This aspect prevents the possibility to retrieve the position of the aiding agent by inverting the problem, thus its location is not exchanged neither explicitly such as for APD nor implicitly such as for the other GNSS-only ranging techniques.

A key point in the analysis of the IAR measurement as a random variable regards the effects of non-linear operators applied on the well-modelled input random variables (i.e. pseudoranges) in (4.30). Although the computation is performed through a non-linear equation, previous works assess that the error distribution of the IAR can be well approximated with a Gaussian distribution when Gaussian inputs are considered and the positioning error is negligible w.r.t. the baseline length [124]. However, statistical moments of the estimated IAR as a generic distribution are hereafter derived expanding the range terms according to the pseudorange error model discussed in Chapter 2. Satellite-to-user ranges are characterized by different standard deviations σ_i^s and σ_j^s for each GNSS receiver and shared satellite s. To limit the notation complexity, all the references to the shared satellite s and time index t_k will be dropped hereafter. Accordingly, the range $\hat{r}_j^{s*}(t_k)$ and the steering vector $\hat{\mathbf{h}}_j^{s*}(t_k)$ will be simply written as $\hat{r}_j$ and $\hat{\mathbf{h}}_j$, respectively.

4.4.4 Mean and variance analytical derivation

Consider a generic function of n random variables

$$Y = g(X_1, X_2, ..., X_n) \tag{4.43}$$

and its Taylor expansion about the mean values $\mu_{X_1}, \mu_{X_2}, ..., \mu_{X_n}$

$$\begin{aligned} Y = g(\mu_{X_1}, \mu_{X_2}, ..., \mu_{X_n}) + \sum_{i=1}^{n}(X_i - \mu_{X_i})\frac{\partial g}{\partial X_i} + \\ + \frac{1}{2}\sum_{i=1}^{n}\sum_{j=1}^{n}(X_i - \mu_{X_i})(X_j - \mu_{X_j})\frac{\partial^2 g}{\partial X_i X_j} + ... \end{aligned} \tag{4.44}$$

where all the partial derivatives of $g(X_1, X_2, ..., X_n)$ are evaluated at $(X_1 = \mu_{X_1}, X_2 = \mu_{X_2}, ..., X_n = \mu_{X_n})$, as well.

By truncating the expansion at the first order and applying the expected value it is straightforward to obtain

$$\mathbf{E}[Y] \simeq g(\mu_{X_1}, \mu_{X_2}, ..., \mu_{X_n}) \tag{4.45}$$

since the first order terms are canceled by the operator itself. The same operations applied to (4.30) lead to

$$\mathbf{E}[\hat{d}_{ij}] \simeq \sqrt{(r_i)^2 + (r_j)^2 - 2r_i r_j \cos\gamma}. \tag{4.46}$$

which is the definition of the ideal d_{AB} (4.28), assuming zero-mean distribution of the error affecting the variables $\hat{r}_A$,$\hat{r}_B$ and $\hat{\gamma}$. According to (4.46), equation (4.30) can be wrongly thought as an unbiased estimator of d_{ij} since $\mathbf{E}[\hat{d}_{ij}] - d_{ij} = 0$. However, the statistical behaviour of the estimated IAR, obtained through a Monte Carlo simulation campaign, shows generally non-null values of the bias, whose distribution depends on the considered geometry. The non-null bias contributions are hence attributed to the terms in the Taylor expansion which are truncated due to their higher order, but they are small values compared to the simulated baseline.

The truncation of the Taylor expansion applied to (4.30) is exploited to obtain a closed-form approximation of the theoretical IAR variance as well. The variance of a function of multiple random variables is derived as

$$\begin{aligned}\sigma_Y^2 &\triangleq \mathbf{E}[Y^2] - \mathbf{E}[Y]^2 \\ &\simeq \sum_{i=1}^{n} \sigma_{X_i}^2 \left(\frac{\partial g}{\partial X_i}\right)^2 + \sum_{\substack{i,j=1,\dots,n \\ i\neq j}} \alpha_{ij}\sigma_{X_i}\sigma_{X_j}\frac{\partial g}{\partial X_i}\frac{\partial g}{\partial X_j}\end{aligned} \tag{4.47}$$

where α_{ij} is the *correlation coefficient* [56] of two random variables X_i, X_j defined as

$$\alpha_{ij} = \frac{\mathrm{cov}(X_i, X_j)}{\sigma_i \sigma_j} \ . \tag{4.48}$$

As a consequence, the variance of $\hat{d}_{ij}$ can be written as

$$\begin{aligned}\sigma_{\hat{d}}^2 \simeq\ & \sigma_i^2 \left(\frac{\partial \hat{d}_{ij}}{\partial \hat{r}_i}\right)^2 + \sigma_j^2 \left(\frac{\partial \hat{d}_{ij}}{\partial \hat{r}_j}\right)^2 + \sigma_{\hat{\gamma}}^2 \left(\frac{\partial \hat{d}_{ij}}{\partial \hat{\gamma}}\right)^2 \\ &+ 2\,\alpha_{ij}\,\sigma_i\sigma_j\,\frac{\partial \hat{d}_{ij}}{\partial \hat{r}_i}\frac{\partial \hat{d}_{ij}}{\partial \hat{r}_j} + 2\,\alpha_{i\hat{\gamma}}\,\sigma_i\sigma_{\hat{\gamma}}\,\frac{\partial \hat{d}_{ij}}{\partial \hat{r}_A}\frac{\partial \hat{d}_{ij}}{\partial \hat{\gamma}} \\ &+ 2\,\alpha_{j\hat{\gamma}}\,\sigma_j\sigma_{\hat{\gamma}}\,\frac{\partial \hat{d}_{ij}}{\partial \hat{r}_j}\frac{\partial \hat{d}_{ij}}{\partial \hat{\gamma}}\end{aligned} \tag{4.49}$$

which can be easily expressed in a closed-form computing the partial derivatives. Equation (4.49) will be referred to as *generalized theoretical formula* for the IAR variance.

In order to simplify (4.49), the random variables involved may be assumed uncorrelated. With this in mind, we can derive a simpler form of (4.47) by setting $\alpha_{ij} = 0$ for $i \neq j$ obtaining

$$\sigma_Y^2 \simeq \sum_{i=1}^{n} \sigma_{X_i}^2 \left(\frac{\partial g}{\partial X_i}\right)^2 \ . \tag{4.50}$$

The variance of the estimated IAR $\hat{d}_{ij}$ can be therefore approximated as

$$\begin{aligned}\sigma_{\hat{d}}^2 \simeq\ & \frac{1}{d_{ij}^2}[\sigma_i^2(r_i - \cos(\gamma)r_j)^2 + \\ &+ \sigma_j^2(r_j - \cos(\gamma)r_i)^2 + \\ &+ \sigma_{\hat{\gamma}}^2(\sin(\gamma)r_i r_j)^2] \ .\end{aligned} \tag{4.51}$$

where d_{ij} is as in (4.28) and highlights the dependency from the true value of the baseline.

Assuming null cross-correlation between estimated satellite-to-user ranges and $\hat{\gamma}$ (i.e. $\alpha_{i\hat{\gamma}} = \alpha_{j\hat{\gamma}} = 0$) is a reasonable choice since the angle γ computed from the steering vectors should maintain a very poor correlation to one specific range among those involved in the

computation of the position solution. The same assumption becomes less reasonable when dealing with the coefficient α_{ij}. The residual error term $\xi_i(t_k)$ affecting the corrected pseudoranges affects in turn the estimated ranges $\hat{r}_i$ and $\hat{r}_j$ and these User-equivalent Range Error (UERE) terms tend to be highly correlated for single-frequency users, due to residual ionospheric errors [90]. Despite this, the experimental validation provided in Chapter 5 supports the removal of cross-correlation terms as an acceptable approximation for the IAR variance model.

In [126] a simplified equation of the IAR variance was computed for two users lying on the same LTP, assuming null steering error, i.e. a perfect estimation of the angle γ (4.29). Under the same assumptions, it can be shown that (4.51) and the solution derived in [126] are equivalent if and only if $r_i = r_j$ i.e. when the satellite is equidistant from the two peers. The characterization provided through this research is therefore coherent with the distribution presented in [126], considering that the condition $\sigma_{\hat{\gamma}} = 0$ cancels the third term in (4.51). Moreover, unlike the empirical derivation in [126], the two users are not supposed to lie on the same LTP.

The variance computed through (4.51) or through the generalized theoretical formula (4.49) can therefore influence the choice of the satellite, provided that the aiding agent is able to estimate σ_j^2, r_j, $\sigma_{\hat{\gamma}}^2$ and γ, while σ_i^2 and r_i can be estimated by the aided agent. Furthermore, it allows to determine a weighted strategy for the averaging of the estimated IAR measurements.

4.5 Final remarks

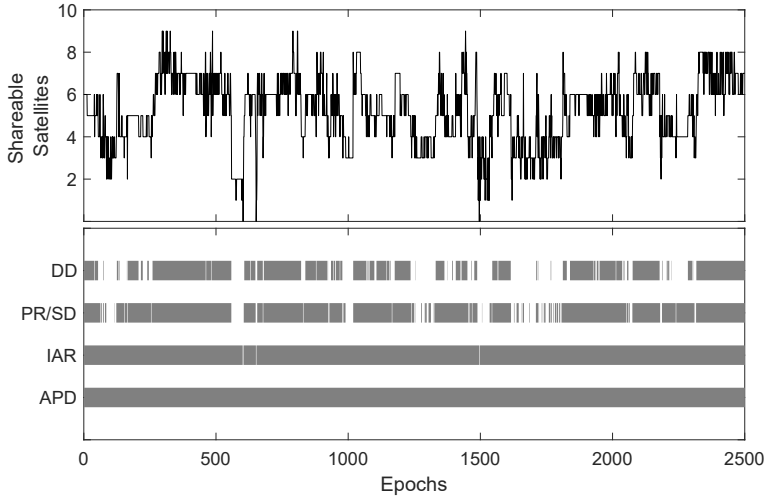

Figure 4.11: Example of simultaneous GNSS satellites visibility for two agents following an experimental trajectory in urban environment (upper) and practicability of GNSS-only ranging methods along the time (bottom).

PR, SD and DD methods, require a substantial exchange of pseudorange measurements between pair of collaborating receivers. When the exchange of at least three pseudorange measurements, any receiver can solve the position of the other user sharing those data. Basically, all the classic methods allow *implicitly* to retrieve and track the position of collaborating agent, and they always need three or more shared satellites. The APD method makes no exception since it requires the *explicit* exchange of absolute positioning solutions

thus allowing to any collaborating receiver to know the location of other users. On the other hand however, it does not require shared satellites thus being suitable even in very poor common visibility conditions.

Each receiver employs a different set of satellites to compute its own position thus the intersection of the two sets could contain less than three satellites, making the aforementioned techniques unsuitable in a harsh environment. Indeed, observing less than three shareable satellites, only APD can be employed to compute the range between the agents. By identifying a worst-case scenario, only one satellite is assumed shareable due to the presence of masking obstacles which obstruct LoS. An example of the number of satellites in common view in a real urban scenario is reported in Figure 4.11, where the variability of the number of satellites along the time (upper plot) prevents the use of some ranging techniques in some time intervals (lower plot). Besides its sub-optimality the IAR method is conceived to require the minimum amount of information to be exchanged between networked receivers, thus reducing both the need of multiple shared satellites and the network overhead.

Chapter 5

Simulation analysis and assessment of GNSS-based baseline length computation

In the perspective of a tight integration of collaborative ranging measurements as additional information to the positioning problem, a model of their statistical distribution has to be accurately known. This hold especially for navigation filters which rely on Bayesian estimation. The scope of this chapter is indeed to provide a detailed analysis of the baseline estimation methods presented in Chapter 4 by means of simulation and experimental analysis specifically designed for this purpose. Although differential techniques have been widely investigated in geodesy and within the framework of relative positioning and DGPS [197, 186, 196], few contributions addressed the statistical characterization of the baseline length between two GNSS receivers. DGPS and RTK typically exploit the baseline measurement to tackle the problem of error mitigation. They aim at providing high-precision and high-accuracy positioning solutions within specifically-designed infrastructures including survey-grade base station and a "radiobeacon" transmitter that broadcasts correction data (i.e. fixed reference base station and fixed receiver or base-rover) [90]. The statistical distribution of the baseline length is often ignored or oversimplified and heuristic rules are used to select the best subset of satellites for the computation of differential corrections. Our interest in a better understanding of the statistical properties of the baseline measurement is oriented to a more suitable design of a hybrid navigation filter capable to integrate such measurements along with GNSS standalone measurements.

An extensive work was pursued in this thesis to characterize the IAR methods which, differently from the state-of-the-art differential solutions, directly provides the *baseline length* without computing the *full baseline vector*, according to the nomenclature of Chapter 4. This key-aspect impact on its statistical properties.

Therefore, an assessment of the IAR statistical model presented in Chapter 4 is provided in this chapter by means of simulation environment in ideal conditions and by means of experimental campaigns. To the purpose, a geometrical framework for relative distance of pairwise cooperating receivers was proposed in [126] and it is recalled hereafter.

In order to perform a fair comparison among the different baseline computation methods which typically exploit multiple satellites weighted measurements, a weighted IAR computation, named W-IAR is then proposed in Section 5.2. Eventually, differential methods and W-IAR will be compared in terms of

- measurement statistical distribution and model
- inter-measurements cross-correlation w.r.t. standalone GNSS measurements

to properly support analysis and results of the following chapters.

5.1 Analysis and assessment of IAR model

This section provides a statistical analysis oriented to the assessment of the IAR statistical model presented in Chapter 4. The validity of the model is fundamental to the aggregation of multiple IAR measurements through weighted strategies and in turn to a reliable initialization and feeding of the hybrid navigation filters which will be described in Chapter 6.

5.1.1 Geometrical Model

The collection of results presented in this section highlights the behaviour of the statistical moments of the IAR equation (4.28), related to the triangular geometry that has been defined by the cooperating pair composed by i-th and j-th agent and the shared satellite s.

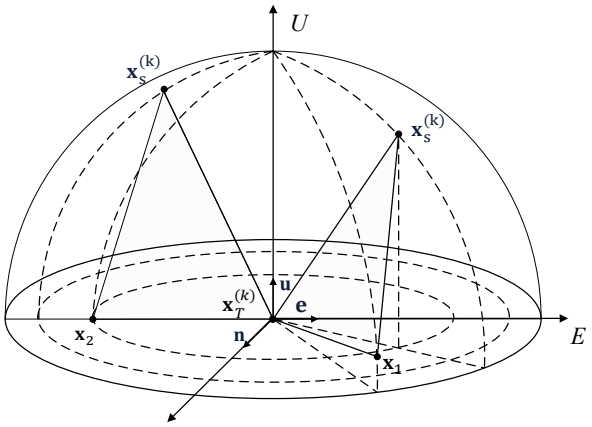

Figure 5.1: Hemispherical cap lying on the LTP centered in $\mathbf{x}_T$.

An exhaustive evaluation of the mean and variance of a single IAR measurement was performed by varying the position of the shared satellite over the hemispherical surface depicted in 5.1. The spherical cap in Figure 5.1 was intended to lie on the LTP of the target agent i, (see Appendix A for details) and it corresponds to the locus of points covered by any possible satellites orbiting the Earth at a given distance r_i^s. It is worth remarking that although a real satellite-to-agent range changes with the position of satellite along its trajectory, this aspect is poorly relevant in terms of relative geometry of the two agents.

Let recall (4.49) as generalized equation to compute the IAR variance $\sigma_{\hat{d}} = \mathrm{Var}(\hat{d}_{(\mathrm{IAR})})$ derived for the IAR as a function of the standard deviations of pseudorange, the angle formed by the steering vectors and the positions of the agents. In order to investigate the relationships between $\sigma_{\hat{d}}$ and the system geometry, the values of the three σ-parameters were kept fixed while the relative coordinates of the shared satellite varied. Given an intuitive strong dependency of the IAR accuracy from the uncertainty on the angle γ included between the steering vectors, the examples reported hereafter are obtained from three representative variations of this parameter: *null* (a), *small* (b) and *severe* (c) error variance on γ, by acting on the parameter $\hat{\sigma}_\gamma$. The values has been chosen according to their relationship w.r.t. the position error covariance of the agents. Even neglecting any GDOP-related effects, it can be shown that the value of $\sigma_{\hat{\gamma}}$ also varies according to the position of the shared satellite.

5.1.2 Variance behaviour in single satellite IAR

The following sample static scenario includes an aiding agent lying on the LTP centered in its true location $\mathbf{x}_T$ and an aiding agent located at a distance of 100 m N-E direction. We are interested in observing the behaviour of $\sigma_{\hat{d}}$ varying the position of the shared satellite, $\mathbf{x}_s$.

Figure 5.3 and Figure 5.2 present the inverse relationship between IAR bias and variance w.r.t. the shared satellite position. All the figures are obtained by Monte Carlo simulations counting for 100.000 trials for each azimuth-elevation pair with a granularity of 1 degree on elevation and 2 degrees on azimuth.

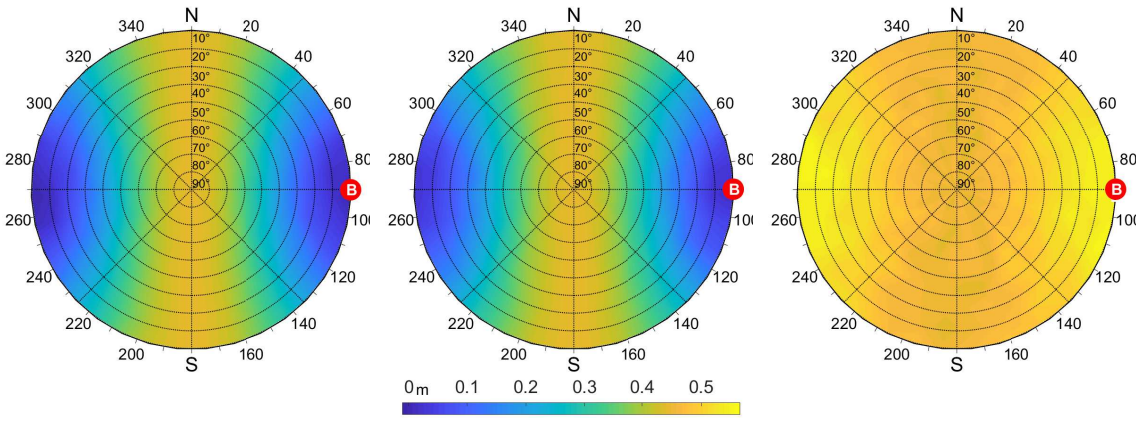

(a) IAR bias for $\sigma_{\hat{\gamma}} = 0$ (b) IAR bias for $\sigma_{\hat{\gamma}} = 1 \cdot 10^{-7}$ (c) IAR bias for $\sigma_{\hat{\gamma}} = 5 \cdot 10^{-7}$

Figure 5.2: Simulated evaluation of the bias of the IAR (color-scale) measurements according to the position of the shared satellite and varying the magnitude of $\sigma_{\hat{\gamma}}$ in $[0, 1 \cdot 10^{-7}, 5 \cdot 10^{-7}]$, $d = 100$ m, $\sigma_i = \sigma_j = 7.03$ m.

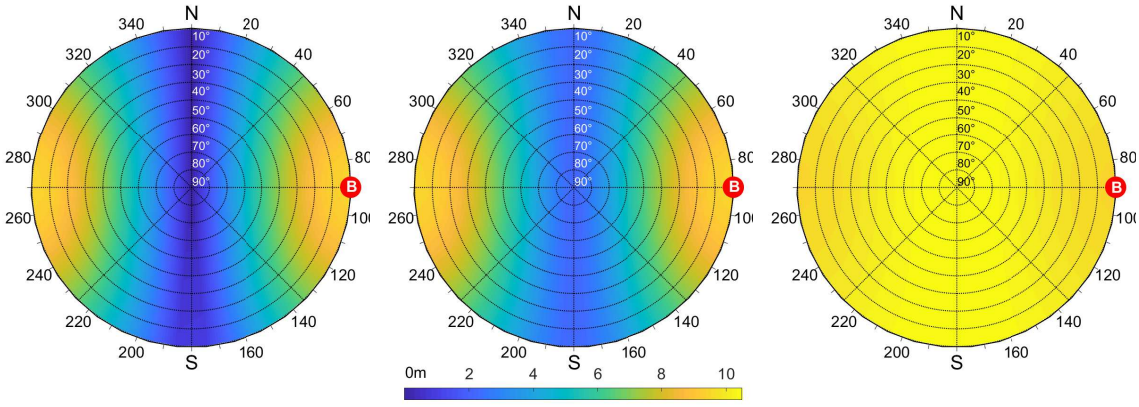

(a) $\sigma_{\hat{d}}$ for $\sigma_{\hat{\gamma}} = 0$ (b) $\sigma_{\hat{d}}$ for $\sigma_{\hat{\gamma}} = 1 \cdot 10^{-7}$ (c) $\sigma_{\hat{d}}$ for $\sigma_{\hat{\gamma}} = 5 \cdot 10^{-7}$

Figure 5.3: Analytic evaluation of $\sigma_{\hat{d}}$ (color-scale) according to the position of the shared satellite and varying the magnitude of $\sigma_{\hat{\gamma}}$ in $[0, 1 \cdot 10^{-7}, 5 \cdot 10^{-6}]$, $d = 100$ m,$\sigma_i = \sigma_j = 7.03$ m.

As it can be observed in the aforementioned plot series, the value of $\sigma_{\hat{d}}$ intuitively increases with $\sigma_{\hat{\gamma}}$ while the its dynamic range over the skyplot overall reduces with its increment. The value $\sigma_\gamma = 5 \cdot 10^{-7}$ was chosen because it is representative of a further inversion phenomenon of both bias and variance independent behaviours over the hemispherical sample space:

higher $\sigma_{\hat{d}}$ regions tends to turn in region characterized by lower value $\sigma_{\hat{d}}$ according to the uncertainty on the angle $\hat{\gamma}$.

In order to extend the discussion, the value of $\sigma_\gamma = 5 \cdot 10^{-7}$ was chosen, and Figure 5.4 shows how varying the position of the aiding agent, the symmetry is maintained w.r.t. to a direction orthogonal to the LoS between the cooperating agents.

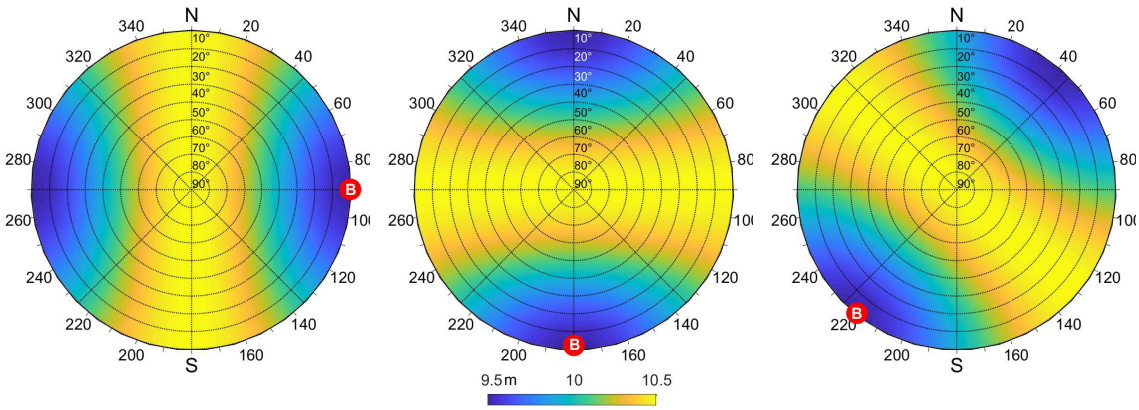

(a) $Az_B = 90°$, $El_B = 0°$ (b) $Az_B = 180°$, $El_B = 0°$ (c) $Az_B = 220°$, $El_B = 0°$

Figure 5.4: Analytic evaluation of $\sigma_{\hat{d}}$ (color-scale) varying the azimuth of the aiding agent j, w.r.t. the aided agent i. Parameters: $\sigma_{\hat{\gamma}} = 0.5 \cdot 10^{-6}$ $d = 100$ m, $\sigma_i = \sigma_j = 7.03$ m.

By changing both and the azimuth of the aiding agent, such as in Figure 5.5, one can notice that the minimum variance can be observed for satellites roughly located in the same area of the skyplot nearby the relative location of the aiding agent. We remark that high values of $\sigma_{\hat{\gamma}}$ reduce the range of the standard deviation which is this case approximately equal to 1 m, meaning the the difference w.r.t. to satellites located in different portion of the sky might be not remarkable.

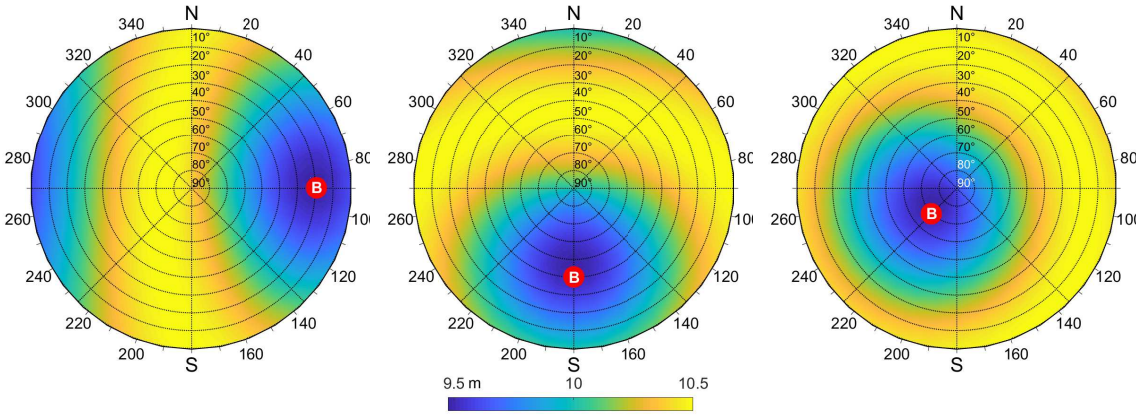

(a) $Az_B = 90°$, $El_B = 20°$ (b) $Az_B = 180°$, $El_B = 40°$ (c) $Az_B = 220°$, $El_B = 70°$

Figure 5.5: Analytic evaluation of $\sigma_{\hat{d}}$ (color-scale) both the azimuth and elevation angle of the aiding agent j, w.r.t. the aided agent i. Parameters: $\sigma_{\hat{\gamma}} = 0.5 \cdot 10^{-6}$ $d = 100$ m, $\sigma_i = \sigma_j = 7.03$ m.

5.1.3 Analytic formula assessment

A sample comparison of the experimental values and results obtained from the generalized equation (4.47) is provided in this section.

The skyplots in Figure 5.6 are obtained as the difference between simulated and theoretical $\sigma_{\hat{d}}$ in the same scenario of Figure 5.3 and Figure 5.2.

As the steering error $\sigma_{\hat{\gamma}}$ increases, a non-negligible error can be observed in the areas characterized by high error standard deviation. This is particularly visible in the skyplot in Figure 5.6c belonging to a plot series obtained by considering the values of $\sigma_{\hat{d}}$ considered in Figure 5.3. This behaviour can be reasonably attributed to the neglected cross-correlated terms in (4.51), that become more relevant as $\sigma_{\hat{\gamma}}$ increases (4.49), as well as to the truncation of the Taylor expansion. However, in this example the simulated IAR variance showed a difference which is in this case less than 0.6 m w.r.t. the theoretical value given by (4.51).

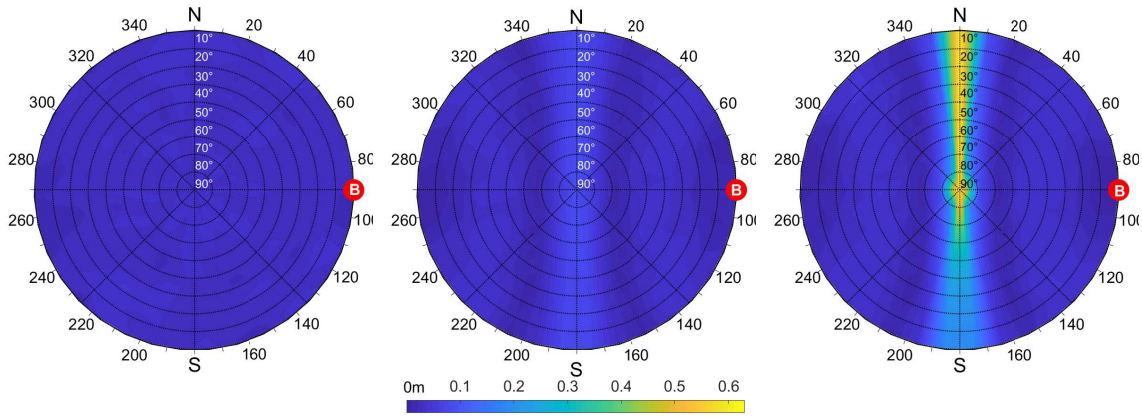

(a) $\sigma_{\hat{\gamma}} = 1 \cdot 10^{-7}$ (b) $\sigma_{\hat{\gamma}} = 1 \cdot 10^{-7}$ (c) $\sigma_{\hat{\gamma}} = 5 \cdot 10^{-7}$

Figure 5.6: Estimation error varying $\sigma_{\hat{\gamma}}$ in case of an aiding peer relatively located at $Az_B = 90°$,$El_B = 0°$.

In case of availability of more than one satellite in common visibility, a suitable theoretical formula allows to make an a priori choice of the shared satellite that will provide the best trade-off between bias and variance of the error of the estimated IAR. Furthermore, the formula can be split in three terms which can be estimated without the mutual knowledge of the explicit positions of the users. Average values and variances of the random variables involved can be derived by the users to obtain an estimation of the IAR variance which can be in turn used within further waiting strategies.

5.1.4 Experimental framework in a controlled static environment

A further validation of the IAR statistical model can be performed in a controlled environment, exploiting realistic RF signals, but preventing the non-modeled impairments from affecting the dataset as in an real scenario such as multipath scattering. Two static receivers have been simulated by means of a professional RFCS IFEN™ NavX®, as shown in the scheme in Figure 5.7. Such a setup guaranteed a considerable flexibility in the configuration of all the involved parameters. Agents have been simulated with fixed baseline distance $d_{ij} = 126.5962$ m, as obtained from euclidean distance of LLA coordinates configured at the RFCS, and reported in Table 5.1.

The same scenario has been scheduled at different times (4-hours step) to collect several constellation geometries. The RFCS has been configured to generate GPS constellation

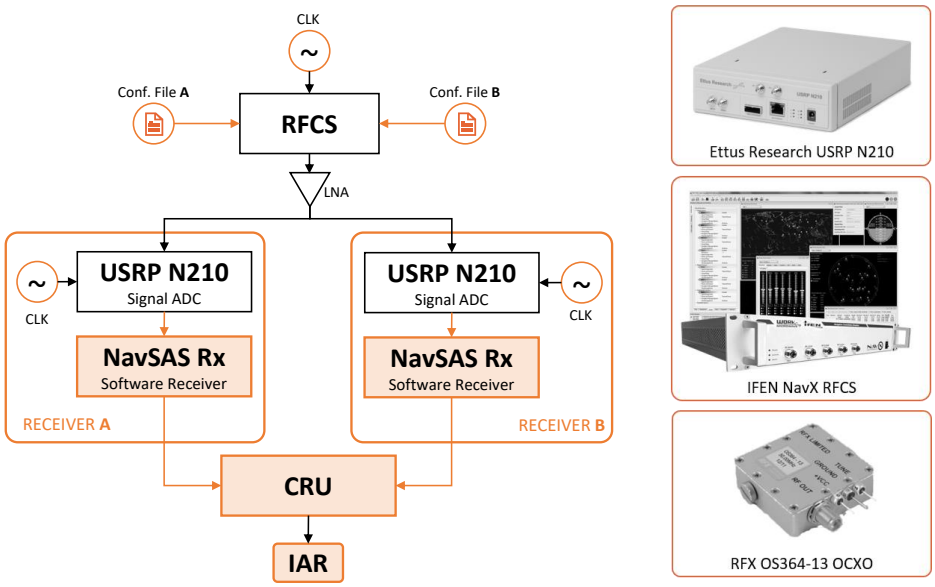

Figure 5.7: Simulation test-bench for IAR performance assessment processing realistic RF signals.

Table 5.1: LLA Coordinates of simulated static agents in a controlled environment.

Agent	**Latitude** (deg)	**Longitude** (deg)	**Altitude** (m)
Aiding	45.065274	7.658969	311.973
Aided	45.064775	7.650414	311.635

according to the scheduled time, thus using realistic geometry and GDOP values at the receiver. The set of generated signals were affected by ionospheric and tropospheric error as well as by satellites clock bias. All the correction parameters were carried by the navigation messages to let the software receiver compensate autonomously for these errors.

Signals have been recorded as digitalized raw samples by means of Ettus Research™ Universal Software Radio Peripheral (USRP) N210 front-end [146]. The samples have been post-processed through MATLAB® NavSAS GNSS software receiver to get code-based observables and positioning solutions. The two independent software-defined GNSS receivers performed the positioning autonomously and asynchronously, both using identical reference oscillators RFX OS364-13 Oven Controlled Xtal Oscillator (OCXO). The most relevant signal generation and acquisition settings are reported in Table 5.3.

Output GNSS observables are processed in a CRU, implemented in MATLAB® through IAR algorithm. Non-synchronized GNSS receivers provided observables and positioning data at different epochs depending on their signal processing loops (i.e. acquisition and tracking) and navigation algorithm as referred in Chapter 3. The time misalignment between the measurements epochs has been compensated through ephemeris to avoid time-inconsistency between independent measurements, according to ephemeris-based misalignment compensation (4.40). By considering a relatively short time-span (600 s) for the observation of the satellites, the de-trended pseudorange measurement have been considered as an ergodic process. Their variance has been estimated by means of a second order discrete derivative [42]. *Time variance* was hence considered as *sample variance* estimated from such modified time series and used to evaluate the theoretical formula. Hereafter, for sake of readability, the

Table 5.2: Hardware configuration.

Table 5.3: Ettus Research USRP N210.

Parameter	Value/Unit
Constellation/Signal	GPS/L1
No. of Channels	10
Integration time	20 s
Doppler step	125 Hz
Coherent accumulations	5
Freq. Lock Loop time	10 ms
PVT rate	1 Hz

Table 5.4: NavSAS Software Receiver.

Parameter	Value/Unit
Carrier frequency	1575.42 MHz
Intermediate frequency	0 Hz
Sampling Frequency	5 MHz
Quantization bit	16
Sampling mode	'IQ'
Reference clock	External
Gain	38 dB

GPS satellites will be identified through the number of their transmitted PRN codes.

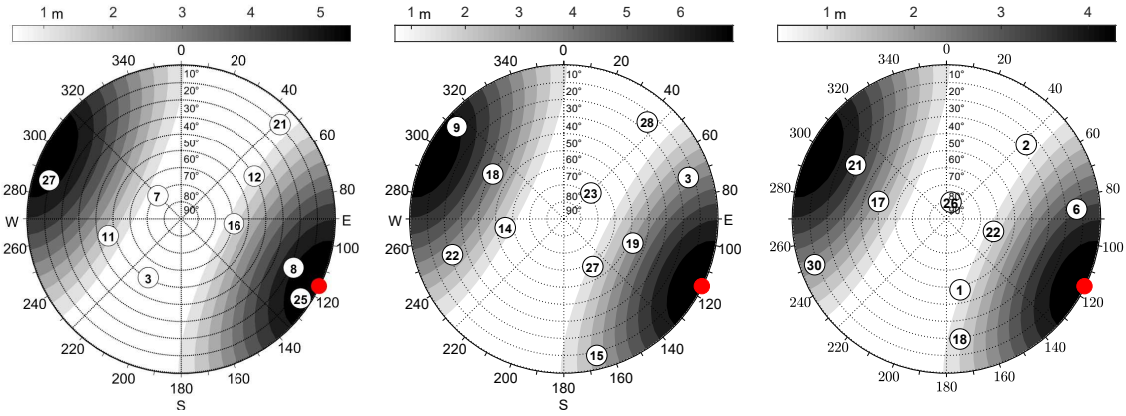

(a) Turin, 00:00, 4th April 2018 (b) Turin, 08:00, 4th April 2018 (c) Turin, 12:00, 4th April 2018

Figure 5.8: Skyplot showing the analytic $\sigma_{\hat{d}}$ (color-scale) along with the superposition of satellites azimuth and elevation generated by the RFCS.

Experimental and theoretical values of $\hat{\sigma_d}$ are shown for different satellites and datasets in Figure 5.9. A good match of the experimental and analytic values is overall present. For given sets of satellites such as PRNs 21,7,12,11,16 in Figure 5.9a , PRN 28 in 5.9b and PRNs 26,1,22,18,30,21 in 5.9c, the relative estimation error is less than the 15%, such matches are highlighted in Figure 5.9 with grey circles.

Considering the satellites for which we observe the largest mismatch, we can notice that they are located nearby the symmetry axis of the skyplot in Figure 5.8.

In fact, Recalling the results presented in Section 5.1.2 and shown in Figure 5.6, this region is known to lead to inaccurate theoretical estimations when the value of $\sigma_{\hat{\gamma}}$ is not negligible. Although the experimental values of $\sigma_{hat\gamma}$ was not computed at the time of the experiment, it can be assumed greater than $5 \cdot 10^{-}6$.

5.1.5 Experimental assessment using COTS GNSS Receivers

The results from an on-field experimental test are hereafter exploited to further assess the validity of the theoretical findings in real environment. The real data were used to obtain an estimate of the IAR variance considering a real satellite constellation and the real receivers positions during the experiments. By exploiting raw pseudorange measurements provided by Commercial Off-the-shelf (COTS) u-Blox® receivers, two different experimental campaigns have been pursued investigating the IAR computation in real environment:

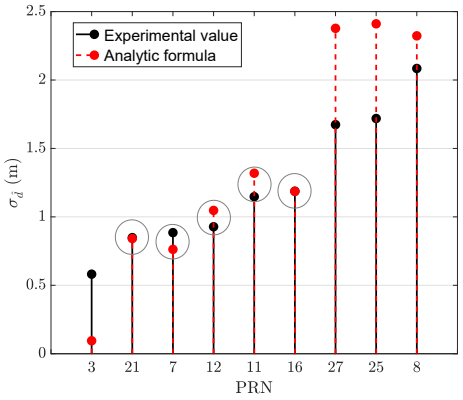

(a) Turin, 00:00, 4th April 2018

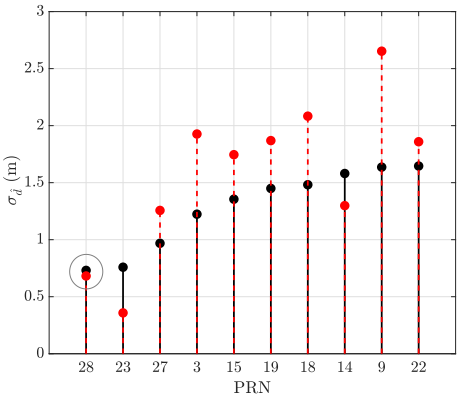

(b) Turin, 08:00, 4th April 2018

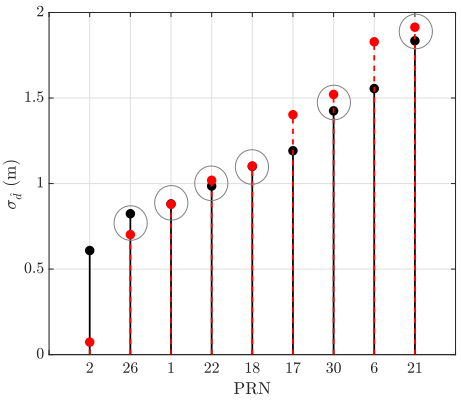

(c) Turin, 12:00, 4th April 2018

Figure 5.9: Ranking plot of all the shareable satellites based on the STD experimentally observed and the interpolation of the analytic model.

- a *static scenario*, where both the *aided* and *aiding* receiver performed static positioning at different baseline lengths.
- a *semi-dynamic scenario*, in which the aiding receivers was kept static while the aided receiver was driven in a dense urban scenario.

The tests locations were set in Turin in correspondence of the geodetic coordinates included in Table 5.5 and 5.6.

The hardware setup of the experiments, shown in Figure 5.10, included two COTS u-blox M8-T receivers identically configured. The navigation solution rate was set to 5 Hz including multi-constellation position computation.

The first M8-T receiver was connected to a georeferenced geodetic antenna (whose coordinates are reported in Table 5.5) while the second was installed on-board a car along with a dual-frequency Swift™ Piksi Multi receiver used as reference. They were both connected to the same Aero Antenna AT1675-382. No clock synchronization was exploited between the two u-Blox receivers: pseudorange measurements and related positioning solutions were collected according to the independent on-board clocks as performed for the controlled experiment. The logged raw pseudorange measurements obtained from the M8-Ts were re-processed offline in order to determine a plain LMS positioning solution considering only the measurements from GPS satellites. The inter-agent distances were then computed according to the IAR method (4.30).

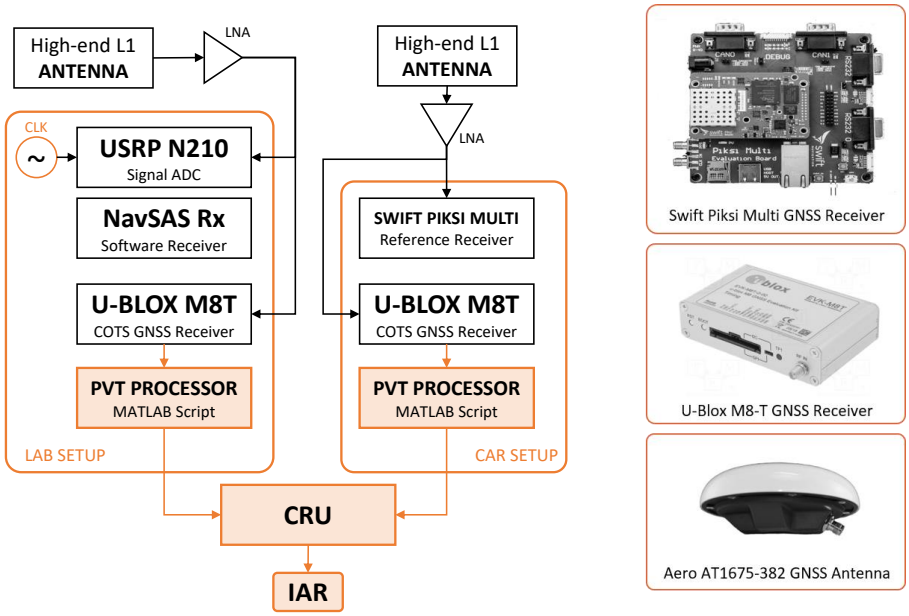

Figure 5.10: Simulation test-bench for performance assessment of GNSS-based ranging methods in real environment.

Table 5.5: LLA Coordinates of georeferenced geodetic antenna (aiding peer).

Latitude (deg)	**Longitude** (deg)	**Altitude** (m)
45.065277	7.658948	311.804

Table 5.6: Test scenarios for GNSS-based ranging (LLA coordinates of the aided peer).

Name	**Latitude (deg)**	**Longitude (deg)**	**Baseline** (m)	**Test Duration** (s)
S00	45.065407	7.657622	100	565.1
S01	45.066450	7.658056	126	640.2
S02	45.068365	7.656880	360	606.2
S03	45.070769	7.656095	630	622.6
D01	Dynamic	Dynamic	$200 - 1000$	$1.3866 \cdot 10^3$

The results presented in this section are obtained by selecting user-to-user output ranges characterized by a reasonable time difference Δt between the measurements of the the collaborating receivers. By considering high values of Δt, indeed the correction provided through (4.40) does not compensate effectively the time-inconsistency of the data. Therefore the maximum Δt considered for the IAR computation was $50 \cdot 10^{-3}$ s, which guarantees a reasonable margin for the misalignment of different high-rate positioning solutions provided by popular COTS receivers [163].

Validation of the theoretical model using COTS receiver

Given the positions of the agents and of the shared satellite at a certain time instant, t_k, it is possible to estimate the expected $\sigma_{\hat{d}}$ by knowing the variances of the random variables involved in the IAR estimation (4.30) (i.e. σ_A^2, σ_B^2, $\sigma_{\hat{\gamma}}^2$). The baseline is evaluated through a

IAR computation based on observations from the experiments and its variance is compared to the variance predicted by (4.51) in the same conditions. Equation (4.51), used for the computation of the IAR standard deviation is used in this case with experimentally-estimated values for the assessment and characterization of STDs of the IAR measurements.

The satellites movement along the tests duration induces a change in the IAR variance (4.51) as well. However the difference between the minimum and maximum variance resulted from (4.51) within the test duration is always below 10^{-5} m in each experiment, thus being negligible. As a consequence, the variance of the experimental IARs is compared to the mean of the set of values computed using (4.51) over the observation window. The result is shown in Figure 5.11, where the theoretical variance reflects the behaviour of the measured variance for the majority of the satellites. The gaps between the two variances are summarized in Table 5.7, averaging among all the available satellites.

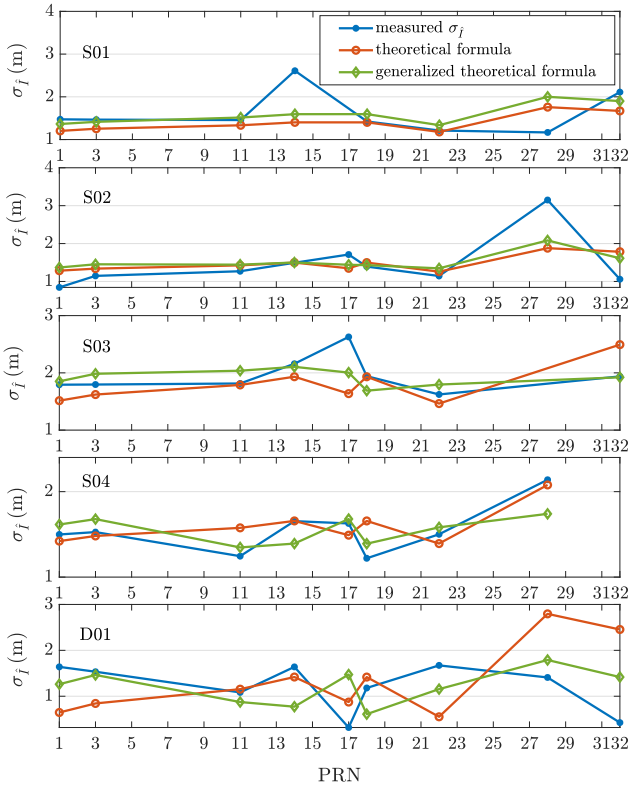

Figure 5.11: Inter-Agent Range standard deviation estimated from experimental data compared to theoretical formulas.

Equation (4.51) models the variance of the IAR computed from the experimental datasets with a good approximation. However, the observations of the random variables ($\hat{r}_A$, $\hat{r}_B$, $\hat{\gamma}$) are collected throughout time and the satellite movement throughout the experiment's duration introduces correlation among the random variables. Such a *bivariate correlation* can be modelled by the coefficients introduced in (4.47), which can be estimated, on M observations, as the PCC

$$\hat{\alpha}_{ij} = \frac{1}{M-1} \sum_{m=1}^{M} \left(\frac{X_{i,m} - \mu_{X_i}}{\sigma_{X_i}} \right) \left(\frac{X_{j,m} - \mu_{X_j}}{\sigma_{X_j}} \right) \tag{5.1}$$

where $X_{i,m}$ is the m-th observation of the random variable X_i and referes to the pseudorange measurement observed by the agent i. The correlation coefficients estimated through (5.1)

Table 5.7: Comparison between theoretical IAR variance and measured variance. The generalized theoretical formula (4.49) and the theoretical formula with the assumption of null cross-correlation (4.51) are compared

Experiment	Gap of theoretical formula	Gap of generalized theoretical formula	Gap reduction
S00	0.362 m	0.322 m	11.1 %
S01	0.749 m	0.698 m	6.8 %
S02	0.151 m	0.099 m	34.4 %
S03	1.049 m	0.698 m	33.5 %
D01	1.683 m	1.094 m	35 %

are employed in the generalized theoretical formula (4.49) to obtain a refined estimation of the IAR variance. Taking into account the correlation between the measurements, a better correspondence between the theoretical and experimental values is achieved and this improvement is quantified in Table 5.7 which highlights a gap reduction between 6.8% and 35%, depending on the experimental conditions.

5.1.6 Weighted IAR measurements

Considering a network A proper variance estimation can be hence reliably obtained for each IAR contributions through (4.49). If the set of shareable satellites includes more than one satellite, an effective weighting of the measurements can be applied.

Let suppose that vector $\mathbf{d}_j^{(k)} = [\ d_j^{1(k)} \quad d_j^{2(k)} \quad \cdots \quad d_j^{s(k)}\ ]^\top$ includes a set of IAR measurements computed combining local pseudorange measurements with measurements retrieved from a generic j-th agent with respect to all the shareable s satellites, $\mathbf{R}_d^{(k)}$ is the covariance matrix estimated for $\mathbf{d}^{(k)}$ and $\mathbf{J} = [\ 1 \quad 1 \quad \cdots \quad 1\ ]^\top$ is a design vector, the minimum variance estimate of $d_{(k)}$ according to the Gauss-Markov theorem is

$$\hat{d}_j^{(k)} = \sigma_{\hat{d}} \left(\mathbf{J}^\top \mathbf{W} \mathbf{d} \right) \tag{5.2}$$

where $\sigma_{\hat{d}} = \mathbf{J}^\top \mathbf{W} \mathbf{J}$ and $\mathbf{W} = \left(\mathbf{R}_d^{(k)} \right)^{-1}$. Equation (5.2) allows to account for correlations among collaborative contributions. In the following the IAR method will be always referred to its weighted version, W-IAR, thus being more suitable for a comparison with the differential techniques.

5.2 Statistical analysis of baseline estimation techniques

By means of a set of examples obtained for a number of analytical trajectories and Monte Carlo simulation, this section provides an overview of the statistical properties of collaborative baseline measurements obtained in semi-dynamic environment through the combination of independent pseudorange measurements affected by WGN. Statistical distribution and cross-correlation among the whole observables set will be discussed for the methods presented in Chapter 4 for a single dynamic agent computing multiple collaborative contributions from independent agents.

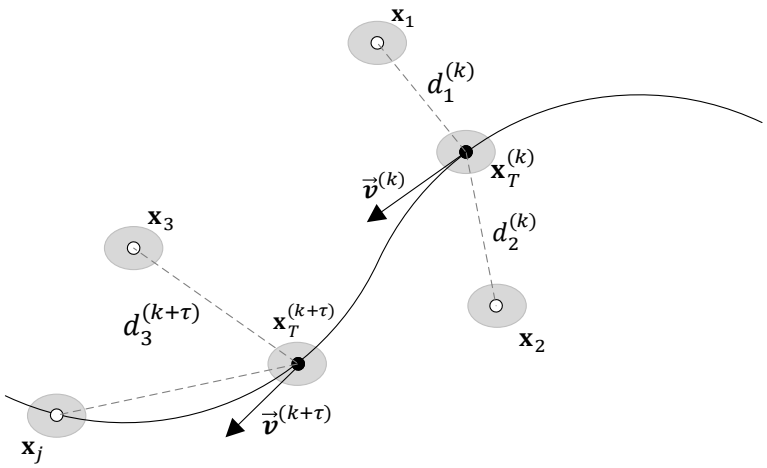

Figure 5.12: Baseline length estimation in simulated vehicular scenario in close proximity assumption.

MATLAB Simulation Environment

A MATLAB®-based simulation environment was conceived to allow a full control over the simulation parameters characterizing the baseline estimation in dynamic scenarios (i.e. vehicular). In the following, each simulation step is described in detail by addressing a dynamic target vehicle moving along a predefined trajectory and collaborating with fixed agents used as anchors of opportunity, as reported in Figure 5.12.

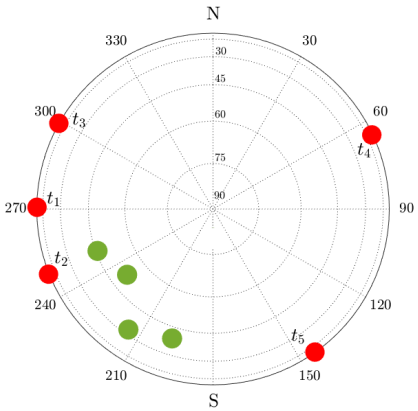

Figure 5.13: Example of satellite and aiding agent visibility experienced by a dynamic agent travelling on a predefined trajectory.

- *Analytic trajectory generation*: A set of analytical trajectories were analysed within the proposed simulation environment. A library of elementary geometrical trajectories such as the Bernoullian lemniscate reported in Figure 5.14 were used for the analysis. The trajectory were defined according to the typical test paths used in literature and available in RFCSs settings.

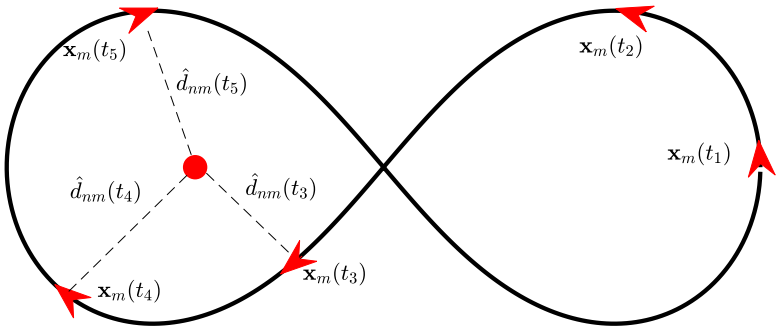

Figure 5.14: Example of a path based on a Bernoullian lemniscate of 1046 7m travelled at an average speed of 26 15m/s. The dashed lines depict the collaborative range measurements retrieved at different time instants.

- *Analytic Dynamic Scenario*: The generated trajectory was travelled by a predefined vehicle within the MATLAB® Driving Scenario Toolbox. An average tangent speed $\vec{\mathbf{v}}$ can be defined for each node of the trajectory thus providing accurate control over the time evolution of the motion.
- *Satellites generation*: satellite constellation can be dynamically generated applying a pre-defined azimuth and elevation mask to simulate limiting visibility conditions.
- *Aiding network and agents position*: The aiding agents can be generated according to their relative position in terms of azimuth and elevation.

5.2.1 Cross correlation among standalone GNSS measurements and collaborative baseline length estimation

With the aim of integrating collaborative measurements as a complementary source of information, it has to be remarked that potential cross correlation will reduce the amount of information carried by each observable to the positioning problem. This aspect will be investigated in detail in Chapter 6 while in this section, the evidence of the cross-correlation among collaborative and standalone measurements is provided for the different GNSS-based baseline computation techniques.

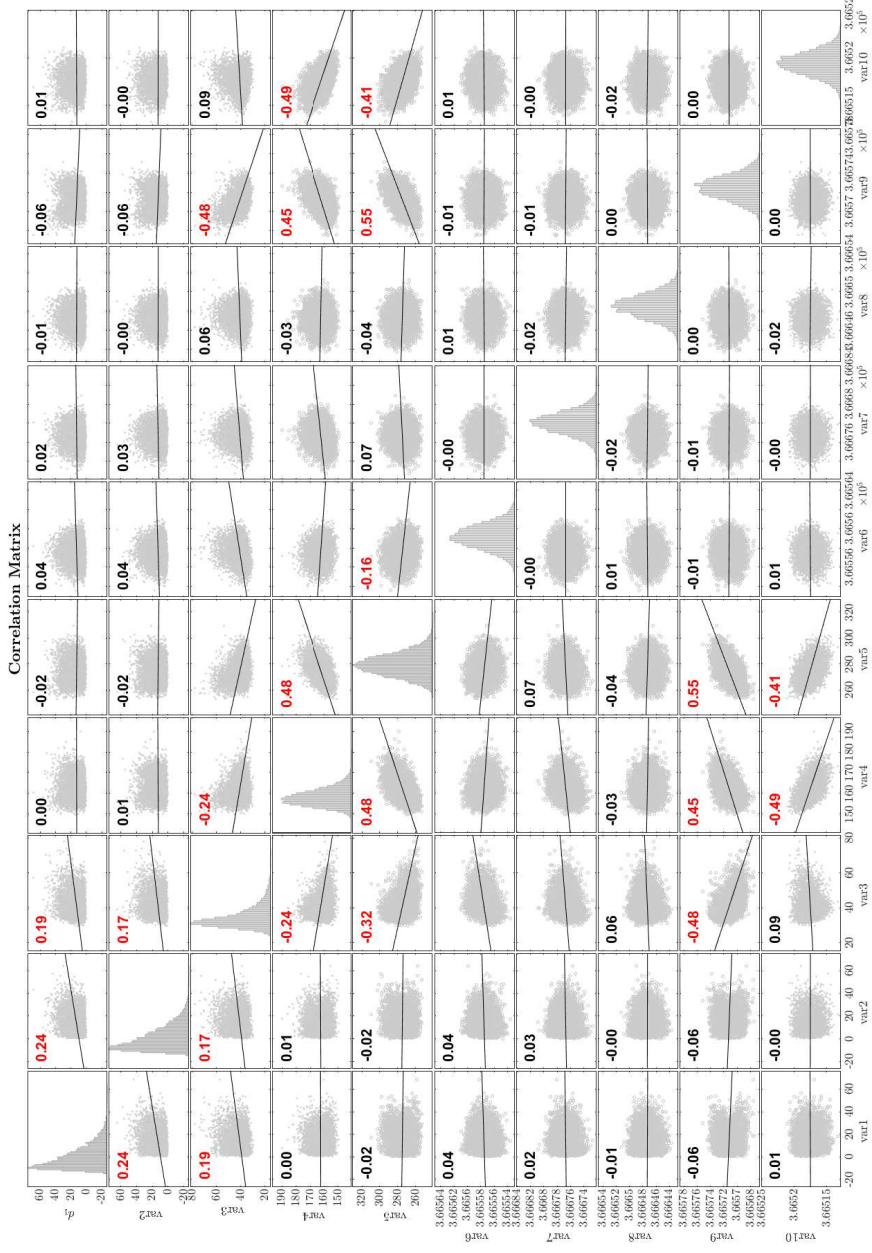

Figure 5.15: Correlation matrix of a set of 10 measurements (5 Inter-agent distances and 5 Normally-distributed pseudorange measurements).

Let us consider a composite measurement vector defined as

$$\mathbf{z}_{(k)} = \begin{bmatrix} \mathbf{d}_{(k)}^{\top} & \boldsymbol{\rho}_{(k)}^{\top} \end{bmatrix}^{T} \tag{5.3}$$

where $\mathbf{d}_{(k)}$ is a row vector of collaborative inter-agent distances while $\boldsymbol{\rho}_{(k)}$ is a row vector of standalone pseudorange measurements.

The cross correlation among the terms of $\mathbf{z}_{(k)}$ is defined by means of PCC computed through Monte Carlo trials in a finite set of instants t_k identified along the whole simulation timespan. Within a Monte Carlo framework, the pairwise bivariate correlation among two measurements can be determined by means of PCC. Given a set of S satellites and C collaborative contributions, a squared PCC ($C+S\times C+S$) matrix can be built and visualized by means of *correlation matrix*, as shown in the example of Figure 5.15. This example shows the correlation matrix of the measurement vector $\mathbf{z}_{(k)}$ composed by $S = 5$ satellites measurements combined with the same measurements provided by $C = 5$ agents to retrieve the respective baseline length measurements, at a generic time instant t_k. The correlation coefficients are obtained from the observation of 100.000 realizations of the WGN samples affecting the pseudorange measurements.

The correlation matrix in Figure 5.15 does not provide an evident information along different time epochs, therefore a simplistic visual representation of such coefficients is provided by means of a different correlation plot, according to scheme in Figure 5.16. In this plot the absolute values of the correlation coeffiecients are determined according to

$$r_{ij}^{(k)} = \left| \frac{\sum_{n=1}^{N} \left(z_{i,n}^{(k)} - \bar{z}_{i}^{(k)} \right) \left(z_{j,n}^{(k)} - \bar{z}_{j}^{(k)} \right)}{\sqrt{\sum_{n=1}^{N} \left(z_{i,n}^{(k)} - \bar{z}_{i}^{(k)} \right)^{2}} \sqrt{\sum_{n=1}^{N} \left(z_{j,n}^{(k)} - \bar{z}_{j}^{(k)} \right)^{2}}} \right| \tag{5.4}$$

where N is the number of Monte Carlo trials and measurements z_i,z_j are respectively the i-th and j-th measurements of the composite measurement vector $\mathbf{z}^{(k)}$, including standalone and collaborative measurements. Being a normalized coefficient, the values assumed by the generic $r_{ij}^{(k)}$ are mapped in the interval (0,1). Such coefficients are hence visualized by means of a colorscale.

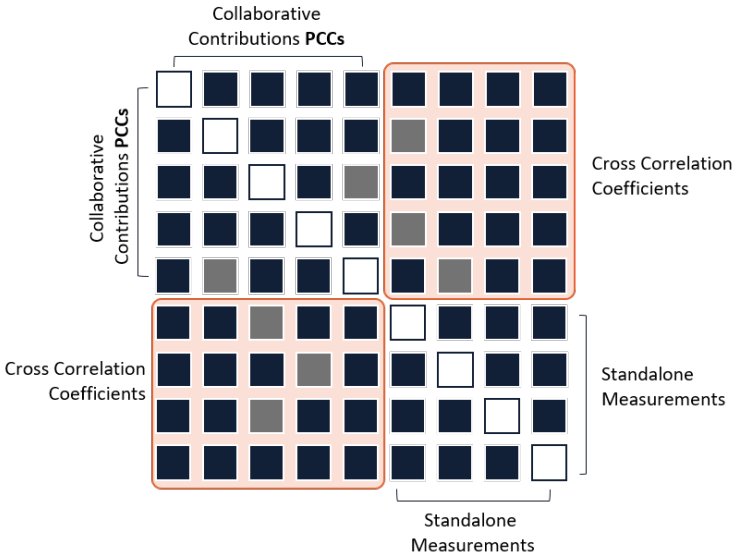

Figure 5.16: PCC plot scheme for hybridized measurement vector (Compact representation of the correlation matrix).

With respect to the correlation matrix used in 5.15, this compact representation provides a qualitative overview of the dependency among the measurements dropping the visualization of their statistical behaviour. Indeed, the analysis of the PDF of the collaborative measurements will be separately provided in Section 5.2.2. Each PCC in the *correlation matrix* varies along the time as it can be observed in the sample time series of the PCC matrix shown in Figure 5.17.

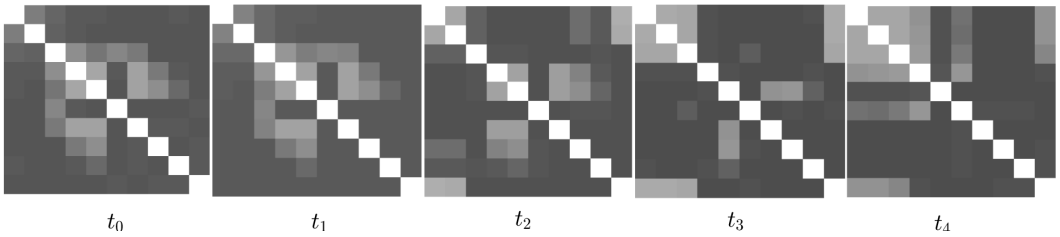

Figure 5.17: Sample PCC matrix time series scheme for hybridized measurement vector including 5 IAR and 4 satellites. Colorscale black (0) - white (1).

Recognizable patterns along subsequent time instants show that cross-correlation among the measurements is time-dependent and this is attributed to the slow geometrical changes due to the reciprocal motion of agents and satellites. In the example reported in Figure 5.17, the PCCs related to standalone measurements are close to zero (black) since the pseudorange measurements are affected by independent WGN samples. On the contrary, the PCCs related to collaborative measurements show non-negligible cross correlation (grey) with standalone measurements in t_0,t_1,t_2 and strong cross correlation within the collaborative subset in t_3 and t_4. All the diagonal terms, r_{ii}, namely the autocorrelation coefficients, are obviously equal to 1.

Let analyse a simulation example in selected time instants. The correlation plots are shown in Figure 5.17 are recomputed for each baseline estimation methods and shown in Figure 5.18. Along the rows it can be noticed that time-dependent changes in correlation coefficients are visible for all the analysed methods.

PCCs evolution in time appears similar for all the differential techniques at rows b,c and d while IAR shows different values. It is worth noticing that the left-bottom (5×5) submatrix highlight the uncorrelation among standalone pseudorange measurements which were independently generated affected by Gaussian noise. Differently, cross correlation among collaborative measurements become strong (about 0.5 at t_4 and t_5 for all the methods. For this upper-left submatrix the IAR measurements show a slight lower correlation on both collaborative and mixed PCC.

5.2.2 Statistical Distribution of the Baseline Length Error considering independent Gaussian inputs

In this section, the variation of the statistical distribution is observed along the time for dynamic agents and different computation methods. A set of simulation data is reported hereafter showing the behaviour of the error of collaborative measurements w.r.t. to the true baseline length.

As discussed in Chapter 4 and shown in the sample correlation matrix of Figure 5.15, the PDF of the baseline length error obtained through differential methods can show a strong skewness. A snapshot of the baseline length error PDF is provided in Figure 5.19 for the proposed techniques. The plot shows similar behaviour for the legacy approaches (i.e. PR,DD and SD) for which the error PDF assumes non-Gaussian behaviour. On the contrary, such

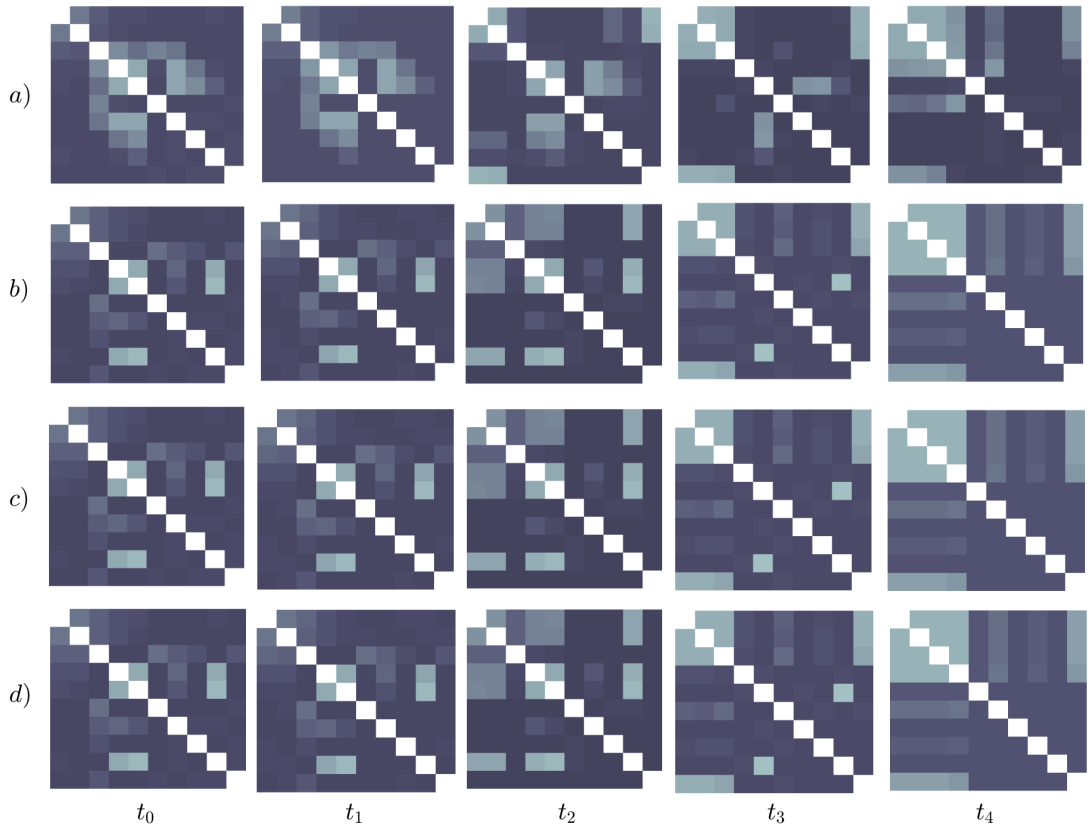

Figure 5.18: PCCs over a selected set of time instants t_k for the measurements set of a dynamic agent travelling over a Bernoullian lemniscate trajectory. Methods: IAR (a), PR(b), SD(c), DD(d). Colorscale black (0) - white (1).

qualitative analysis shows that the IAR method offers a reduced variance and a Gaussian-like probability distribution. A BIC has been used within the Monte Carlo simulation to classify the error PDF of the baseline length estimations. The output occurrences along the simulation timespan were normalized by the total number of simulation epochs to provide the percentage of occurrence of each tested distribution. The true distance was subtracted to the estimated quantity for 3 different aiding agents. For each aiding agent, histograms were generated showing the percentage of occurrences of the most representative distributions for each baseline estimation technique. According to the plots in Figure 5.20, W-IAR measurements showed a Gaussian distribution for the most of the simulation time while differential techniques behave according to more skew statistical distributions such as Rayleigh and Generalized Extreme Value (GEV)). It is worth mentioning that PR and SD showed identical statistics thus being equivalent in terms of statistical properties.

An analysis of the time-evolution of the statistical distribution of the baseline length was computed over a Bernoullian trajectory and is presented in the boxplots in Figure 5.21. As noticeable from the behaviour of the statistics of the baseline length errors, all the methods show a stable distribution at the beginning of the simulation (static agents). When the target agent starts moving, the distribution of the baseline length error shows evident variance fluctuations in the case of the differential techniques. Differential baseline computation methods are hence more sensitive to the relative dynamics of the agents while the W-IAR measurements show a higher precision and a stabler behaviour along the simulation time.

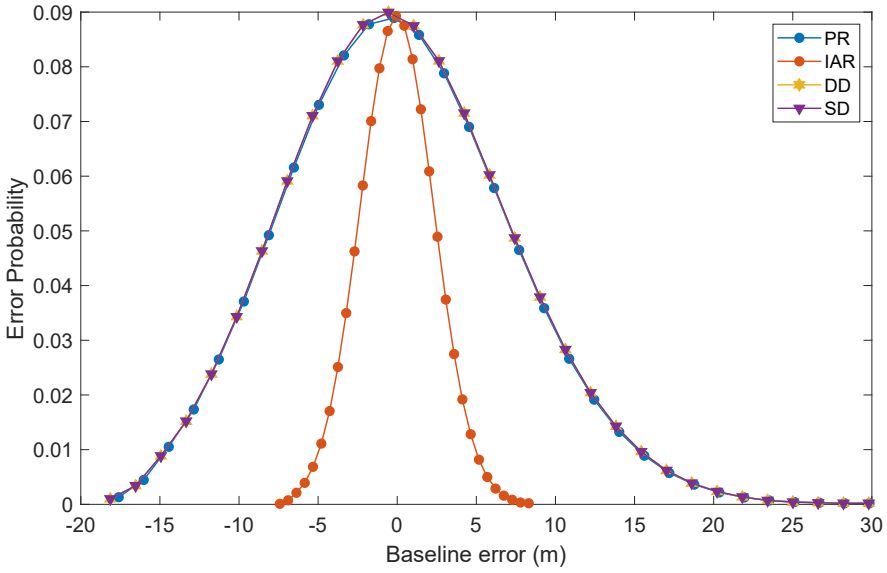

Figure 5.19: Snapshot of the estimated probability distribution over 10000 samples taken at a random time instant t_k.

5.3 Final remarks

It can be shown that the general behaviour which characterize the baseline length estimation presented in this chapter is strongly recurrent in different analytic trajectories. According to the aforementioned statistical analysis, when unbiased Gaussian-distributed pseudorange measurements are combined in the computation of collaborative baseline measurements, IAR is a powerful method for obtaining low variance and stable measurements with good cross-correlation properties but on the other side it does not allow to deal effectively with error cancellation as for differential techniques. On the other hand, according to the theoretical aspects and the example shown in Figure 5.21, the standard deviation of differential approaches is approximately 4 times the standard deviation of the W-IAR. IAR is hence suitable for the combination of corrected pseudoranges while differential techniques still offers the best performances with raw measurements. Despite of the non-linearity of the IAR equation (4.28), the error distribution has been verified to be mostly Normal [126] so that the analysis of the first and second order moments is sufficient to reliably describe the statistical behaviour of the measurements obtained through this technique.

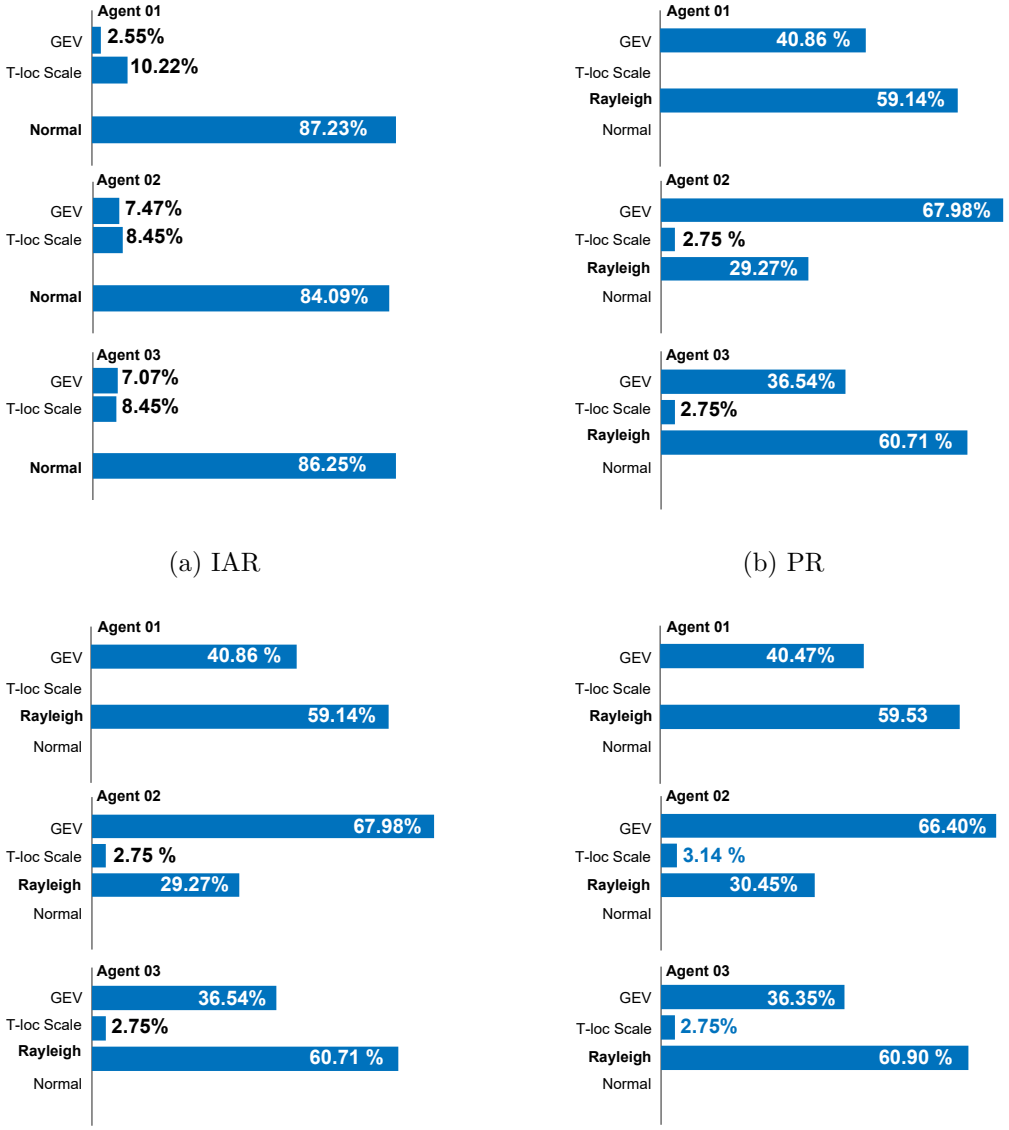

(a) IAR

(b) PR

(c) SD

(d) DD

Figure 5.20: Goodness of fit occurrences for the baseline length error of three independent agents over a Bernoullian trajectory

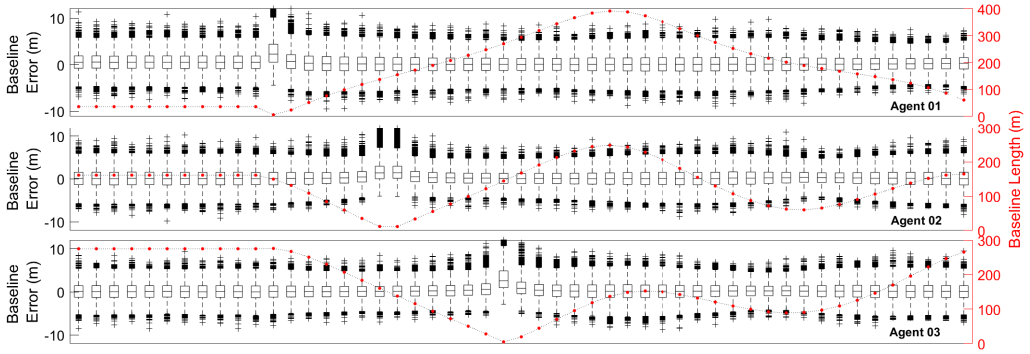

(a) IAR

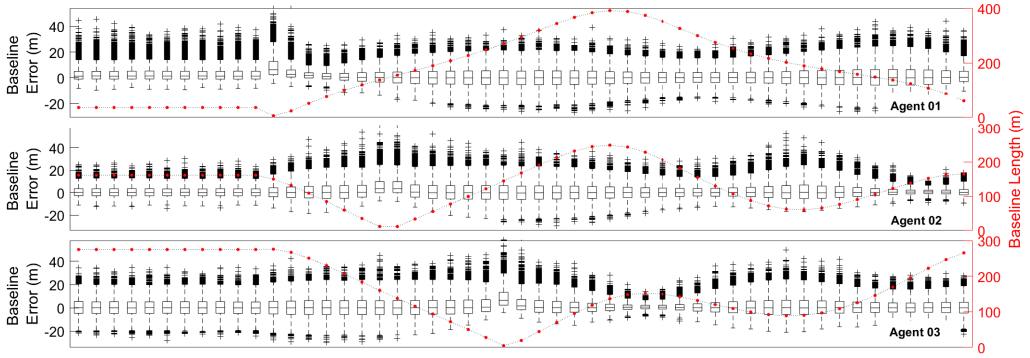

(b) PR

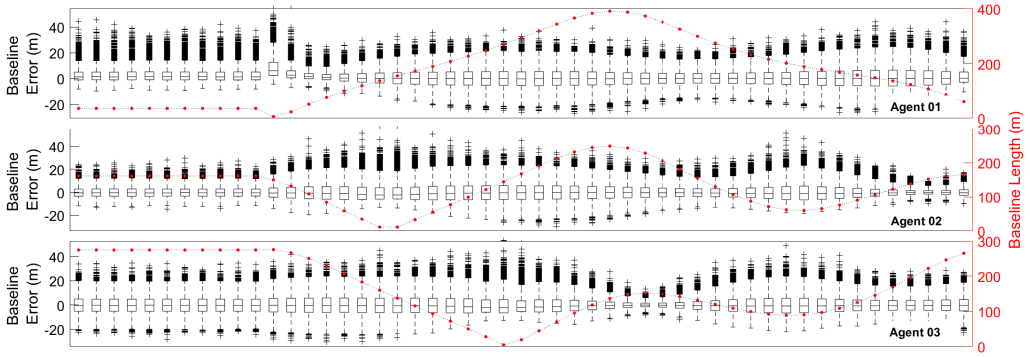

(c) SD

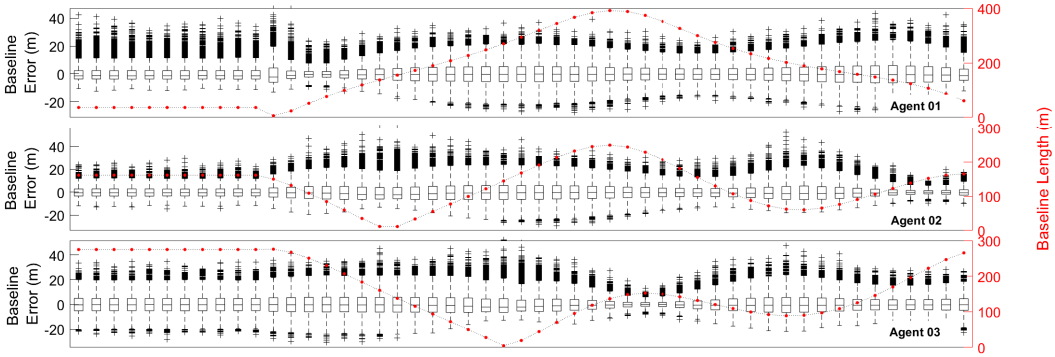

(d) DD

Figure 5.21: Box plot of the time evolution of the PDF of the baseline length error for the different methods.

Chapter 6

Hybridized Navigation Filters and theoretical limits on positioning with correlated measurements

In the last decades, a relevant effort has been spent to investigate the combinations of GNSS and auxiliary sources of RF signals (e.g. cellular base stations, Wi-Fi™ access points) from a single receiver perspective. The *joint exploitation* of these sources has been oriented to the achievement of a *seamless positioning system*, with the aim of overcoming the limitations of GNSS[31, 202].

The combination of multiple signal sources is generally known in PNT as *hybridization* and concerns the merge of different localization technologies available at the RF receivers.

The simplest approach for the *hybridization* of multiple localization technologies consists in the geometrical weighted averaging of the positioning solutions obtained through each of them. In the context of proprioceptive sensors integration, this is known as *loose coupling*. Provided that this approach is highly suboptimal, different solutions were developed to fuse information at a lower architecture level, thus exploiting *tight integration*. Further advances have been recently pursued in sensor fusion through ultra-tight integration which aim at merging auxiliary information prior to the generation of pseudorange measurements in GNSS-based positioning systems. Tight and ultra-tight integration schemes have been deeply investigated in GNSS literature for the integration of inertial sensors [7, 53, 26]

In the following, the inclusion of additional collaborative measurements will be performed at measurements level by pursuing *tightly integrated* solution according to which a statistical approach is preferred rather than a geometrical average (e.g. loose integration). Ultra-tight schemes are not suitable to integrate such a kind of additional information.

The approach proposed in this chapter aim at providing a subset of potential tight integration solutions of correlated information according to the architecture of the most popular navigation filters. Well-known alternatives to the traditional EKF such as the Unscented Kalman Filter (UKF) will not be analysed in this chapter since they are designed to deal with strong non-linearity of the target system. Therefore, after the introduction of the Bayesian estimation theory related to the HMMs associated to the positioning problem, this chapter provides a formal description of hybridized navigation filters starting from a basic Minimum Mean Square Error (MMSE) filter such as the Hybrid Weighted Least Mean Square (H-WLMS), suitable for static systems and for the initialization of Bayesian navigation algorithms. The chapter will continue with the presentation of the hybrid version of two popular recursive Bayesian estimators, namely Hybrid Extended Kalman Filter (H-EKF) and Hybrid Particle Filter (H-PF) whose indirect formulations have been implemented within this work. The last section provides a theoretical analysis based on previous and original

contributions about the theoretical limits of the hybrid positioning including the novel IAR measurements discussed in Chapter 4, as well.

6.1 Modified HMM for correlated measurements

The estimation problem to be solved in positioning and navigation is often referred in literature to as *object tracking*, where the *object* can be indeed a GNSS receiver in the form of a stand-alone equipment or embedded in a number of possible devices (e.g. vehicular navigation systems, smartphones, smartwatches). The term *tracking* can be easily confused with the *signal tracking* performed by the receiver, therefore it will be replaced by *state estimation* in the following.

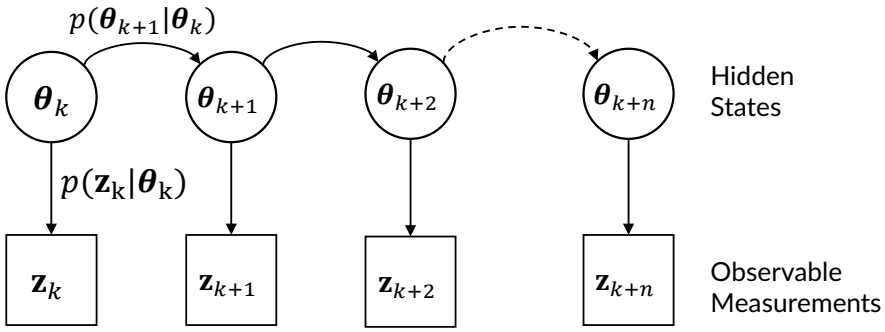

Figure 6.1: Hidden Markov Model (HMM) for a single agent retrieving direct observable measurements.

6.1.1 A model of the positioning problem: the HMM

As depicted in Figure 6.1, the problem can be modelled as a discrete-time HMM where the *state space*, $\boldsymbol{\theta}_k$, of the target dynamic system can be known only through a set of *observable measurements*, $\mathbf{z}_k$[155]. In the following, the state space vector is defined as

$$\boldsymbol{\theta}_k = \begin{bmatrix} x_k & y_k & z_k & b_k & \dot{x}_k & \dot{y}_k & \dot{z}_k & \dot{b}_k \end{bmatrix} \tag{6.1}$$

while the set of s *observable measurements*

$$\mathbf{z}_k = \begin{bmatrix} z_k^1 & z_k^2 & \dots & z_k^s \end{bmatrix}. \tag{6.2}$$

Equation (6.1) describes the relevant information about the agent position, $\mathbf{x}_k = \begin{bmatrix} x_k & y_k & z_k \end{bmatrix}$, and its velocity $\dot{\mathbf{x}}_k = \begin{bmatrix} \dot{x}_k & \dot{y}_k & \dot{z}_k \end{bmatrix}$, defined in a conventional reference frame. The terms b_k and $\dot{b}_k$ are respectively the bias and the drift of the local clock obtained w.r.t. the GNSS time scale. It is worth mentioning that (6.1) can be extended with higher order terms such as axial accelerations and axial jerk or with attitude data such as yaw, pitch and roll [53] but all these additional information cannot be directly retrieved by satellite observables only.

The Bayesian navigation filters are devoted to the joint estimation of the state vector $\boldsymbol{\theta}_k$ and the associated error covariance matrix

$$\mathbf{P}_k = \mathrm{E}\left[\left(\boldsymbol{\theta}_k - \mathrm{E}\left(\boldsymbol{\theta}_k\right)\right)\left(\boldsymbol{\theta}_k - \mathrm{E}\left(\boldsymbol{\theta}_k\right)\right)^T\right] \tag{6.3}$$

which describes the uncertainty on the estimated solution[92]. In order to determine $\mathbf{P}_k$, the error covariance matrix of $\mathbf{z}_k$ has to be measured or estimated according to

$$\mathbf{R}_k = \mathrm{E}\left[\left(\mathbf{z}_k - \mathrm{E}\left(\mathbf{z}_k\right)\right)\left(\mathbf{z}_k - \mathrm{E}\left(\mathbf{z}_k\right)\right)^T\right] \tag{6.4}$$

as detailed later.

The state transitions, represented by the horizontal arrows in Figure 6.1, are associated to a *transition probability*, $p\left(\boldsymbol{\theta}_k|\boldsymbol{\theta}_{k-1}\right)$ which is defined accordingly to a discrete-time stochastic *state transition function*

$$\boldsymbol{\theta}_k = f_{k-1}\left(\boldsymbol{\theta}_{k-1}, \mathbf{v}_{k-1}\right) \tag{6.5}$$

where f_{k-1} is a possibly non-linear function of the vector state, and $\mathbf{v}_k$ is a multivariate random variable describing the noise affecting the states. A sequence of noisy measurements is performed by the receiver at each discrete time instant t_k and each measurement links the current state vector to a specific reference point (e.g. GNSS satellites, terrestrial anchors, etc.). The relationship between state and measurements is hence described by the prior probability $p\left(\mathbf{z}_k|\boldsymbol{\theta}_k\right)$, according to

$$\mathbf{z}_k = h_k\left(\boldsymbol{\theta}_k, \mathbf{w}_k\right) \tag{6.6}$$

where h_k is a possibly non-linear function linking the observation vector to $\boldsymbol{\theta}_k$ and $\mathbf{w}_k$ is a multivariate random variable describing the measurements noise.

The state estimation is based on the Bayesian rule of conditioned probability given by

$$p(\boldsymbol{\theta}_0, \cdots, \boldsymbol{\theta}_k|\boldsymbol{z}_0, \cdots, \boldsymbol{z}_k) = \frac{p(\boldsymbol{z}_0, \cdots, \boldsymbol{z}_k|\boldsymbol{\theta}_0, \cdots, \boldsymbol{\theta}_k)p(\boldsymbol{\theta}_0, \cdots, \boldsymbol{\theta}_k)}{p(\boldsymbol{z}_0, \cdots, \boldsymbol{z}_k)} \tag{6.7}$$

where

$$p(\boldsymbol{z}_0, \cdots, \boldsymbol{z}_k) = \int p(\boldsymbol{z}_0, \cdots, \boldsymbol{z}_k|\boldsymbol{\theta}_0, \cdots, \boldsymbol{\theta}_k)p(\boldsymbol{\theta}_0, \cdots, \boldsymbol{\theta}_k)\delta\boldsymbol{\theta}_0 \cdots \delta\boldsymbol{\theta}_k \tag{6.8}$$

$$p(\boldsymbol{z}_0, \cdots, \boldsymbol{z}_k|\boldsymbol{\theta}_0, \cdots, \boldsymbol{\theta}_k) = \prod_{l=0}^{k} p(\boldsymbol{z}_l|\boldsymbol{\theta}_l) \tag{6.9}$$

$$p(\boldsymbol{\theta}_0, \cdots, \boldsymbol{\theta}_k) = p_0(\boldsymbol{\theta}_0)\prod_{l=0}^{k} p(\boldsymbol{\theta}_l|\boldsymbol{\theta}_{l-1}) \tag{6.10}$$

The relationships mentioned in the previous equations hold if the observables are independent at each time instant and if the state vector only depends on the values it assumed at the previous epoch. The hybridization with additional independent sources of information simply extends $\mathbf{z}_k$ but it does not modify the Bayesian estimation problem. On the opposite, when correlated information such as GNSS-based inter-agent distances are integrated a modification of the HMM has to be considered to model the new set of cross-correlated observables.

6.1.2 Combined Observable Measurements and Implicit Belief Propagation

In a simple pairwise hybridization, the *auxiliary observable measurements* are assumed to be generated by combining the independent observables of two agents in a *hybrid measurement vector*, as shown in Figure 6.2. The output data can be used as a joint information about the estimation of the two states $\boldsymbol{\theta}_{i,k}$ and $\boldsymbol{\theta}_{j,k}$ in a centralized fashion, or they can be exploited by one of the two agents as a complementary source of information provided that the shared observables are reliable [117].

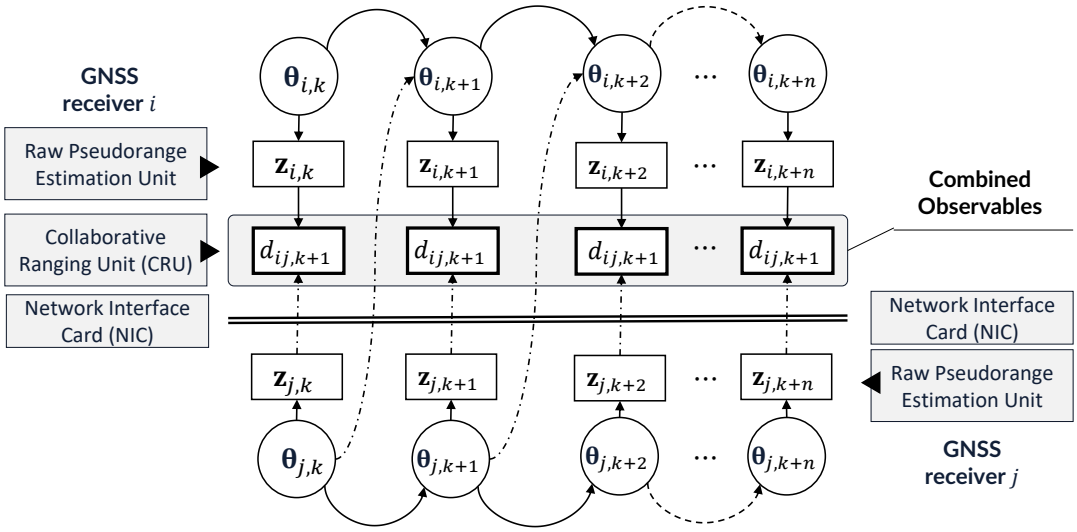

Figure 6.2: Modified HMM for dual agent state-space estimation with combined, correlated measurement generation. MM referred to the functional scheme of networked GNSS receiver.

In the collaborative techniques relying on belief propagation, the set of observables is extended by sharing the statistics of the estimated positions (i.e. estimate and estimated covariance), which are considered independent among the agents [97, 19, 178, 18]. Relying on the differential techniques described in Chapter 4 instead, the belief is implicitly shared through the transmission of a sufficient number of observables, according to the size of the state vector.

When cooperative observables can be computed, the (6.11) can be extended to incorporate also *inter-agent distances*, such that

$$\bar{\mathbf{z}}_{\mathbf{k}} = \begin{bmatrix} \mathbf{z}_k^\top & \mathbf{d}_k^\top \end{bmatrix}^T \tag{6.11}$$

where $\mathbf{d}_k = (d_{1,k} \;\; d_{2,k} \;\; \dots \;\; d_{C,k})^T$, is a $(C \times 1)$ vector of combined observables obtained by C independent collaborating agents. For the computation of the collaborative contributions it holds

$$\mathbf{d}_k = g\left(\mathbf{z}_{i,k}, \mathbf{z}_{j,k}\right) \tag{6.12}$$

where $g(\cdot)$ can identify a collaborative technique such as the ones mentioned in Chapter 4. Equation (6.7) must be updated by including collaborative correlated measurements such that the probability distribution of the overall measurements vector, $\bar{\mathbf{z}}_k$, also depends on the measurements $\mathbf{z}_{j,k}$ of the aiding agent, formally

$$p(\bar{\mathbf{z}}_k|\boldsymbol{\theta}_i, \boldsymbol{\theta}_j) \tag{6.13}$$

The *hybrid measurement vector* does not contain only independent measurements such that the error covariance matrix of $\mathbf{z}_k$ is no longer diagonal, by definition. Differently from the hybridization with independent measurements, the amount of information is somehow reduced by this correlation because

$$p(\mathbf{d}_k|\mathbf{z}_k) \neq p(\mathbf{d}_k)p(\mathbf{z}_k) \tag{6.14}$$

Despite of such a reduction, the redundancy of the observables is expected to reinforce the estimation of the aided agent. The last section of this chapter suggests a theoretical tool to investigate this reinforcement in terms of CRLB analysis.

6.1.3 Hybrid Measurements Modelling in GNSS

In standalone GNSS positioning, $\mathbf{z}_k$ consists of a *measurement vector* composed by $(S\times 1)$ satellite-to-receiver pseudorange measurements vector, $\boldsymbol{\rho}_k$, and $(S \times 1)$ pseudorange change rates or Doppler shift measurements vector, $\boldsymbol{\phi}_k$ [90], measured by the received GNSS signals. When multiple collaborating agents are available, a set of of inter-agent distances can be integrated in the measurement vector as additional although correlated information

$$\bar{\mathbf{z}}_k = \begin{bmatrix} \boldsymbol{\rho}_k^\top & \boldsymbol{\phi}_k^\top & \mathbf{d}_k^\top \end{bmatrix}^T. \tag{6.15}$$

Equation (6.15) represents the measurements vector that can be used for the state estimation through the single agent HMM depicted in Figure 6.3.

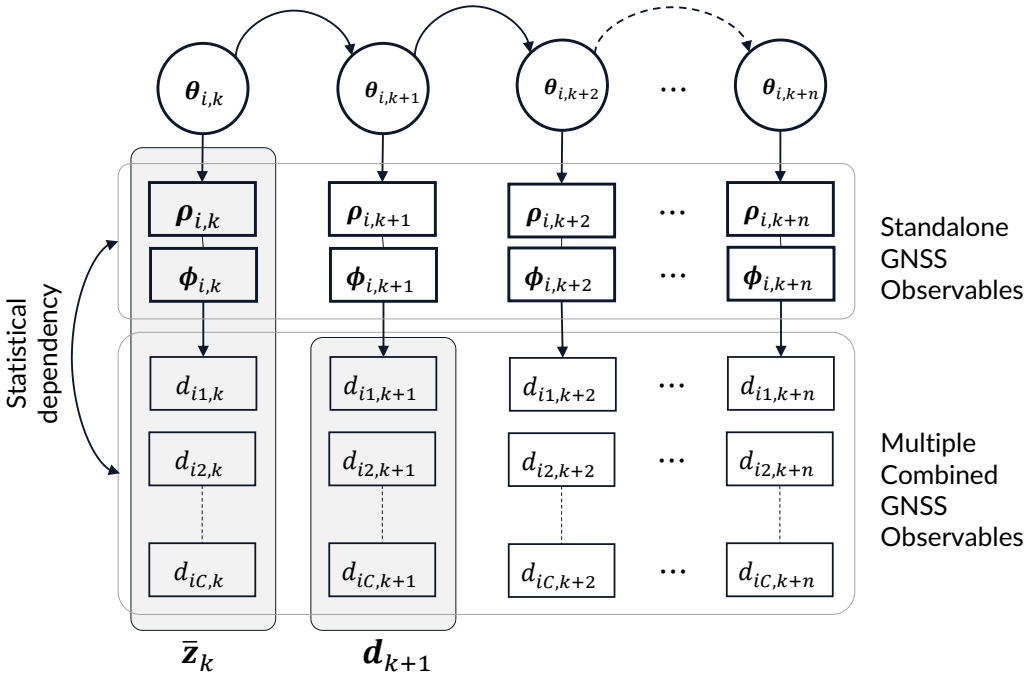

Figure 6.3: HMM in GNSS aided system state estimation.

When measurements can be modelled as unbiased pseudorange, the associated covariance matrix $\mathbf{R}_k$ is usually a $(S \times S)$ diagonal matrix, with pseudorange variances σ_s^2 on the main diagonal, since no correlation is assumed between these quantities [16]. In this cooperative

framework however, also collaborative ranges are involved in the measurement process and therefore the hybrid covariance matrix $\bar{\mathbf{R}}_k$ should include the elements associated to these quantities. In particular, each collaboratively-derived range may be dependent on several pseudoranges among those included in $\bar{\mathbf{z}}_k$ such that cross-correlation terms may have to be taken into account for the filter design.

To properly model these characteristics, the error covariance matrix designed for the proposed algorithms is then defined by means of four sub-matrices (and the respective transposed versions):

$$\bar{\mathbf{R}}_k = \begin{bmatrix} \mathbf{R}_{\rho,k} & \mathbf{R}_{\rho\phi,k} & \mathbf{R}_{\rho d,k} \\ \mathbf{R}_{\rho\phi,k}^{\top} & \mathbf{R}_{\phi,k} & \mathbf{R}_{\phi d,k} \\ \mathbf{R}_{\rho d,k}^{\top} & \mathbf{R}_{\phi d,k}^{\top} & \mathbf{R}_{d,k} \end{bmatrix} \tag{6.16}$$

where $\mathbf{R}_{\rho,k}$ and $\mathbf{R}_{d,k}$ are the covariance matrices related respectively to the pseudorange set and the cooperative measurement set as in 6.11, while $\mathbf{R}_{\rho d,k}$ is a matrix containing the cross-correlation terms between each element of $\boldsymbol{\rho}_k$ and each element of $\mathbf{d}_k$.

As mentioned, $\mathbf{R}_{\rho,k}$ is a diagonal matrix, but the same cannot be said for $\mathbf{R}_d$. In fact in (6.16), the dependency of cooperative ranges on pseudoranges is responsible of non-zero cross-correlation terms in both matrices $\mathbf{R}_{d,k}$ and $\mathbf{R}_{\rho d,k}$. The correlation between a cooperative range and the set of pseudoranges from which is derived is defined by the elements of $\mathbf{R}_{\rho d,k}$, while the off-diagonal elements of $\mathbf{R}_{d,k}$ describe the cross-correlation between two different cooperative measurements. This value is generally non-null for cooperative ranges which shares one or more pseudoranges employed in their respective computation.

Basically in order to fill $\bar{\mathbf{R}}_k$, the variances of the elements in $\boldsymbol{\rho}_k$ and $\boldsymbol{d}_k$ are needed as well as the cross-correlation values among their entries. They may all be based on pseudorange variance σ_s^2, but a closed expression is dependent on the specific derivation process of the cooperative ranges [183]. However a bound can be set on the entries of $\mathbf{R}_{\rho d,k}$, thanks to the Cauchy-Schwarz inequality.

The $\mathbf{R}_{\rho d,k}$ sub-matrix contains the cross-correlation terms which link pseudorange measurements and collaborative ranging contributions. For these terms, the covariance propagation of the LMS estimation (4.26) can be exploited to assign to the proper covariance terms. The transposed matrix $\mathbf{R}_{\rho d}^{\top}$ can be then defined accordingly. Assigning the maximum correlation between $\mathbf{d}_k$ and $\boldsymbol{\rho}_k$ is a worst-case assumption.

6.2 Hybrid WLS

By referring to the extended HMM model and to the basic positioning solution as in Section 2.3, the WLS can be easily modified to tightly integrate the collaborative measurements. It is worth recalling that besides being a simple algorithm, a generic LMS is preparatory for the effective initialization of any Bayesian filters such as KF and PF. This Section describes how the hybrid terms are built in the positioning algorithm and how ill-conditioned set of equations can be managed for reliable solutions [79].

Let us consider the state vector $\boldsymbol{\theta}_k$, and the hybrid set of observables $\bar{\mathbf{z}}_k$ along with its error covariance matrix $\bar{\mathbf{R}}_k$. The linear problem can be expressed as

$$\bar{\mathbf{z}}_k = \bar{\mathbf{H}}\boldsymbol{\theta}_k + \mathbf{v}_k \tag{6.17}$$

where $\mathbf{v}_k$ is a noise vector whose components are assumed to be normally-distributed while $\bar{\mathbf{H}}$ is the Direction Cosine Matrix (DCM) and describes the linearized relationship

among all the measurements collected in $\bar{\mathbf{z}}_k$ and the state vector $\boldsymbol{\theta}_k$, at the discrete time t_k. Naming $\mathbf{H}_{\rho,k}$ the observation matrix related to the GNSS pseudorange measurements as in (2.14), the resulting hybrid DCM, $\bar{\mathbf{H}}_{\rho,k}$, is a matrix defined as

$$\bar{\mathbf{H}}_k = \begin{bmatrix} \mathbf{H}_{\rho,k} & \mathbf{0}_{S\times 4} \\ \mathbf{0}_{S\times 4} & \mathbf{H}_{\rho,k} \\ \mathbf{H}_{d,k} & \mathbf{0}_{C\times 4} \end{bmatrix} \tag{6.18}$$

where the s-th row of the submatrix $\mathbf{H}_{\rho,k}$ can be expressed as

$$[\mathbf{H}_{\rho,k}]_s = \left[\begin{array}{cc} \frac{(\mathbf{x}_s - \mathbf{x}_i)}{||\mathbf{x}_s - \mathbf{x}_i||} & 1 \end{array} \right] = \left[\begin{array}{cc} \mathbf{h}_{is} & 1 \end{array} \right] \tag{6.19}$$

where $\mathbf{x}_s$ and $\mathbf{x}_i$ are the satellite and user coordinates, respectively. $\mathbf{h}_{i,s}$ is the *unitary steering vector* pointing towards the s-th satellite and the unitary term is referred to the bias clock term common to all the measurements. Similarly, the set of equivalent steering vectors points at the collaborating agents so that the c-th row of $\mathbf{H}_{d,k}$ is defined as

$$[\mathbf{H}_{d,k}]_c = \left[\begin{array}{cc} \frac{(\hat{\mathbf{x}}_c - \mathbf{x}_i)}{||\hat{\mathbf{x}}_c - \mathbf{x}_i||} & 0 \end{array} \right] = \left[\begin{array}{cc} \mathbf{h}_{ic} & 0 \end{array} \right]. \tag{6.20}$$

While the GNSS satellite position is known with a high accuracy from the ephemeris data, the *measurement equations* of the hybridized system (6.6) have to be referred to a rough estimate, $\hat{\mathbf{x}}_c$, of the aiding agent position. This estimation can be performed autonomously by the aided receiver i through the received measurement data from receiver j.

With the need of approaching a general case in which the measurements in $\bar{\mathbf{z}}_k$ are not independent neither identically distributed, the covariance matrix $\mathbf{R}_k$ must be considered. The strong assumption is still a zero-mean Gaussian distribution which can limit the performance [179]. If this condition is satisfied, the associated ML estimate is expressed as

$$\theta_k = \underset{\boldsymbol{\theta}}{\operatorname{argmax}} \frac{1}{(2\pi)^{N/2}|\bar{\mathbf{R}}_k|^{1/2}} e^{\frac{1}{2}(\bar{\mathbf{z}}_k - \bar{\mathbf{H}}_k\boldsymbol{\theta}_k)^\top \bar{\mathbf{R}}_k^{-1}(\bar{\mathbf{z}}_k - \bar{\mathbf{H}}_k\boldsymbol{\theta}_k)} \tag{6.21}$$

$$= \underset{\boldsymbol{\theta}}{\operatorname{argmin}} (\bar{\mathbf{z}}_k - \bar{\mathbf{H}}_k\boldsymbol{\theta}_k)^\top \bar{\mathbf{R}}_k^{-1}(\bar{\mathbf{z}}_k - \bar{\mathbf{H}}_k\boldsymbol{\theta}_k) \tag{6.22}$$

The solution is obtained by differencing (6.21) w.r.t. $\boldsymbol{\theta}_k$, and equalizing the result to zero, as

$$\boldsymbol{\theta_k} = \left(\bar{\mathbf{H}}_k^\top \mathbf{R}_k^{-1} \bar{\mathbf{H}}_k\right)^{-1} \bar{\mathbf{H}}_k^\top \bar{\mathbf{R}}_k^{-1} \bar{\mathbf{z}}_k \tag{6.23}$$

The error covariance matrix, $\mathbf{P}_k$, can be easily computed through

$$\mathbf{P}_k = \left(\bar{\mathbf{H}}^\top \bar{\mathbf{H}}\right)^{-1} \bar{\mathbf{H}}^\top \bar{\mathbf{R}}_k \bar{\mathbf{H}} \left(\bar{\mathbf{H}}^\top \bar{\mathbf{H}}\right)^{-1} \tag{6.24}$$

As mentioned in Chapter 2, iterative solutions such as the recursive WLS can be used to improve the convergence of the solution.

6.2.1 Weighted SAIA for robust measurement integration in WLS

If multiple collaborative contributions are obtained from a number of aiding agents, the H-WLMS PVT algorithm can lead to a typical ill-conditioned problem and it shows high instability of the convergence of the solution [124]. An iterative algorithm can be implemented to enhance the convergence of each WLS iteration by avoiding the inversion of the ill-conditioned ($\bar{\mathbf{H}}_k \bar{\mathbf{R}}_k^{-1} \bar{\mathbf{H}}_k^\top$) product. This optimization is performed by means of a

weighted variation of the SAIA algorithm proposed in [38]. For sake of completeness, the core steps of SAIA method are recalled hereafter with a more familiar notation and extending the original formalism by considering the covariance of the measurements, $\bar{\mathbf{R}}_k$.

Let consider to freeze the time instant t_k and the WLS n-th iteration. As a general assumption, all the measurements expressed in their differential notation $\Delta\bar{\mathbf{z}}_k^n$ (i.e. pseudoranges, IARs) are affected by Gaussian-distributed errors as reasonably stated in the previous section. The Weighted SAIA (W-SAIA) algorithm can be feed by the state estimate $\Delta\boldsymbol{\theta}_k^{n-1}$ obtained at the previous WLS iteration and two variables can be introduced at the j-th iteration to split (6.23) as

$$\begin{cases} \mathbf{N}_j = \left(\bar{\mathbf{H}}_k^n\right)^\top \bar{\mathbf{R}}_k^{-1} \bar{\mathbf{H}}_k^n + \Lambda_j \mathbf{I} \\ \mathbf{W}_j = \left(\bar{\mathbf{H}}_k^n\right)^\top \bar{\mathbf{R}}_k^{-1} \Delta\bar{\mathbf{z}}_k + \Lambda_j \Delta\boldsymbol{\theta}_{k,j-1}^n \end{cases} \tag{6.25}$$

where the perturbation parameter, Λ, is computed before the iterative process and it is then iteratively adjusted to accelerate the convergence of the solution. Λ must satisfy the condition $0 \leq \Lambda \leq 1$, and it is computed through the following steps

$$\begin{cases} \lambda_j = min\left\{ |\text{eig}\left[\left(\bar{\mathbf{H}}_k^n\right)^\top \mathbf{R}_k^{-1} \bar{\mathbf{H}}_k^n \right]| \right\} \\ \Lambda_j = \lambda_j 10^{0.5|log_{10}(\lambda_j)|+1} \end{cases} \tag{6.26}$$

where λ_j indicates the eigenvalues of the argument and $\mathbf{U}_j$ is calculated given the upper triangular matrix $\mathbf{C}_j$ obtained from the Cholesky decomposition of $\mathbf{N}_j$

$$\mathbf{C}_j \mathbf{U}_j = \mathbf{W}_j \tag{6.27}$$

and then $\boldsymbol{\theta}_{k,j}^n$ is calculated solving the problem

$$\mathbf{C}_j^\top \Delta\boldsymbol{\theta}_{k,j}^n = \mathbf{U}_j \tag{6.28}$$

The algorithm iterates on j trials determining at each iteration the residual error as

$$\xi_j = ||\mathbf{N}_j \Delta\boldsymbol{\theta}_j^\top - \mathbf{W}_j|| \tag{6.29}$$

the self-adaptation is performed according to the relative error, $\nu = \frac{\xi_j}{\xi_{j-1}}$ w.r.t. the previous iteration. By comparing ν w.r.t. two predefined thresholds, the value of Λ can be adjusted to increase the convergence. As an example if ν at the j-th iteration is smaller than 0.25 the perturbation parameter can be doubled, otherwise if $\nu > 0.75$, Λ_j can be divided by two before the next iteration.

It is worth mentioning that the recursion introduced by the W-SAIA within each iteration of a WLS PVT routine increases the computational complexity of the positioning problem by a multiplicative factor which corresponds to the number of inner iterations.

6.3 Approximated Bayesian Estimation

Real scenarios can show critical aspects such as nonlinear, non-Gaussian and non-stationary target states and measurement. Therefore, optimal filtering is infeasible in such a kind of situations, and approximated or suboptimal solutions have to be considered for a reliable state estimation. In the following, two examples of approximated Bayesian filters are presented. The EKF which exploits an analytic approximation and the PF which approximates the unknown distributions through a set of particles according to a sampling process.

6.3.1 Hybrid Extended Kalman Filter

The popular KF is an optimal Bayesian recursive filter (in MMSE sense) which is capable to estimate the state, $\boldsymbol{\theta}_k$, of a linear dynamic system relying on a set of noisy measurements according to the following assumptions:

- $\mathbf{v}_{k-1}$ in (6.5) is the realization at time t_{k-1} of a multivariate Gaussian random variable of known mean and covariance
- f_{k-1} in (6.5) is a known linear function of $\boldsymbol{\theta}_{k-1}$ and $\mathbf{v}_{k-1}$
- h_k is (6.6) is a known linear function of $\boldsymbol{\theta}_k$ and $\mathbf{w}_k$.

In GNSS, these conditions are typically too strict to be satisfied. Especially in urban environment where multipath reflections are frequent and ubiquitous, the noise distribution of the pseudorange measurements is likely to be modelled as Rayleigh or Rice distributed according to presence of an actual LoS component. The relationship between subsequent states can be highly non-linear in case of complex dynamics such as curvilinear accelerated manoeuvres. The relationship between measurements and states related to multi-lateration is then non-linear by definition.

From these considerations, it is natural to use a more robust filter such as the EKF or UKF.

Models equations

The theory of the EKF is based on a linearized *system model equation* (6.5) and *measurement model equation*. The system model considered in this framework is described as a linear equation which is widely applied to estimation problems in vehicular navigation [72]. Hence it describes the relation between past and current state through

$$\bar{\boldsymbol{\theta}}_k = \boldsymbol{\Phi}\bar{\boldsymbol{\theta}}_{k-1} + \mathbf{v}_k \ . \tag{6.30}$$

where

$$\boldsymbol{\Phi} = \begin{bmatrix} \mathbf{I}_{3\times3} & T_s \cdot \mathbf{I}_{3\times3} & \mathbf{0}_{3\times2} \\ \mathbf{0}_{3\times3} & \mathbf{I}_{3\times3} & \mathbf{0}_{3\times2} \\ \mathbf{0}_{2\times3} & \mathbf{0}_{2\times3} & \begin{matrix} 1 & T_s \\ 0 & 1 \end{matrix} \end{bmatrix} \tag{6.31}$$

is a time-invariant *transition matrix* depending on the time step T_s; and $\boldsymbol{\eta}$ is the *system noise* such that

$$\eta_k \sim \mathcal{N}(\mathbf{0}, \mathbf{Q_k}) \tag{6.32}$$

with $\mathbf{Q}_k$ covariance matrix.

The system model is driven by the dynamics of the system and is independent of the observed measurements. It is in fact defined regardless of the nature of the observations, whether they are stand-alone GNSS or collaboratively-derived measurements.

The measurement model equation provides a relation between the state $\bar{\boldsymbol{\theta}}_k$ and a *measurements vector* $\mathbf{z}_k$. For what concerns GNSS this relation is non-linear, thus the equation is in the form

$$\mathbf{z}_k = h(\bar{\boldsymbol{\theta}}_k) + \mathbf{w}_k \tag{6.33}$$

where h is a known non-linear function. In (6.32), $\mathbf{v}_k$ represents the measurement noise and it is modeled such that

$$\mathbf{v}_k \sim \mathcal{N}(\mathbf{0}, \bar{\mathbf{R}}) \tag{6.34}$$

with $\bar{\mathbf{R}}$ covariance matrix.

Since the relationship between state variables and measurements cannot be described by a linear equation [90], the EKF exploits linearization to deal with the multi-lateration problem. The *linearized measurement equation* is then

$$\Delta\mathbf{z}_k = \bar{\mathbf{H}}_k \Delta\bar{\boldsymbol{\theta}}_k + \mathbf{v}_k \tag{6.35}$$

where $\Delta\mathbf{z}_k$ and $\Delta\bar{\boldsymbol{\theta}}_k$ are the incremental vectors of respectively, the measurements vector $\mathbf{z}_k$ and the state vector $\bar{\boldsymbol{\theta}}_k$, w.r.t. a linearization point $\bar{\boldsymbol{\theta}}_k^* = [\boldsymbol{\theta}_k^*\, b_k^*\, \dot{\boldsymbol{\theta}}_k^*\, \dot{b}_k^*]$, updated at every time step k [16]. The *observation matrix* $\bar{\mathbf{H}}$ contains the coefficients linking the two linearized vectors, which arise after the linearization of the equations relating measurements and state variables [90].

Equation (6.35) relates to the observations to the state vector. In standalone GNSS positioning, $\Delta\hat{\mathbf{z}}_k$ consists of the observables retrieved from the radio navigation signal (i.e. $\Delta\boldsymbol{\rho}_k$), the incremental vector of the pseudorange measurements vector and $\Delta\boldsymbol{\phi}_k = \{\Delta\phi_i^s(t_k)\}_{s\in\mathcal{S}}$ and the incremental measurement vector derived from Doppler measurements.

When collaborative ranges are integrated in the measurement set, the linearized measurement vector is extended to incorporate also incremental *inter-agent distances*, such that

$$\Delta\hat{\mathbf{z}}_k = \begin{bmatrix}\Delta\boldsymbol{\rho}_k & \Delta\boldsymbol{\phi}_k & \Delta\mathbf{d}_k\end{bmatrix}^\top \tag{6.36}$$

where all the variables are vectors of incremental quantities, one for each integrated collaborative range, built similarly to $\boldsymbol{\Delta}\rho$. The observation matrix is extended as well once the coefficients related to cooperative measurements are defined, accordingly to the inter-agent distance. Naming $\mathbf{H}_\rho$ the observation matrix related to the standard GNSS measurements $\boldsymbol{\Delta}\rho$ the resulting *hybrid observation matrix* can be built according to the hybridized DCM as in (6.2).

EKF routine

Following the definition of system and observations models and the related covariances, the EKF routine applied to collaborative ranging measurements is hereafter reported for the sake of completeness. The EKF routine starts with a prediction step that involves the projection of the last state estimation $\hat{\boldsymbol{\theta}}_{k-1}$ on the current instant k by means of the transition matrix:

$$\hat{\boldsymbol{\theta}}_k^- = \boldsymbol{\Phi}\hat{\boldsymbol{\theta}}_{k-1}\ . \tag{6.37}$$

At each step of the EKF routine, the predicted state estimation $\hat{\boldsymbol{\theta}}_k^-$ is chosen as linearization point $\boldsymbol{\theta}_k^*$, around which incremental quantities are build. The use of the estimated trajectory $\hat{\boldsymbol{\theta}}_k^-$ is a reasonable choice, since it is presumably the best estimate available at time k before the measurement update. However, a poor choice for $\boldsymbol{\theta}_k^*$ could cause the EKF estimate to diverge if the first-order approximation on which the linearization is based is not enough. Due to the feedback of measurements into the estimate equations, instability phenomena may arise in the EKF. Several works have investigated the conditions for EKF stability, but such requirements are often too restrictive for realistic applications [152].

Then, the incremental measurements $\Delta\mathbf{z}_k$ and the hybrid matrix $\bar{\mathbf{H}}_k$ are computed w.r.t. this reference point. The prediction is performed also on the *error covariance matrix* $\mathbf{P}_{k-1}$:

$$\mathbf{P}_k^- = \mathbf{\Phi}\mathbf{P}_{k-1}\mathbf{\Phi}^\top + \mathbf{Q} \ . \tag{6.38}$$

Following the prediction phase, the *Kalman gain* is computed as

$$\mathbf{K}_k = \mathbf{P}_k^-\bar{\mathbf{H}}_k^\top(\bar{\mathbf{H}}_k\mathbf{P}_k^-\bar{\mathbf{H}}_k^\top + \bar{\mathbf{R}})^{-1}. \tag{6.39}$$

Notice that the gain is dependent on the measurement matrix $\bar{\mathbf{H}}_k$, which, as stated, is updated according to the approximation point at each time k. Therefore, since $\mathbf{x}_k^* = \hat{\boldsymbol{\theta}}_k^-$, the gain sequence will depend on the sequence of measurements of a particular realization of the experiment [16].

Now, considering the incremental state estimate

$$\Delta\hat{\boldsymbol{\theta}}_k = \Delta\hat{\boldsymbol{\theta}}_k^- + \mathbf{K}_k(\Delta\mathbf{z}_k - \bar{\mathbf{H}}_k\Delta\hat{\boldsymbol{\theta}}_k^-) \tag{6.40}$$

it should be noticed that, since $\mathbf{x}_k^* = \hat{\boldsymbol{\theta}}_k^-$, the term $\Delta\boldsymbol{\theta}_k^-$ is zero. Thus the (6.40) becomes

$$\Delta\hat{\boldsymbol{\theta}}_k = \mathbf{K}_k\Delta\mathbf{z}_k \ . \tag{6.41}$$

Finally the state estimation can be obtained by correcting the approximation state with the incremental estimate update:

$$\boldsymbol{\theta} = \boldsymbol{\theta}_k^* + \Delta\hat{\boldsymbol{\theta}}_k \ . \tag{6.42}$$

The error covariance matrix is updated as well. This equation is implemented in a symmetric form (Joseph form), which is resilient to divergence phenomena [16]:

$$\mathbf{P}_k = (\mathbf{I} - \mathbf{K}_k\bar{\mathbf{H}}_k)\mathbf{P}_k^-(\mathbf{I} - \mathbf{K}_k\bar{\mathbf{H}}_k)^\top + \mathbf{K}_k\bar{\mathbf{R}}_k\mathbf{K}_k^\top \ . \tag{6.43}$$

A direct EKF is rarely used due to its high computational load and low reliability [25], for this reason the EKF approach considered and implemented in the following analysis is known as indirect filtering, also called the *error-state* EKF.

Error-state EKF indirect routine

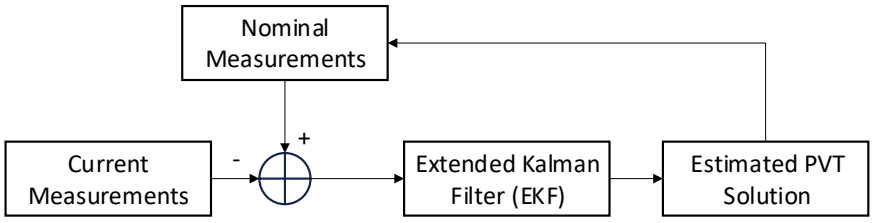

Figure 6.4: Indirect KF scheme.

Indirect filtering can be structured as a feed-forward or a feedback KF. In feed-forward approach, if the errors which enter as input in the filter remain small, the linear dynamics model is acceptable. While, if they become larger, the errors estimated by the KF will drift with time. For this reason in navigation applications which integrate INS, a feedback loop is added to mitigate this drawback [169]. In this thesis, since there are not additional systems as INS, the error is estimated as the difference between the current measurements exposed

by the GNSS chipset and the nominal ones, which are evaluated by applying the corrections found at the previous step, as represented in Figure 6.4. Furthermore, to avoid the error drift , overconfidence or uncontrolled growth of $\mathbf{P}_k$, a reset is performed periodically, by means of a WLS PVT evaluation instead of the Kalman routine. The same result can be achieved by setting the process covariance matrix $\mathbf{Q}_k$ to infinite.

In the indirect filtering, the prediction step is fed with a zero state vector

$$\boldsymbol{\theta}_k = \begin{bmatrix} 0 & 0 & 0 & 0 & 0 & 0 & 0 & 0 \end{bmatrix} \tag{6.44}$$

Then a priori error covariance matrix $\mathbf{P}_k^-$ and the Kalman gain $\mathbf{K}_k$ are computed as in (6.38) and in (6.39), respectively. Differently from the direct formulation, $\Delta\mathbf{z}_k$ is in this case the difference between current measurements and nominal measurements

$$\Delta\hat{\mathbf{z}}_k = \begin{bmatrix} \Delta\boldsymbol{\rho}_k & \Delta\boldsymbol{\phi}_k \end{bmatrix}^T \tag{6.45}$$

where

$$\Delta\boldsymbol{\rho}_k = \Delta\boldsymbol{\rho}_k^N - \Delta\boldsymbol{\rho}_k^C \tag{6.46}$$

and

$$\Delta\phi_k = \Delta\boldsymbol{\phi}_k^N - \Delta\boldsymbol{\phi}_k^C. \tag{6.47}$$

Current measurements are the pseudorange measurements vector, $\boldsymbol{\rho}_k$, and $\boldsymbol{\phi}_k$, the measurement vector including Doppler measurements. Nominal measurements are instead the measured pseudoranges and pseudoranges rates with corrections found at state $\hat{\theta}_{k-1}$.

The pseudoranges are corrected by the receiver clock bias, the relativistic correction and the satellite clock error estimated through the ephemeris data

$$\boldsymbol{\rho}_k^N = \boldsymbol{\rho}_k - b_{k-1} + dt_{k-1}^s \cdot c \tag{6.48}$$

while the pseudoranges rates are corrected by the user clock drift

$$\boldsymbol{\phi}_k^N = \boldsymbol{\phi}_k - \dot{b}_{k-1} \tag{6.49}$$

The approximation state in indirect filtering is the state estimated as

$$\boldsymbol{\theta}_k^* = \boldsymbol{\theta}_{k-1} \tag{6.50}$$

By performing the estimation as in (6.40), the current state $\boldsymbol{\theta}_k$ is found.

6.3.2 Hybrid Particle Filter

The PF is a Monte Carlo approximation of optimal sequential Bayesian state estimation which performs state updates relying on a sampling procedure often referred to as SIS [71].

The use of PF in PNT, GNSS and CP has been widely investigated in literature [182, 77, 76, 8, 175, 70] and despite its computational complexity, its implementation allows to relax the constraints mentioned for the EKF:

- $\mathbf{v}_{k-1}$ and $\mathbf{w}_{k-1}$ are drawn from the realization at time t_{k-1} of generic densities of known mean and variance
- $f_{k-1}(\boldsymbol{\theta}_{k-1}, \boldsymbol{v}_{k-1})$ can be a linear or non-linear function such that $\boldsymbol{\theta}_k = f_{k-1}(\boldsymbol{\theta}_{k-1}) + \mathbf{v}_k$
- $h_k(\boldsymbol{\theta}_k, \boldsymbol{w}_k)$ can be a linear or non-linear function such that $\mathbf{z}_k = h_k(\boldsymbol{\theta}_{k-1}) + \mathbf{w}_k$.

Model Equations

PFs have become attractive due to their capability of dealing with non-linearity and non-gaussian models. For this aspect the model equations used in this case correspond to the equations of the general model introduced in 6.1.1. Indeed, the state transition function (a.k.a. system model) is the same as (6.5) and the *measurement equation* is the same as in (6.6).

The non-Gaussian posterior probability $p(\boldsymbol{\theta}_k|\mathbf{z}_k)$ extended in (6.7) is represented by a set of randomly drawn samples, named particles, with their associated weights $\left\{\boldsymbol{\theta}_k^{(i)}, \mathbf{w}_k^{(i)}\right\}_{i=1}^{I}$. This set of particles provides a discrete approximation of the (6.7) according to

$$p(\boldsymbol{\theta}_k|\mathbf{z}_k) \approx \hat{\boldsymbol{\theta}}_k \triangleq \sum_{i=1}^{I} w_k^{(i)} \boldsymbol{\theta}_k^{(i)} \tag{6.51}$$

The PF approximates the a posteriori distribution of (6.1)

$$p\left(\boldsymbol{\theta}_k|\mathbf{z}_k\right) \approx \sum_{i=1}^{N} w_k^{(i)} \delta\left(\boldsymbol{\theta}_k - \hat{\boldsymbol{\theta}}_k^{(i)}\right) \tag{6.52}$$

where δ is the Dirac delta function and $\hat{\boldsymbol{\theta}}_k^{(i)}$ is a propagated particle. The approximation is performed by generating and propagating a set of particles $\hat{\boldsymbol{\theta}}_k^{(i)}$ and associated weights $w_k^{(i)}$ according to the following steps:

1. *Initialization*: Generation of a set of N particles $\hat{\boldsymbol{\theta}}_k^{(i)}$ according to $\hat{\boldsymbol{\theta}}_k \sim p(\hat{\boldsymbol{\theta}}_{k-1}, P_{\theta,k-1})$.

2. *Prediction*: All the generated particles are propagated according to the dynamic system model

3. *Weights computation*: The weights are obtained by relying on a pre-defined likelihood $p\left(\mathbf{z}_k|\hat{\boldsymbol{\theta}}_k^{(i)}\right)$ w.r.t. the expected measurements computed for each particle, the weights are hence defined as

$$w_k^{(i)} = \frac{\prod_i p\left(z_{n,k} - z_{n,k}^{(i)}\right)}{\sum_{i=1}^{N} \prod_i p\left(z_{n,k} - z_{n,k}^{(i)}\right)}. \tag{6.53}$$

   One of the most relevant aspects of PF is that each class measurement can be treated independently from the other, such that Gaussian-distributed pseudorange measurements can be processed by means of a Gaussian likelihood, while the likelihood of the collaborative inter-agent distances can be determined accordingly to the specific error distribution.

4. *Resampling*: This step is of prominent importance since it guarantees the algorithm effectiveness avoiding particle collapse and overoptimistic covariance estimation. A number of resampling methods can be used to optimize the filter behaviour [106]. As an example, the *Bayesian Bootstrap* foresees the selection of N samples from the particle set $\left\{\boldsymbol{\theta}_k^{(i)}\right\}$ with a picking probability $w_k^{(i)}$. When a uniform distribution is used as picking probability, $w_k^{(i)} = 1/N$ the method is also referred to Sampling Importance Resampling (SIR). An alternative strategy is named *Importance Sampling* and it foresees the re-sampling according to the Bayesian bootstrap only if the number of samples is lower than a threshold

$$N_\theta = \frac{1}{\sum_i \left(w_t^i\right)^2} < N_{th} \tag{6.54}$$

provided that the number of effective particles $1 \leq N_\theta \leq N$ [77, 40].

5. *Estimation*: The bayesian estimation is eventually given by the weighted average of the generated particles, as in (6.51)

Given a sufficient number of simulated particles, the covariance matrix $\mathbf{P}_k$ associated to the state estimate $\boldsymbol{\theta}_k$, can be estimated by computing the *sample covariance* over the set of output particles $\left\{\boldsymbol{\theta}_k^{(i)}\right\}$.

Similarly to the indirect formulation of the error-state EKF, also the PF has been implemented with an indirect scheme. However for sake of simplicity, such an error-state PF will be simply referred to as PF or H-PF.

6.4 On the approximation of a CRLB for hybrid navigation filters

This section provides a theoretical analysis about the information carried by the correlated measurements proposed in Chapter 4 when they are used to improve the position estimation. This original contribution which is published in [123, 127] has been inspired by a set of research papers and articles about the formalization of the limits of hybrid positioning including auxiliary terrestrial measurements [142, 122, 85, 57, 101, 81, 66, 82] and also by a couple of pioneering works that first identified the profitability of the exploitation of differential GNSS measurements [166, 99, 154, 6, 5, 102].

The CRLB defined for H-WLMS and H-EKF respectively, allows to emphasize the limiting conditions which guarantee or not a higher precision in the position estimation both in linear and non-linear estimation.

The amount of information carried by an observed unbiased range measurement w.r.t. the estimated position is related to the relative position of the reference points and to the quality of the observable measurements [90]. The goodness of this information is indeed inversely proportional to the variance of the measurement error itself and on the other hand, the ranges direction condition the GDOP [131]. As detailed in Chapter 2, the GDOP affects the positioning solution by altering the shape of the spatial distributions of its realizations, namely its precision which is evaluated through the *position error covariance matrix*. The position error covariance matrix is a subset of $\mathbf{P}_k$ related to the spatial coordinates included in $\boldsymbol{\theta}_k$. The combination of the variance of such measurements and the GDOP characterizes the whole positioning error, derived as in [20] from the CRLB of the positioning estimator.

In light of this, the analysis presented in [85] investigates a composite dilution of precision for cooperative positioning, named Cooperative Dilution of Precision (CDOP), by including generic terrestrial ranging contributions in the measurements set used for the computation of the position. The study provides the theoretical and experimental demonstration of a fundamental result by stating that

$$\sqrt{Tr\left(\bar{\mathbf{H}}^\top \bar{\mathbf{H}}\right)^{-1}} \leq \sqrt{Tr\left(\mathbf{H}^\top \mathbf{H}\right)^{-1}}. \tag{6.55}$$

where $Tr(\cdot)$ indicates the trace operation and $\bar{\mathbf{H}}$ is the hybrid DCM drawn accordingly to satellites and terrestrial anchors positions.

As it has been demonstrated for standalone satellite-based navigation, any additional range contribution provided w.r.t. terrestrial reference points can only decrease the geometrical dilution factor. However, the variance of the estimated position depends also on the error contribution affecting the measurements. The analysis of the CRLB for the position estimation allows indeed to include the measurements uncertainties along with their correlation in the evaluation of the profitability of a GNSS-based hybrid collaborative navigation.

6.4.1 FIM and CRLB: definitions

The CRLB is employed to identify the minimum variance that can be reached by a given unbiased estimator [92]. Indeed, the related CRLB inequality states that this variance is bounded by the inverse of the *Fisher Information* carried by a generic set of observable measurements $\mathbf{z}_k$. This fundamental limit can be generalized in its matrix form, as

$$[\mathbf{P}_k]_{mn} \geq [\mathbf{F}_k]^{-1}_{mn} = \left[-\mathbf{E}\left(\frac{\partial^2}{\partial\theta_m \partial\theta_n} \log f\left(\bar{\mathbf{z}}_k; \boldsymbol{\theta}\right)\Big|_{\boldsymbol{\theta}_k} \right) \right]^{-1} \tag{6.56}$$

where the pair (mn) identifies the element of the matrix located at the m-th row and n-th column, $\boldsymbol{\theta}_k = \left[\ \theta_1, \theta_2, \ldots, \theta_M \ \right]^T$ is a $M \times 1$ vector which defines the target state, and $\bar{\mathbf{z}}_k = \left[\ z_1, z_2, \ldots, z_N \ \right]^T$ is the observed realization of a multivariate measurements vector which is associated to $\boldsymbol{\theta}_k$ by means of the PDF $f\left(\bar{\mathbf{z}}_k; \boldsymbol{\theta}_k\right)$. The $\mathbf{F}_k$ is a $M \times M$ matrix named FIM and its inverse is namely the CRLB matrix.
Given that both $\mathbf{P}_{\hat{k}}$ and $[\mathbf{F}_k]^{-1}$ are positive definite, an ordering relation can be defined to compare two estimators $T = T(\mathbf{z}_k)$ and $T' = T(\bar{\mathbf{z}}_k)$, as

$$[\mathbf{F}_{T,k}]^{-1} > [\mathbf{F}_{T',k}]^{-1} \rightarrow \mathrm{Tr}\left([\mathbf{F}_{T,k}]^{-1} \right) > \mathrm{Tr}\left([\mathbf{F}_{T',k}]^{-1} \right) \tag{6.57}$$

where $\mathrm{Tr}\left(\cdot\right)$ is the trace operand which sums the diagonal elements of a given matrix.
When unbiased estimators are considered, the comparison of the respective CRLB (6.56) allows to identify the most advantageous solution.

This study, starting from the definition of the CRLB for hybrid positioning obtained under realistic assumptions, shows how a terrestrial correlated range brings information to the position estimation process depending on the observation conditions.

Besides the aforementioned definitions have been presented for a generic state vector $\boldsymbol{\theta}_k$, the CRLB will be derived for position state only for sake of simplicity and readability.

6.4.2 Range Contributions Modelling

In the framework of this study, two classes of range measurements have been identified in Section 6.1 as observables belonging to the measurement vector, $\bar{\mathbf{z}}_k$, in (6.56). They are defined w.r.t. the *target agent*, i:

- $\hat{\rho}^s_{i,k}$ is an estimate of the *pseudorange* between the agent i and the satellite s at a given instant t_k [90], defined as

$$\hat{\rho}^s_{i,k} = ||\mathbf{x}_{s,k} - \mathbf{x}_{i,k}|| + b_{i,k} + w_k \tag{6.58}$$

  where $b_{i,k}$ is a bias term due to the clocks misalignment and w_k is the noise due to residual errors affecting the measurements [90]. It is assumed Gaussian-distributed with zero-mean and variance $\sigma^2_{is,k}$.

- $\hat{d}_{ij,k}$ is an estimate of a pseudo inter-agent distance between the terrestrial agents i and j

$$\hat{d}_{ij,k} = ||\mathbf{x}_{i,k} - \mathbf{x}_{j,k}|| + b_{ij,k} + w_k \tag{6.59}$$

  where $b_{ij,k}$ is a generic bias term due to the ranging technique and $w_{ij,k}$ is the additive noise term affecting the measurements. For simplicity, as for the first class, it is assumed Gaussian-distributed with zero-mean and variance $\sigma^2_{ij,k}$ but its distribution can vary according to the baseline computation method described in Chapter 4.
  Inter-agent distances can be distinguished in *independent* and *dependent* from (6.58), according to the implementation of the selected method.

Let consider multiple ranges are expected to be obtained for each class assuming that measurements coming from the same class are independent. Given that this analysis addressed the positioning improvement, only the subset of $\bar{\mathbf{z}}_k$ containing range measurements (i.e. satellites and collaborative) is considered. According to this assumption their error covariance matrices are diagonal and defined as $\mathbf{R}_{\rho,k} = \mathbf{E}\left[\boldsymbol{\rho}_k \boldsymbol{\rho}_k^\top\right] - \mathbf{E}\left[\boldsymbol{\rho}_k\right]\mathbf{E}\left[\boldsymbol{\rho}_k\right]^\top$ and $\mathbf{R}_{d,k} = \mathbf{E}\left[\boldsymbol{d}_k \boldsymbol{d}_k^\top\right] - \mathbf{E}\left[\boldsymbol{d}_k\right]\mathbf{E}\left[\boldsymbol{d}_k\right]^\top$ where $\boldsymbol{\rho}_k$ and $\boldsymbol{d}_k$ are generic *measurements vectors* composed by a set of S and N range measurements from each class, respectively. A hybrid positioning solution combines the column vectors $\boldsymbol{\rho}_k$ and $\mathbf{d}_k$ in a *hybrid measurements vector*,

$$\bar{\mathbf{z}}_i(t_k) = \begin{bmatrix} \boldsymbol{\rho}_i(t_k)^T & \boldsymbol{d}_i(t_k)^T \end{bmatrix}^T \tag{6.60}$$

and the related *measurements noise covariance matrix* is hence defined as

$$\mathbf{R}_{\bar{\mathbf{z}}}(t_k) = \begin{bmatrix} \mathbf{R}_{d,k} & \mathbf{R}_{dr,k} \\ \mathbf{R}_{rd,k} & \mathbf{R}_{r,k} \end{bmatrix} \tag{6.61}$$

where the sub-matrices $\mathbf{R}_{rd,k} = \mathbf{R}_{dr,k} = \underline{\mathbf{0}}$ if and only if terrestrial ranges are obtained independently from satellite-ranges included in $\bar{\mathbf{z}}_k$. This specific case has been heavily investigated for hybrid positioning with ranging sensors [142, 82] while in this analysis such a restrictive assumption will be relaxed.

6.5 Fisher Information Matrix in Positioning Estimation

As in (6.56), in order to evaluate the FIM it is sufficient to compute the second order derivative of the logarithm of the likelihood w.r.t. the vector $\boldsymbol{\theta}_k$, were

$$\boldsymbol{\theta}_k = \begin{bmatrix} \mathbf{x}_{i,k} & b_{i,k} \end{bmatrix}^T. \tag{6.62}$$

In order to focus on the improvement of accuracy and precision of the positioning estimate, the bias term, $b_{i,k}$, will be eventually dropped as it is compensated from previous solutions $\hat{\boldsymbol{\theta}}_{k-1}$, being functional to the position computation [90]. In the following derivation, time index will be dropped as well for readability reasons.

6.5.1 Fisher Information Matrix for Satellite-only Contributions

The theoretical log-likelihood for a generic Gaussian random variable is defined as

$$\mathcal{L}(\theta, \rho, \sigma_i) = \log \frac{1}{\sqrt{2\pi}\sigma_i} - \frac{1}{2}\frac{(\mathbf{x}-\theta)^2}{\sigma_i^2}. \tag{6.63}$$

Consequently, the log likelihood for a Gaussian pseudorange measured from a generic satellite, s, is obtained as

$$\begin{aligned}\mathcal{L}(\mathbf{x}_i, r_{i,s}, \sigma_{i,s}) &= \log p\left(\hat{\rho}_{i,s}|x_i, b_i\right) \\ &= C - \frac{|\hat{\rho}_{i,s} - ||\mathbf{x}_s - \mathbf{x}_i|| - b_i|^2}{2\sigma_{i,s}^2}\end{aligned} \tag{6.64}$$

where C is the constant term resulting from the first term of the summation in (6.63), and $\sigma_{i,s}$ is the standard deviation associated to the pseudorange measurement $\hat{\rho}_i^s$.
As shown in [142], the FIM is computed as

$$F_i = -\mathbf{E}\left\{H_i\left[\sum_s^{S_i}\mathcal{L}(\mathbf{x}_i, r_i^s, \sigma_{i,s})\right]\right\} \tag{6.65}$$

where H_i is the Hessian operator of the second order partial derivatives. The FIM is hence defined as

$$F_m = \begin{bmatrix} F_{\mathbf{x}_i} & \mathbf{f}_{x_i,b_i} \\ \mathbf{f}_{x_i,b_i}^T & F_{b_i}\end{bmatrix} \tag{6.66}$$

where each submatrix can be computed as

$$\mathbf{F}_{\mathbf{x}_i} = \sum_{s\in\mathcal{S}_i}\frac{1}{\sigma_{i,s}^2}\mathbf{h}_{i,s}\mathbf{h}_{i,s}^T \tag{6.67}$$

$$F_{b_i} = \sum_{s\in\mathcal{S}_i}\frac{1}{\sigma_{i,s}^2} \tag{6.68}$$

$$\mathbf{f}_{\mathbf{x}_i,b_i}^T = \sum_{s\in\mathcal{S}_i} -\frac{1}{\sigma_{i,s}^2}\mathbf{h}_{i,s}. \tag{6.69}$$

where S_i indicates in turn the set of satellites used by the target agent, i, to compute its own PVT estimate.

6.5.2 Fisher Information Matrix for Cooperative Contributions

For the sake of simplicity, an estimate of a terrestrial range, $\hat{d}_{ij}(t_k) = \hat{d}_{ij}(t_k) - b_i(t_k)$, is considered by means of IAR algorithm presented in Chapter 4. Given multiple shareable satellites between the collaborating agents, the $\hat{d}_{ij}$ can be computed as the weighted average of a set of contributions, as

$$\hat{d}_{ij} = \sum_{s=1}^{S} w_s \hat{d}_{ij}^s \tag{6.70}$$

where the terms w_s are the weights attributed to each measurement according to its variance. Although it has been shown that IAR is characterized by a Gaussian-like distribution, its statistics is very sensitive to geometrical conditions [126]. By neglecting on purpose this peculiar behaviour, the same approach discussed for the evaluation of the FIM about satellite range measurements is applied to the likelihood defined for GNSS-only collaboratively-computed range measurements

$$\log p\left(\hat{d}_{ij}|x_i\right) = C - \frac{|\hat{d}_{ij} - ||\mathbf{x}_i - \mathbf{x}_i|| - b_{ij}|^2}{2\sigma_{ij}^2}. \tag{6.71}$$

Therefore, (6.65) is applied to (6.71) neglecting any dependency with respect to the other measurements. Eventually, the $\mathbf{F}_i$ for the hybrid system is still computed according to (6.66).

6.5.3 FIM computation in non-linear system estimation

Given that a reduced uncertainty about the computed position is not useful for real-time applications it is instead intuitive that a refinement of the position at a given instant t_k by means of the proposed integration scheme could lead to an improved estimate of the position at the following instant t_{k+1}. The update step provided by Bayesian estimation algorithms can benefit from this early refinement, such as in the case of the proposed modified EKF. The EKF is a Bayesian estimator widely used in the estimation of system dynamics due to the capability of constraining the positioning solution according to a model of the dynamics of the motion and exploiting the relationship of the state at the previous instant with the current state. Such an estimation typically outperforms LMS estimation both in terms of accuracy and precision. Furthermore, EKF is a non-linear extension of the plain KF, thus it allows to integrate non-linear measurements through a linearized model which links state and measurements such as for LMS estimation. Additional details about EKF fundamentals and implementation are left to the reader and they can be found in [16].

The CRLB for dynamic systems is modelled by non-linear time-varying state vector differential equations with deterministic inputs and non-linear time-varying observations on the state variables, corrupted by additive Gaussian white noise [185]. It has been demonstrated that FIM propagates according to the error covariance matrix for an EKF linearized w.r.t. the true trajectory. For this reason, the FIM can be computed as

$$\mathbf{F}_k = \left(\mathbf{\Phi}_{k-1}^{-1}\right)^\top \mathbf{F}_{k-1}\mathbf{\Phi}_{k-1} + \bar{\mathbf{H}}_k^\top \mathbf{R}_k^{-1}\bar{\mathbf{H}}_k \tag{6.72}$$

6.5.4 On the Approximation of the FIM for Hybrid Navigation Filters

Actually, the CRLB of the hybrid solution can be used as an estimation of the error covariance matrix of the hybrid position estimate. As proposed in [142], the hybrid FIM can be obtained by the sum of the satellite-only FIM and the cooperative FIM if and only if independent measurements are considered.

In order to deal with measurements correlation the FIM should be instead computed as $\mathbf{F}_{\theta,\boldsymbol{\mu}} = \mathbf{F}_{\theta,\boldsymbol{\rho}} + \mathbf{F}_{\theta,\boldsymbol{d}|\boldsymbol{\rho}}$, where $\mathbf{F}_{\theta,\boldsymbol{d}|\boldsymbol{\rho}}$ is the Fisher information related to the conditional probability density of the inter-agent range measurements for the given set of pseudoranges measurements, $\boldsymbol{\rho}$. The computation of the mutual Fisher information is out of the scope of this study provided that the likelihood of the inter-agent range measurements must be derived specifically for any given geometrical conditions [126]. The proposed solution does not contemplate correlation among the two classes of measurements, therefore the hybrid FIM is obtained through the computation of (6.67),(6.68),(6.69) for all the available measurements in the hybrid measurement vector, $\boldsymbol{z}_i$. Although it is assumed that $\mathbf{F}_{\theta,\boldsymbol{d}|\boldsymbol{\rho}} \simeq \mathbf{F}_{\theta,\boldsymbol{d}}$, no remarkable losses were observed in terms of covariance estimation accuracy, as it will be shown in the results in the following chapters.

In the example shown in Figure 6.5, given a pre-defined trajectory and an a-priori knowledge of the measurements variances, the CRLB is expected to identify the profitable time instants in which cooperative approach guarantees improved precision w.r.t. GNSS standalone positioning.

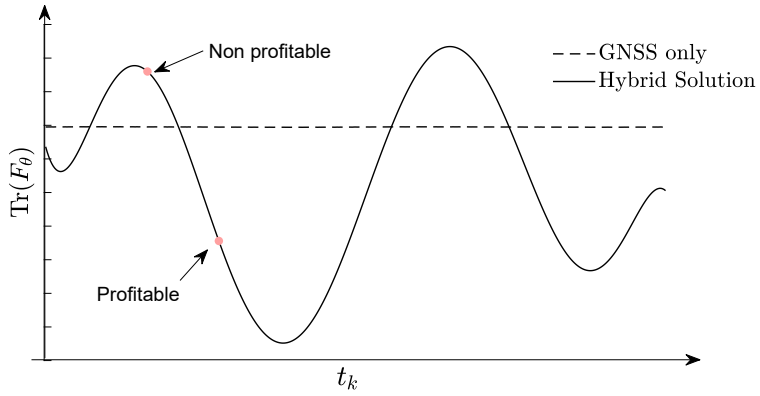

Figure 6.5: Example of theoretical computation of satellite-based positioning CRLB vs. hybrid positioning CRLB for a dynamic trajectory.

Moving from these considerations and from the FIM derivation for the Gaussian-distributed satellite range measurements recalled so far, the same quantity is computed for correlated terrestrial range measurements to estimate and compare the overall uncertainty of the computed position estimates.

Chapter 7

GNSS-based Cooperative Positioning Implementation and Performance Analysis

Availability, precision and accuracy are among the key performance parameters for the evaluation of a positioning and navigation system. This chapter presents a set of fundamental results concerning the expected performance of the hybridized navigation filters described in Chapter 6. A preliminary investigation, presented in[124] was performed through H-LMS integrating IAR collaborative contributions to compensate for GNSS outages in conditions of poor sky visibility. The fundamental results of such an analysis were obtained exploiting a further processing stage including a KF acting on the positioning solution as presented in Section 7.1. A deep analysis was then performed through the computation of the CRLB for H-LMS and H-EKF to show by means of numerical examples that IAR measurements can increase the overall amount of information about the positioning problem despite being correlated to satellite range measurements. Section 7.2 provides indeed a general overview about the precision improvement in the hybrid GNSS collaborative positioning [127]. A further simulation analysis concerning the estimation accuracy is presented in Section 7.3. The investigation was based on realistic RF signals processed through a fully-software receiver modified to perform CP. The positioning performance were evaluated for a H-EKF integrating DD ranging varying the number and the geometry of contributing aiding agents and the number and position of visible satellites. Therefore, Section 7.3 presents the analysis of the positioning accuracy in a collaborative multi-agent system, thus integrating multiple collaborative measurements at each time epoch. Eventually, Section 7.4 presents the comparative results of the hybridization of EKF and PF along with a discussion about the applicability of each filter in a non-parallel architecture.

7.1 Multiagent collaborative IAR measurements for compensation of GNSS outages

GNSS-based CP can be a useful technique to mitigate GNSS outages, thus ensuring improved positioning availability of networked GNSS receivers. The study presented hereafter extends the preliminary results published in [125] and [124]. The proposed technique allows to mitigate GNSS service unavailability experienced in urban scenario through the proposed collaborative ranging measurements and a combination. The solution affords an updated LMS state solution exploiting KF prediction and collaborative ranging information of, at least, one collaborating agent with a single satellite in common view. It will be shown that,

in some specific conditions, the implementation of IAR and the H-LMS induces an improvement of the availability of GNSS-based PVT solutions. It is worth mentioning that as far as the study was conceived, all the results are referred to simulated data and they aim at assessing the usability of collaborative measurements and their consistency w.r.t. pseudorange measurements used in the standalone LMS PVT solution.

7.1.1 Pseudo-IAR-based Robust Collaborative Algorithm

The GNSS/IAR integration algorithm introduced in [125] has been redesigned according to the following conditions:

- at a given instant t_k, agent A experiences a lack of pseudoranges measurements due to harsh conditions. The GNSS failure is due to instantaneous or persistent LoS obstruction for a given receiver-satellite pair. Therefore, it will be referred as *target* or *aided agent*.
- Agent B does not experience visibility issues and it gets reliable fixes along the time relying on its GNSS receiver. It can hence be classified as *aiding agent*.
- both the receivers observe the same portion of the sky but their constellation visibility is related to different harshness conditions, thus a reduced set of visible satellites is in common view.

Kalman state prediction as a-priori state estimate

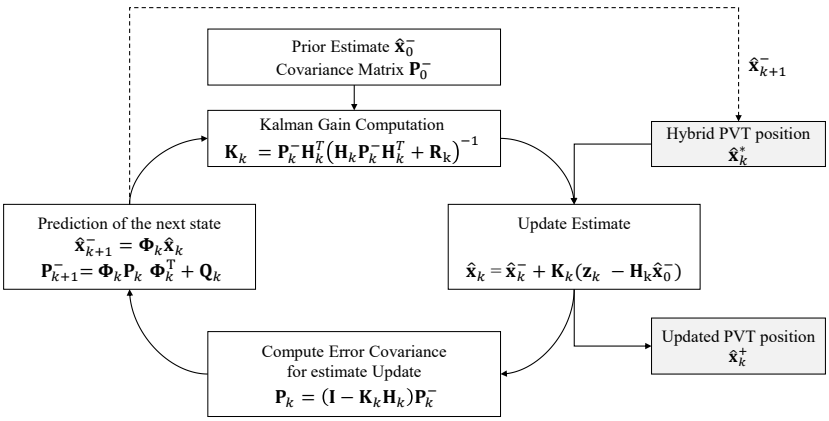

Figure 7.1: KF Loop for the smoothing of hybrid PVT solutions.

Differently from the implementation discussed in Chapter 6 for the tight-integration of collaborative measurements, this section investigate the use of a direct KF for the smoothing of the positioning solution provided by a H-LMS navigation filter. Supposed to rely on a warning system which provides information about the stability of the signal tracking according to visibility condition and the received signal quality, the GNSS receiver of a given agent should evaluate the level of harshness for the experienced environment asking for collaborative aids, if needed. Every instant t_{k-1}, at which a receiver is capable to solve for its position, it can also propagate such a solution to the next epoch t_k exploiting a direct KF PVT routine [16]. The KF is supposed to rely on a-priori dynamic model, predicting at the

time t_{k-1} the next state vector, x_k^- and merging further GNSS measurements, z_k, at time t_k to update the position estimate x_k as show in the block scheme depicted in Figure 7.1.

According to the fundamental theory presented in Chapter 6, the motion of each agent is modelled and propagated by means of a transition matrix Φ_k following a standard constant-velocity model [16]. Motion and velocity noise components will be considered as a process noise modelled by a *process covariance matrix*, Q_k. The use of a direct KF for the smoothing of the positioning solutions is generally discouraged in GNSS navigation since it introduces memory in the process estimation, thus causing potential drifts. To mitigate the memory effect of the estimation process, KF was implemented only for hybrid PVT relying on previous estimations and augmenting the measurements through the collaborative inter-agent distances. This strategy limited the drift of the positioning solution computed along a random trajectory. The key point in the implementation of the KF is the estimation of the measurements covariance matrix R, which jointly considers IAR measurements and all the available pseudoranges. For this implementation, $\mathbf{R}$ is defined as a diagonal matrix including the variance of each measurement. Given the potential correlation among the measurements, this solution is highly suboptimal for the position estimation and a more accurate estimation is advisable for a proper cooperative estimation of such a covariance matrix, such as distributed KF approaches [161].

In practice, the aided agents iteratively smooth the position estimates obtained from the hybrid GNSS/IAR system. The predicted state $\mathbf{x}_A^{(k+1)}$ is used as an approximation of the future position. In this way, the system has a guard time for the lags introduced by the Round-trip Time (RTT) and the processing time required by the cooperative solution in potential real implementation. This solution allows to enhance the robustness of the original algorithm in terms of time-consistency of the shared measurements, as well as contributing to the reduction of the drag-back effect of the solutions obtained using previous fixes and observed in [125].

Displacement vector and pseudo-position as a virtual landmark

In order to grant the privacy of the user and avoid the direct exchange of the position estimations, a strategy to mask the position of the aiding agent is introduced still preserving the effectiveness of the cooperative solution. This requires the definition of the ρ-IAR as $\tilde{d}_{AB}^{s(k)}$ between agents A and B w.r.t. the satellite s. Each aiding agent generates a virtual landmark w.r.t. its estimated position by introducing a *displacement vector* defined as $\overrightarrow{\delta d}_{B\to\tilde{B}}$ for the agent B. New virtual pseudoranges and angles are generated considering a given satellite position $\mathbf{x}_s^{(k)}$ and the virtual landmark, as

$$\rho_{\tilde{B}}^{s(k)} = \rho_B^{s(k)} \cdot \mathbf{h}_B^{s(k)} + \overrightarrow{\delta d}_{B\to\tilde{B}} \tag{7.1}$$

$$\hat{\alpha}_{A\tilde{B}} = \cos^{-1}\left(\mathbf{h}_{\tilde{B}}^{s(k)}\mathbf{h}_A^{s(k)}\right) \tag{7.2}$$

Given $\alpha_{AB}^{s(k)}$, $\rho_B^{s(k)}$ and $\tilde{x}_B^{(k)}$, the landmark point can be considered as a virtual pseudo-satellite with its relative range ρ-IAR w.r.t. the user. The geometrical configuration of the cooperating system and the GNSS constellation influences the quality of the calculated ρ-IAR.

CP algorithm implementation and simulation parameters

The actual implementation of the GNSS/INS in the simulation environment followed the steps listed in **H-LMS IAR algorithm**

H-LMS IAR algorithm Basic cooperative positioning algorithms between agents sharing raw pseudorange measurements

1: $A \rightarrow B$: The aided agent A broadcasts to the potential aiding agent B its h_i^s related to the prediction of its KF-based position for the satellite s.
2: B : The aiding agent B generates a virtual landmark $\tilde{B}$ by adding a randomly generated displacement vector to its position
3: B : B computes $\alpha^s_{A,B}$ w.r.t. B
4: $B \rightarrow A$: B replies to A sending $\alpha^s_{A,\tilde{B}}$, ${\rho_{\tilde{B}}}^s$ and its virtual position estimate $\tilde{B}$.
5: A : A estimates $d^s_{(AB)}$ through the IAR method.
6: A : A solves for the hybrid positioning equations according to H-LMS discussed in Chapter 6.

The random displacement generated by agent B foreseen the generation of a vector steered towards a random orientation with a reasonable magnitude. The magnitude can be established according to the specific application.

The simulation parameter are reported in Table 7.1. The simulation scenario includes a set of agents, $\mathcal{C}$, and a set of visible satellites, $\mathcal{S}$. The ECEF positions of the trackable satellites are provided each second by a constellation simulator, based on non-synthetic RINEX files, w.r.t. a given position. From this reference location, the positions of the set of aiding agents is generated according to a spherical Gaussian distribution centred around the reference with a pre-defined diagonal covariance matrix.

Table 7.1: Simulation parameters.

Simulation Parameter	Variable	Value
Number of agents	$C = \|\|\mathcal{C}\|\|$	30
Number of satellites	$S = \|\|\mathcal{S}\|\|$	8
Simulation Time	T	$100s$
Visibility Matrix update rate	R	3 s
Standard deviation of geographical distribution	σ_{geo}	$1000m$
User Equivalent Range Error	σ_{URE}	2 m
Average speed	$\dot{x}$,$\dot{y}$,$\dot{z}$	15m/s
LMS iterations	J	20
SAIA iterations	L	20
Simulation step	dt	1s

7.1.2 Numerical Results

This section discusses the results obtained simulating the aforementioned algorithm and addressing the case in which the continuity of the GNSS solution is not granted. Therefore, Figure 7.2a shows a receiver moving on a trajectory along which the GNSS service is not always available. The red dots represent fixes obtained from a hybrid navigation filter while green dots are standalone GNSS-only PVT fixes. Satellites visibility from the receivers is determined by random transition of a binary matrix V_k, every simulation step, dt. Available aiding agents for each target agent are then determined according to a *cross-visibility matrix* which defines the shareable satellite available for the IAR computation at each time epoch t_k. Such matrix is randomly changed along the simulation to simulate changes in satellite visibility. Thus, collaborative IAR contributions are computed whenever it is needed. Once the equations are collected and processed, the composite $\bar{\mathbf{H}}$ matrix is defined for each receiver independently, thus iterating the SAIA algorithm for L iterations within the PVT algorithm performed for J iterations [38].

Legacy PVT algorithm (green markers) and IAR-based positions (red markers) are used depending on either full or partial satellites visibility conditions, respectively. This demonstrates the good coherence and integrability of IAR with pseudorange measurements for positioning purposes. The availability of the positioning service is increased along the path and the hybridized solutions are indeed well-distributed along the trajectory although they show a higher variance of the error w.r.t. the GNSS estimates. It is visible from Figure 7.2a that the positioning solution recovered by CP show drifting phenomena and error higher than 10 m. Despite of the drift introduced and referred to as *back-drag effect*, an absolute positioning solution is still available, thus confirming the relevance of GNSS-based collaborative ranging measurements.

It is worth to recall that the set of linearized equations involved in the hybrid PVT, populated by cooperative and standard measurements, typically leads to an ill-conditioned configuration. A valuable countermeasure is the adoption of specific PVT algorithm (i.e. SAIA). Alternatively, a modification of the considered linearization point for the LMS iteration should be considered by providing the previous fix as a linearization point fr the following iterative.

As depicted in Figure 7.2a, the realization of the hybrid PVT solution applied to the simulation environment shows acceptable axis-related error on the estimated position. The curve depicts the solution that is pure GNSS-based when enough satellites are available, and hybridized with the IAR when outages are experienced. Thus, time epochs at which target agents experience GNSS outages are highlighted by the small blue dots on the time axis in Figure 7.2b. If compared to the results obtained in [125], on average, the quality of the positioning was improved.

7.1.3 Remarks on H-LMS smoothed solution

The algorithm previously proposed in [125] has been refined introducing a KF-smoothed solution, that improves the accuracy of the estimation, and allows roughly compensate for the time-inconsistency of the exchanged measurements. It is indeed worthy to recall that time compensation is not foreseen in this preliminary study. The exploitation of CP for the compensation of outages in GNSS requires a network infrastructure and a properly designed networked receiver. Despite the scientific relevance of the aforementioned results, similar and better performances can be obtained through the integration of inertial systems [26] or finely tuning the KF for reliable dead-reckoning position estimations. Furthermore, it must be recall the H-LMS estimation often leads to ill-conditioned problems thus requiring a further iterative solution for each outer iteration of the algorithm. This increases considerably the computational complexity and suggests to address tight integration schemes which in parallel guarantee improved precision and accuracy in the positioning estimation.

7.2 Precision GNSS and Collaborative Relative Ranges Integration

This section presents the results of a deep investigation on the theoretical fundamentals of GNSS-based CP, published in [123]. By keeping in mind the derivation of the FIM for the Gaussian-distributed satellite range measurements discussed in Chapter 6, the same quantity is computed for correlated terrestrial range measurements to estimate and compare the minimum uncertainty achievable for the position estimates. In this section, results from the aforementioned Bernoullian trajectory are first presented addressing a statistical analysis of W-IAR measurements according to the methodology presented in Chapter 5. The determination of the profitability of the H-LMS is then detailed by comparing the values

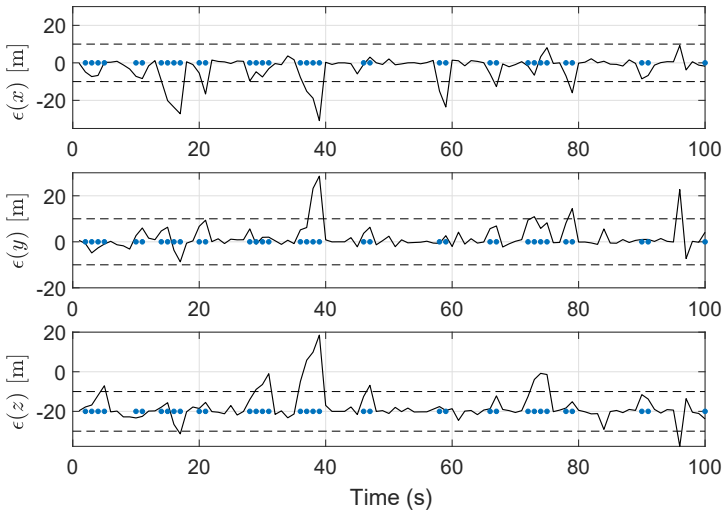

(a) Axial position error. Blue dots indicate GNSS-denied instants.

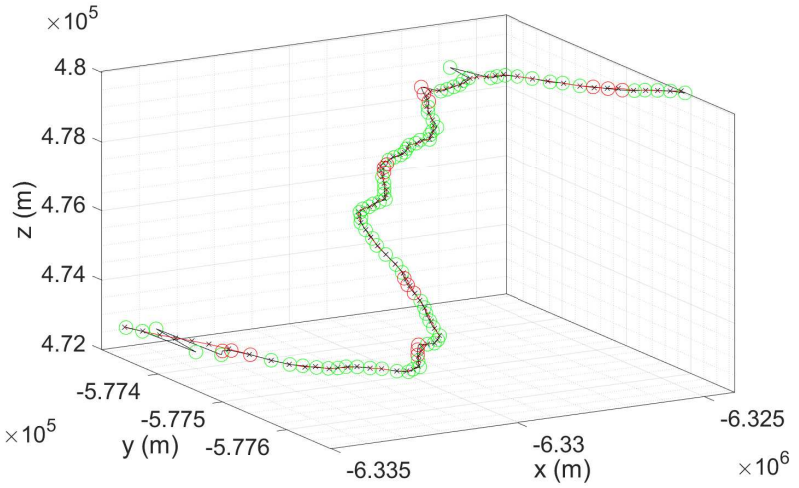

(b) Random motion trajectory. Red dots indicate hybrid fixes in GNSS-denied conditions.

Figure 7.2: Software simulation in ECEF coordinates along which GNSS outages are compensated by hybrid navigation solutions.

obtained from numerical simulation and the theoretical bound, namely CRLB. A set of alternative analytic trajectories is eventually tested to extend the analysis to a wider range of geometrical conditions for the target agent and relative satellites positions.

7.2.1 Methodology

The proposed numerical simulation aims at analysing the impact in terms of precision of the positioning solution computed by the target agent which integrates correlated collaborative range measurements with standalone GNSS measurements. Furthermore, the analysis aim at verifying whether an approximation of the CRLB can still be suitable to identify the profitability of such an integration, despite the cross-correlation among the full set of measurements.

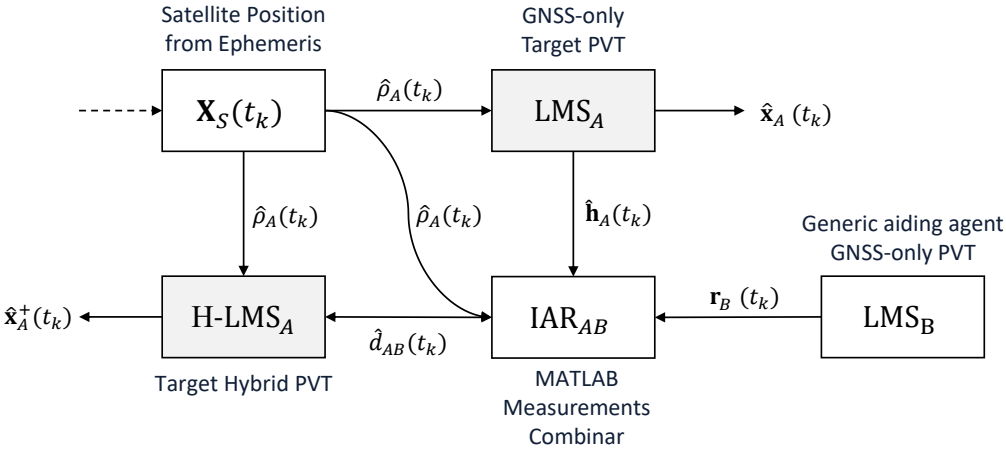

Figure 7.3: Block scheme of numerical simulations. The outputs of the LMS blocks were compared to assess the positioning performance. $\mathbf{X}_s$ indicates the positions matrix of the visible satellites.

A target agent, A, is supposed to travel along a predefined path while a single aiding agent, B, keeps its static position, $\mathbf{x}_B$, thus constituting a static anchor for every instants t_k. In the considered scenario both the agents compute their position estimates, $\hat{\mathbf{x}}_A^{(k)}$ and $\hat{\mathbf{x}}_B^{(k)}$, by relying on a given set of S visible satellites. The target agent is designed to exploit the IAR information obtained for each time instant, t_k, through the collaboration with the aiding agent. As depicted in Figure 7.3, the GNSS-only positioning solution, obtained through a plain LMS, is first performed to obtain a coarse estimate of $\hat{\mathbf{x}}_A^{(k)}$. For the sake of simplicity of the simulation environment, the pseudorange noise was characterised by the same value of σ_{UERE} for all the available satellites, thus making the LMS solution equivalent to a WLS. Afterwards, the navigation data are used to determine collaborative ranges $\hat{\mathbf{d}}_{AB}^{(k)}$ which are integrated in a further hybrid positioning solution, named H-LMS, to refine the previous outcome, hereafter referred as to $\hat{\mathbf{x}}_A^{+(k)}$. In order to emphasize the effects of collaborative measurements, limited satellite visibility conditions were investigated and $S = 4$ satellites were considered for the simulations. The axial standard deviations were measured from the numerical simulation and, in parallel, estimated through the CRLB.

The results presented hereafter are based on Monte Carlo simulation by considering W realizations of the target trajectory. The IAR measurements are expected to vary along with the time, t_k, while satellites are assumed static to limit the variability of the scenario, without any loss of generality. The measurement and the positioning estimates are performed for each run at the same time instant, t_k. Pseudorange measurements are generated by perturbing true satellite-to-agent ranges with independent WGN samples. The error covariance matrix of each positioning solution is estimated as *sample covariance*, according to

$$\hat{\mathbf{P}}_x^{(k)} = \frac{1}{W-1} \sum_{w=1}^{W} \left(\hat{\mathbf{x}}_w^{(k)} - E[\mathbf{x}_w^{(k)}] \right) \left(\hat{\mathbf{x}}_w^{(k)} - E[\mathbf{x}_w^{(k)}] \right)^\top \tag{7.3}$$

In the following, the horizontal components of (7.3) are plotted as *information ellipses* according to the eigenvalues of the position error covariance matrix [171]. Further details about (7.3) and its visual bi-dimensional representation (error ellipses or information ellipses) can be found in Appendix B. The positioning bias is computed as the mean error w.r.t. the true position of the target agent

$$\hat{\xi}_{\mathbf{x}}^{(k)} = \frac{1}{W}\sum_{w=1}^{W}\left(\hat{\mathbf{x}}_w^{(k)} - \mathbf{x}^{(k)}\right). \tag{7.4}$$

Let consider a set of S pseudorange measurements and C collaborative contributions. In order to observe the cross-correlation of such elements included in the hybrid measurements vector $\boldsymbol{\mu}^{(k)}$, the PCCs of the measurements are computed according to

$$C(\boldsymbol{\mu}_1^{(k)}, \boldsymbol{\mu}_2^{(k)}) = \frac{\operatorname{cov}\left[\boldsymbol{\mu}_1^{(k)}, \boldsymbol{\mu}_2^{(k)}\right]}{\sigma_{\boldsymbol{\mu}_1}^{(k)}\sigma_{\boldsymbol{\mu}_2}^{(k)}}. \tag{7.5}$$

where $\operatorname{cov}(\cdot)$ indicates the same covariance estimator as for (7.3) and the generic $\boldsymbol{\mu}(t_k)$ is a $(S+C)\times W$ matrix collecting a set of W realizations of the measurements vector for the instant t_k. The *profitability* of the hybrid solution is evaluated by means of the trace inequality, thus computing the ratio of the time instants t_k in which the condition

$$\operatorname{Tr}\left(\left[F_{\text{H-LMS}}^{(k)}\right]^{-1}\right) > \operatorname{Tr}\left(\left[F_{\text{LMS}}^{(k)}\right]^{-1}\right) \tag{7.6}$$

is satisfied w.r.t. the overall simulation time. The *profitability percentage* of the methods will be referred to as τ_{exp} and τ_{CRLB} to describe the advantage of H-LMS computed from the numerical simulation and from CRLB, respectively.

7.2.2 H-LMS Positioning on Bernoullian Trajectory

The results presented hereafter are referred to the example of collaborative scenario depicted in Figure 7.4 and obtained by means of a Monte Carlo simulation, using $W = 10000$ trials for each time instants t_k. A set of four satellites was randomly generated with azimuth $\phi \in \left\{\pi, \frac{3}{2}\pi\right\}$ and elevation $\alpha \in \left\{\frac{\pi}{24}, \frac{\pi}{2}\right\}$ as in Figure 7.5.

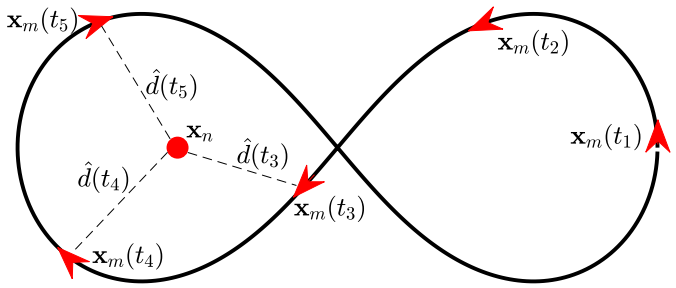

Figure 7.4: Example of a Bernoullian lemniscate path of 1046.7 m travelled at an average speed of 26.15 m/s. The dashed lines represent the collaborative terrestrial ranges provided according to the W-IAR method.

As depicted in the skyplot of Figure 7.5, the relative position of the aiding agent changes according to the motion of the target agent. Red dots in Figure 7.5 shows the relative position in terms of azimuth and elevation of the aiding agent observed at time instants t_k for $k \in$ (1,2,3,4,5) which are also highlighted in Figure 7.4.

Statistics of collaborative IAR measurements

In order to use a Gaussian likelihood (6.71) such as proposed in Chapter 6 to model the W-IAR contributions, an analysis on the statistical distribution of the collaborative

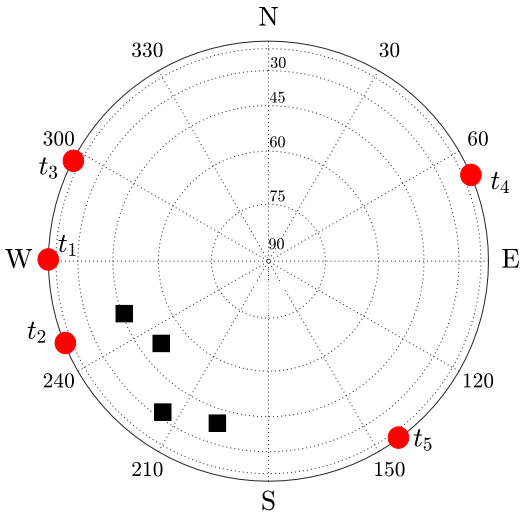

Figure 7.5: Skyplot of the relative azimuth, ϕ, and elevation, α, of the satellites and the aiding agent w.r.t. the target agent position at different time instants t_k where $k \in (1,2,3,4,5)$.

range measurements has been performed. Figure 7.6a shows a time series of the statistical distributions of the W-IAR error w.r.t. the true distance between the target and aiding agent.

The qualitative representation of Figure 7.6a was assessed by a full quantitative analysis based on a BIC, used to classify the error distribution of the W-IAR measurements. In Figure 7.6b, the histogram indicates the normalized occurrences of each fit test. It can be shown that in this scenario the ranging error is mostly Normally-distributed (95.11% of the overall simulation time), thus supporting the general derivation of the CRLB for a considerable set of time instants, t_k. Provided that a BIC analysis relies on the maximization of the likelihood for a set of observations, this result strongly supports the choice of a Gaussian likelihood in the FIM computation also for the the collaborative contributions. This aspect allows to treat the collaborative contribution like satellite range measurements without any specific adjustments in the navigation filter. Other distributions such as T-location and GEV can be observed fitting the error statistics with a relatively low number of occurrences ($\leq 5\%$). Non-Gaussian occurrences are expected to induce a mismatch between experimental values and theoretical bound.

On the comparison of theoretical and experimental limits

In Figure 7.7, the positioning solution of the LMS (left) and H-LMS (right) are presented. The shape and orientation of information ellipses show a remarkable difference between the two approaches in terms of error covariance matrix of the positioning solution. The most significant improvement can be observed between the time instants t_3 and t_5 (see Figure 7.4). It is evident from these plots that the hybrid solution integrating W-IAR measurements reduces the uncertainty in some specific portions of the path. The time series of axial biases and standard deviations are reported in Figure 7.8a and Figure 7.8b, respectively. It is worth noticing that both the metrics show a higher dynamics for the hybrid solution due to the fast variations in the relative positions of the agents w.r.t. the slower satellites-to-target dynamics.

By considering the standard deviation behaviour depicted in Figure 7.8a, it is remarkable that on y-axis the aforementioned improvement is still well visible between t_3 and t_5, when

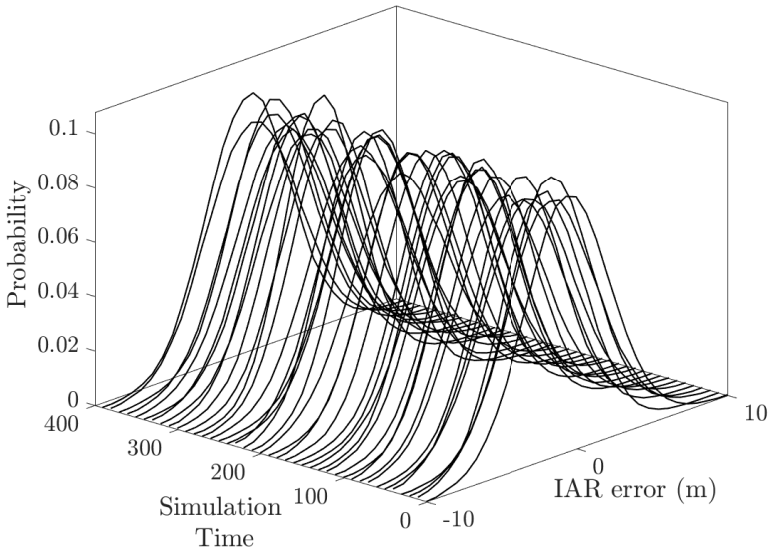

(a)

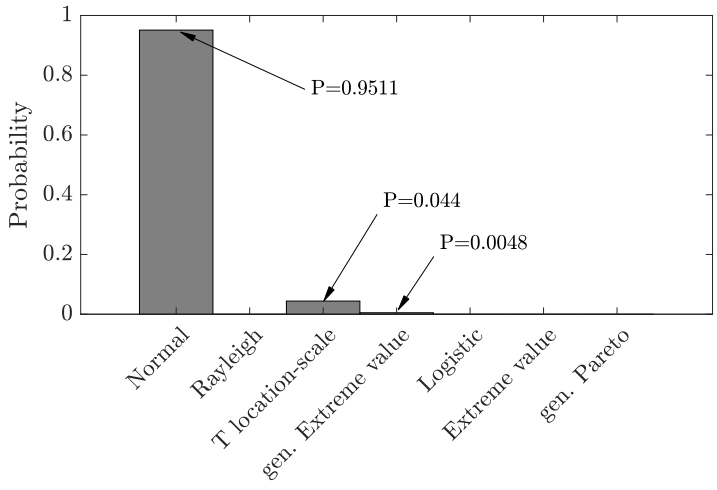

(b)

Figure 7.6: Discrete time series of IAR error PDFs evaluated in a set of time instants along the Bernoullian trajectory (a). Occurrences percentage of BIC best fits of the W-IAR error w.r.t. to a set of known statistical distributions (b).

the collaborating agent is roughly observed in the opposite direction w.r.t. the satellites constellation. The z-axis is instead less sensitive to the dynamics of the agents since their relative elevation does not vary along the trajectory. As shown in Figure 7.8b, also the bias presents a similar behaviour, showing improved performance according to the same favourable position of the collaborating agent, $\mathbf{x}_B$.

The CDF of the Root Mean Square (RMS) error, computed along the simulation, shows that the hybrid scheme overall improves the positioning performance for error values included in approximatively 0 2m and 0 9m w.r.t. the standalone GNSS solution.

The plots in Figure 7.11 shows the Pearson correlation coefficients (7.5) of the measurements at the different time instants t_k. The first row and column of each matrix indicates the correlation coefficients related to the dependent W-IAR measurement. It can be ob-

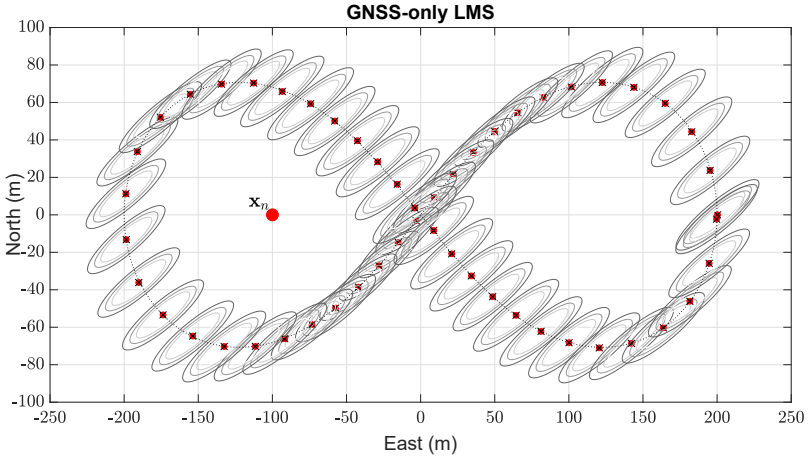

(a) GNSS standalone positioning solution.

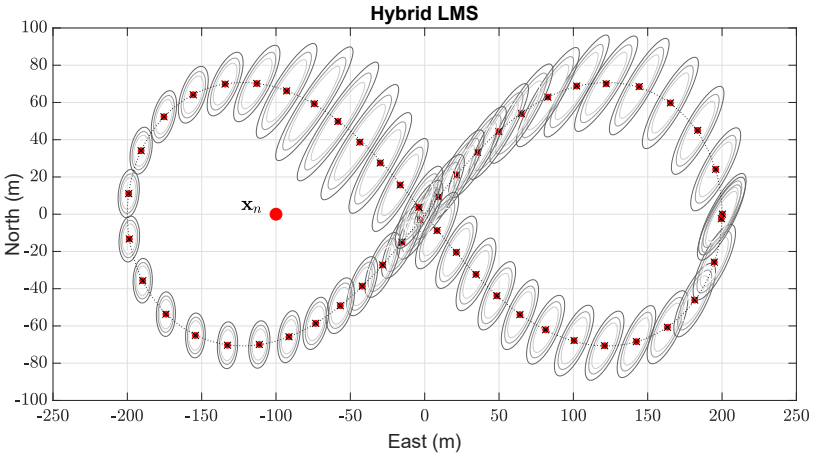

(b) Hybrid positioning solution.

Figure 7.7: Estimated positioning solutions according to the scenario in Figure 7.4. The information ellipses describe the horizontal standard deviation at 90%, 99% and 99.9% of confidence interval, obtained from the eigenvalues of the matrix $P_{\mathbf{x}}^{(k)}$ in a subset of time instants, t_k. Results from a Monte Carlo simulation with parameters $W = 10000$, $\sigma_{sA}^{(k)} = 1 \forall k$, $max(d_{AB}^{(k)}) = 200$ m.

served that in correspondence to t_4, which it has been a-posteriori identified as the most beneficial time-instant for cooperation, a very low correlation can be observed among the measurements.

To observe the benefits of H-LMS from the theoretical point of view, Figure 7.10 shows the comparison of the standard deviation computed via numerical simulation and the estimated ones obtained for the CRLB estimation of both the solutions. While the quantities match perfectly in the case of WLS, CRLB is not accurate for H-LMS due to the measurement correlation among IAR and pseudorange measurements. In correspondence of t_4, where the lowest correlation value has been observed, numerical values and theoretical estimations tends to match. The profitability percentage in terms of horizontal precision of the H-LMS is evaluated computing the percentage of the time in which the trace of the covariance matrices and the CRLB of the H-LMS are lower than the respective values from the LMS. The profitability percentage computed by means of estimated CRLB is 91.93%, which is remarkably close to the value obtained from simulated data, 89.73%.

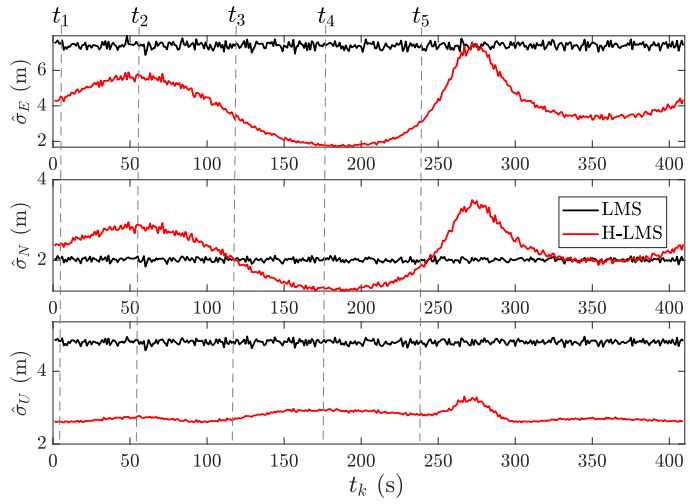

(a) Standard deviation of the position error in ENU frame.

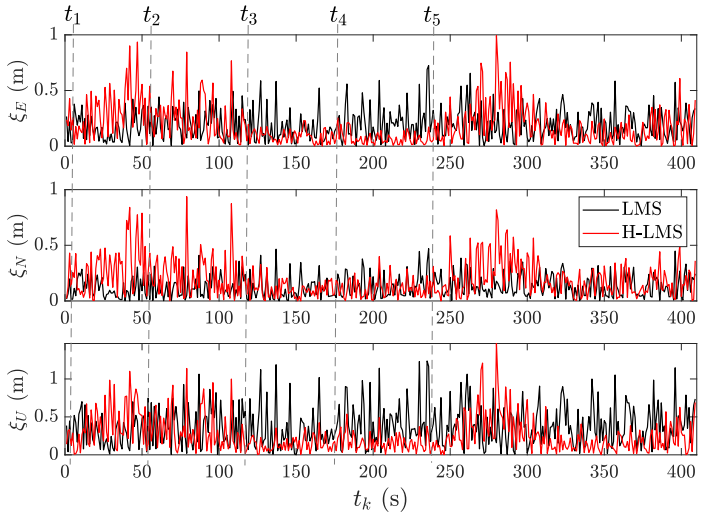

(b) Mean bias of the position error in ENU frame.

Figure 7.8: Statistical analysis of experimental biases and standard deviations of standalone and hybrid positioning solutions by means of Monte Carlo simulations.

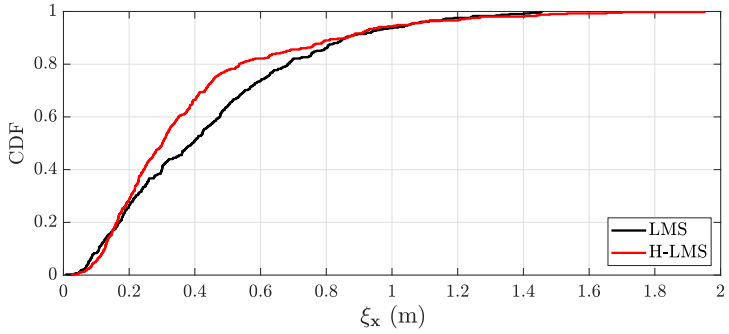

Figure 7.9: Empirical CDF of the positioning error $\hat{\xi}_{\mathbf{x}}$ for each time instant t_k.

Provided a coarse knowledge of the position of the collaborating agents and of the uncertainties of their GNSS measurements, an estimation of the uncertainty of the collaborative

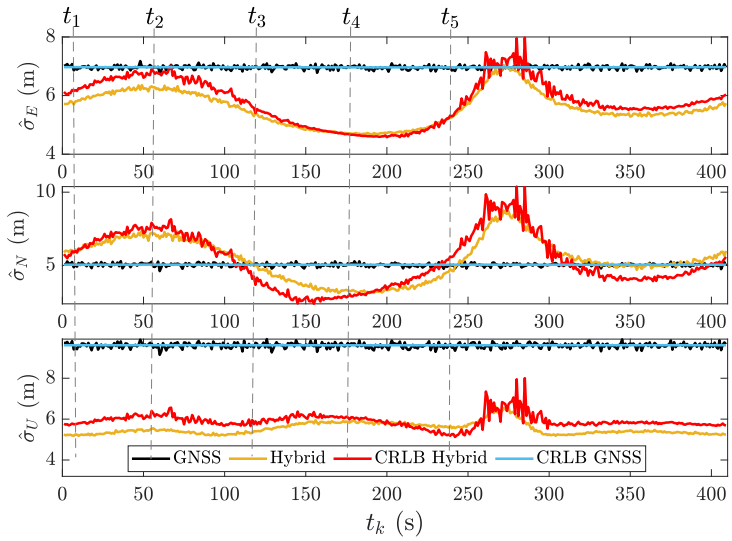

Figure 7.10: Comparison of measured axial standard deviations and estimated standard deviations from the CRLB for LMS positioning and H-LMS by Monte Carlo simulations.

ranges can be in turn computed [126]. Finally, the approximation of the CRLB for the hybrid positioning algorithm can be used to enable hybrid positioning according to (6.57) or to exclude unprofitable terrestrial contributions through the minimization of the CRLB, as in [32].

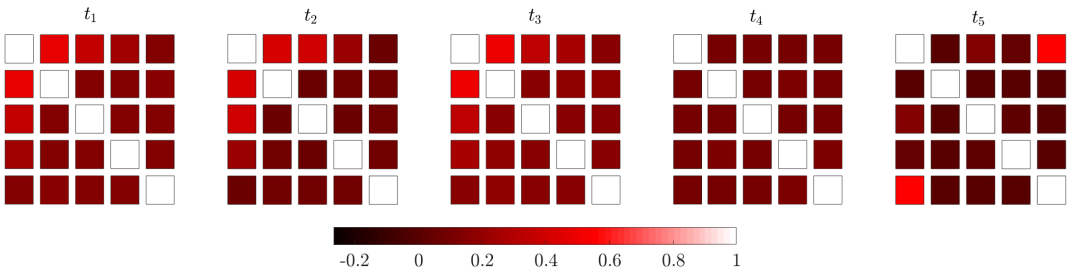

Figure 7.11: Matrices of PCC (7.5) computed for the measurement error covariance $\mathbf{R}_\rho$, and observed at sample time instants t_k, where $k \in \{1,5\}$.

7.2.3 H-LMS Estimation on Other Trajectories

The same scenario in terms of satellites visibility and single aiding agent contribution is used to analyse a set of different trajectories to identify the profitable behaviour of the hybrid solution with different geometrical configurations. All the trajectories are centred around the origin of the simulated scenario. As shown in Table 7.2, the evaluation of the profitability percentage, τ_{CRLB}, through the proposed estimation is more conservative w.r.t. the actual simulation results. Furthermore, the MSE computed along the trajectory between simulated and theoretical standard deviation value can be considered negligible for all the tested trajectories. Figure 7.12 summarizes the horizontal values of the theoretical CRLB computed for the H-LMS using different geometrical trajectories. The values are compared to the CRLB computed for H-LMS which is almost constant along all the trajectories due to the large distance of the satellites from the target at each instant t_k.

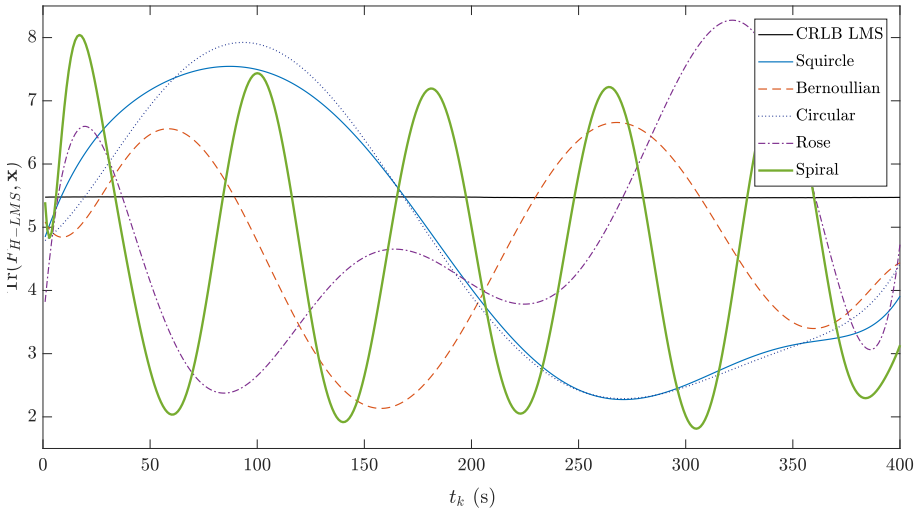

Figure 7.12: Horizontal CRLB computed for H-LMS in different elementary geometrical trajectories vs. horizontal CRLB computed for LMS.

Table 7.2: Comparison of profitability of H-LMS for other elementary geometrical trajectories

Trajectory Shape	τ_{exp}	τ_{CRLB}	$\Delta\tau$	MSE (m)
Squircle	72.21	81.90	9.69	0.26
Circular	73.11	79.46	6.35	0.21
Rose lemniscate	74.57	77.50	2.93	0.16
Archimedea Spiral	75.41	80.67	5.26	0.13
Bernoullian lemniscate	89.73	91.93	2.20	0.15

7.2.4 H-EKF Estimation on a Bernoullian Trajectory

Figure 7.13 shows the same Bernoullian path presented in Figure 7.7 along with the estimated position and associated information ellipses computed through the Monte Carlo trials of a H-EKF. Differently from the H-LMS solutions, the benefits of the hybridization are less evident in the H-EKF navigation algorithm. However it is still remarkable to notice a faster convergence of the covariance in correspondence of the beginning of the simulation (coordinates (200,0) in the trajectory plots).

The CRLB defined for a H-EKF is less sensitive to the geometry of the system as shown in the theoretical limit computation in Figure 7.14. This is partially due to the convergence of the covariance along the trajectory path which masks the dynamics of the CRLB. However, the example shows that the theoretical advantage between EKF and H-EKF is remarkable. It can be observed that as far as the trace value converges, the information carried by collaborative measurements becomes less relevant, differently from what we expect in theory. It has to be noticed that approaching the time instant t_4, the CRLB for H-LMS shows a faster decrement which matches the analysis performed for the H-LMS algorithm while the same behaviour is not evident in the experimental values. The profitability analysis of the integration of auxiliary measurements in EKF scheme provided values of 100% for all the tested trajectories shown in Table 7.2 but due the peculiar considerations made for the EKF, the comparison between theoretical and experimental values is not worthy to be reported.

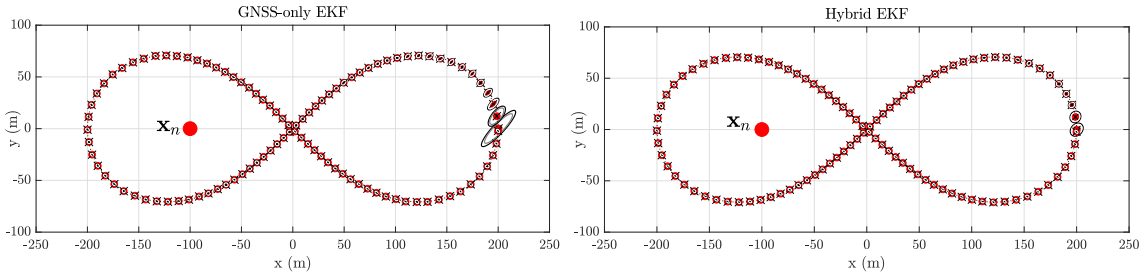

Figure 7.13: Estimated EKF and H-EKF positioning solutions according to the scenario depicted in Figure 7.4. The information ellipses describe the horizontal standard deviation at 90%, 99% and 99.9% confidence intervals, obtained from the eigenvalues of the matrix $P_{\mathbf{x}}$ in a subset of time instants, t_k. Results from a Monte Carlo simulation with parameters $W = 10000$, $\sigma_{sA} = 1$, $max(d_{AB}) = 300$ m.

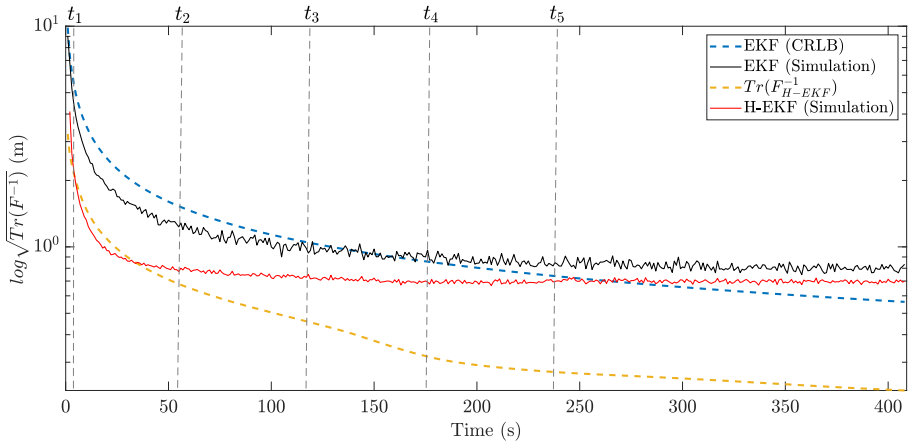

Figure 7.14: CRLB computed for EKF and H-EKF compared to the statistical values of the trace of the error covariance of the position obtained from the Monte Carlo simulation. The ordinate axis is logarithmic scale for improved readability.

7.2.5 Remarks on hybrid positioning solution

Under proper conditions, the hybridization of satellite-based and dependent terrestrial measurements can increase the performance of standalone GNSS positioning similarly to the integration of independent terrestrial ranging contributions. In particular, when the geometry of the visible satellites is poor, the additional information provided by collaborating agents mostly compensates for the dilution of precision.

The non-linear formula employed for the computation of single IAR contributions between the two agents returns non-independent non-Gaussian range measurements whose distribution does not always match with the estimation model employed in LMS and used to derive the related CRLB. In these cases the simulated standard deviation can be lower than the CRLB as shown in the example discussed in Section 7.2.2. This results are supported by the theory related to biased estimators and stability conditions of the CRLB.

The relevance of the presented results is threefold. On one side it has been shown that non-independent measurements can bring information to the positioning estimation. Furthermore, the simplistic usage of the likelihood function for Gaussian distributed variables with W-IAR measurements shows that their distribution can be non-Gaussian, thus leading to overoptimistic and over-pessimistic outcomes mainly depending on pseudoranges quality and geometry of the collaborating agents. In the end, the advantage of the proposed hybrid

positioning strictly depends on the combined geometry and quality of the terrestrial ranging information and satellites constellation. Summarizing, relying on a proper knowledge of the measurements uncertainties, the used likelihoods definition and the related CRLB for the hybridization of cooperative range measurements can be used as an approximation of the expected position error covariance matrix to determine whether GNSS-based inter-agent collaboration can improve navigation and positioning performances.

7.3 Accuracy Improvement of Position Estimation through GNSS-only Collaborative Navigation Systems

This section includes a set of results obtained by processing realistic GNSS signals through networked MATLAB-based software receiver. The following results show the effectiveness of the tight-integration of collaborative measurements up to the definition of a general trend which relates number of cooperating agents and number of visible satellites. Due to the analysis of realistic signals affected by ionospheric and tropospheric impairments, the collaborative measurements were obtained through DD ranging method that better mitigates correlated pseudorange errors w.r.t. the IAR methods, according to the theory included in Chapter 4. The section also describes the scenario and the whole experimental setup employed to investigate the integration scheme described in Chapter 6.

7.3.1 Simulated scenario and experimental setup

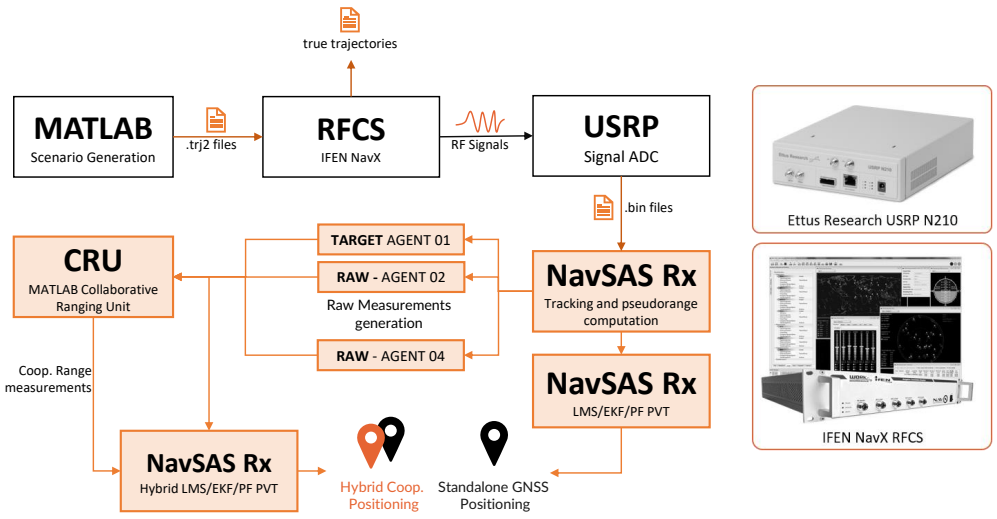

Figure 7.15: High-level block scheme of the experimental setup.

Each agent was simulated as an unspecified vehicle getting independent pseudorange measurements from the others within the same timespan.

The setup, described in Figure 7.15, was selected to simulate the proposed hybridization dealing with realistic GNSS signals and dynamic GPS satellite constellation. The other GNSSs constellations (i.e. Galileo, GLONASS, Beidou) are omitted without any loss of generality. A vehicular scenario was first generated to extract the reference trajectory and the states vector of each simulated agent with a position update rate of 10Hz. The generated

files were then processed through a RFCS IFEN® NavX. The GNSS signals were generated for a dynamic GPS constellation provided in Figure 7.5.

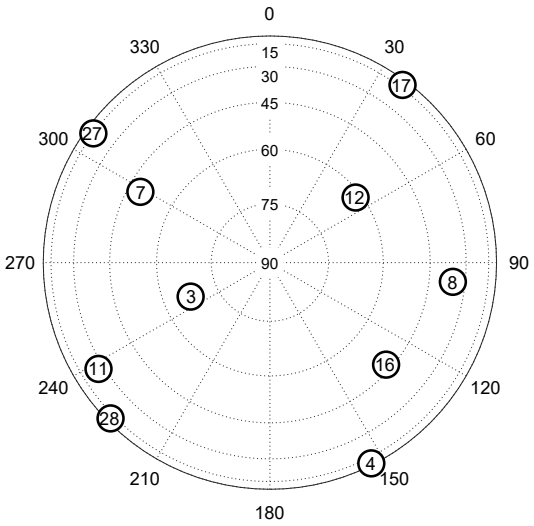

Figure 7.16: Snapshot of simulated satellites positions by IFEN® NavX.

They were transmitted by the RFCS and hence sampled by means of the ADC converter of a USRP N210, disciplined in turn by a compact RFX-OS364 OCXO. The resulting binary files were then processed through a MATLAB-based fully-software receiver (NavSAS Rx) to obtain pseudorange raw measurements out from the tracking stage and the epochs timestamps out from the coarse PVT stage. A further MATLAB script was used to combine external and own pseudorange measurements. Eventually, a modified EKF PVT stage was in charge of the position refinement according to the integration scheme proposed in Chapter 6. A detailed description of the relevant simulation aspects is provided hereafter.

7.3.2 Scenario generation

In order to reduce the amount of time-consuming single-agent simulations and with the aim of preserving a considerable variability of the observable processes, a Bernoullian path was designed as shown in Figure 7.17. The Bernoullian trajectory was centered at a given reference location (45.067825° Latitude and 7.591147° Longitude), over an area of approximately 0.4 km^2.

The seven agents indicated by the dots were kept static while the target moves along the path according to the dynamics reported in Figure 7.18. The choice of static collaborating agents has not to be considered as a simplification of the scenario. In fact, the focus of the study is the behaviour of an hybridized system with a variable relative dynamics among the receivers, which is fully described in Figure 7.19.

The state vector of each agent was generated trough a Matlab® simulation environment and stored as `.trj2` file to feed the RFCS for the generation of the trajectories. The snapshot in Figure 7.17 shows a possible realization of the test in which the target agent from the collaboration of agents 5,6 and 7. In order to cover all the configurations of the scenario, two parameters are devoted to the identification each simulation:

- $S \in$ (4,6,8,10): is the number of channels in tracking. Given a reasonable proximity among the receivers, it corresponds also to the number of visible and shareable satellites, without any loss of generality. The granularity was chosen equal to 2 to show

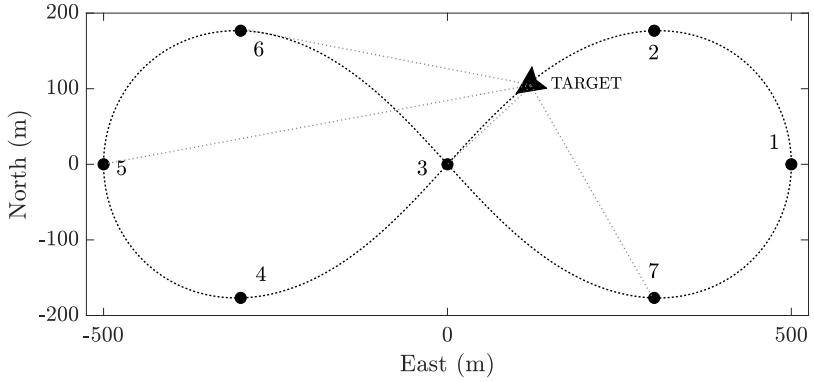

Figure 7.17: Multi-agent simulation scenario. 7 fixed GNSS receivers and a Target agent moving on a Bernoullian trajectory with lobes of radius $r_{\mathcal{L}} = 500$. Heading information indicates the motion direction.

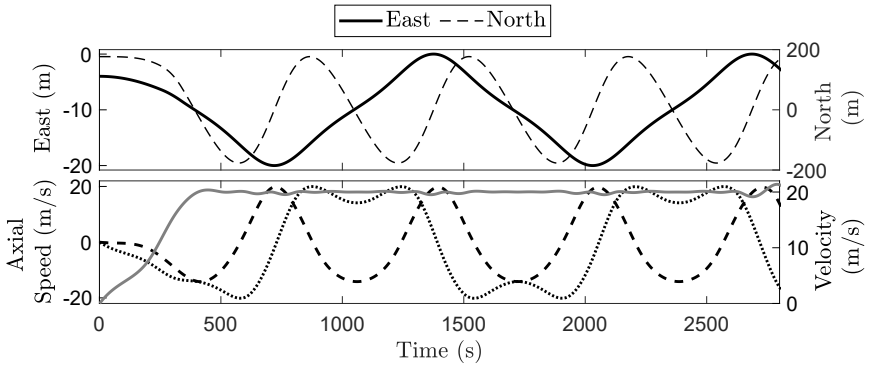

Figure 7.18: Simulated dynamics of the target agent.

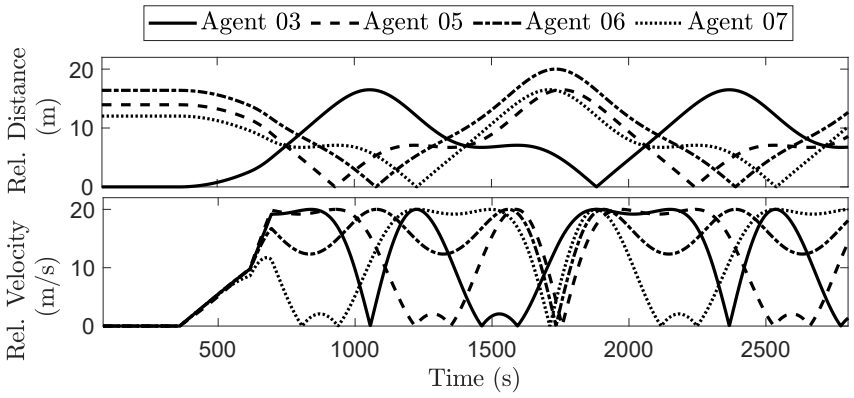

Figure 7.19: Simulated relative dynamics of the agents w.r.t. the target agent.

appreciable difference among the different configurations while the minimum number of satellites needed for the initialization of the positioning algorithm is set to 4.

- $C \in (1,2,3,4)$: is the number of collaborative contributions obtained according to DD.

As shown in Figures 7.18 and 7.19, there was an evident periodicity due to the multiple

laps on the Bernoullian lemniscate which is the reason why a further distinction were set based on the dynamics of the target agent. A shorter time span was chosen from 5s to 80s considering a low dynamic portion of the target trajectory while a longer one was chosen in 5s to 160s, thus including a higher relative dynamics.

7.3.3 Epochs misalignment

As discussed in Chapter 3, the simulated GNSS receivers compute their first fixes at independent time instants, as shown in Figure 7.20, in which epochs are represented by squared black markers.

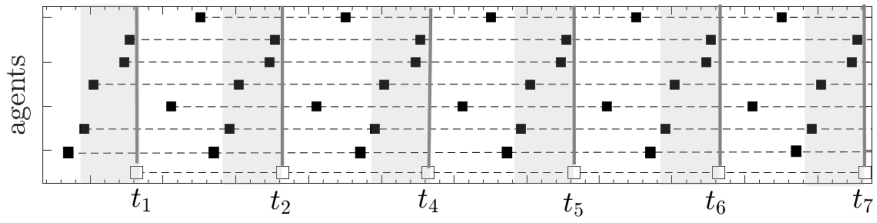

Figure 7.20: Epochs misalignment for 8 asynchronous, independent GNSS receivers observed at 10 Hz w.r.t. to the reference GPS time scale.

We already discussed the importance of compensating for this misalignment both in Chapter 3 and 4 to preserve a good time-consistency of the measurements. In order to accomplish this task, Doppler-based alignment is used. It can be shown that an inaccurate Doppler shift estimation performed by the target receiver leads to large double difference mean errors. In Figure 7.21 is shown the effect of underestimating the Doppler shift w.r.t. the value measured by the receiver. The Doppler shift factor reported on the x-axis is expressed as a fraction of the Doppler value estimated by the target receivers.

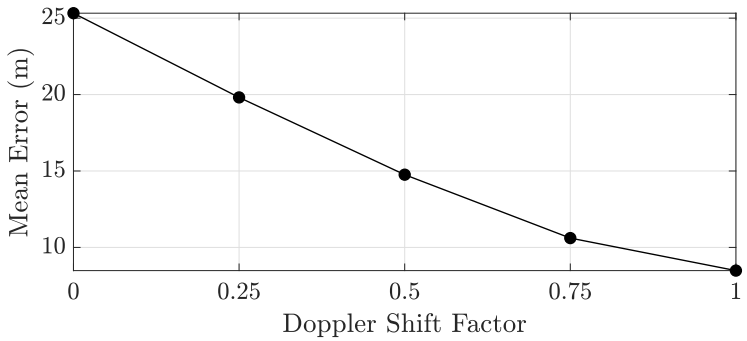

Figure 7.21: Mean error trend on a single inter-agent GNSS-based measurement in case of underestimation of the Doppler shift by the target receiver.

In order to preserve the effectiveness of the Doppler-based compensation presented in Chapter 4, available aiding agents are chosen within a pre-defined guard time w.r.t. the current target epoch. The guard-time value chosen in this framework was 40 ms (before each t_k) and is remarked in Figure 7.20 by means of grey areas. This approach was used to limit the amount of collaborative contribution by facing a realistic availability which could depend both on network constraints or on timing issues, as well.

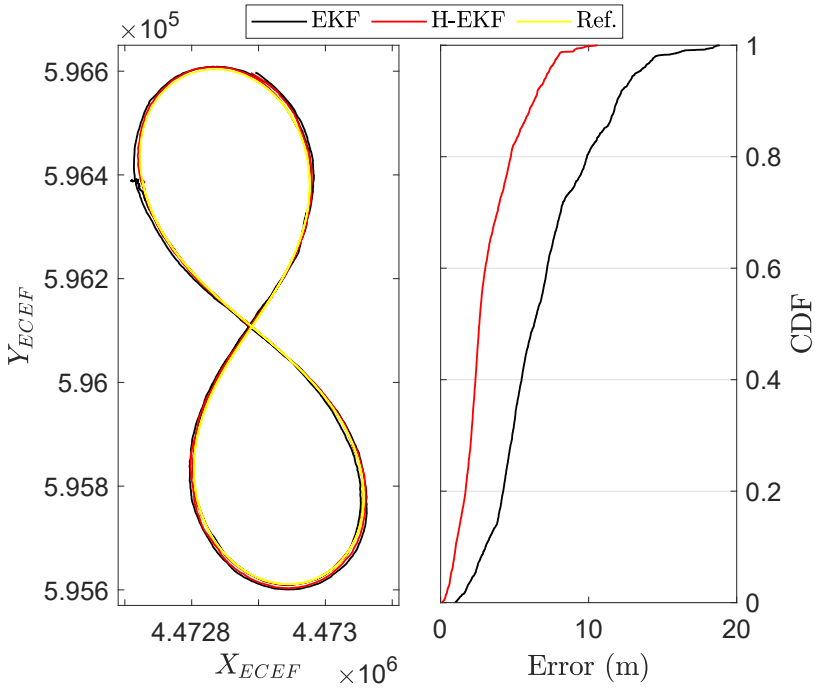

Figure 7.22: Example of standalone vs. hybrid CDF on the positioning error evaluated on a long path (280 s) with $S = 6$ and $C = 4$ in Earth Centered Earth Fixed (ECEF) reference frame.

7.3.4 Results

This section presents the quantitative results concerning the accuracy improvement provided by the tight integration of collaborative DD collaborative contributions and standalone GNSS pseudorange measurements.

Performance metrics for positioning assessment

By fixing the number of available satellite channels, $S \in (4,6,8,10)$, and the number of aiding contributions, $C \in (1,2,3,4)$, the positioning error was evaluated as the Euclidean distance between the reference trajectory obtained from the RFCS and the computed position for each epoch

$$\xi_{\mathbf{x}}(t_k) = \|\hat{\mathbf{x}}_{\text{EKF}}(t_k) - \mathbf{x}(t_k)\|. \tag{7.7}$$

A CDF of the positioning error was then evaluated for each parameter combination as shown in the example of Figure 7.22. A set of percentiles was then extracted from the CDFs of the position error obtained at each epoch t_k, to show the reduction of positioning error according to the number of aiding contributions. Each plot shows a different number S of satellites and the granularity was chosen in order to show appreciable quantitative differences.

A comparison between the standalone and hybrid solutions is provided instead by computing the Mean Accuracy Improvement along the time for each scenario. By considering the number of possible combinations of c aiding agents as the binomial coefficient $P_c = \binom{C}{c}$, the index $\mu \in (1,2,\ldots,P_c)$ is used to identify the improvement

$$\nu_{c,\mu}(t_k) = \frac{E\left[\xi_{\mathbf{x},\text{H-EKF}}(t_k)\right]}{E\left[\xi_{\mathbf{x},\text{EKF}}(t_k)\right]} \cdot 100 \tag{7.8}$$

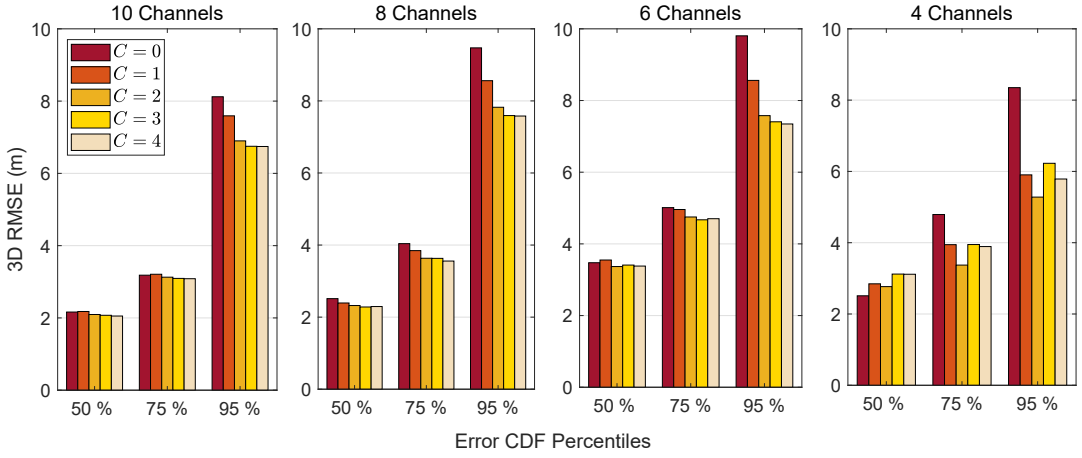

(a) Low-relative dynamics

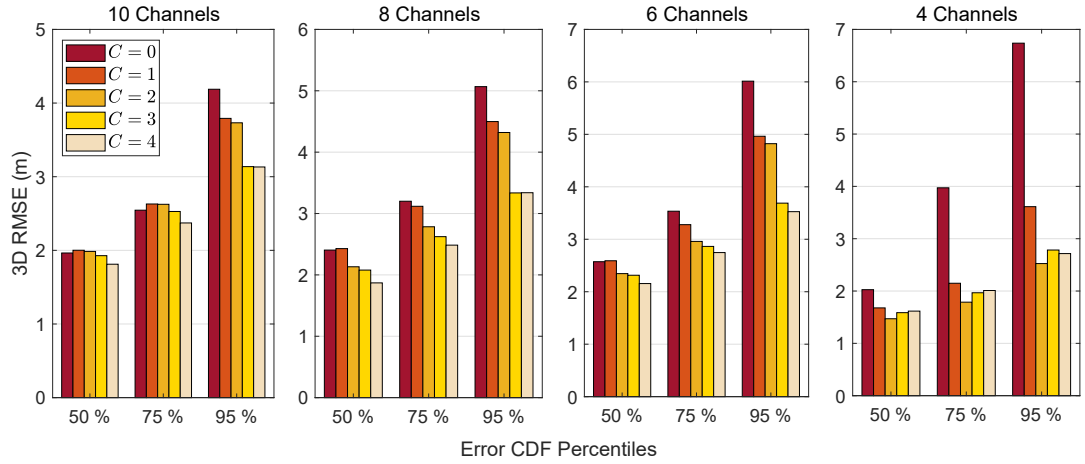

(b) High-relative dynamics

Figure 7.23: Percentiles extracted from the position error CDF.

where the fractional terms are the time average of the (7.7), for the EKF and H-EKF estimators, where H-EKF is used to identify the hybridized algorithms. An aggregated metrics is hence conceived as the average among all the possible combinations of aiding contributions in order to mitigate the effects of the specific geometry of a single set of aiding agents. The Aggregated Accuracy Improvement is computed as

$$\bar{\nu}_c = \frac{1}{P_c} \sum_{\mu=1}^{P_c} \nu_{c,\mu}. \tag{7.9}$$

and it gives a direct information on the benefits of the proposed solution.

Experimental results

The results presented hereafter are obtained through the analysis of the two different timespans of the sample trajectory presented in Section 7.3.1. For the sake of clarity, all the data refer solely to the target agent. The starting time has an offset of 5 second because a first LMS positioning stage is used at the beginning of the trajectory. Within this interval the target agent is static. 7.3.1.

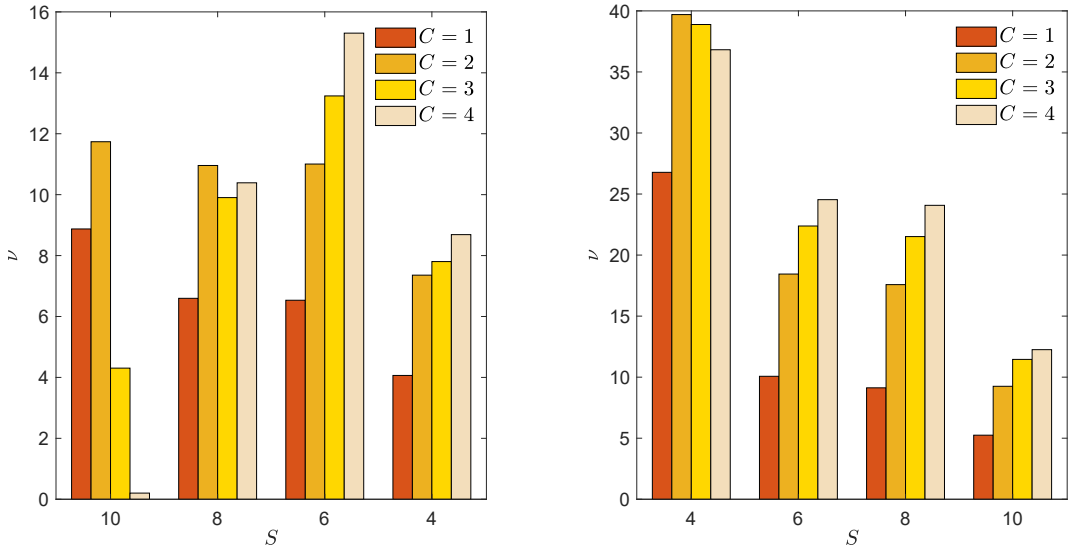

(a) Low-relative dynamics test case [5-80 s] (b) High-relative dynamics test case [5-160 s]

Figure 7.24: Average Performance improvement varying the number of satellites (available channels) and the number of aiding agents (color-scale).

The overlap between the time-spans allowed to identify an increase of the positioning error due to the complexity of the dynamics of the target agents which is not always properly modelled in the EKF design equations.

The sets of bar plots in Figures 7.23a and 7.23b summarize the values of the CDF of position error in (7.7) for the selected percentiles. By considering respectively high relative dynamic and low relative dynamic, the results are obtained varying the number of the collaborative range contributions (represented by the color scale) and the available satellites (through different plots).

On average the positioning solutions always benefits from the proposed integration showing relevant improvement in all the analyzed conditions. It is worth to remark that collaborative contributions allow to effectively compensate for a lack of satellites visibility. As an example, it can be seen in low relative dynamic 7.23b, that the combination of 8 satellites and 2 aiding agents turns in similar accuracy w.r.t. the unaided position solution obtained by exploiting 10 satellites. Similarly 1 aiding agent with 6 visible satellites matches the performance of standalone GNSS positiong of 8 satellites for all the percentiles. Similar behaviour can be observed in high relative dynamics.

High relative dynamics

Looking at the aggregated metrics in Figure 7.24, it is worthy to notice that the benefits of the integration of new ranging measurements decrease with the number of available channels when high-relative dynamics is investigated. The average improvement increases for 6, 8 and 10 channels according to the number of ranging contributions while it shows an inverse trend when only 4 channels are considered. In spite of the use of an EKF, the overall positioning performances with 4 satellites are generally very poor especially considering the low Gemetrical Dilution of Precision affecting the estimation. However, the minimum improvement is about 6% ($N = 10$,$C = 1$) in the worst case up to the 39% of the best case ($N = 4$,$C = 4$).

Low relative dynamics

The behaviour in low relative dynamics still shows a remarkable improvement due to the proposed integration. The maximum error reduction is over the 15%. However the number of position samples is lower and the performance about the static portion of the simulation severely affect the whole results. EKF is indeed less effective in estimation when the target is not moving because it keeps modelling the motion as linear according to the model in Chapter 6. For this reason, the following analysis will be restricted to the high relative dynamic dataset in which a large statistics about the trajectory drives the trend of the accuracy improvement.

7.3.5 Data fitting of Mean Aggregated Improvement

The polynomial fittings shown in Figure 7.25 summarize the benefits of the approach by analysing the aggregate average improvement versus the number of contributions from satellites and cooperating agents.

The goodness of fittings related to the figures are evaluated in the Table 7.3.

Table 7.3: Goodness of fit of the average accuracy improvement with SSE and related quality metrics.

Metric	3^{rd} **Order Fit**	1^{st} **order fit**
SSE	8.329	288.8
R-square	0.995	0.84
Adjusted R-square	0.989	0.815
RMSE	1.178	4.714

Despite the 3^{rd} order polynomial better approximates the experimental behaviour of the data, the 1st order fit provides a more readable interpretation of the experiment. As far as the number of available satellites increases, the improvement in the accuracy decreases approaching zero in correspondence of 10 satellites in view. This suggests that the additional information carried by inter-agent contributions is less effective in good visibility conditions while it is worthy otherwise. Furthermore, it can also be assessed that remarkable improvement in terms of accuracy can be provided in good visibility when a high number of collaborating agents are exploited by the target.

7.3.6 Remarks on the accuracy improvement

Double differencing technique has been used to determine auxiliary inter-agent distances among the agents by first synchronizing the measurements through a pre-emptive clock bias estimation and a further Doppler-based compensation. The integration of such measurements in the navigation algorithm allowed to effectively compensate for inaccurate dynamics model in EKF-based positioning reducing the error in the position estimates, thus improving the accuracy of the solution. The method has been applied to a vehicular scenario contemplating multiple agents in low and moderate relative dynamics conditions. It has been observed that cooperative tight integration copes with a misleading modelling of the dynamics of the users (low values in model covariance matrix) used in the EKF. A comparison between a standalone positioning and a cooperative algorithm based on EKF navigation algorithm was presented relatively to an experimental realistic using realistic GNSS signals. The behaviour of the performance improvement showed an increasing trend in low visibility condition while the benefits of the integration decrease when an high number of shareable satellites are available. The integration of a small set of DD-based inter agent distances compensate for

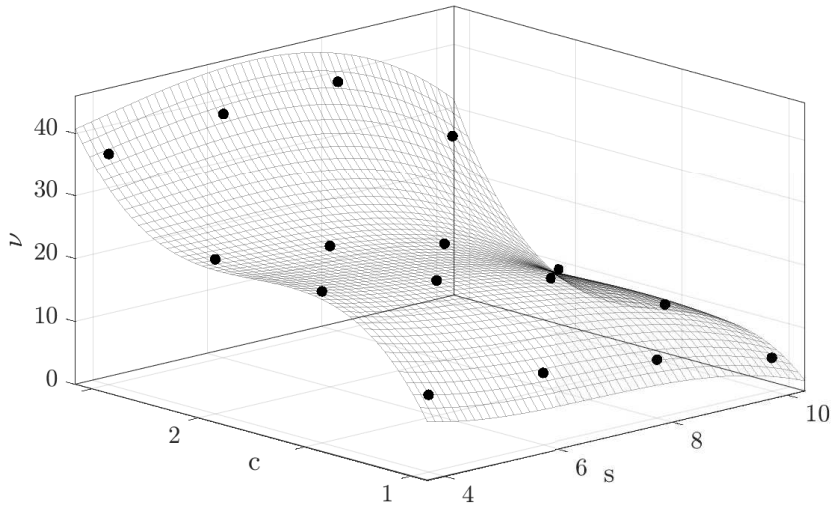

Figure 7.25: *X-Y* 3rd order data fitting with multi-dimensional polynomial showing the trend of the average accuracy improvement in *high relative dynamics* varying the number of satellites and aiding agents in high relative dynamics.

severe drifts even in good sky visibility conditions. The benefits show an increasing trend as far as the number of collaborative ranges increases at any available number of channels. In parallel, the benefits of such an integration slightly decrease as far as the number of visible satellites increase. Eventually, this work shows a clear improvement in the sharing of pseudorange measurements among connected receivers especially in contexts in which a limited amount of satellite is visible for which, the experimental results showed an average improvement in accuracy of about 39% in the worst sky visibility conditions, by relying on the collaborative measurements of 4 aiding agents.

7.4 Assessment of the computational complexity of Bayesian positioning estimation in EKF and PF

This section aim at contributing to the selection of a proper navigation filter for the hybridization of the PVT computation using collaborative inter-agent measurements. According to the theory presented in Chapter 6, PF is appealing for the superior performance in terms of estimation accuracy. Despite this, EKF still dominates the real implementations of positioning and navigation algorithms due to its lower computational complexity. A suboptimal implementation of a PF named suboptimal PF (s-PF) is hereafter proposed for a fair comparison of the positioning estimations performed through the two navigation filters. All the results presented in this chapter are referred to a single aided agent benefiting from multiple aiding agents sharing their raw measurements. Due to their relevance in the context of GNSS-based CP, they have been published in [128].

Suboptimal implementation of a Particle Filter (s-PF)

The strategy of implementing a s-PF (a.k.a. in literature as Extended Particle Filter (EPF) [120, 2]) aims at providing a fair comparison among the two Bayesian filters. The proposed implementation does not exploit on purpose the capability of PF of dealing with non-Gaussian density function but it is worthy to consider that even restricting this condition,

the accuracy of the estimation is higher than EKF. Furthermore, it is remarkable that an accurate modelling of the statistics of the measurements is not suitable in practice for an optimal implementation of the PF and the Gaussian approximation is hence applicable for a large variety of situations.

If a linear state transition function of the EKF is used for the *prediction stage* of the PF and a Gaussian likelihood is chosen for the weights computation (6.53), the PF implementation turns to be a suboptimal estimation algorithm but the performance can be properly compared as it will be shown in the results. It is worth mentioning that the step 1 can be oversimplified by generating Gaussian-distributed particles according to the estimated covariance matrix at $\mathbf{P}_{k-1}$ prior to the prediction.

7.4.1 Computational complexity of Bayesian Estimation

A formal analysis about the complexity of the two Bayesian navigation filters presented in this chapter is summarized hereafter. By comparing the main computational steps presented in [77], it can be noticed that the most time-consuming computation in EKF regards the recursion about the matrix $\mathbf{P}_k$ which is not required in PF. Let n_θ the dimension of the state vector and N the number of particles used in the PF, the computational complexity can be approximated to $\mathcal{O}(2n_\theta^3)$ and to $\mathcal{O}(Nn_\theta^2)$ for EKF and PF, respectively [76]. According to the number of elements of the state vector (6.1), it is worth to consider that the number of operations is comparable for the two navigation filters when $N \simeq 16$ [77]. As far as n_θ grows the difference reduces because the measurement update becomes more complex. The complexity issue is imperative for the implementation of the algorithms in low-power hardware architectures and it can be determinant for the choice of a specific Bayesian navigation filter. PF/EKF implementations have been discussed in literature to limit the computational burden of the standalone PF for a subset of state elements [77, 2] but they are out of the scope of this work.

7.4.2 Test Scenario

The Bernoullian trajectory shown in Figure 7.26 was considered for the generation of the vehicular scenario. The trajectory was chosen among a set of geometrical paths centred at the point C_1. The four agents indicated by the black dots C_c where $c \in$ (1,4), are kept

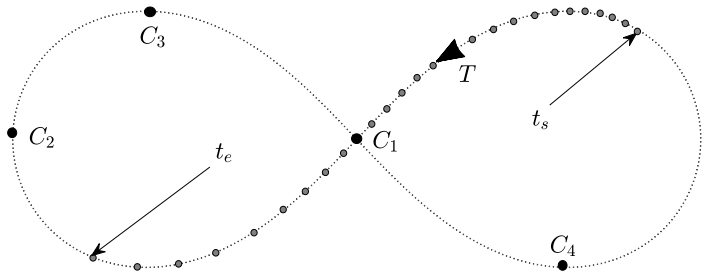

Figure 7.26: Bernoullian Lemniscate test trajectory. The results are referred to the S-shaped portion included between instants t_s and t_e and crossing the location of agent C_1.

fixed while the target moves along the path according to a predefined uniformly accelerated dynamics, represented in Figure 7.26 by the small grey dots. The tangent speed of the target agent spans from 5 m/s to 10 m/s in a timespan of 60 s. The true state vector (6.1) of each agent was generated with an update rate of 10 Hz trough a Matlab® simulation environment. The true trajectories were stored as `.trj2` file to feed the IFEN NavX for the generation

of GPS constellation and of the realistic satellite signals. Two different visibility conditions were considered in which the available satellite set has been randomly changed to observe the estimation performance of the two navigation filters in different conditions, as reported in Table 7.4. A set of 4 satellites were considered to satisfy the minimum conditions to initialize the positioning algorithm [90], while a set of 10 satellites simulates the open sky visibility of the GPS constellation. These alternatives also affected the quality of the inter-agent ranging and the overall estimation refinement obtained from the integration.

Table 7.4: Satellite visibility in the simulation scenario.

Visibility	**No. of Satellites**	**Satellite IDs (PRN)**
Good (Open Sky)	10	3,4,7,8,11,12,16,17,27,18
Poor (Urban Canyon)	4	4,7,8,27

A first set of results, shown in Figure 7.27, describes the improved average accuracy of the s-PF estimation w.r.t. to the EKF. The fact that the same accuracy is not affordable for an EKF, clearly remarks the benefits of using such a computational expensive algorithm for the PVT solution. In fact, while PF estimation can be asymptotically improved by increasing the number of particles, EKF already provides the best achievable solution which can be only improved by better environmental conditions experienced by the receiver. Although

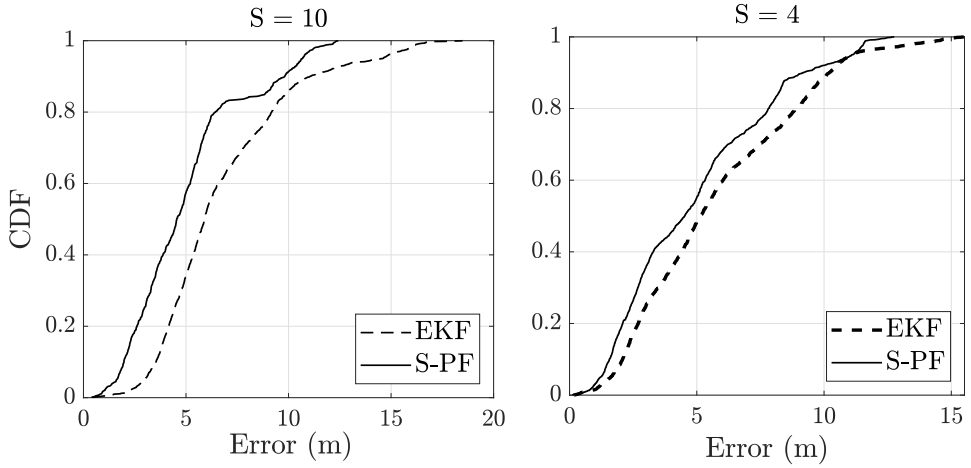

Figure 7.27: CDFs of the estimated trajectory with plain s-PF ($N = 1000$) and EKF navigation filters.

the considered implementation of the PF is suboptimal, an average accuracy improvement of 23.02% for the 50th percentile of the error distribution has been achieved in good visibility. A reduced improvement of 12.36% at the 50th percentile is instead observable in poor visibility conditions, as depicted in the right CDF in Figure 7.27. According to the approximation of the computational complexity discussed in Chapter 6, the usage of 1000 particles requires a considerable computational effort, thus making the PF filter 62.5 times slower in the estimation routine. By focusing on PF implementation, the results in Figure 7.28 show that a considerable advantage is provided by integrating auxiliary measurements when a lower number of particle is used for the PF-based estimation ($N = 200$). On the left plot, it can be noticed that the hybridization cannot provide a strong improvement, thus discouraging the cooperative effort when a high number of particle is used. On the other hand, the CDFs provided in Figures 7.29 and 7.30 confirm that the integration of collaborative

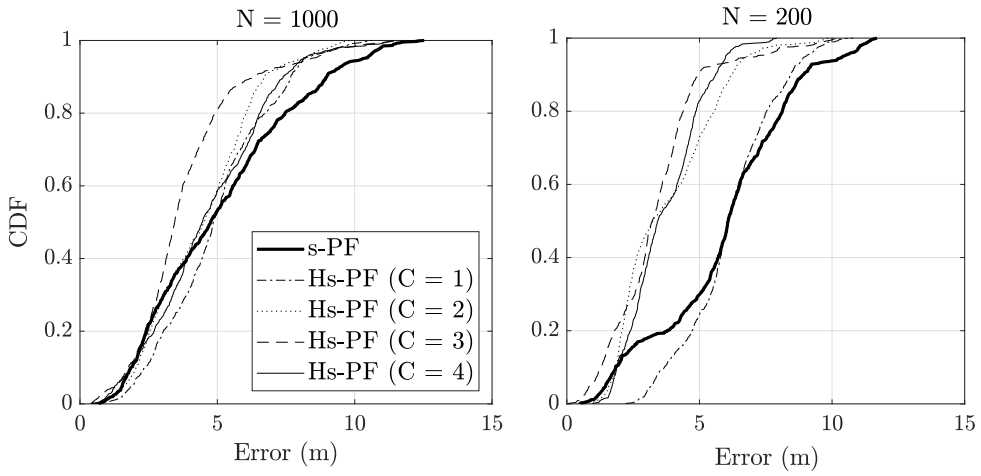

Figure 7.28: CDFs of the estimated trajectory with Hybrid s-PF using different numbers of particles and varying the number of collaborative contributions.

range measurements can dramatically improve the EKF performance avoiding the increase of complexity required by the PF. The results show that EKF can be enhanced by integrating auxiliary correlated information more efficiently than what can be done by PF implementation. This suggests a trade-off in preferring collaborative solutions w.r.t. high-complexity navigation filters.

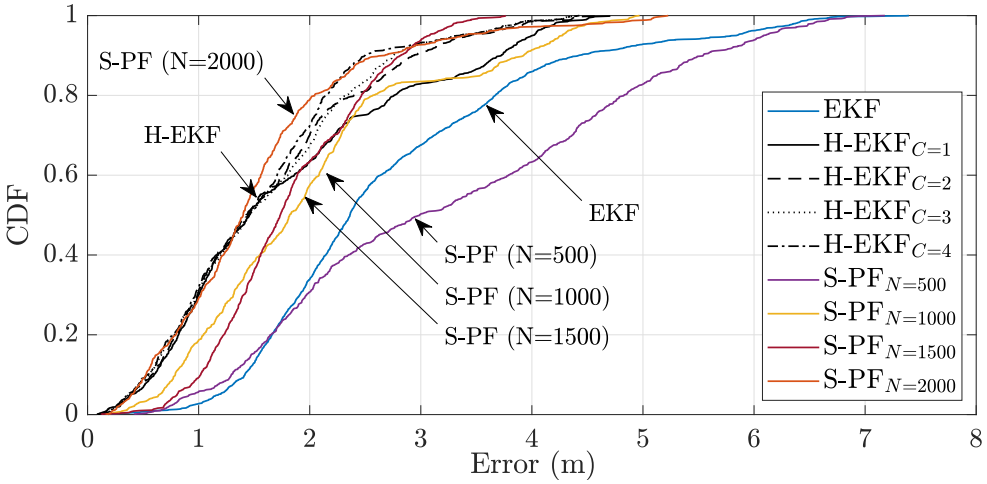

Figure 7.29: CDF of EKF and PF trajectory estimation varying the number of particles and the number of collaborative contributions in good satellite visibility.

7.4.3 Final remarks

This investigation compares the benefits of the integration of GNSS-only auxiliary measurements to positioning and navigation by proposing the extension of the measurements vector with collaborative measurements. The analysis were performed along a low-dynamics portion of a Bernoullian trajectory to properly compare the performance of an EKF and a suboptimal PF in different satellites visibility conditions. The s-PF reaches better accuracy and precision performance at a high computational cost while EKF offers practicable computational complexity although it leads to lower accuracy. The accuracy improvement provided

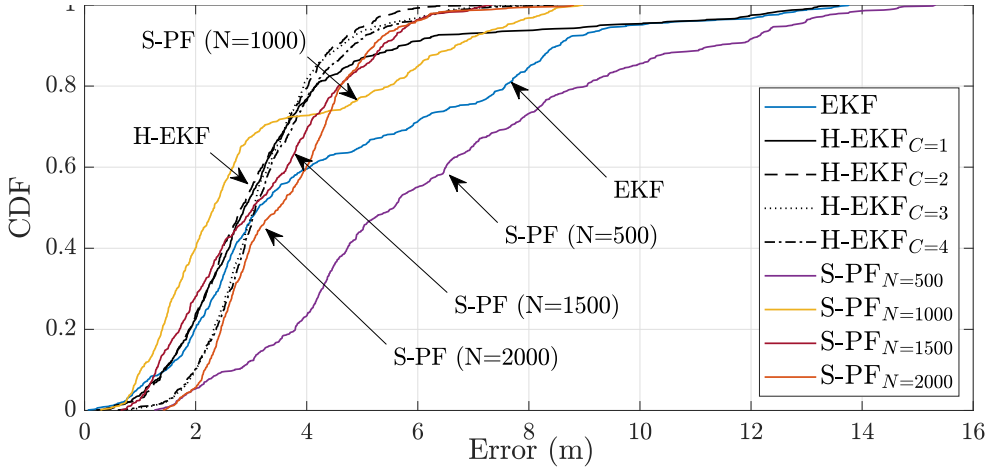

Figure 7.30: CDF of EKF and PF trajectory estimation varying the number of particles and the number of collaborative contributions in poor satellite visibility.

by multi-agents collaborative range measurements is less significant when a high number of particles is used for PF position estimation. On the other hand, the EKF-based integration considerably increase the accuracy of the estimation reaching values close to highly-complex s-PF and by also maintaining a lower computational complexity.

Chapter 8

Implementation of a Proof Of Concept

This chapter presents the development of a PoC for the GNSS-based CP approach discussed in this thesis. A general framework, named CAPS.loc, was conceived to provide a CP solution for GNSS users experiencing poor positioning and navigation performance, over general purpose network connectivity[1](e.g. Wi-Fi 802.11x or 4G). A preliminary implementation of such a framework was designed in the context of HANSEL[2], a project founded by the ESA. A demonstrator was contextually developed to assess the feasibility and the effectiveness of a pairwise GNSS-based CP using Google Android™ smartphones. By relying on the access to GNSS raw measurements provided by the devices, the PoC aimed at assessing the feasibility of the CP paradigm.

Practically, the implementation concerned the mutual exchange of GNSS raw measurements obtained from integrated ultra-low cost GNSS receivers for a near-real-time computation of the collaborative inter-agent distances among the agents (5). By operating in such a collaborative context, the devices were expected to improve their positioning and navigation performance according to the hybrid scheme proposed in Chapter 6, thus integrating such asynchronous inter-agent distances. Basically, CAPS.loc was conceived as GNSS-only, sensor-less and collaborative positioning and navigation framework.

An introductory discussion is provided in Section 8.1 concerning the context of Smart City addressed by the HANSEL project. Beside this, recent research works about GNSS advances in ultra-low-cost receivers embedded in smartphones are also discussed as background and motivation of the proposed contribution about GNSS-based CP. An overall description of the framework and its real implementation is then provided in Section 8.3 and a set of metrics for the evaluation of the positioning performance are presented along with a general classification of the investigated scenarios in Section 8.5.

8.1 The role of GNSS in smart connected environments

The GNSS-based CP defined within this thesis can be considered a general CP framework which can be potentially implemented in a variety of networked GNSS receivers. Despite this aspect, CAPS.loc addresses specifically smart devices by focusing on their positioning and navigation capabilities in urban environment.

[1]The CAPS.loc framework won the Italian Prize and it was awarded at Galileo Masters 2019, Space Week 3-5 December 2019 Helsinki

[2]ESA contract number 4000126230/18/NL/CRS

In fact, smart cities with their urban characterization perfectly combine a considerable number of smart devices equipped with ultra-low-cost GNSS receivers and critical threats to GNSS itself. Indeed, within this context GNSS satellites are often in Non-Line-of-Sight (NLOS) and their visibility is often limited due to obstruction. Even considering the integration of auxiliary sensors, the quality of absolute positioning solution can be highly-compromised or unreliable [55, 43].

The paradigm of Smart Cities has attracted many research works in the last decade, although a proper definition has not been identified yet. They can be defined as limited geographic and/or administrative area in which several types electronic devices can provide and exchange information among themselves within a given network. This exchange allows improving resource usage, mobility and quality of life by providing benefit to civilian, governmental and business users.

Furthermore, the ubiquity of such *smart* technologies, the advent of Internet of Things (IoT), and the recent advances of the telecommunication networks have actually enabled new connectivity and technological challanges, among which the cooperative or cloud-based location and navigation approaches are readily available examples [108, 114]. In these domains, such positioning approaches are of high interest for several applications in which size, power or computational constraints constitute the limiting factors of potential implementations.

In such a smart city context, a relevant aspect is the provision of location and navigation related services for both the users and within the network itself. This appears immediate when applications such as traffic management, access control, geofencing, autonomous mobility, precise positioning, public health and safety, critical infrastructure, or security are among the killer application of the urban scenarios [75]. As the readers know, it comes naturally that one of the key enablers of such services is GNSS, through its global coverage and free of charge provision of positioning solution. Together with the growing adoption and availability of GNSS signals, frequencies and services, user technologies have evolved and disseminated in a multitude of devices and applications. At the same time, other technologies have continuously emerged and evolved into the PVT domain, such as 4G/LTE/5G [204, 29], increasing even further possibilities for positioning solutions and the synergies with GNSS in providing better location and navigation capabilities to the users.

8.1.1 GNSS advances in mass-market smart devices

In order to support specific applications in the area of GNSS, ad-hoc radio-links have been used in high-end geodetic receivers for real-time surveys since the mid-1980s when RTK was first conceived. Legacy radio links in UHF or Very High Frequency (VHF) are implemented in professional receivers for the exchange of differential corrections. Modern solutions rely on Bluetooth™ or even on wired/wireless internet connectivity such as for example the products in [188, 189]. Such solutions were not conceived for a peer-to-peer real-time collaboration and they cannot be addressed for the target application described in this chapter.

Despite the quality and the reliability of the hardware, an interesting solution to exploit the synergy between network connectivity and low level processing of GNSS measurements has been recently offered by Google Android mobile devices [74]. To support and encourage the rapid innovation trends involving LBS indeed, in 2016 Google made available raw GNSS measurements, retrieved from the enabled GNSS chipsets for mobile devices. The measurements can be retrieved from the on-board GNSS chipset through Android's Application Programming Interface (API) 24 on devices running Android 7+ equipped with enabled chipsets, thus improving their positioning and navigation performance [206, 74]. Thanks to this innovation, a number of recent research works successfully investigated GNSS positioning in smartphones. Preliminary investigation on the measurements quality obtained through

smartphones GNSS receivers could lead to innovative CP frameworks for ultra-low-cost mass market GNSS devices.

A controlled scenario analysis was performed on a set of different mobile devices in [68], Xiaomi Mi 8 positioning solutions has been recently investigated in [156] and the migration of DGNSS and RTK positioning has been proposed for smartphones in several contributions [205, 30, 84, 107, 181] as well as PPP [147, 104, 10, 150]. On one hand such analysis often emphasized technical and technological limits of this market segment such as bad antenna design and poor quality of code pseudorange measurements while on the other hand they opened a variety of potential solutions for the improvement of positioning and navigation.

Thanks to the disclosure of such measurements in Android devices, the collaborative combination of GNSS data can be performed prior to the positioning computation, by actually increasing the number of measurements available at the PVT stage, as proposed in Chapter 6. In the past, this challenging approach has been investigated mostly by simulations rather than analysing real implementations, due to the many technical aspects about the combination of asynchronous and heterogeneous measurements from different receivers, as presented in Chapter 4.

Therefore, within the definition of an innovative testbed in the framework of the smart cities, the CAPS.loc framework has been implemented as collaborative solution to generally improve GNSS navigation performance in urban environment.

8.1.2 The HANSEL project

The HANSEL project addresses the design and test of a set of GNSS-based technologies appealing in the context of smart cities. In particular, the overall objective was the definition and provisioning of a conceptual testbed demonstrating the means and tools for exploiting GNSS techniques and applications in a connected smart environment.

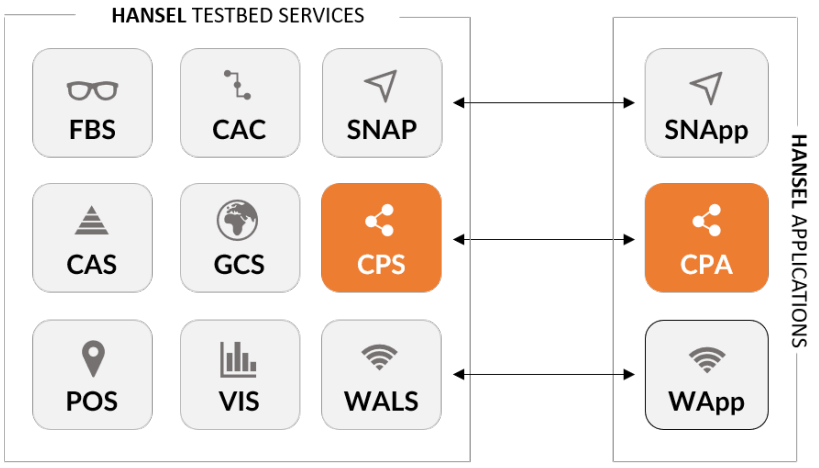

Figure 8.1: HANSEL testbed high-level block scheme.

Figure 8.1 shows two blocks identifying the main components of the testbed, on the left block we can identify a set of independent services which are expected to run in parallel for different categories of users. A brief description of each service is provided in Table 8.1.

In the right block of Figure 8.1 three front-end applications which are expected to work at receiver level are included. The applications included in the testbed are described in Table 8.2.

Acronym	Definition	Description
CAC	Command and Control	Back-end service which provides alerts for assisted navigation when positioning solutions do not match with the selected trajectory.
SNAP	Snapshot processing relay service	Back-end service for the cloud-based snapshot positioning conceived for sensors networks [115].
CAS	Testbed GNSS NTRIP caster	is a back-end wrapper of the BKG caster provided by IGS at https://igs.bkg.bund.de/ntrip/download
GCS	GNSS receivers monitoring service	is a back-end service for the monitoring of GNSS receivers operational status
CPS	Cooperative Positioning Service	is a back-end service for the exchange of GNSS raw measurements among connected smart devices to support GNSS-based CP
POS	Position Relay Service	is a back-end JASON-based positioning relay service.
VIS	Visibility service	is a back-end service which provides visual information about the satellite visibility w.r.t. to a predefined location.
WALS	Wi-Fi location service	is a back-end service which support the GNSS+Wi-Fi positioning computation.

Table 8.1: GNSS-based back-end services running on the HANSEL testbed

Acronym	Definition	Description
SNApp	SNAP Application	is a front-end Python application which interacts with the SNAP service running on the testbed.
CPA	Cooperative Positioning Application	The Collaborative Positioning App interacts with the ac-CPS to provide to the mobile GNSS users, improved localization capabilities.
WApp	WALS application	The WALS app interacts with the WALS service to provide to mobile users a GNSS+Wi-Fi positioning solution.

Table 8.2: GNSS-based front-end services running on the HANSEL testbed

The project requirements helped to define the main entities in which the CAPS.loc framework could be composed: a back-end service for a peer-to-peer exchange of GNSS measurements and a front-end application for the hybridization of the positioning computation. Therefore, the contribution of Politecnico di Torino was addressed to the full development of these two main entities supporting and demonstrating the feasibility of GNSS-based CP, namely CPS and CPA, respectively. Further technical details about this work will be included in the HANSEL project deliverables.

8.2 From smartphones to networked GNSS receivers

A networked GNSS receiver able to support the GNSS-based CP proposed in this thesis must have access to raw measurements and output GNSS navigation solutions as they are provided by the Google API with the GNSS measurements class. A functional scheme of networked GNSS receiver was presented in Chapter 3, in Figure 3.13. The following description relies on the real implementation of the concept in mass market smart devices.

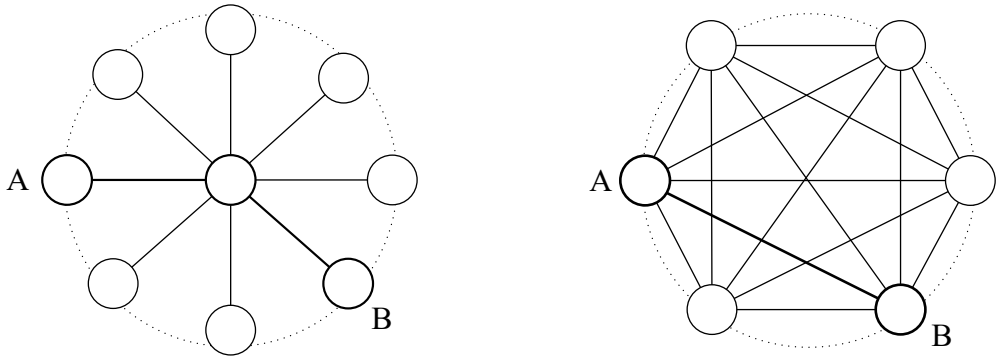

(a) (b)

Figure 8.2: Network topologies for the CP paradigm among networked receivers.

Such a framework allows to implement all the presented collaborative ranging method and provides all the needed data for further integration. The CRU can be configured to exploit the external heterogeneous measurements by compensating for their time misalignment and applying different algorithms suitable for GNSS-only ranging. The hybrid PVT processor can implement a proper hybrid navigation filter such as the one described in Chapter 6 of this thesis.

In order to provide the facilities needed for the measurements exchange, two different topologies can be chosen: a star topology, represented in Figure 8.2a, or a fully-meshed topology, as shown in Figure 8.2b. The computational power needed to maintain functional connectivity among the nodes is distributed according to the chosen topology. In the first case, the central node of the star topology has to discipline the inter-agent connectivity: it can be a central server or a super node, so an agent with extra duties. It is the only one with many interactions to manage, while agents nodes establish a unique connection towards the central node. In addition, the central node has to store all the data coming from agents nodes and distribute them according to the aiding requests. In the second case, every node has multiple connections, each one toward a different agent, but it is in charge of managing only its own data, sharing them when required. In this case, although the data management is lighter, but an exponential number of connections has to be established according to the agents participating to the service. In addition to this, a set of strategies to discover the other agents has to be designed and implemented in order to join the service. Accordingly to the evaluation of pros and cons of the different structures, a star topology has been chosen, with a plain client-server structure. A distributed framework over a general purpose network connectivity, i.e. 4G/LTE/Wi-Fi, has been exploited to create such infrastructure. This topology ensures a centralized data collection and independent and distributed PVT computation. In this way, only the computational load is demanded to the agents nodes, while the central node is in charge of managing the data distribution and the networking strategies.

The whole software receiver has been originally designed to run on the user terminals. This approach moves all the computational complexity to the receiver thus being a scalable solution in terms of positioning computation. It is indeed preferable to have a terminal-based solution instead of a server-based centralized computation in which the central node is in charge of calculating the position for all the users. Such an approach is typically exploited for snapshot positioning techniques which implement server-based assisted-GNSS strategies but is hardly scalable to a large amount of users. Furthermore, the distributed terminal based

solution better copes with the modern architectures of heterogeneous networks, with different and somewhat variable topologies, which in principles can include also ad-hoc connections such as Direct Short-Range Communication (DSRC), and local networks connecting close users (i.e. public Wi-Fi access points). The main API is anyway centralized at the server level through the available communication network, in order to report the position of the aided user and to play an active role for the continuous monitoring and assessment of the exchanged data. This architecture was particularly suitable in the context of the HANSEL testbed, being the central node relevant for data collection and monitoring purposes of the implemented technology.

In the following, further details on the designed system will be provided concerning an overview of the hardware and software architectures proposed for the definition of the HANSEL testbed.

8.2.1 Hardware selection: Xiaomi Mi 8 Pro and Braoadcom BCM47755

An advisable achievement of the design of the CAPS.loc was to identify a platforms capable of providing at the same time ultra-low cost GNSS receiver and highly-precise positioning solution with a reasonable computational power, 4G connection capabilities and access to multi-constellation and multi-frequency raw GNSS measurements. Different devices were tested in controlled and real environment [68] and an assessment of their raw measurements was pursued to identify potential candidates. Despite the best quality of the antenna integrated in the Nexus 9 (Tablet), the Xiaomi Mi 8 Pro, shown in Figure 8.3, was selected as reference device for the proof of concept of the CAPS.loc within the HANSEL project. The previous light version, Xiaomi Mi 8, was launched in May 2018 being the first dual-frequency GNSS smartphone produced by Xiaomi and equipped with a Broadcom BCM47755. The Pro version natively includes relevant firmware upgrades preserving the capability of receiving dual frequency L1/E1 and L5/E5 signals from GPS and Galileo, Beidou (B1), and GLONASS (L1).

Figure 8.3: Xiaomi™ Mi 8 Pro and Broadcom™ BCM47755 Dual-frequency GNSS chip.

The onboard Broadcom® BCM47755 location hub is a single-chip component which combines location awareness capabilities with the typical functions of a sensor hub. The combination provides synergistic benefits that cannot be achieved with multiple integrated circuits, such as low power consumption, higher accuracy, and reduced footprint [1].

According to the technical notes of the manufacturer, thanks to the support of dual-frequency and multi-constellation navigation, the chip potentially provides lane-level accuracy outdoors and higher resistance to multipath and reflected signals in urban scenarios, as well as higher interference and jamming immunity.

Furthermore, the BCM47755 incorporates numerous technologies that enable ultra-low power consumption in both the location function and the sensor hub function. The device features a low-power RF path, a Big/Little Control Processing Unit (CPU) configuration composed of an ARM-based 32-bit Cortex-M4F (CM4), an ARM-based Cortex-M0 (CM0), and is built in a 28 nm process. It natively supports for position batching, geofencing, sensor fusion and sensor navigation (dead reckoning), and the sensors list includes gyroscope, accelerometer, electronic compass and barometer which can be actively integrated to provided precise and accurate positioning solution. Xioami Mi 8 Pro turns to be a fully integrated reference receiver for the test of GNSS-based navigation algorithms, thus providing at the same time raw GNSS measurements and reference solution, as detailed afterwards.

The BCM47755 is equipped with an integrated 12-bit, 2-channel ADC which could be used in different multiplex configuration for the simultaneous acquisition and tracking of multiple satellites. The receiver is also equipped with a Real Time Clock (RTC) (42 bits, 32.768 kHz) and with two general-purpose 32-bit microsecond timers. A further 48-bit microsecond counter is also implemented for better resolution timestamps than the RTC can provide [1].

Further, details concerning the location provider foreseen by Android in the selected devices ad how the relative APIs have been used in the development are reported in Appendix D.

8.3 CAPS.loc: Framework overview

The high-level infrastructure on which the CAPS.loc is based, is a star topology which relies on a center node (e.g. remote server) implementing the CPS. The CPS is at the same time a private temporary repository of raw GNSS measurements and a virtual agent-to-agent channel established between registered applications (CPA) as shown in Figure 8.4.

- the **CPS** provides registration and authentication facilities to the agents through the methods of an API and it foresees a database, named `db`, for the buffering of raw measurements posted by the registered users. It exposes available and timely raw measurements coming from the potential aiding agents.
- the **CPA** constitutes the engine for the collaborative PVT computation. The CAPS.loc paradigm is indeed centralized for the exchange of the measurements but is distributed at logical level for the positioning computation. CPA provides the interface for posting and getting measurements (upload and download via User Datagram Protocol (UDP) services. Furthermore, it foresees a fully-customizable PVT algorithm which integrates collaborative baseline length contributions (if available) from registered aiding agents according to hybridization schemes provided in Chapter 6.

8.3.1 Collaborative Positioning Service

The main components of the CPS are

- the **db**, which will store raw measurements, coarse position estimates and a set of useful data provided by the agents registered to the CPS. It also includes records about the registered agents and their interactions.

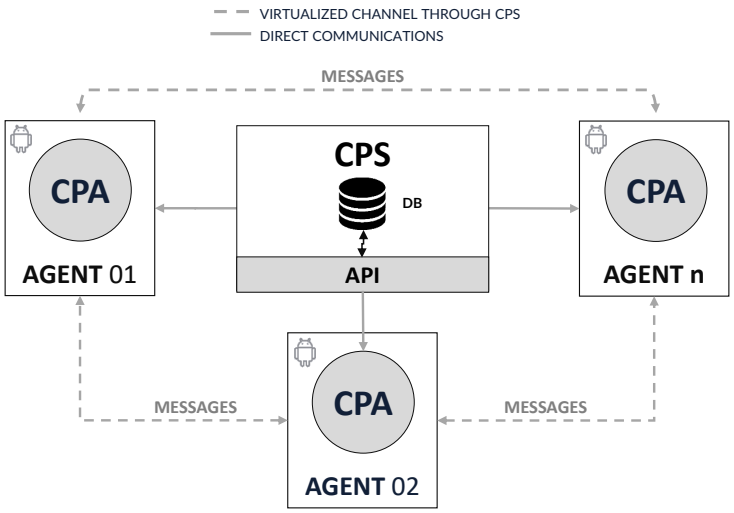

Figure 8.4: High-level configuration of the scalable CAPS.loc client-server topology (exploited in the real implementation.

- the **API**, which provides the interface towards the CPA (Android Application at the agent level) and allows the exchange of information among the registered agents.

Raw Measurements Database (db)

The `db` is intended as a dynamic, centralized data buffer oriented to a low-latency exchange of measurements and navigation data through the network infrastructure. A MongoDB database was implemented following a document data model paradigm [132]. The data are stored in collections of files which are dynamically allocated whenever an agent performs the registration to the CPS, and whenever it shares new measurements through the service. Such a document-oriented paradigm, foresees the storage of data in JSON-like documents, which is the most suitable solution according to the data the CPS has to deal with. When a new document is stored, an index is automatically generated by MongoDB as a unique identifier, referenced as _id. In each collection the data indexes are used as keys for manipulating data with the CPS APIs. The agents collection stores the data of devices subscribed to service.

Agents documents have format described Table C.2 and Table C.1 in Appendix C. When a new agent subscribes to the CPS, a new entry is created and continuously updated by the CPA running on mobile devices.

The DB structure is based on three non-relational collections of files named `agents`, `raw_id`, `db_config` and it is worth to mention that the paradigm does not support relationships among the collections.

All the data of interest for localization such as *raw measurements*, *coarse position estimates*, *time references* and *cooperative parameters* provided by the agents are stored in a instance of MongoDB database running on the server.

The collection `agents` includes a set of files (one per each agent) which are continuously updated with new incoming data. These files are accessible through the CPS API and they can be visualized in the Graphic User Interface (GUI) of the HANSEL testbed. For each agent in the collection, a measurement collection, `raw_id`, is dynamically allocated and linked to the agent through the field `agent_id`. The collection `db_config` hosts a set of configuration parameters for the maintenance of the `db` that can be extended if necessary.

The following tables summarize the structure of the files hosted in the DB, along with a brief description of each field. All the files are formatted in JSON[3] according to the project requirements.

Cooperative Positioning System API

As shown in Figure 8.4, the CPS API is conceived as a unique entry point of the CAPS.loc framework for the mobile agent. It is implemented through a Python script and it exploits the following actions:

- **Agent registration**: It is provided by the interaction between CPS and CPA instances running on the Android smartphones and registered users list can be monitored runtime according to the methods in Table 8.3.

API	Description
`subscribe_agent`	Creates a new entry in the file `agents` and initializes the `db` data structures for each new entry.
`unsubscribe_agent`	Removes a specific registered agents from the file `agents` and deletes all the related data from the DB.
`unsubscribe_all_agents`	Removes all the registered agents from the file `agents` and deletes all the related data structures from the DB.
`agents_id`	Returns a list of identifiers of all the registered agents

Table 8.3: Agent registration API methods.

- **Raw measurements download and monitoring**: UDP sockets are provided by the CPS to manage the upstream and downstream of data among the agents. Such data are encapsulated in UDP messages called Cooperative Raw Message (CRM) which can be downloaded from the CPS to perform CP, according to the methods in Table 8.4.

API	Description
`agent_fix`	returns a set of GNSS data related to the last available fix of a specified agent, according to the Table C.2.
`agent_measurements`	returns a set of GNSS raw measurements related to the last available epochs for the specified agent, according to the Table C.1.

Table 8.4: Raw measurement API methods.

- **Housekeeping of the database content**: The CPS provides a storage-efficient housekeeping routine in order to delete all the outdated raw measurements collections. Through the methods listed in Table 8.5 allow to define a refresh time for the deletion of outdated records (`db_upkeep`) and to download all the records stored in DB for further analysis and post-processing (`all_db`).
- **Remote agent configuration**: CPS can force agents configuration by restricting the measurements availability through the method in Table 8.6.

[3]https://www.json.org/json-en.html

API	Description
`db_upkeep`	allows to refresh the measurements files to ensure updated measurements to the agents.
`all_db`	downloads all the documents stored in the `db` in a single file.

Table 8.5: DB housekeeping API methods.

API	Description
`agents_visibility`	sets which satellites and aiding agents are used for the PVT/**HPVT!** computation.

Table 8.6: Agent configuration API methods.

- **Data reports and visualization**: The API provides callbacks to retrieve update navigation data from the collaborative agents for the visualization on the GUI of the testbed.

For security reasons, all the API methods can be used only with a proper API key. A detailed description and output samples of the methods included in the CPS API v1.0 developed for the HANSEL project are described in Appendix C.

8.3.2 Collaborative Positioning Application - CPA

The CPA is a mobile application developed for Android™ which is mainly in charge of implementing the EKF-based tight integration of collaborative measurements. It allows an agents running it locally to interact with other agents through the CPS. Multiple instances of the CPA (installed in a set of smartphones) are expected to interact through the CPS by means of the API described so far in order to take advantage on the CAPS.loc. The application has been developed in Java by using the Android Studio environment. The CPA requires at least API level 27 (Android 8) to provide full support to the public class `GNSSMeasurements`. In the following, the actions and interactions between CPA and CPS are described in detail along with technical aspects implemented during the development.

The CPA is a multi-thread application which foresees a main script managing a set of sub-threads running in parallel. They can be seen as microservices producing and consuming local and external measurements. Beside this, a set of other components among which the GUI provides general services for such a demonstrator. In Figure 8.5 the overall scheme of the CPA is provided.

According to the functional scheme presented in Figure 8.5, the following subsections briefly describe each component in detail.

Main activity

Such a block is the entry point of the CPA and is in charge of managing the GUI and the lifecycle of the whole application. It runs specific threads according to the incoming commands from the users.

Agent Subscriber

The registration to the CPS is a prerogative to join the collaborative framework. The subscription of each agent is made through the method `subscribe_agent`, but it is mostly

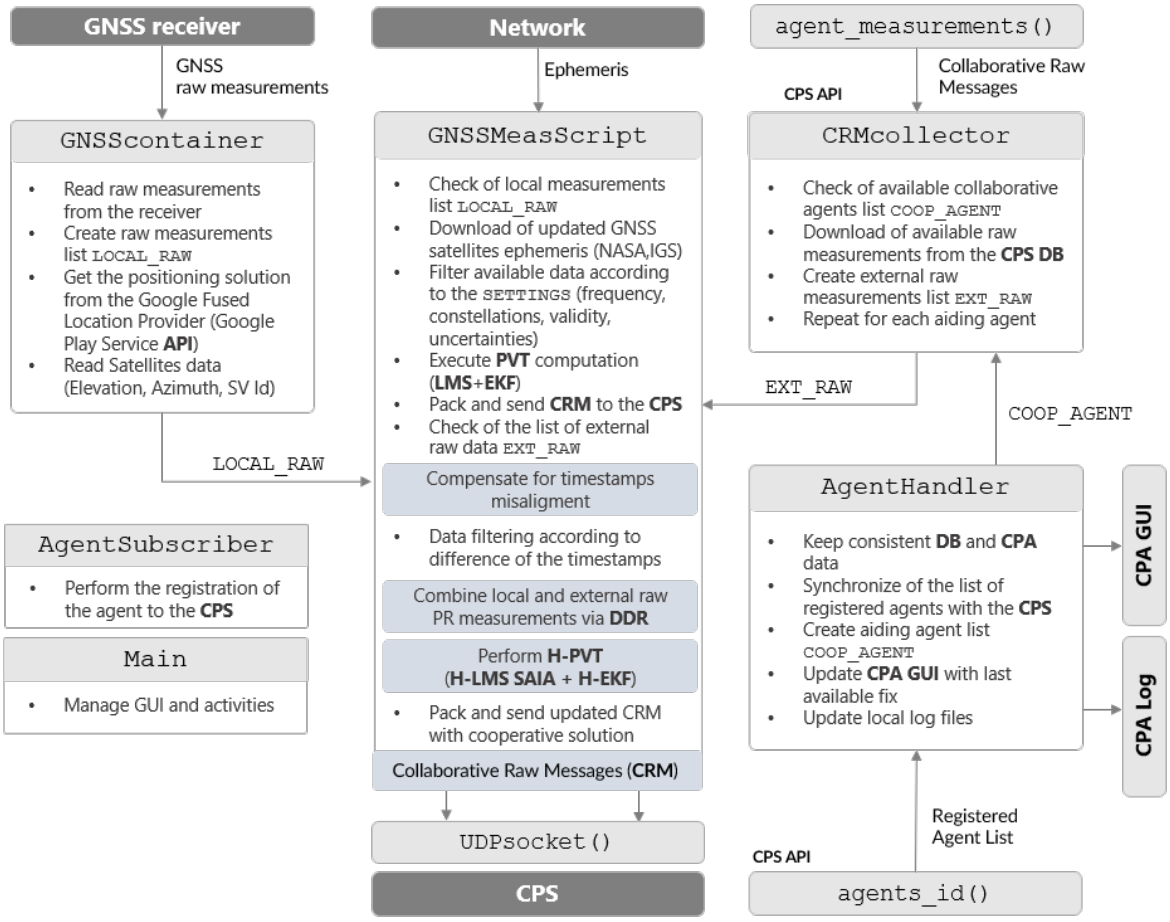

Figure 8.5: Full CPA functional scheme showing all the threads and the communication processes among them.

handled by the CPA in order to reduce the workload of the CPS in case of a high number of concurrent requests. In Figure 8.6, the flow chart of the registration process is presented.

First, the CPA `AgentSubscriber` retrieves the list of already registered agents, `COOP_AGENT`. By scanning the list, the agent finds the first available agent `id` which will be the smaller integer not yet assigned (starting from 1). To reduce the probability that the same id is chosen by other agents, the `AgentSubscriber` waits for 2 seconds before retrieving again the list of subscribed agents: if the chosen id is still unused, it will register as a new agent using that `id`, otherwise, it will select a new id, sleep for 2s and check again the actual availability of the new id.

Once the subscription is done, the four main parallel thread are started by the CPA in order to allow to the new agent to provide and get raw measurements: the `GNSSContainer`, the `CRMcollector`, the `AgentHandler` and the `GNSSMeasScript`. In addition, a UDP datagram socket is opened for sending and receiving UDP CRM through the network. The registered Android agents are hence able to share raw measurements and navigation data being both aiding or aided agents at the need.

GNSS Container

The `GNSScontainer` is a data generator. This thread is in charge of reading raw measurements from the on-board GNSS-receiver through the Android GNSS raw measurements API. It manages the creation of a list named `LOCAL_RAW` including raw pseudorange and

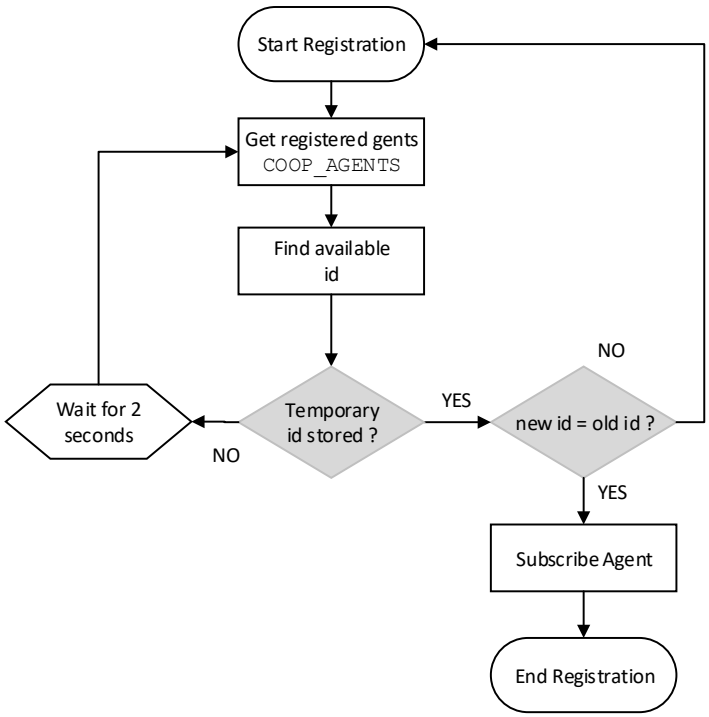

Figure 8.6: Agent registration process as it is forseen for the CPA/CPS interaction.

Doppler measurements obtained at the current epoch. Visible and trackable satellites are also identified as well as their relative position (azimuth, elevation) w.r.t. to the agent location. All the data along with their unique identifiers (i.e. IGS standard) are also logged to know current visibility conditions through the callback `android.location.GnssStatus`. In parallel, it collects the last available fix through the Google Fused Location provider to be used as a ground-truth for the GNSS-only positioning solutions. The list `LOCAL_RAW` is eventually sent to `GNSSMeasScript` to be processed within the PVT algorithm.

Agent Handler

The `AgentHandler` thread is in charge of keeping coherent and updated the information between CPA and the `db`. It is the only thread interacting with the CPS API during the operational life of the service. This implementation ensures a strong independence among the components aiming at guaranteeing an effortless portability of the framework.

As first, through the method `agents_id` it downloads the list of all the potential aiding agents. It is worthy to remark that this list changes dynamically according to new subscriptions or unsubscriptions. Then, through the method `agent_fix` it downloads information about the current agents, in order to verify potential set of shared satellites to be combined in collaborative inter-agent distances. A list containing the identifiers of all the available agents, `COOP_AGENT`, is created and sent to the `CRMcollector`. Furthermore, if the flag `all` mentioned in Table C.2 is equal to false, an override of the satellite visibility has been applied, thus the subsequent PVT solution will be computed exploiting only the specified satellites. Otherwise, all the visible satellites can be used. After this operation it uses the method `agent_visibility` to update the agent entry on the database in order to keep coherent the information about number of visible satellites, last available fix and its current status. The `status` of the agent will be *active* (true) when the service is running properly, *inactive*

(false) if it is not able to obtain a fix or if the CPA is running in background. All the HTTPS requests are started as asynchronous tasks, in order to not freeze the thread if internet connection is slow or temporally absent. As shown in Figure 8.5, the `agent_handler` thread is also in charge of updating the information exposed on the GUI and to collect a log file for data collection purposes. Once the task is accomplished, it sleeps for 1s and then it wakes up again.

As mentioned so far, the agents have access to the data shared by the other agents trough the CPS by registering to the CAPS.loc service. The registration queries in the API manages the token-based authentication of the mobile users by providing them a unique authentication token for further queries along with the registration confirmation.

CRMcollector

If the `GNSScontainer` can be seen as the interface between the CPA and the GNSS receiver, the `CRMcollector` constitutes the interface between the CPA and the network of aiding agents. Indeed, it receives the updated list of potential aiding agents, `COOP_AGENT` from the `AgentHandler` and is in charge of retrieving the available raw measurements stored in the db by invoking the method `agent_measurements`. The download of such data is performed through the aforementioned UDP socket. The early version of the CPA foresees a serial `CRMcollector` which sequentially creates a list of raw measurements and GNSS standalone fixes from each aiding agent, named `EXT_RAW`. The list `EXT_RAW` is then sent to the `GNSSMeasScript` to perform the collaborative task.

GNSSMeasScript

The collaborative approach relies on a two-steps refinement of the positioning solution obtained though GNSS. Agents which experience high variance in their positioning solutions can retrieve available raw data to improve their navigation performance relying on agents with good navigation performance. Despite the availability of raw measurements contained in `EXT_RAW`, each agent can process local raw measurements included in `LOCAL_RAW` to perform its own GNSS standalone positioning solution.

1. **Coarse Position-Time Solution**: this step is performed to get a coarse positioning solution which will be used as reference location for the next integration steps. Despite the estimated clock bias allows to retrieve an accurate time-stamp of the raw data, the current version of the CPA directly exploits the timestamps provided by the raw measurements API. The timestamps provided by the GNSS receivers are used to label each set of raw measurements and related fix included in the CRM with the field `epoch`, according to Table C.1.

2. **Compensation of time-misalignment of local and downloaded measurements**: This step exploits the local raw Doppler shift measurements provided by the Android API, to compensate for the time misalignment among the measurements in `LOCAL_RAW` and the ones included in `EXT_RAW`.

3. **Computation of collaborative range contribution**: Compensated measurements are combined through DD to determine the inter-agent distances among the target agent and the aiding ones.

4. **Hybridized tight integration for Position-Time-Velocity refinement**: The raw measurements obtained from the `GNSScontainer` are processed to compute a GNSS standalone positioning solution, referred to as *coarse PVT*. Such a solution can be

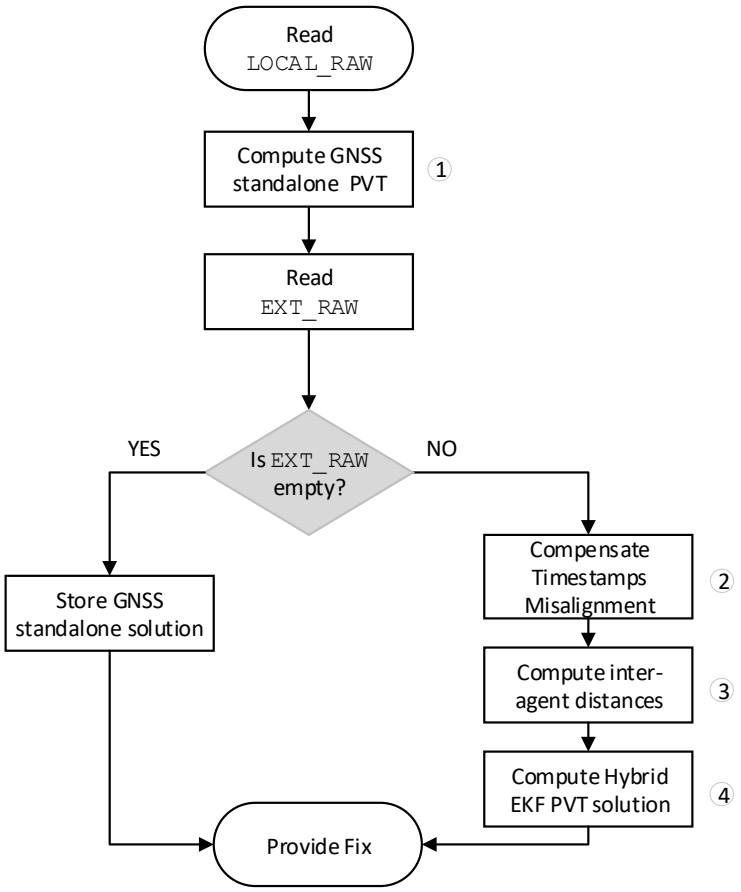

Figure 8.7: Hybrid positioning flow chart.

computed both through a H-WLMS or through a H-EKF. Both the navigation filters are intended to hybridize local GNSS pseudoranges (`LOCAL_RAW`) and inter-agent distances to obtain a collaborative positioning solution as discussed in 6. An initial H-WLMS/WLS solution is mandatory for the initialization of the main navigation filter and it is forced every N fixes to avoid unexpected drifting phenomena due unmodelled threats. For the same reason H-EKF/EKF can be disabled when it is not suitable for the positioning computation in order to reduce fix correlation along the time (i.e. static scenario).

The functional blocks 2,3 and 4 are highlighted in the scheme of Figure 8.4 since they can be easily replaced with improved algorithms to accomplish each specific task. As discussed in Chapter 4 indeed, different theoretical solutions can be used to determine inter-agent distances. According to the different ranging methods, a proper solution for the compensation of the epochs misalignment must be defined, as well. The same can be though for what concerns the hybrid PVT solution which can rely on a wide choice of navigation filters such as the ones discussed in Chapter 6.

Graphic User Interface and Settings

As a technology demonstrator the CPA provides a simple GUI which addresses mostly simulation and test needs. The structure of the GUI is shown in Figure 8.8, in which the

same elements are also labelled in the list on the left. The GUI has been designed to collect both GNSS standalone and GNSS-collaborative fixes represented by the dark gray and green dots respectively. The small play button on the upper right corner of the GUI (H) allows to actively subscribe/unsuscribe to the service while the configuration button (G) opens a pop-up panel in Figure 8.9 to configure a set of parameters for the computation of the hybrid solution (Number of satellites, number of aiding agents, weight of the EKF measurements covariance matrix, navigation filter, variance estimation method for inter-agent distances).

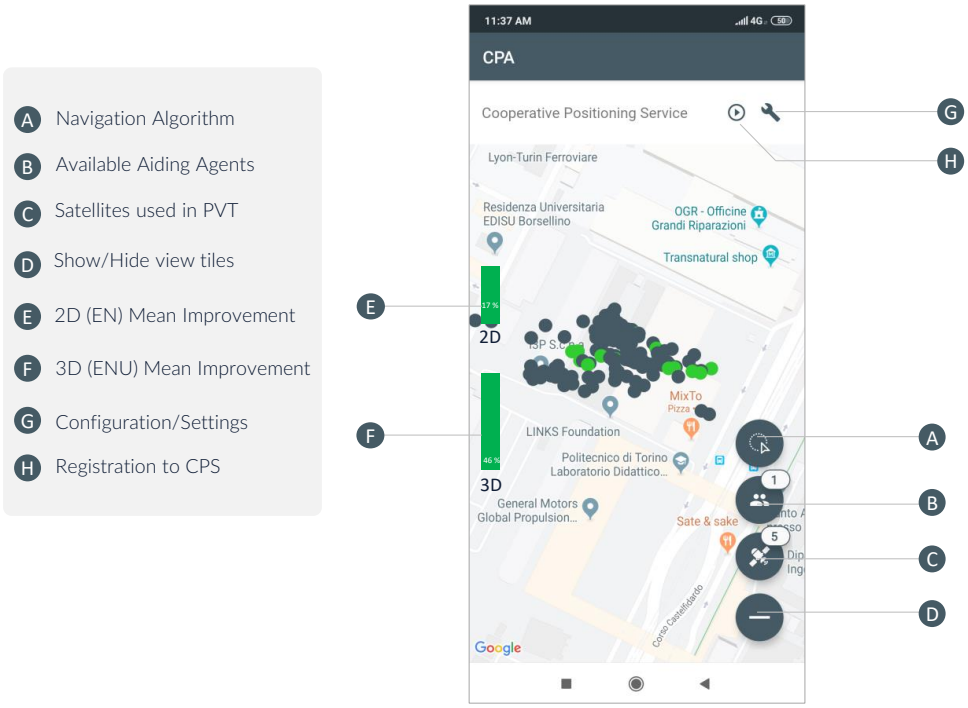

Figure 8.8: Screenshots of the CPA developed within the HANSEL project.

The two dynamic bars on the left of the screen (E,F) show the instantaneous improvement provided by CP w.r.t. to the GNSS standalone solution. The improvement is measured as the error reduction w.r.t. the Google Fused Location Provider. The series of tiles that can be shown acting on the plus/minus button (D) allows to verify the number of satellites (C) and aiding agents (B) used in the computation as well as the navigation filter used for the computation (A), in real-time. They can be modified through the configuration/settings both locally and remotely through the CPS API. The parameters which can be tuned are divided in categories and listed according to following:

- *GNSS settings*
  - Constellation type used in PVT (e.g. GPS, Galileo, Beidou, GLONASS)
  - Signal frequency for the selected constellations (e.g. GPS, Galileo, Beidou, GLONASS)
  - Maximum number of satellites used in PVT
- *EKF settings*

  - Activate/Deactivate H-EKF for the PVT computation
  - Additional weighting to reduce the influence of measurements
  - Maximum number of satellites used in PVT

- *Cooperative Settings*
  - Weighting strategies for the collaborative contributions (e.g. trace of the covariance of the displacement vector)

- *Ephemeris Configuration*
  - Ephemeris cache cleaner

The tunable parameters can be updated runtime while the CPA is running though the configuration panel shown in Figure 8.9. This is helpful to identify peculiar behaviours in the quality of the positioning when for example reduced satellite visibility cannot be achieved in real environment.

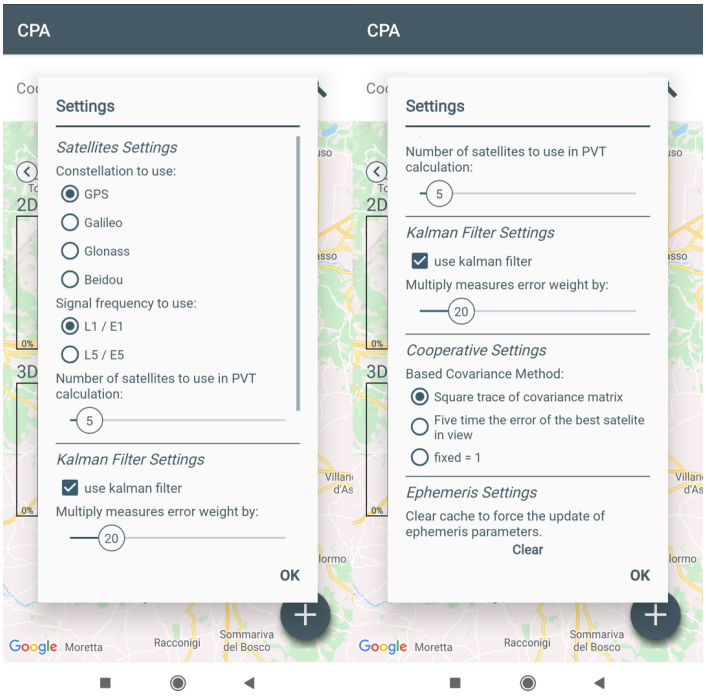

Figure 8.9: Screenshots of the CPA configuration panel.

After the presentation of the CAPS.loc framework in Chapter 8, its feasibility and effectiveness are discussed in this chapter through the analysis of preliminary experimental results. For the sake of conciceness, low-level details about raw measurements quality investigation (C/N_0, multipath detection, etc.) are omitted to better focus on the investigation of positioning solution at the application layer. Therefore, the chapter includes two main investigations: a preliminary discussion is provided in Section 8.4 concerning the off-line combination of smartphones raw pseudorange measurements, as presented in [67] to experimentally assess the feasibility of the proposed collaborative ranging approach. A further analysis, presented in Section 8.5, collects a set of on-field experiments performed through the CAPS.loc framework. The CAPS.loc has been conceived for urban applications, therefore the most of the tests reported afterwards addresses urban and mild-urban environment for pedestrian and vehicular use cases. In order to clarify to the reader the features of each

experiment and of the different investigated scenarios, a classification based on the dynamics of the agents is detailed in Section 8.5.3. In Section 8.5.2 the performance metrics are formalized to provide quantitative results about the feasibility of the approach, its availability and the accuracy of the cooperative solution when CP was available and profitable. Four significant experiments are analysed in detail in Section 8.6. Within the same section, the performance metrics of the overall test campaign are summarized and commented to provide a general picture of the technology. This preliminary test campaign was oriented to the feasibility assessment and an overall understanding of the real potential of the CAPS.loc framework, but a set of optimization strategies is left to the further works (future releases of the framework) and they are reported in the final remarks, in Section 8.7.

8.4 Offline asynchronous measurements combination

By relying on the log of the raw measurements observed by two devices we first tested an off-line combination according to the weighted DD ranging method introduced in Chapter 4. Instead of using a remote server for the exchange of raw measurements as implemented in the CAPS.loc, a single-hop Wi-Fi 802.11g connection was establish among the device through a Android-based Robot Operating System (ROS) framework [160]. By means of this approach, the network contributions in terms of additional communication delay due to further hops is totally avoided. However, the measurements epochs were still asynchronous due to the independent processing of the devices.

As presented in Chapter 4, pseudorange rate or equivalently Doppler shift measurements was used to compensate for asynchronous measurements epochs. Therefore, an effective implementation of this method depends on the goodness of the timestamps which are attributed to the sets of data by the devices. The accuracy of the timestamps are indeed related to the stability of their internal clocks. The analysis provided in the following has been published in the proceedings of VTC Fall 2019 (Honolulu, USA) within the workshop "Reliable Ubiquitous Navigation in Smart Cities". The conference contribution [67] is recalled as an introductory analysis to justify the implementation details of the CAPS.loc framework and the results which will be presented in the next sections of this chapter.

8.4.1 Baseline length estimation through Android GNSS raw measurements

By dealing with real low-quality code pseudorange measurements from Android smartphones, the implementation of DD ranging provided the best solution to cope with correlated errors in the measurements sets, at least considering two devices in close proximity.

In the following, the results of two basic off-line tests are presented to support the implementation of GNSS differential ranging in the PoC.

Static non-zero-baseline test

A 10-minute static datasets were collected in the Campus of the Politecnico Di Torino (approximately 45.062099° N, 7.663334° E), Torino, Italy, with two Xiaomi Mi 8 devices located with a separation of 20 m, on the 22nd of February 2019 in a sub-urban environment with moderate sk visibility. Android raw measurements were collected through a IEEE 802.11x Wi-Fi connection and processed through an internal version of the open source MATLAB `gps-measurement-tools` software [94]. The Xiaomi Mi 8 offers the option to turn off the *duty cycle* of the device through its developer mode and that was an added consideration during the data collection. Duty cycle is a power saving function of most smart devices where commonly, the hardware clock is switched off for a fraction of every second resulting mainly

in carrier phase tracking discontinuity [74]. Although multi-frequency, multi-constellation measurements were recorded, only GPS L1 signal measurements were processed for initial validation. The use of GPS only does not imply a lack of generality since the same procedure can be applied to the other constellations or different multi-constellation solution can be developed for an improved baseline estimation. Furthermore, multi-constellation implementation is also possible once the user clock bias with respect to each constellation has been removed (i.e. a solution has been obtained).

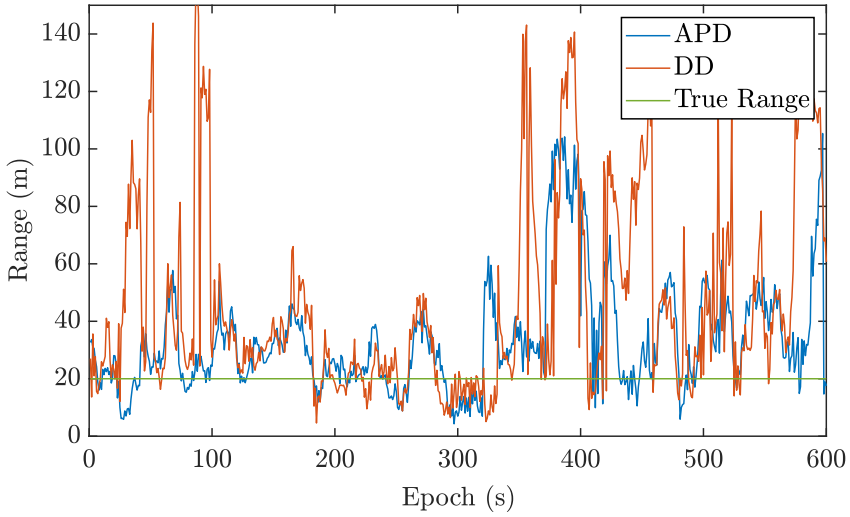

Figure 8.10: 20 m baseline test with DD and APD comparison. GDOP= 2.0 .

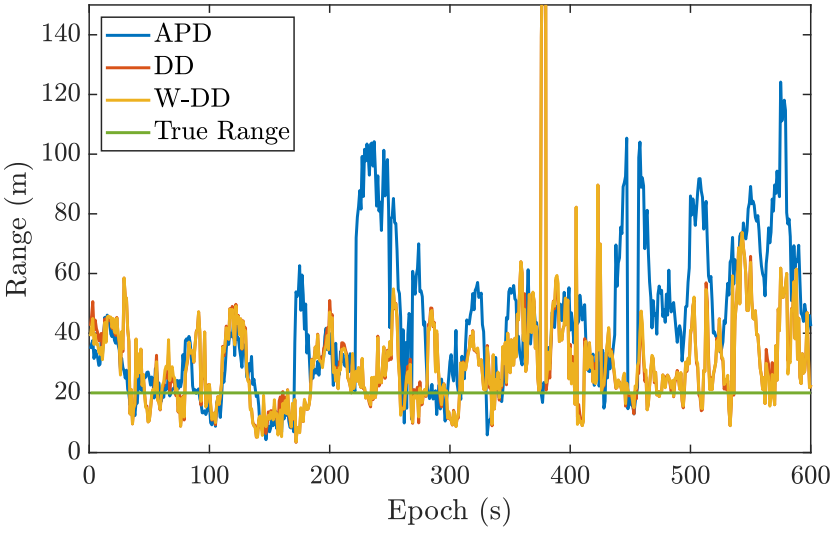

Figure 8.11: 20 m baseline test with DD, W-DD and APD comparison. GDOP= 2.5, increased by filtering bad measurements.

The unreliable quality of smartphone raw measurements is a hindrance due to poor antenna performance, hence a runtime satellite filtering strategy as well as a weighted solution was adapted based on the parameter `ReceivedSvTimeUncertaintyNanos` [69]. Three different ranging strategies between the devices were compared; DD and Weighted Double

Difference (W-DD) (both Doppler compensated) and the Euclidean Range (PVT-R) calculated after standalone-PVT solution computation of the receivers individually. For the standalone solution, some satellites were excluded for a fair comparison with the filtering strategy.

Figure 8.10 shows the basic comparison of the ranges without taking into consideration the quality of the pseudoranges and it is seen that both the ranges are noisy with the PVT-R being slightly better. On filtering out poor measurements,a significant improvement to the DDR and W-DD ranges is seen in Figure 8.11 and it is on average better than the simplistic PVT-range, barring a few outliers which the weighted solution fails to take account of. The mean GDOP value was around 2 and 2.5 before and after filtering respectively. This observation is consistent with the other dataset measurements and in dataset 3 (5-minute observation), the improvement in the mean error is 4-5 times higher. Table 8.7 presents a comparison of the quality of the GNSS-based ranges in the different datasets with respect to the standard deviation, σ, and mean error, μ). There is still a significant bias and noise present in the measurements due to the uncorrelated noise being quadrupled after double differencing, as shown in [36], but this relatively superior range output produced taking advantage of Android raw measurements only without the PVT computational burden confirms the potential of cooperation among Android smartphones.

		APD	**DD**	**W-DD**
Dataset 1	σ (m)	19.4	12.2	12.1
	μ (m)	10.5	9.9	7.6
Dataset 2	σ (m)	9.5	8.7	8.6
	μ (m)	8.4	5.4	5.4
Dataset 3	σ (m)	18.2	10.4	10.2
	μ (m)	24.7	6.3	5.8

Table 8.7: Test with two Comparison of the quality of time-compensated GNSS-based ranges with different optimizations.

8.5 Real-time CAPS.loc experiments

This section describes the methodology and the metrics used during the preliminary test campaign of the CAPS.loc framework developed within the HANSEL project. An high-level functional scheme of the system is reported in Figure 8.12.

Differently from the off-line analysis presented in Section 8.4, in this case all the tasks were executed runtime according to the setup described hereafter in Section 8.5.1.

8.5.1 Setup

All the tests were performed addressing different static and dynamic scenarios to verify and assess feasibility and effectiveness of CP through the interaction of two Xiaomi Mi 8 Pro running independent instances of the CPA. GNSS capabilities of both the smartphones were limited to single constellation (GPS) and single frequency (L1) positioning computation by further limiting the number of visible satellites to emulate poor sky visibility, if necessary. The devices were handled by two operators walking or driving vehicles according to the designed test scenarios. The multiplicative weight described in Chapter 8 was used as a

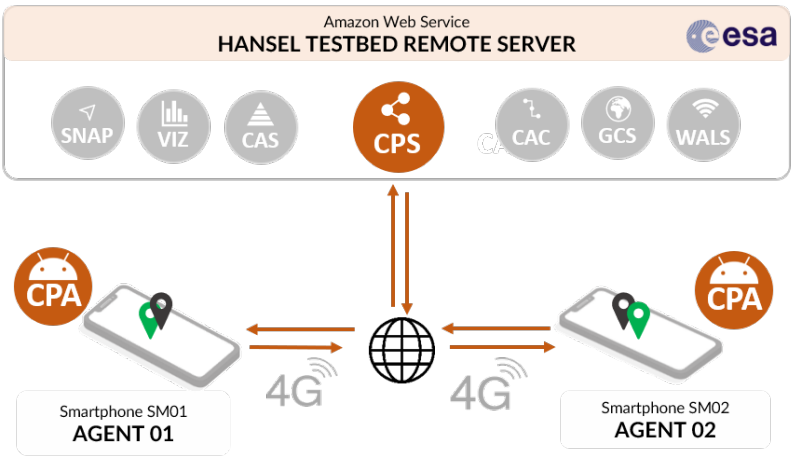

Figure 8.12: Experiment setup exploiting 4G connectivity and CPS on a remote server (Amazon Web Service located in Ireland).

EKF design parameter to reduce the impact of the GNSS measurements in the position estimation algorithm for both collaborative and standalone solutions.

This preliminary testing phase addressed the peer-to-peer cooperation with ultra-short, short and moderate baseline conditions. Being independently from the behaviour of the other agent, both the smartphones tried to improve their accuracy by exploiting GNSS raw measurements and coarse fixes shared by the others, thus acting simultaneously as aiding and aided agents.

The two smartphones, referred hereafter as agent `SM01` and agent `SM02`, were indeed configured in order to continuously exchange GNSS data by exploiting 4G data connectivity and a general-purpose remote server hosting the CPS. Each device was hence able to compute collaborative inter-agent measurements independently by combining external and local pseudorange measurements independently. Such an operational mode was helpful to observe both benefits and disadvantages of the proposed integration by identifying timespans in which CP was actually effective and other timespans in which it induced degradation of the positioning solution. Given that such a *peer-to-peer continuous mode* could degrade the positioning performance, such a solution turned to be fundamental to the understanding of the paradigm although it must be considered not meaningful for a real deployment of such a technology. Indeed, it is trivial to inhibit CP when a-priori conditions suggest a potentially degraded performance.

Similar or different paths were travelled by the operators holding the devices as shown in the example of Figure 8.13 and different effects were hence observed for each smartphone.

All the positioning data were sent to the CPS and logged locally in form of ECEF and LLA positioning solution. Both cooperative and standalone solutions were then compared to the reference location foreseen by the Google Fused Location Provider, according to the metric defined in 8.5.2.

8.5.2 Performance metrics

A set of performance metrics are defined hereafter to evaluate the benefits of GNSS-based CP within the on-field tests of the CAPS.loc framework.

- **CPS availability**, $\mathcal{A}_{\text{CP}}$: It measures the availability of the cooperative service for a given agent by assessing the possibility of computing a hybrid positioning solution. It is an indirect indicator of the of the network status and the overall availability of

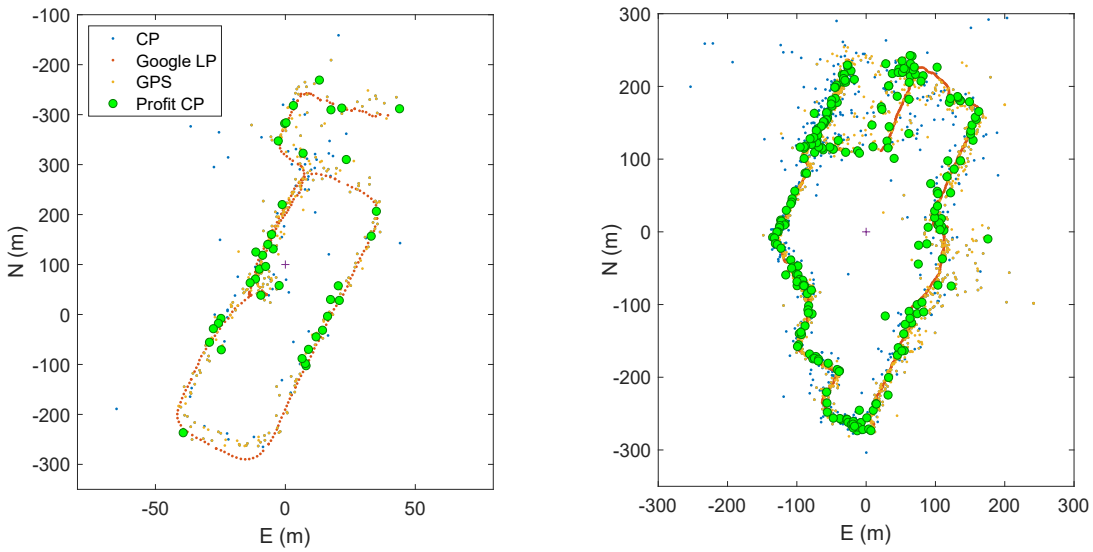

(a) Agent 1 (SM01)

(b) Agent 2 (SM02)

Figure 8.13: Example of pedestrian urban paths with different profitability of the paradigm (greed dots indicate profitable integration). The cross marker indicates the origin of the local EN frame (Up direction is omitted for readability).

raw measurements provided by registered aiding agents. It formally counts the ratio between the number of CP fixes, N_{CP}, and the overall number of available GNSS standalone fixes, N_{SA}

$$\mathcal{A}_{\mathrm{CP}} = \frac{N_{\mathrm{CP}}}{N_{\mathrm{SA}}} 100. \tag{8.1}$$

Even considering a full availability of the service, $\mathcal{A}_{\mathrm{CP}} = 100$, as known from the theoretical analysis presented in Chapter 7, GNSS-based CP could be profitable or unprofitable according to the quality of the collaborative measurements and to the combined relative geometry of visible satellites and aiding agents. To asses the advantages of the proposed technique, the following key metrics have been defined to quantify the accuracy of the positioning solutions.

Statistically speaking, RMS error is typically used to evaluate the positioning error but in real experiments we deal with one positioning sample per each epoch, t_k. Therefore, the positioning error can be evaluated as the Euclidean distance of the estimated position from the ground truth in 3-D

$$\xi_{\text{3-D}}(t_k) = \sqrt{(\Delta E^2(t_k) + \Delta N^2(t_k) + \Delta U^2(t_k))} \tag{8.2}$$

and in 2-D

$$\xi_{\text{2-D}}(t_k) = \sqrt{(\Delta E^2(t_k) + \Delta N^2(t_k))} \tag{8.3}$$

where the squared terms in (8.3) and (8.2) are the difference of each component in a East-North-Up (ENU) reference frame [193, 131]. It is helpful to recall that ENU coordinates are obtained from linear transformation of ECEF coordinates (refer to Appendix A for details on reference frames) so that (8.2) can be equivalently computed in ECEF. The ground truth is provided in this case by the Google Fused Location Provider according to its higher

accuracy due to inertial sensors integration. For the sake of simplicity, the errors will be always referred to as ξ_{SA} and ξ_{CP} for standalone and CP solutions, respectively. Separate metrics for 3-D and 2-D will be then clearly distinguished in tables and figures reported in Section 8.6.

- **CP profitability** (2-D,3-D), $\mathcal{P}_{\mathrm{CP}}(\%)$: It indicates the percentage of CP fixes in which CP error is lower than standalone positioning error (i.e. GPS-only), formally

$$\mathcal{P}_{\mathrm{CP}}(\%) = \frac{\sum_{k=1}^{k=N_{\mathrm{CP}}} p(t_k)}{N_{\mathrm{CP}}} \tag{8.4}$$

  where $p(t_k)$ assumes boolean values according to the following conditions

$$\begin{cases} p(t_k) = 0 & \xi_{\mathrm{SA}}(t_k) - \xi_{\mathrm{CP}}(t_k) < 0 - T_H \\ p(t_k) = 1 & \xi_{\mathrm{SA}}(t_k) - \xi_{\mathrm{CP}}(t_k) > 0 + T_H \end{cases}$$

  where T_H is a threshold used to perform a conservative classification of profitable/unprofitable epochs. A further conditions defined according to T_H and named *hysteresis*, identifies a region of non-significant improvement/worsening in accuracy, as shown in Figure 8.14.

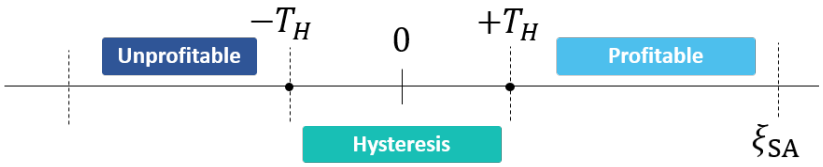

Figure 8.14: Classification of profitability according to the hysteresis threshold T_H.

- **CP hysteresis**, $\mathcal{H}_{\mathrm{CP}}(\%)$: It counts all the epochs t_k in which $|\xi_{\mathrm{SA}}(t_k) - \xi_{\mathrm{CP}}(t_k)| < T_H$, as depicted in 8.14.

  Profitability and *hysteresis* of an experiment can be seen through the pie charts of Figure 8.15 which provide a direct view of the benefits of the CP for each device and for the whole duration of the experiments. As shown in this experimental example, the remaining percentage identifies the unprofitable amount of epochs which reveals degrading effects of the CP over the positioning computation. Nevertheless, it is worth remarking that this percentage highlights epochs in which CP does not guarantee benefits and it must be inhibited.

- **Mean CP error** (2-D,3-D), $\mathcal{E}_{\mathrm{CP}}(\mathrm{m})$: It computes the mean positioning error of CP w.r.t. Google Fusion Location Provider over the time epochs in which CP is profitable

$$\mathcal{E}_{\mathrm{CP}} = \frac{1}{W} \sum_{k=1}^{W} \xi(t_k) \tag{8.5}$$

  where $W = \sum p(t_k)$ counts the overall amount of profitable epochs, formally $\forall k | p(t_k) = 1$.

- **Mean SA positioning error**(2-D,3-D), $\mathcal{E}_{\mathrm{SA}}$ (m): It is equivalent to $\mathcal{E}_{\mathrm{CP}}$ evaluated for the GNSS standalone solution

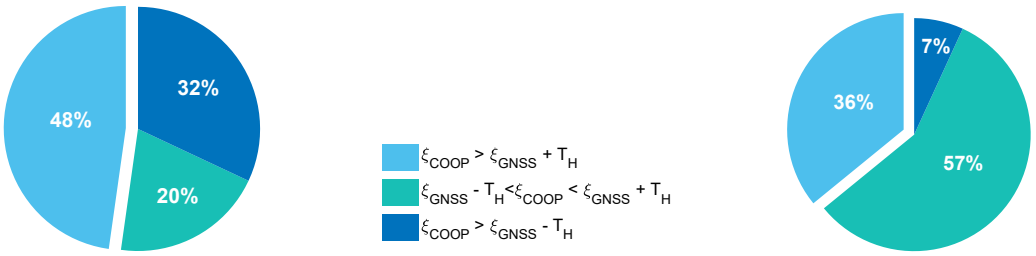

(a) Agent 1 (SM01) (b) Agent 2 (SM02)

Figure 8.15: Example of pie charts showing CP profitability/unprofitability for two different smartphones.

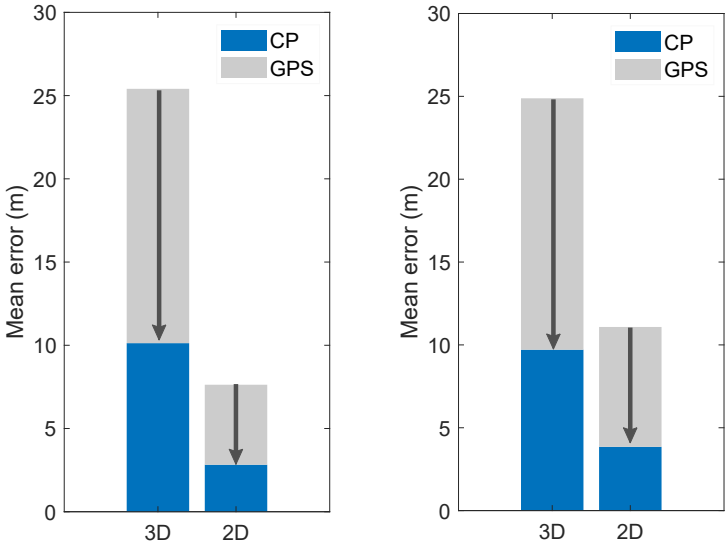

(a) Agent 1 (SM01) (b) Agent 2 (SM02)

Figure 8.16: Example of barplot showing superimposed (3-D and 2-D) of the positioning solution for profitable CP and GNSS-only (GPS) PVT for dataset `0210219-01`.

In Figure 8.16 we can observe a sample comparison of $\mathcal{E}_{\text{SA}}$ and $\mathcal{E}_{\text{CP}}$ in which the advantage of CP is highlighted by the dark arrows showing the mean error reduction occurring during profitable epochs.

- **CP accuracy mean improvement** (2-D,3-D), $\mathcal{I}_{\text{CP}}$: It provides the percentage of the improvement in accuracy guaranteed epoch-by-epoch by the CP when the cooperation is profitable. It can be also seen as GNSS-relative error reduction, formally

$$\mathcal{I}_{\text{CP}}(\%) = \frac{1}{W}\sum_{j=1}^{W} 1 - \frac{\xi_{CP}(t_j)}{\xi_{SA}(t_j)} \tag{8.6}$$

$\mathcal{I}_{\text{CP}}$ immediately provides an indicator of the accuracy improvement of the hybrid solution w.r.t. the GNSS-only fix. When $\mathcal{I}_{\text{CP}} \simeq 100\%$, the hybrid solution shows an appreciable match with the fix provided by the Google Fused Location Provider, while when $\mathcal{I}$ approaches 0, the hybrid fix fairly matches with the GNSS-only solution.

All the accuracy metrics in (8.6),(8.5) and (8.4) can be computed for 2-D and 3-D by replacing the equivalent errors (8.3) and (8.2), in the respective equations.

8.5.3 Test Scenarios

Test scenarios were classified according to two main properties: the *agents dynamics* and the *baseline length*. Each experiment was labelled using the format `ddmmyyyy-nn-T`, where the first six digits indicate the date of the experiment,`nn` indicates the experiment identifier and `T` classify the dynamics of the agents pair. For each experiment and each device, the resulting metrics are associated to a given receiver through the identifiers `SM01` and `SM02`.

Agents dynamics

Considering a single GNSS receiver, we are typically interested in observing positioning performance in static and kinematics conditions. Differently, when multiple GNSS receivers are involved in CP, four typology of pairwise relative dynamics must be taken into account despite the behaviour of each single agent, according to the terminology of inertial/non-inertial systems

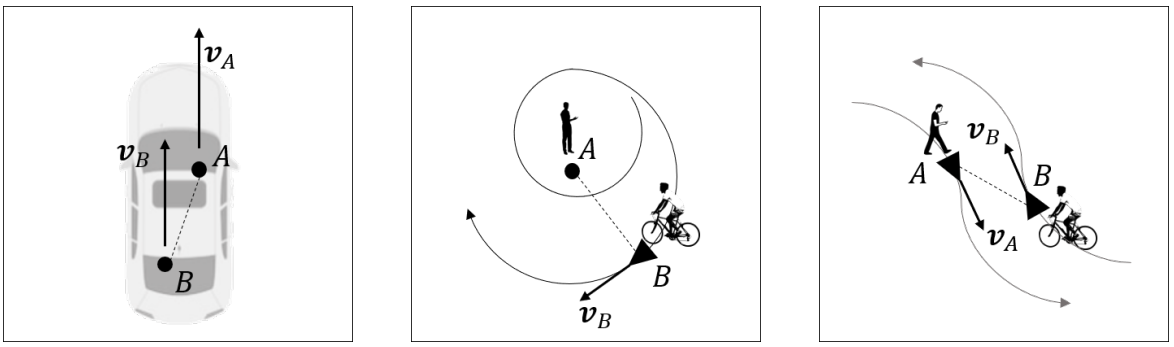

(a) Type **B** (b) Type **C** (c) Type **D**

Figure 8.17: Relative dynamics example between two cooperating agents.

- **Static (type A)**: both the receivers are static such that $\mathbf{v}_A(t_k) = \mathbf{v}_B(t_k) = \overrightarrow{0} \forall k$. No variations are considered for the respective velocities and the resulting baseline vector, such that $\mathbf{d}_{AB}(t_k) = \mathbf{d}_{AB}(t_{k+1}), \forall k$.
- **Time-invariant baseline length (type B)**: both the agents move according to the same direction and with velocity vectors with the same magnitude, such that $\mathbf{v}_A(t_k)$ is nearly-parallel to $\mathbf{v}_B(t_k)$ and $||\mathbf{v}_A(t_k)|| \simeq ||\mathbf{v}_B(t_k)||, \forall k$, as shown in Figure 8.17a. Relative speed can be considered null and their baseline length, $d_{AB}(t_k)$ is kept nearly-constant while the baseline vector can change in direction w.r.t. to a reference inertial system.
  Example: GNSS receivers carried on-board the same vehicle (i.e. multiple passengers in a car).
- **Anchored variable baseline vector (type C)**: one of the agent is static (anchor) and the other moves according to a given dynamics, as in the example of Figure 8.17b. The origin of the baseline vector is kept static but it is allowed to change both in direction and magnitude.
  Example: Parked and moving cars or pedestrian waiting for a cab ride.
- **Fully variable baseline vector (type D)**: this conditions represents the generalization of the previous scenarios. Two receivers move according to independent dynamics

such that $\mathbf{v}_A(t_k) \neq \mathbf{v}_B(t_k)$ and $||\mathbf{v}_A(t_k)|| \neq ||\mathbf{v}_B(t_k)||, \forall k$, as shown in Figure 8.17c.

Example: Receivers A and B are installed on two bikes travelling in opposite directions with different speeds.

Baseline length

The distance between the agents was classified according to

- **Ultra-short**: 0 m to 5 m, suitable for experiments of types **A** and **B** including zero-baseline tests.
- **Short**: 0 m to 50 m, suitable for kinematic scenario of types **C** and **D**
- **Moderate**: 50 m to 100 m

It is worth remarking that the baseline length, d_{AB} can influence the effectiveness of the error cancellation provided by differential ranging techniques.

The whole set of experiments pursued within the CAPS.loc Test Campaign in October 2019 is listed in Table 8.8. All the experiment are referred hereafter according to the nomenclature defined in 8.5.3 and sorted according to the execution date.

Code	Date-nn-T	Environment	SVs	d_{AB}	Scenario
a-01	02102019-01-B	Urban	GPS(5)	Short	Pedestrian
b-01	04102019-01-C	Urban	GPS(5)	Short	Pedestrian
b-02	04102019-02-D	Urban	GPS(5)	Short	Pedestrian
b-03	04102019-03-D	Urban/Open Sky	GPS(5)	Short	Pedestrian
b-04	04102019-04-C	Urban/Open Sky	GPS(5)	Short	Pedestrian
c-01	09102019-01-B	Urban	GPS(5)	Ultra-short	Pedestrian
c-02	09102019-02-B	Urban	GPS(5)	Ultra-short	Pedestrian
d-02	11102019-02-B	Open Sky	GPS(5)	Ultra-short	Vehicular
d-03	11102019-03-A	Urban	GPS(5)	Ultra-short	Vehicular
d-04	11102019-04-B	Urban	GPS(5)	Ultra-short	Pedestrian
d-05	11102019-05-B	Urban	GPS(5)	Ultra-short	Vehicular
e-01	13102019-01-B	Open-Sky	GPS(5)	Ultra-short	Vehicular
f-01	16102019-01-A	Urban/Open Sky	GPS(5)	Short	Pedestrian
f-02	16102019-02-D	Urban/Open Sky	GPS(5)	Short	Pedestrian
g-01	30102019-01-A	Urban/Open Sky	GPS(5)	Ultra-short	Pedestrian
g-02	30102019-02-A	Urban/Open Sky	GPS(5)	Ultra-short	Pedestrian
g-03	30102019-03-D	Urban/Open Sky	GPS(5)	Short	Pedestrian
g-05	30102019-05-D	Urban/Open Sky	GPS(5)	Moderate	Pedestrian+Bike
g-06	30102019-06-D	Urban/Open Sky	GPS(all)	Moderate	Pedestrian+Bike

Table 8.8: List of experiments conducted within the internal CAPS.loc test campaign in October 2019. The blue rows indicate the selected samples detailed in 8.6.

8.6 Results

A set of meaningful experiments have been chosen to discuss the relevant results observed for suitable use cases and dynamics (Type A,B,C and D). Detailed results are shown for the

selected experiments according to analyse the CP profitability. Quantitative data are instead collected in a summary of the whole test campaign and presented in Section 8.6.1.

Experiment f-01 16102019-01-A: Static receivers at zero-baseline

- *Description*: `SM01` and `SM02` are statically co-located at centre of a parking lot in the Politecnico Campus.
- *Visibility*: urban environment (buildings, trees) with good portion of open sky.
- *Constraints*: forced to poor visibility using the best 5 GPS satellite in view.
- EKF parameters: multiplicative measurements covariance weight set to 20.

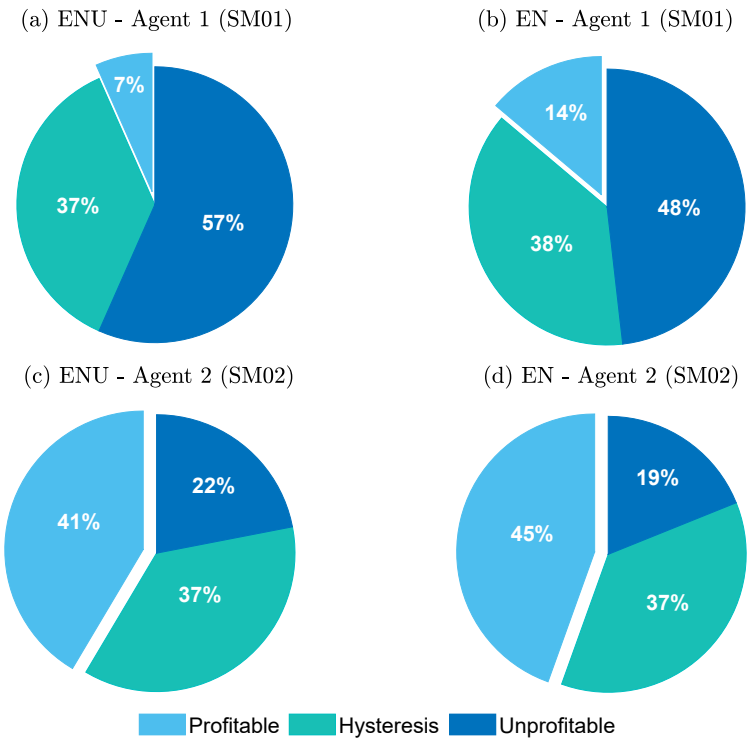

Figure 8.18: Pie charts of CP profitability for the two smartphone in the experiment `f-01`

This test was helpful to assess the feasibility of CAPS.loc dealing with raw measurements coming from co-located identical devices, thus in ultra-short baseline length. According to the profitability results shown in Figure 8.18, it is worth noticing that `SM02` benefits from CP for more than 40% of the data collection. It is reasonable to assume that `SM01` did not benefit from the aids of `SM02` during the same epochs.

By the way, the plot presented in Figure 8.19 highlights a fundamental aspects of this pairwise collaboration: by looking at time t_k from 40 s to 140 s we notice indeed that the collaboration is mostly profitable from `SM01` to `SM02` (SM01. This behaviour is attributed to the quality of the raw measurements and consequently to the goodness of the coarse fix of `SM02`. It is indeed worthy to recall that the coarse position of the aiding agents is used as reference for the tight-integration of the inter-agent distance, as detailed in the tight-integration algorithm defined in Chapter 6. The quantitative comparison of the mean positioning error shown in the upper-right quadrant of Figure 8.24 confirms that, during profitable epochs,

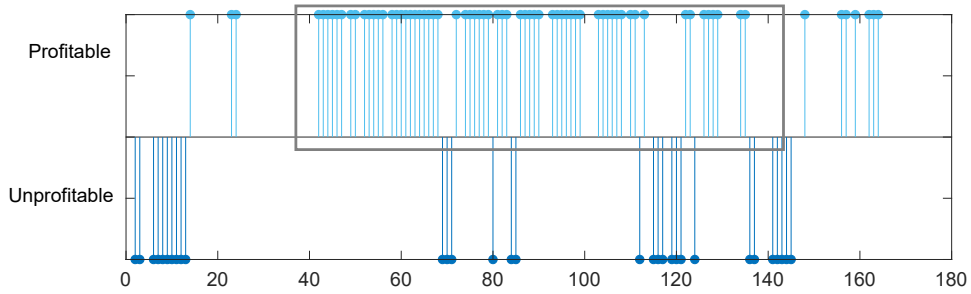

(a) Agent 1 (SM01)

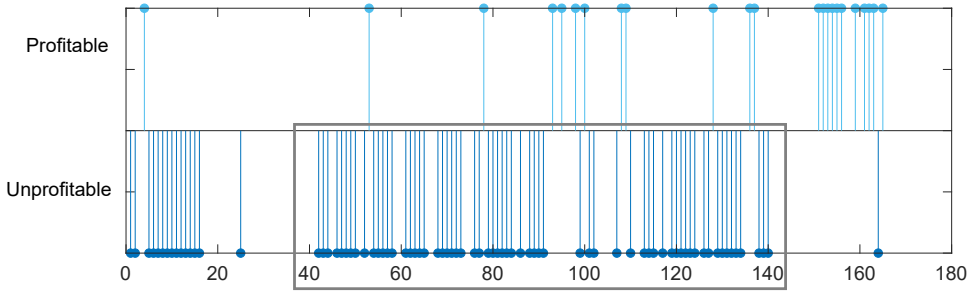

(b) Agent 2 (SM02)

Figure 8.19: Time series of profitability/unprofitability of CP in the experiment `F-01`.

`SM01` obtained a non-relevant advantage from cooperation while the opposite is shown for `SM02`.

Experiment d-02 11102019-02-B: side-by-side pedestrian walk with variable speed and baseline

- *Description*: pedestrian test, SM01 and SM02 moves around a parking area.
- *Visibility*: urban environment (buildings, trees, open sky).
- *Constraints*: forced to poor visibility using the best 5 GPS satellite in view.
- EKF parameters: multiplicative measurements covariance weight set to 20.

In this experiment, an evident unbalancing of the profitability can be seen in Figure 8.20. Neglecting any additional information it is reasonable to conclude that `SM02` was experiencing good positioning performance providing meaningful data to `SM01`. This behaviour is confirmed by the lower-right quadrant of Figure 8.24 where standalone GNSS accuracy of `SM02` was initially better w.r.t. the one experienced by `SM01`.

Experiment g-05 30102019-05-D: Vehicular (Bicycle) and pedestrian dynamics with variable speed and baseline

- *Description*: urban mobility test, SM01 moving on a bike and SM02 walking around a parking area.
- *Visibility*: urban environment (buildings, trees, open sky).
- *Constraints*: forced to poor visibility using the best 5 GPS satellite in view.
- EKF parameters: multiplicative measurements covariance weight set to 20.

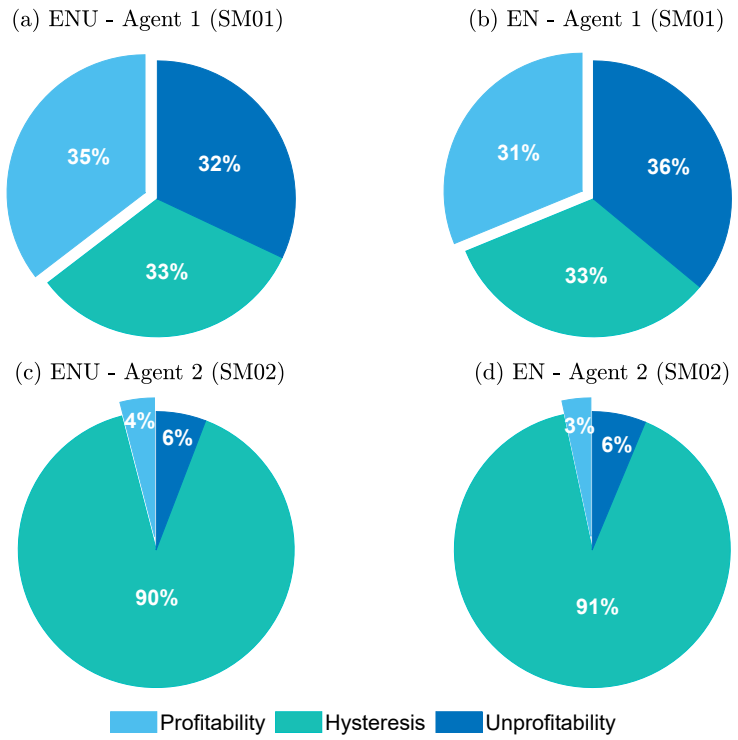

Figure 8.20: Pie charts of CP profitability for the two smartphones in the experiment `d-02`.

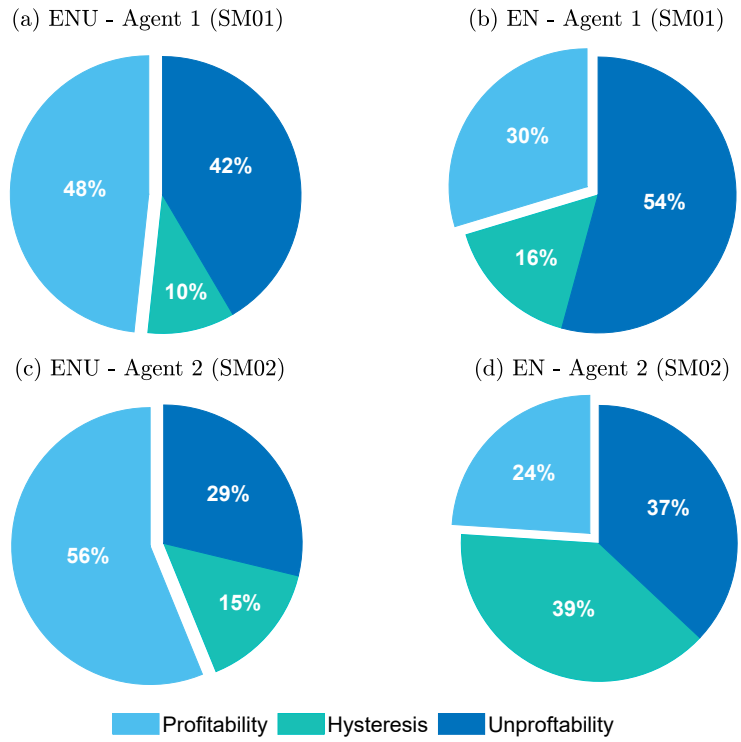

Figure 8.21: Pie charts of CP profitability for the two smartphones in the experiment `g-05`.

The *bike agent* (SM01) followed a longer path w.r.t. to the *pedestrian agent* (SM01), by slightly varying its altitude as well as multipath and visibility conditions along the trajectory. Furthermore, in this specific scenario the SM02 experienced a lower availability than usual, caused by temporary network failures which were not affecting SM01.

Pedestrian agent (SM01) showed a considerably higher profitability w.r.t. the bike agent in 3-D reference frame, as shown in Figure 8.21. SM01 benefited from the moving agent and its variable quality of the measurements along the trajectory. This is due in particular to capabilities of the EKF to guarantee better positioning performance in dynamics scenario. The results appears reversed in 2-D frame, thus underlying that the more evident improvement was on altitude. This effect of CP has been shown from the theoretical analysis presented in Chapter 7. As shown in the left-bottom quadrant of Figure 8.24, the error reduction due to CP is remarkable and $\mathcal{I}_{\text{CP}} \simeq 50\%$ has been reached in the profitable epochs, considering both 2-D and 3-D frames. Generally speaking, pedestrian experienced a higher accuracy in the standalone solution w.r.t. the bike agent, so it can potentially provide a valuable aiding.

Experiment c-01 04102019-01-C: Pedestrian relative dynamics with variable speed, baseline and altitude

- *Description*: pedestrian test, SM01 moves in an urban canyon with considerable multipath effects while SM02 is static on the roof of the building.
- *Visibility*: urban canyon for SM01 (buildings) and open sky for SM02.
- *Constraints*: forced to poor visibility using the best 5 GPS satellite in view.
- EKF parameters: multiplicative measurements covariance weight set to 20.

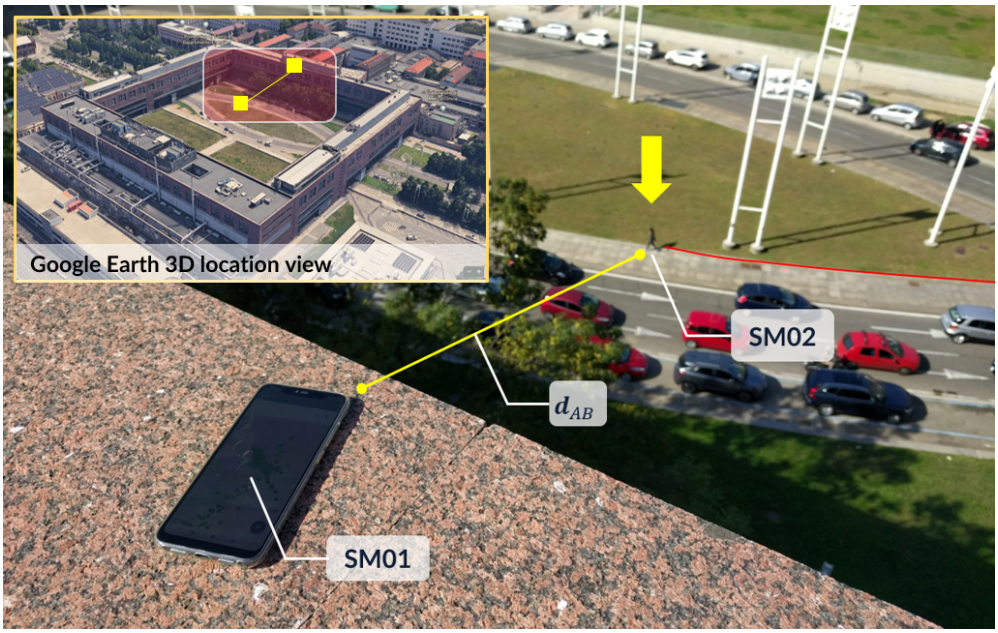

Figure 8.22: Example of pedestrian urban scenario with anchored variable baseline vector (experiment C-01) which exploit the CAPS.loc framework for CP.

A well-known critical environment was selected for this test nearby Politecnico di Torino for SM01, as shown in Figure 8.22. Despite of the favourable conditions of SM02 located on a rooftop, the benefits for SM01 were not remarkable. As depicted in Figure 8.23, this experiment showed very low profitability in both the smartphones although the accuracy

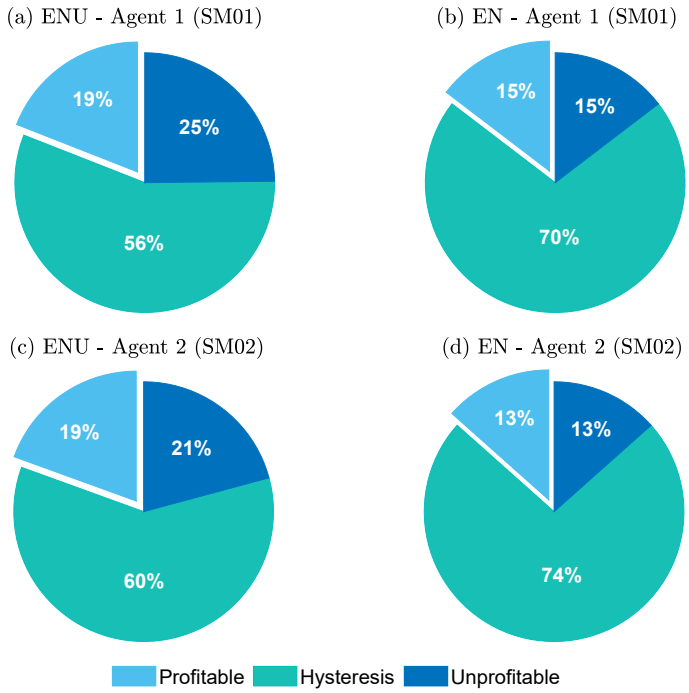

Figure 8.23: Pie charts of CP profitability for the two smartphones in the experiment `c-01`.

improvement in profitable epochs was remarkable, as shown in upper-left quadrant of Figure 8.24. This could be due to the very different conditions of the agents but especially to the high multipath conditions experienced by `SM01` which is responsible for the degradation of both raw measurements and coarse fix shared by the agent. As commented for experiment g-05, a further penalizing factor is the use of EKF for the estimation of the static position of `SM02`.

A further assessment of the simulation results is given through the analysis of the CDFs of the positioning errors, provided in Figure 8.25. Differently from the previous analysis, the plots depict the overall error of the positioning solutions along the whole test duration. A comparison is shown between standalone and cooperative solution and we can notice negligible improvement for low dynamics scenarios such as the experiments `c-01` (upper-left quadrant) and `d-01` (lower-right quadrant). On the contrary, a higher advantage is provided on average for high relative dynamics as for the sample experiment `d-02`, in which the cooperation was established within bicycle-pedestrian pair (bottom-left quadrant). A different case is instead shown in the upper-right quadrant for the experiment `f-1` in which a clear aiding-aided configuration would be advisable as `SM01`→`SM02`. This finding is clearer in static experiments during which two identical devices surprisingly experienced different navigation conditions stably along the whole timespan.

8.6.1 Summary of experimental results and general comments

The performance of all the experiments included in Table 8.8 are reported for `SM01` and `SM02` in Table 8.9 and Table 8.10, respectively. It is worth mentioning that, despite of the high variability of the scenarios (different environmental conditions, baseline lengths, relative dynamics), the statistical results presented in this chapter support the promising performance of the paradigm. According to the values reported in such a summary, the following considerations generally hold for this preliminary test campaign of the CAPS.loc

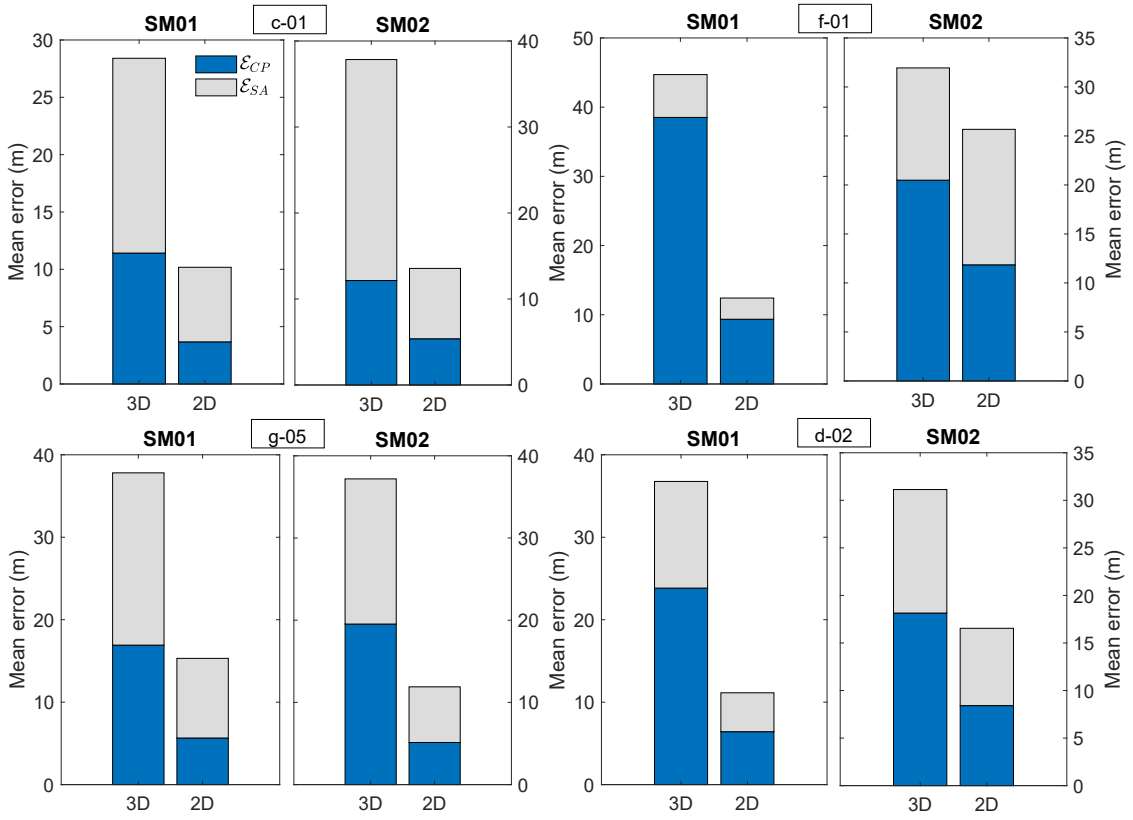

Figure 8.24: Collection of mean errors comparisons for the experiments described in 8.6.

	$\mathcal{A}_{\text{CP}}$(%)	$\mathcal{P}_{\text{CP}}$ (%)		$\mathcal{H}_{\text{CP}}$ (%)		$\mathcal{E}_{\text{CP}}$ (m)		$\mathcal{E}_{\text{SA}}$ (m)		$\mathcal{I}_{\text{CP}}$ (%)	
		3-D	2-D	3-D	2-D	3-D	2-D	3-D	2-D	3-D	2-D
a-01	89.62	11.9	12.35	64.38	76.92	20.26	5.65	30.56	9.61	30.83	36.57
b-01	86.39	19.05	14.63	56.12	70.74	11.42	3.67	16.99	6.5	29.21	40.91
b-02	87.50	18.67	16.62	56.78	73.15	13.13	4.72	22.97	8.97	36.46	40.38
b-03	88.08	47.76	35.89	20.25	57.26	21.96	5.23	30.09	8.45	25.41	32.75
b-04	89.80	4.1	3.33	87.08	90.61	15.14	8.78	36.12	16.45	74.15	36.04
c-01	90.00	17.15	10.02	64.61	64.49	15.52	4.43	26.26	7.9	38.04	34.3
c-02	89.47	1.21	1.52	96.04	96.04	28.33	8.26	41.21	14.95	29.63	41.26
d-02	89.40	35.4	31.2	32.6	32.8	11.92	3.2	18.38	5.57	31.96	38.83
d-03	90.00	27.61	38.65	28.83	29.45	10.08	5.45	16.31	8.78	35.45	36.1
d-04	89.88	26.45	24.03	35.39	36.72	15.47	6.72	24.58	11.14	31.77	33.96
d-05	89.70	47.18	39.47	31.45	32.34	15.1	5.32	41.8	14.21	49.42	48.61
e-01	89.76	19.03	17.33	44.24	44.73	13.48	5.35	18.19	7.58	23.68	28.42
f-01	89.40	6.63	13.86	36.75	37.95	38.52	9.35	44.71	12.42	14.05	25.99
f-02	89.48	36.98	29.17	33.85	33.33	24.64	9.15	46.67	18.85	40.58	41.86
g-01											
g-02	83.21	22.36	20.18	3.94	3.07	18.96	8.41	26.26	13.19	25.19	35.29
g-03	75.96	67.09	24.05	8.86	35.44	12.4	4.39	21.29	6.76	40.02	36.61
g-05	98.37	38.84	27.27	14.88	28.1	16.27	6.56	48.76	21.51	50.13	56.7
g-06	100.00	51.87	29.32	9.023	18.05	22.74	11.07	61.47	32.6	57.15	64.11

Table 8.9: Xiaomi Mi 8 Pro [SM01]: Static and semi-kinematic pedestrian tests in proximity to Politecnico Campus (Mixed urban environment). $T_H = 0.05\,\text{m}$.

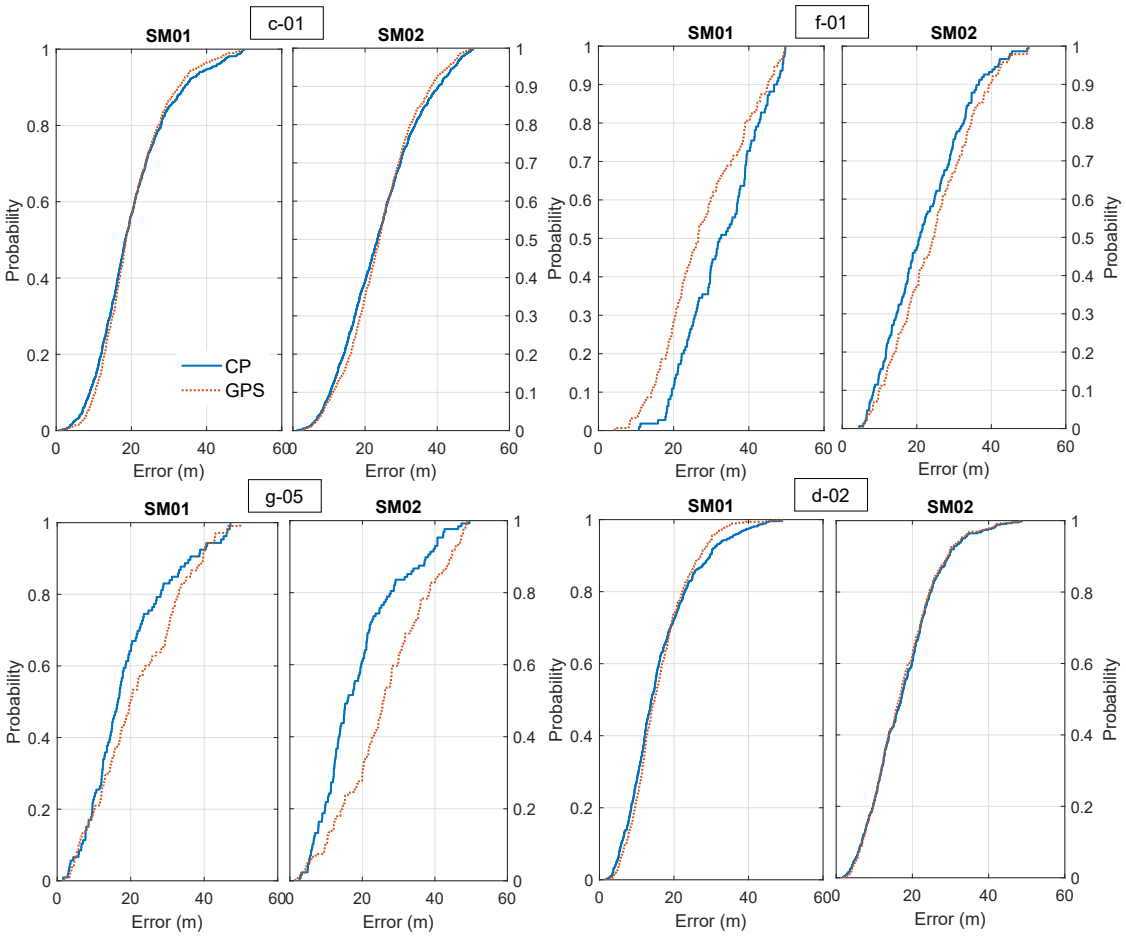

Figure 8.25: Collection of CDFs for the sample experiments described in Section 8.6.

	$\mathcal{A}_{\mathrm{CP}}$(%)	$\mathcal{P}_{\mathrm{CP}}$ (%)		$\mathcal{H}_{\mathrm{CP}}$ (%)		$\mathcal{E}_{\mathrm{CP}}$ (m)		$\mathcal{E}_{\mathrm{SA}}$ (m)		$\mathcal{I}_{\mathrm{CP}}$ (%)	
		3-D	2-D	3-D	2-D	3-D	2-D	3-D	2-D	3-D	2-D
a-01	86.61	16.32	12.30	59.50	71.88	19.42	7.70	30.34	14.46	31.15	38.39
b-01	90.00	19.46	13.42	59.73	73.15	12.15	5.37	25.70	8.18	34.56	32.95
b-02	86.98	20.84	20.35	59.80	60.05	11.93	5.54	19.80	9.05	34.34	37.24
b-03	89.16	14.29	10.18	71.00	72.14	14.59	5.23	19.58	8.45	22.58	34.30
b-04	76.46	8.01	7.63	84.16	84.35	19.04	2.36	23.99	6.20	17.23	54.67
c-01	87.07	25.08	18.41	41.98	42.14	22.11	10.39	38.62	19.38	38.64	38.02
c-02	89.09	0.92	1.00	97.01	97.01	23.60	10.02	36.27	15.78	33.58	34.32
d-02	89.33	4.03	3.36	90.13	90.36	18.14	8.41	31.13	16.54	43.47	39.99
d-03	89.38	44.10	34.78	11.80	11.80	13.32	4.65	17.44	7.80	22.78	38.94
d-04	85.30	35.02	30.46	28.98	29.71	19.92	9.39	32.68	14.70	36.37	39.34
d-05	89.39	55.31	44.68	23.71	24.01	16.34	6.85	44.50	15.66	51.80	48.96
e-01	89.86	32.42	27.19	19.35	20.39	12.50	5.50	16.59	7.69	22.47	28.76
f-01	87.61	41.46	44.51	36.58	36.58	20.48	11.85	31.94	25.68	31.82	47.97
f-02	90.00	38.02	36.98	14.58	13.54	23.95	9.83	48.03	17.77	43.87	38.67
g-01	62.50%	30.52	20.00	15.78	14.73	22.26	15.16	31.55	21.61	29.82	33.50
g-02	81.48%	31.81	18.18	15.50	21.59	11.63	3.64	23.14	8.58	43.97	57.32
g-03	55.55%	12.50	12.50	22.50	35.00	11.78	6.61	17.21	13.27	40.34	53.47
g-05	58.54%	43.75	14.58	10.41	33.33	21.52	9.28	44.82	25.41	47.41	62.55
g-06	65.47%	56.16	23.97	15.07	39.04	19.53	5.12	37.19	11.89	45.72	57.30

Table 8.10: Xiaomi Mi 8 Pro [SM02]: Static and semi-kinematic pedestrian tests in proximity to Politecnico Campus (Mixed urban environment). $T_H = 0.05\,\mathrm{m}$.

framework.

Availability

The average availability of the CP across all the experiments was about 86.94 % and 81.23 % of the whole test duration for `SM01` and `SM02` respectively. If we do not consider the set of experiments `g-0x` for which the device `SM02` experienced unexpected connectivity issues, the availability can be generally considered above the 87 % for a pairwise CP exploiting 4G connectivity. Let us remark that this metric is tightly related to the connectivity conditions and the network latencies which can be considerably different according to the network infrastructure and topology; The measurement combination was indeed excluded if the difference between raw data timestamps of the devices exceeded a given threshold (i.e. 1 s), according to the CAPS.loc implementation described in Chapter 8. Although it is fundamental to rely on low-latency communication networks to limit the amount of discarded data, QoS policies which could guarantee priority to the CRMs are out of the scope of this work.

Expected improvement in real scenarios

By looking at all the statistics collected in Table 8.9 and Table 8.10, the mean 2-D accuracy improvement provided by the CP across al the experiments is about 40.7 % for `SM01` and 43.5 % for `SM02`. By considering the different conditions of each experiment, this experimental result suggests an expected value of the accuracy improvement (in case of profitable conditions) for a single collaborative contribution in poor satellite visibility (`g-06` is not considered in this average) and mild-urban environment. Despite of the considerable improvement provided by CP during the profitable epochs, in most of the experiments the overall balancing between profitability and unprofitably was expected from the simulation results presented in Chapter 7 about single agent contribution.

8.7 Final remarks and further works

The CAPS.loc framework has been implemented within the context of the HANSEL project through a PoC of the GNSS-based CP. It is based on a client-server infrastructure allowing the cooperation among Android smartphones equipped with GNSS receiver. A specific message, named CRM, is designed to transport navigation data among collaborating agents. Such a message is sent to a central service, namely the CPS, which is in charge to maintain an updated buffer of raw measurements. CRMs are built and exchange among the agents through the CPA, an application running on the smart devices. The communication rely on a general-purpose data connectivity such as Wi-Fi 802.11x or mobile networks such as 4G/LTE.

This PoC has enabled further investigation about feasibility constraints on a mass-market scenario such as in the context of smart cities. On one hand, the client-server approach has a huge potential in terms of optimization to further analyse CRLB-based censoring strategies as discussed in Chapter 7. On the other hand it represent a limit on the communication latencies which could impact negatively on the synchronization of the raw measurements among the agents. A direct communication approach could lead to a timely transmission of CRMs but it could be practically infeasible in NLOS conditions.

Despite of being a preliminary implementation, the CAPS.loc results obtained in the experimental campaigns showed a great potential in terms of accuracy improvement, whenever the paradigm is profitable. For the sake of simplicity, the preliminary tests discussed in this chapter were conducted according to the pairwise configuration described in Section

8.5.1. The average performance of such a single agent CP were expected to be around the 5-10 % according to the simulation results obtained through realistic signals in Chapter 7. According to the theoretical achievements presented in this thesis, an optimization of the GNSS-based CP and further exhaustive analysis of the CAPS.loc are surely advisable for the future development. However, such an optimization step falls outside the scope of this experimental assessment. As guidelines for the next investigation, the following modifications are suggested to improve positioning and navigation performance. Further analysis are indeed mandatory to observe the behaviour of the collaboration and recompute the performance metrics according to different architectural blocks. Regarding the actual implementation of the CAPS.loc paradigm the performance analysis can be extended through the following points:

- Replacement of functional blocks (i.e. CRU, Hybrid PVT (H-PVT)) with different GNSS-based ranging algorithms and positioning algorithm, according to the proposals of Chapter 4 and Chapter 6, respectively.
- Improving the estimation of the inter-epochs time misalignment through accumulated statistics and continuous monitoring of agent's independent clocks.
- Implementation of multi-constellation/multi-frequency algorithms both for the coarse fix and the computation of inter-agent distances
- Implementation of advanced Bayesian estimation for inter-agent distance computation
- Implementation of advanced features for the joint censoring of GNSS measurements and collaborative contributions when they are poorly effective to the refinement of the positioning estimation.
- Limit the cross-cooperation by determining aiding-target collaborative pairs runtime, according to CRLB and theoretical findings presented in Chapter 7.

Regarding the system architecture and the investigated scenarios:

- Comparison of availability performance with different network architectures (e.g. IEEE Wi-Fi 802.11x, 5G).
- Evaluate multi-agent cooperation including and optimizing multiple collaborative contributions runtime.
- Evaluate multi-agent statistics in crowded areas both for pedestrian and vehicular navigation

These aspects are subordinated to the development of future CPA releases. An extended set of configuration parameter will be hence suitable for widening the analysis of the framework to different algorithms and optimization strategies. In this early experimental phase, the GNSS-based CP was conceived to act as a "GNSS augmentation layer" prior to the integration of potential auxiliary sensors such as on-board gyros, accelerometer and electronic compass [208]. An extension of this concept towards a O.S. augmented location provider was presented at the Galileo Masters 2019 and classified in the top ten ideas. Contextually, the framework won the Italian Regional Prize promoted by Italian Space Agency as shown by the certificate in Figure 8.26.

Figure 8.26: Galileo Masters 2019 award certificate for CAPS.loc.

Chapter 9

Conclusions

The GNSS has been mostly considered as a reliable navigation technology providing absolute positioning with good accuracy, precision, continuity and reliability. However, GNSS-based navigation is characterized by critical limitations due to the intrinsic nature of the system (e.g. poor satellite visibility, low signal quality due to atmospheric impairments and multipath). Among these, GNSS navigation in harsh environment was addressed as one of the major challenge to the quality of the positioning solution. A considerable effort has been focused on the improvement of this technology at any system level (ground segment, space segment, augmentation systems). In the last decade, absolute positioning determination is slowly becoming less relevant in new paradigms such as autonomous driving, however, the effectiveness of situational awareness, surroundings sensing and recent applications is still a challenging task to be accomplished effectively without contemplating GNSS. The advent of sophisticated algorithms providing sensor fusion addressed the compensation for the weakness of GNSS thus fuelling new effort in research towards PNT. Fundamental research on GNSS has been dropped up to the disclosure of raw measurements from mass market devices which opened a range of opportunities in the fields and allowing in parallel to rise paradigms belonging to different fields such as robotics and multi-agent systems.

In parallel with the advances in sensor fusion and complementary positioning systems, CP has been conceived in the last decades as a paradigm for the localization of navigating users relying on the exchange of independent information. The basic approach is addressed to the estimation of relative position and the sharing of these data among networked agents through ad-hoc communication channels or permanent network infrastructures. With this in mind, it was natural in this work to consider the exploitation of redundant visible satellites among interconnected users (i.e. collaborative agents) as a powerful resource for the improvement of GNSS-based solutions.

This study was indeed based on the concept of networked GNSS receivers being able to share GNSS measurements to enable enhanced positioning and navigation capabilities. The theoretical limits of a collaborative DGNSS were presented in Chapter 7 and according to these findings, the exchange of pseudorange measurements has been demonstrated as a source of auxiliary information for networked receiver.

A set of DGNSS strategies were implemented to combine such measurements into relative distance measurements among networked GNSS receivers. Well-known Single Difference and Double Difference baseline estimation methods were compared with a novel geometrical solution suitable for reduced visibility environment. A comparison of the statistical properties of the techniques was pursued to provide the most suitable solution to CP.

This thesis investigated the proposed CP paradigm by looking mostly at the position estimation. Such a vector quantity is surely the most appealing for LBS and receivers in general. However, the approach can be extended to the velocity estimation of cooperating

kinematic agents exploiting collaborative differential velocity computation through independent, correlated Doppler measurements. Such a solution could be effective the reduce the dependency of the velocity determination to sensors and odometers, thus presenting the same advantages of GNSS-only enhanced positioning. Doppler measurements are considerably more stable both for high-end and mass market receivers and this aspect could lead to outstanding performance.

According to the results presented in this thesis by means of numerical simulation, and assessed through realistic simulations and through real-time implementation, in Chapter 8, a proof of the benefits led by cooperative enhancement in GNSS positioning can be clearly remarked, even in case of ultra low-cost receivers embedded in smartphones. Moreover, many further improvements were suggested to improve positioning and navigation performance of the proposed CP framework in order to avoid non-profitable integration, thus turning the technique into a robust solution in the next development steps.

9.1 Further works

Among the potential extensions of this work addressing a prototype for the paradigm, it is worthy to mention the development of multi-constellation and multi-frequency algorithms for improved inter-agent distance estimation, the analysis of the geometrical displacement of both satellites and agents through the estimation of the precision bound for correlated/uncorrelated ranging information and the development of advanced filtering of the raw measurements exchanged among the agents. Despite of the clear contributions provided towards improved GNSS-only positioning and navigation, the proposed framework, CAPS.loc, can also open a variety of possibilities for centralized/distributed real-time processing of GNSS raw measurements in different class of receivers. Among the potential applications we can mention collaborative anti-spoofing techniques based on outliers detection, a source of big-data about monitoring of ionospheric indexes or for real-time mapping of the quality of GNSS positioning in harsh context. Furthermore, the implementation of this CP paradigm provided a baseline for further scientific investigation on state-of-the art cooperative algorithm inherited from different fields which could support a sustainable GNSS navigation in the near future.

Appendix A

Fundamentals on Reference Systems and Frames

All the satellite-based navigation systems such as GNSS require the definition of a common reference frame to locate both satellite coordinates and user receivers. It is worthy to remark the difference among *reference system* and *reference frame*: the first is theoretically defined according to a standard model while the latter is an empirical implementation based on observations and further reference coordinates. The rigorous definition of the reference frames used in GNSS is out of the scope of this work and further details on the topic can be found in theory books on geodesy or summarized in [164, 165]. Therefore, the scope of this appendix is to recall the fundamentals about the conversion among different frames and their definitions.

A.1 Conventional Celestial Reference System CRS

The CRS coordinate system adopts the Earth's center of mass as the origin of a Cartesian reference frame. The fundamental plane corresponds to the average equatorial plane calculated at J2000.0 [1]. The system is also known as Earth-Centered Inertial (ECI) and it is represented in Figure A.1a by considering the following mapping of the corresponding Cartesian orthogonal components:

$\mathbf{z}_{CRS}$: axis crossing the average geographic north pole

$\mathbf{x}_{CRS}$: average vernal equinox

$\mathbf{y}_{CRS}$: coordinate axis with respect to $\mathbf{z}_{CRS}$ and $\mathbf{x}_{CRS}$

Actually, the CRS is quasi-inertial reference frame since it is characterized by the annual revolution, thus by the accelerated motion of the Earth w.r.t. the Sun.

A.2 Conventional Terrestrial Reference System (TRS)

The system is often referred as Earth Centered Earth Fixed (ECEF) with origin in the center of mass of the Earth and a fundamental plane corresponding to equatorial plane. Despite CRS/ECI, the coordinate axis system is coherent with Earth's daily rotation, that is

[1] J2000.0 or J2000 indicates 12h00 of 1st January 2000 of Gregorian Calendar (UT)

to say it is not inertial. The fundamental plane contains the origin and it is perpendicular to the Conventional Terrestrial Pole (CTP). The $\mathbf{z}_{ECEF}$ axis is the intersection point between equator and Greenwich meridian as shown in Figure A.3b. Axis convention is hence reported:

$\mathbf{x}_{TRS}$: axis crossing the intersection between the equator and the Greenwich meridian

$\mathbf{z}_{TRS}$: axis passing through the CTP

$\mathbf{y}_{TRS}$: coordinate axis w.r.t. $\mathbf{x}_{TRS}$ and $\mathbf{y}_{TRS}$

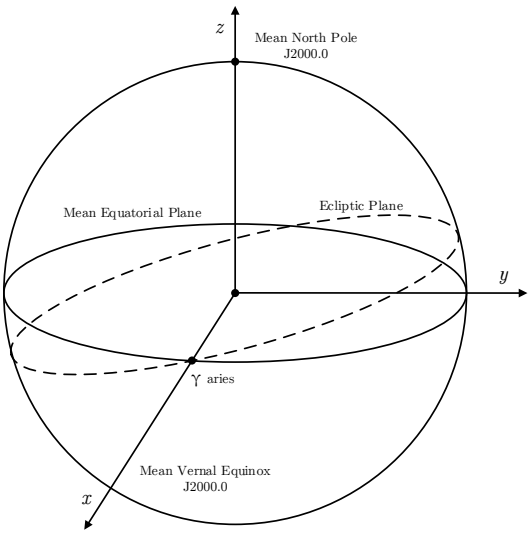

(a) CRS Earth Centered Inertial (ECI)s.

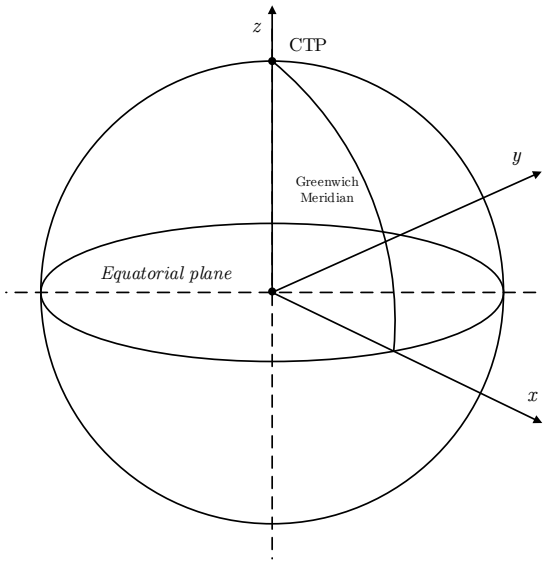

(b) Earth Centered Earth Fixed reference frame.

Figure A.1: Coordinates Reference Systems.

The main GNSSs adopt different reference frames:

- GPS: World Geodetic System WGS-84 (US DoD)[37].
- GLONASS: Parametry Zemli 1990 (Parameters of the Earth 1990) (PZ-90).
- GALILEO: Galileo Terrestrial Reference Frame (GTRF)(GeoForschungsZentrum Potsdam)(IGS).

A.3 Conversion between reference systems

A conversion of the ECEF coordinates is required to visualize the position in terms of latitude and longitude. For each coordinate pair, the height of a point is defined w.r.t. the geoid and a relative given model (e.g. WGS84 for GPS). Such coordinates are referred as LLA or LLH and they represent the usual coordinate system adopted to identify the position of a point on the Earth, namely through its *ellipsoidal coordinates*.

Ellipsoidal Coordinates (ϕ, λ, h) The Cartesian ECEF can be mapped on an ellipsoidal model. The conversion is performed through the following transformation, according to Figure A.2

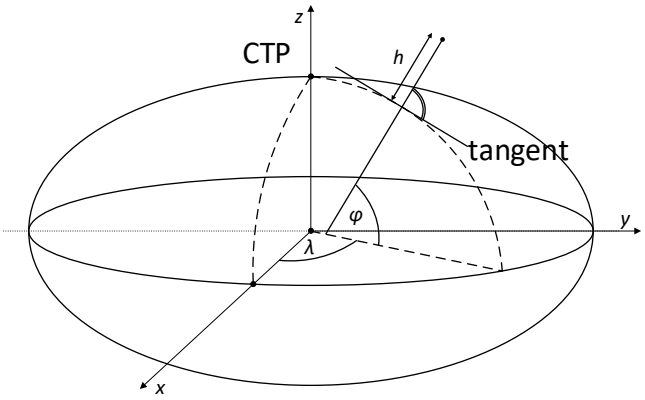

Figure A.2: Ellipsoidal Coordinates LLA/LLH.

$$\begin{aligned} \mathbf{x}_{TRS} &= (N+h)\cos(\phi)\cos(\lambda) \\ \mathbf{y}_{TRS} &= (N+h)\cos(\phi)\sin(\lambda) \\ \mathbf{z}_{TRS} &= ((1-e^2)N+h)\sin(\phi) \end{aligned} \tag{A.1}$$

Where N is the curvature radius along the meridians by varying ϕ:

$$N = \frac{a}{\sqrt{1-e^2\sin^2\phi}} \tag{A.2}$$

and e is the eccentricity of the ellipsoid (often referred as *stretching factor*)

$$e^2 = \frac{a^2-b^2}{a^2} = 2f - f^2 \tag{A.3}$$

where a and b are the semi-major and the semi-minor axis respectively. The eccentricity can also be expressed in function of flattening coefficient f.

Inverse conversion from Ellipsoidal Coordinate System to ECEF can be approximated by iterative solution.

Conversion between ECEF to Local Tangent Plane (LTP) Coordinates LTP coordinate system usually referred as East, North and Up (ENU) coordinates is widely adopted in GNSS terrestrial receiver and is suitable for the sought application. The ENU coordinates are derived from ECEF, thus the oblate ellipsoidal configuration is still valid. The axis are described as follows:

N: is the axes (coordinated to the tangent plane) which points towards north Pole identified by $\mathbf{z}_{TRS}$.

E: it corresponds to the east axis and is aligned to the local parallel

U: it is the normal vector of the LTP

In order to perform the conversion between ECEF to ENU and viceversa, two linear transformation are required. They correspond to two rotations of a Cartian reference system.

1. Rotation of $90\,\text{deg} - \phi$ on E-axis to align U-axis with $\mathbf{z}_{TRS}$ $\mathbf{R_1}[-(\pi/\mathbf{2} - \phi)]$
2. Rotation of $90\,\text{deg} + \lambda$ on U-axis to align $\mathbf{x}_{TRS}$ to E-axis. $\mathbf{R_3}[-(\pi/\mathbf{2} + \lambda)]$

where R_1, R_2 and R_3 are defined as follows:

$$\mathbf{R_1}(\theta) = \begin{bmatrix} 1 & 0 & 0 \\ 0 & \cos\theta & \sin\theta \\ 0 & -\sin\theta & \cos\theta \end{bmatrix}, \mathbf{R_2}(\theta) = \begin{bmatrix} \cos\phi & 0 & -\sin\phi \\ 0 & 1 & 0 \\ sin\theta & 0 & \cos\theta \end{bmatrix}, \mathbf{R_3}(\theta) = \begin{bmatrix} \cos\theta & \sin\theta & 0 \\ -\sin\theta & \cos\theta & 0 \\ 0 & 0 & 1 \end{bmatrix} \tag{A.4}$$

The conversion in matrix form is expressed as:

$$\begin{bmatrix} x \\ y \\ z \end{bmatrix} = \mathbf{R_1}[-(\pi/2 + \lambda)]\mathbf{R_3}[-(\pi/2 - \phi)] \cdot \begin{bmatrix} E \\ N \\ U \end{bmatrix} \tag{A.5}$$

computing the overall transformation matrix

$$\mathbf{R_c} = \mathbf{R_1}[-(\pi/2 + \lambda)]\mathbf{R_3}[-(\pi/2 - \phi)] = \begin{bmatrix} -\sin\lambda & -\cos\lambda\sin\phi & cos\lambda\cos\phi \\ \cos\lambda & -sin\lambda\sin\phi & \sin\lambda\cos\phi \\ 0 & \cos\phi & \sin\phi \end{bmatrix} \tag{A.6}$$

By substituting Equation (A.6) in matrix Equation (A.5) the coordinates are hence obtained as follows:

$$\begin{aligned} \hat{\mathbf{e}} &= (-\sin\lambda, \cos\lambda, 0) \\ \hat{\mathbf{n}} &= (-\cos\lambda\sin\phi, -\sin\lambda\sin\phi, \cos\phi) \\ \hat{\mathbf{u}} &= (\cos\lambda\cos\phi, \sin\lambda\cos\phi, \sin\phi) \end{aligned} \tag{A.7}$$

By applying trivial properties from elementary algebra $R_i^{-1}(\alpha) = R_i(-\alpha) = R_i^T(\alpha)$ it is possible to obtain the reverse relation as follows:

A.3.1 Range, Elevation and Azimuth computation from ENU frame

Azimuth and elevation are relevant to describe the satellite relative observation from the receiver perspective. From a set of coordinates defined in ENU reference frame, the *range versor* is defined as follows:

$$\hat{\rho} = \frac{r^{sat} - r_{rcv}}{||r^{sat} - r_{rcv}||} \tag{A.8}$$

where r^{sat} and r_{rcv} are the geocentric satellite and receiver coordinates respectively. Azimuth and elevation can be computed from LTP reference by applying elementary trigonometric rules, according to Figure A.3

$$\begin{aligned} \hat{\rho} \cdot \hat{e} &= \cos E \sin A \\ \hat{\rho} \cdot \hat{n} &= \cos E \cos A \\ \hat{\rho} \cdot \hat{u} &= \sin E \end{aligned} \tag{A.9}$$

By inverting the previous equations:

$$\begin{aligned} E &= \arcsin(\hat{\rho} \cdot \hat{u}) \\ A &= \arctan\left(\frac{\hat{\rho} \cdot \hat{e}}{\hat{\rho} \cdot \hat{n}}\right) \end{aligned} \tag{A.10}$$

Let us remark that if λ and ϕ are *ellipsoidal coordinates* hence, the vector $\hat{u}$ is orthogonal to the LTP and to the reference ellipsoid. Otherwise, if they are in *spherical coordinates* the same plane is tangent to a sphere.

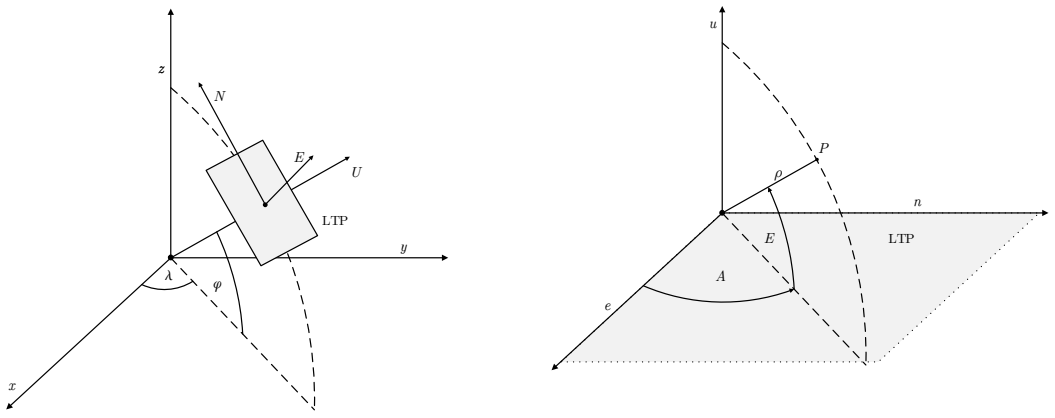

(a) LTP shown in LLA system.

(b) LTP Coordinates Reference.

Figure A.3: LTP shown w.r.t. a LLA frame and as reference frame.

Appendix B

Position Error Covariance Matrix and Geometrical representations

The position uncertainty associated to the output of an unbiased estimator, such as a WLS, describes the *precision* of the estimate itself. The scope of this appendix is to provide the basic knowledge for the computation and visualization of *position error ellipses* representing estimated or measured covariance matrices of the positioning solution in simulation environment. The content of this appendix has been rearranged from [48, 47] to support visualization tools used within this research.

B.1 Sample Covariance Matrix estimation

The *sample covariance matrix* at a given time instant t_k is by definition a $N \times N$ matrix $\mathbf{P}_k = [p_{ij}]$ modelling the probability distribution of a given multi-variate random variable such as the estimated state vector of a GNSS receiver, $\boldsymbol{\theta}_k = \begin{bmatrix}\theta_1 & \theta_2 & \dots & \theta_N\end{bmatrix}^{\mathrm{T}}$. By fixing a discrete time instant t_k for the sake of readability, the entries of $\mathbf{P}_k$ are defined as

$$p_{ij} = \frac{1}{W-1}\sum_{w=1}^{W}\left(\theta_i^{(w)} - \bar{\boldsymbol{\theta}}_i\right)\left(\theta_j^{(w)} - \bar{\boldsymbol{\theta}}_j\right) \tag{B.1}$$

where $\theta_i^{(w)}$ is the w-th observation of the i-th random variable belonging to $\boldsymbol{\theta}_k$ and $\bar{\boldsymbol{\theta}}_i$ is the mean value of the same i-th random variable over W observations. Therefore, p_{ij} is an estimate of the covariance between the i-th variable and the j-th variable of the considered multi-variate random variable, $\boldsymbol{\theta}_k$. In terms of the observation vectors, an equivalent formulation of the sample covariance is

$$\mathbf{P}_k = \frac{1}{W-1}\sum_{w=1}^{W}(\boldsymbol{\theta}^{(w)} - \bar{\boldsymbol{\theta}})(\boldsymbol{\theta}^{(w)} - \bar{\boldsymbol{\theta}})^{\mathrm{T}} \tag{B.2}$$

Alternatively, arranging the observation vectors as the columns of a matrix,

$$\boldsymbol{\Theta}_k = \begin{bmatrix}\boldsymbol{\theta}^{(1)} & \boldsymbol{\theta}^{(2)} & \dots & \boldsymbol{\theta}^{(W)}\end{bmatrix} \tag{B.3}$$

which is a matrix of N rows and W columns, the sample covariance matrix can be computed as

$$\mathbf{P}_k = \frac{1}{W-1}(\mathbf{\Theta}_k - \bar{\boldsymbol{\theta}}\,\mathbf{1}_W^{\mathrm{T}})(\mathbf{\Theta}_k - \bar{\boldsymbol{\theta}}\,\mathbf{1}_W^{\mathrm{T}})^{\mathrm{T}} \tag{B.4}$$

where $\mathbf{1}_N$ is an $W \times 1$ vector of ones. If the observations are arranged as rows instead of columns, so $\bar{\boldsymbol{\theta}}$ is now a $1 \times N$ row vector and $\mathbf{M} = \mathbf{\Theta}^{\mathrm{T}}$ is an $W \times N$ matrix whose column j is the vector of W observations on variable j, then applying transposes operators

$$\mathbf{P}_k = \frac{1}{W-1}(\mathbf{M}_k - \mathbf{1}_W\bar{\mathbf{x}}^{\mathrm{T}})^{\mathrm{T}}(\mathbf{M}_k - \mathbf{1}_W\bar{\mathbf{x}}^{\mathrm{T}}) \tag{B.5}$$

Like covariance matrices for random vector, sample covariance matrices are positive semi-definite. To prove it, note that for any matrix $\mathbf{A}$ the matrix $\mathbf{A}^T\mathbf{A}$ is positive semi-definite. Furthermore, a covariance matrix is positive definite if and only if the rank of the $\theta_i - \bar{\boldsymbol{\theta}}$ vectors is N.

B.2 Covariance Matrix and Error Ellipse

For a given set of applications such as road positioning navigation, horizontal precision models the Horizontal Positioning Error (HPE) which is considered a fundamental Key Performance Indicator (KPI) in GNSS [193]. For bivariate observations indeed, a valuable method to investigate the precision of the positioning solution is the use of *error ellipses* a.k.a. *information ellipses* in Information Theory or *confidence ellipses* in statistics. An error ellipse represents an *iso-contour* of a Gaussian distribution, and allows you to visualize a bi-dimensional confidence interval. The limitation to a 2D Cartesian reference system does not constitute a loss of generality, since the following derivations can be arbitrarily extended to multi-variate random variable by extending the number of degrees of freedom, as well. Let us remark that error ellipse representation is rarely meaningful for non-spatial coordinates, therefore in the following, only geometrical coordinates will be considered.

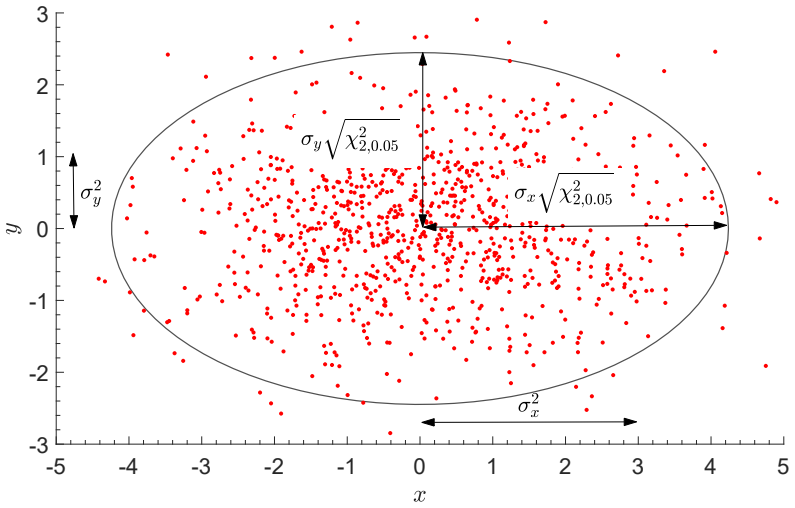

Figure B.1: Error ellipse of uncorrelated 2D positioning unbiased solutions drawn for 95% of the confidence interval.

Figure B.1 shows a 95% confidence ellipse for a set of uncorrelated, bivariate normally distributed positioning solutions. This confidence ellipse defines the region that contains 95% of all the samples (red dots) that can be drawn from a zero-mean Gaussian distribution with covariance equal to

$$\mathbf{P}_k = \begin{bmatrix} \sigma_x^2 & \sigma_{xy} \\ \sigma_{yx} & \sigma_y^2 \end{bmatrix} \tag{B.6}$$

where $\sigma_x^2 = 3$ and $\sigma_y^2 = 1$ and $\sigma_{xy} = \sigma_{yx} = 0$.

It is evident that the magnitudes of the ellipse axes depend on the variance of the data. The largest variance is in fact in the direction of the x-axis, whereas the smallest variance lies in the direction of the y-axis.

The generic equation of an axis-aligned ellipse with a major axis of length $2a$ and a minor axis of length $2b$, centered at the origin, is defined by the following equation:

$$\left(\frac{x}{a}\right)^2 + \left(\frac{y}{b}\right)^2 = 1$$

In our case, the length of the axes are defined by the standard deviations σ_x and σ_y of the data such that the equation of the error ellipse becomes:

$$\left(\frac{x}{\sigma_x}\right)^2 + \left(\frac{y}{\sigma_y}\right)^2 = s \tag{B.7}$$

where s defines the scale of the ellipse and could be any arbitrary number (e.g. s=1). The question is now how to choose s, such that the scale of the resulting ellipse represents a chosen confidence level (e.g. a 95% confidence level corresponds to $s = 5.991$).

Our 2D data is sampled from a multivariate Gaussian with zero covariance. This means that both the x-values and the y-values are normally distributed too. Therefore, the left hand side of equation (B.7) actually represents the sum of squares of independent normally distributed data samples. The sum of squared Gaussian data points is known to be distributed according to a Chi-Square distribution. A Chi-Square distribution is defined in terms of *degrees of freedom*, which represent the number of unknowns. In the case of bivariate data there are two unknowns, thus two degrees of freedom.

Therefore, we can easily obtain the probability that the above sum, and thus s equals a specific value by calculating the Chi-Square likelihood. In fact, since we are interested in a confidence interval, we are looking for the probability that s is less then or equal to a specific value which can easily be obtained using the cumulative Chi-Square distribution, such that to collect the 95% of probability, the following holds

$$P(s < 5.991) = 1 - 0.05 = 0.95$$

Formally, a 95 % confidence interval corresponds to $s = 5.991$. In other words, 95% of the data will fall inside an ellipse defined as:

$$\left(\frac{x}{\sigma_x}\right)^2 + \left(\frac{y}{\sigma_y}\right)^2 = 5.991$$

Similarly, a 99% confidence interval corresponds to $s = 9.210$ and a 90% confidence interval corresponds to $s = 4.605$.

The error ellipse shown in Figure B.1 can be drawn as an ellipse with a major axis length equal to $2\sigma_x \sqrt{5.991}$ and the minor axis length to $2\sigma_y \sqrt{5.991}$.

Exploiting the decomposition of the covariance matrix through its eigenvalues and eigenvector it is possible to visualize arbitrary confidence intervals of our solution, thus to visually evaluate the precision of the estimated solution for a generic covariance matrix.

B.2.1 Eigendecomposition of Covariance

As shown in Figure B.1, $\mathbf{P}_k$ defines both the *spread* (variance), and the *orientation* (covariance) of the observation. It is of interest to find the vector directed into the direction of the largest spread of the data, and whose magnitude equals the spread (variance) in this direction for an arbitrarily correlated set of data.

When the covariance terms of $\mathbf{P}_k$ are not null, the resulting error ellipse will not be aligned to the Cartesian axis. The previous considerations hold only if we consider a new reference system in which the ellipses can be actually aligned to the axis.

Instead of computing the variance along the y and x axis , we aim at determining the variance along the major and minor axis of the error ellipse, as shown by red and black arrows in Figure B.2. A covariance matrix can be considered as a linear transformation which scales and rotates a set of originally uncorrelated data. In light of this, the directions of the axis of the error ellipse are still defined by the eigenvectors of such a transformation matrix. Thus, the 95% confidence ellipse can be defined similarly to the axis-aligned case, with the major axis of length $2\sqrt{5.991\lambda_1}$ and the minor axis of length $2\sqrt{5.991\lambda_2}$, where λ_1 and λ_2 represent the eigenvalues of the covariance matrix.

It is hence possible to draw a covariance ellipse representing the covariance matrix of uncorrelated data and aftwerwards applying a rotation according to the angle

$$\alpha = \arctan \frac{\mathbf{v}_1(y)}{\mathbf{v}_1(x)}$$

which is the angle of the largest eigenvector towards the x-axis and $\mathbf{v}_1$ is the eigenvector of the covariance matrix that corresponds to the largest eigenvalue. The angle α determines the rotation of the ellipse according to the true statistical properties of the observations.

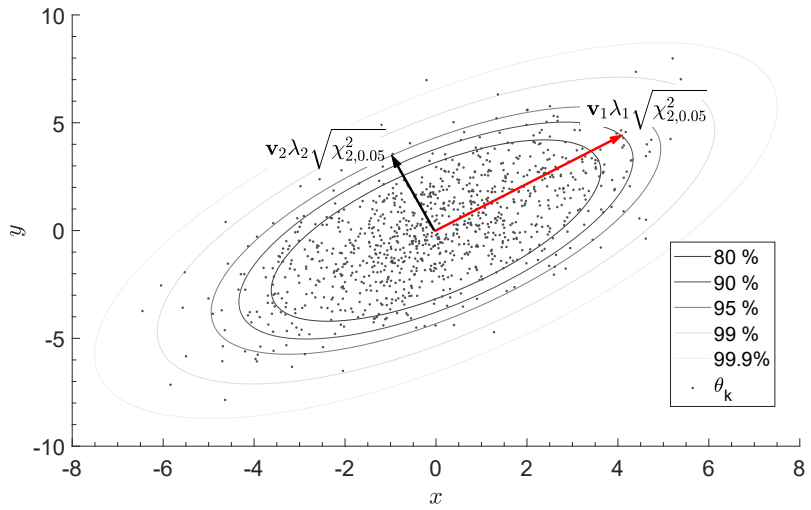

Figure B.2: Error ellipses of correlated 2D positioning solutions shown for 5 confidence intervals indicated in the legend. Eigenvector are multiplied by the respective eigenvalue with a factor 2 to reach 95% confidence value.

Based on the minor and major axis lengths and the angle α between the major axis and the x-axis, it becomes trivial to plot the confidence ellipse as shown in Figure B.2.

Let us suppose to compute a set of point $\begin{bmatrix}\mathbf{x} & \mathbf{y}\end{bmatrix}^\top$ describing (B.7), the ellipse modelling the covariance matrix of a generic dataset can be draw by means of

$$\begin{bmatrix}\mathbf{x}'\\ \mathbf{y}'\end{bmatrix} = \begin{bmatrix}\cos(\alpha) & -\sin(\alpha)\\ \sin(\alpha) & \cos(\alpha)\end{bmatrix}\begin{bmatrix}\mathbf{x}\\ \mathbf{y}\end{bmatrix}\begin{bmatrix}\cos(\alpha) & -\sin(\alpha)\\ \sin(\alpha) & \cos(\alpha)\end{bmatrix}^{\top} \tag{B.8}$$

Summarizing, a generic 2D error ellipse can be computed according to the following pseudo-code

Error ellipse Pseudocode for the generation of error ellipses

1: Calculate the eigenvectors and eigenvalues through the eigendecomposition of the covariance matrix
2: Get the largest eigenvalue
3: Compute the confidence intervals according to the number of degrees of freedom.
4: Draw the ellipse in x and y coordinates according to (B.7).
5: Define a rotation matrix $\mathbf{R}$.
6: Rotate the ellipse according to (B.8).

B.2.2 Covariance conversion between reference frames

When the estimation of a covariance matrix is provided in ECEF coordinates, the visualization of the confidence interval in terms of error ellipses does not provide useful information about its geometrical distribution on a local frame (e.g. ENU). A conversion of the 3D covariance matrix must be performed to project the 2D error ellipse to the local reference frame.

According to Appendix A, the conversion of a set of positioning observations between different reference frame can be performed applying a proper rotation matrix as

$$\boldsymbol{\theta}'_k = \mathbf{R}\boldsymbol{\theta}_k. \tag{B.9}$$

According to the following derivation, the same rotation matrix can be used to perform the conversion $\mathbf{P}_k \rightarrow \mathbf{P}'_k$ [177].

Proof.

$$\begin{aligned}\mathbf{P}'_k &= \mathrm{E}(\boldsymbol{\theta}'\boldsymbol{\theta}'^{\top}) - \mathrm{E}\left(\boldsymbol{\theta}'\right)\mathrm{E}\left(\boldsymbol{\theta}'^{\top}\right)\\ &= \mathrm{E}(\mathbf{R}\boldsymbol{\theta}\boldsymbol{\theta}^{\top}\mathbf{R}^{\top}) - \mathrm{E}(\mathbf{R}\boldsymbol{\theta})\mathrm{E}(\boldsymbol{\theta}^{\top}\mathbf{R}^{\top})\\ &= \mathbf{R}\mathrm{E}(\boldsymbol{\theta}\boldsymbol{\theta}^{\top})\mathbf{R}^{\top} - \mathbf{R}\mathrm{E}\boldsymbol{\theta}\mathrm{E}(\boldsymbol{\theta}^{\top})\mathbf{R}^{\top}\\ &= \mathbf{R}(\mathrm{E}(\boldsymbol{\theta}\boldsymbol{\theta}^{\top}) - \mathrm{E}(\boldsymbol{\theta})\mathrm{E}(\boldsymbol{\theta}^{\top}))\boldsymbol{\theta}^{\top}\\ &= \mathbf{R}\mathbf{P}_k\mathbf{R}^{\top}\end{aligned} \tag{B.10}$$

□

This transformation is particularly needed when sample covariance cannot be computed through of the observations such as in PF-based estimation but is directly estimated from the navigation filter (e.g. KF-based Bayesian estimation) in a different reference frame w.r.t. to the one of interest. Once the conversion $\mathbf{P}_k \rightarrow \mathbf{P}'_k$ is performed, the eigendecomposition of $\mathbf{P}'_k$ can be used to draw covariance ellipse in the new reference frame.

Appendix C

CPS message fields

C.1 Data fields description

The messages exchanged within the CAPS.loc infrastructure are defined according to a JASON-like format and they are stored in the DB keeping the same structure. The fields are briefly described in Table C.1 and Table C.2.

Cooperative Raw Message (CRM)	
_id	MongoDB unique CRM identifier.
agent_id	CPS-CPA multi-agent unique identifier of the sender.
epoch	Received GNSS satellite time, at the measurement time, in seconds.
sat_subset	Array of the unique identifiers of the satellites used to compute the PVT contained in the navigation message.
ag_subset	Array of the unique identifiers of the collaborating agents used to compute the PVT contained in the navigation message.
sat_raw_range	Raw satellites pseudoranges measured by the GNSS sensor and used to compute the PVT contained in the navigation message.
sigma	Error estimated by the GNSS sensor (1-sigma) for the received GNSS time
llh_pos	GNSS-only positioning solution expressed in latitude longitude and height (above the sea level) .
llh_coop_pos	Collaborative positioning solution represented in latitude longitude and height (above the sea level).
llh_povider	Android positioning solution represented in latitude longitude and height (above the sea level).
ecef_pos	GNSS-only Positioning solution expressed in cartesian Earth Centered Earth Fixed reference frame.
distance	Array of distances from other cooperative agents.
cov	Upper triangular portion of the estimated error covariance matrix of the positioning solution in `llh_pos`.
cov_coop	Upper triangular portion of the estimated error covariance matrix of the cooperative positioning solution in `llh_coop_pos`.

Table C.1: Database organization. Raw measurements collection entry.

Agent	
_id	MongoDB unique user identifier.
agent_id	CPS-CPA multi-agent unique identifiers.
type	Mobile device used by the agent
status	Actual status of the agent. It is active when the service is running, while it is not when the CPA is stopped without unsubscription is performed or when the agent has a bad fix.
all	Flag indicating that the agent can use all the visible satellite and the cooperative agent using the CPS. It is used to optimize the CPA code in term of time and computational cost when the service runs normally.
visible_satellites	Array of the unique identifiers of the visible satellites: GNSS satellites identifiers are conventionally distinguished by the letters G (GPS), R (GLONASS), E (Galileo), C (Beidou) associated with a unique identifier (PRN) for each satellite within a constellation.
usable_satellites	Array of the unique identifiers of the usable satellites. It is equal to the visible satellite array if the FBS
ag_subset	Array of the unique identifiers of the collaborating agents.
llh_pos	GNSS-only positioning solution expressed in latitude longitude and height (above the sea level) .
llh_coop_pos	Collaborative positioning solution represented in latitude longitude and height (above the sea level).
llh_povider	Android positioning solution represented in latitude longitude and height (above the sea level).
distance	Array of distances from other cooperative agents.
cov	Upper triangular portion of the estimated error covariance matrix of the positioning solution in `llh_pos`.
cov_coop	Upper triangular portion of the estimated error covariance matrix of the cooperative positioning solution in `llh_coop_pos`.

Table C.2: Database organization. Agent collection entry.

C.2 APIs

This section includes the description of the methods designed within the CPS API and a set of examples showing the JSON-compliant messages (when foreseen) which can be downloaded from the CPS.

Registration/Unregistration of a the agents

The methods described in Table C.3, Table C.4 and Table C.5 are implemented to manage the set of collaborating agents. Any explicit output message is generated for such methods.

The method `/subscribe_agent` is used to initialize the device to be ready for cooperation within the CAPS.loc framework.

The API method /unsubscribe_agent ask to the server for the removal of one agent subscribed to the CPS. The agent entry is removed from the *agents* collection if the MongoID passed as params match with the stored one. Also the *raw measurements* collection corresponding to the `agent_id` passed as params is deleted. It can be requested from the user at the end of service usage.
Table C.4 shows the API's details.

The API method `/unsubscribe_all_agents` deletes all agents in the *agents* collection and all the *raw measurements* collections. It is used at the closure of CPS.

/subscribe_agent	
Method	POST
Access	External
Uri	`subscribe_agent`
Params	`API-key`: hash code used for authentication
Returns	Unique database identifier MongoID
Example	`https://hansel.rokubun.cat/cps/api/subscribe_agent ?api-key={API-key}`

Table C.3: API description. Agent subscription.

/unsubscribe_agent	
Method	GET
Access	External
Uri	`unsubscribe_agent`
Params	`API-key`: hash code used for authentication `_id`: unique database identifier MongoID `agent_id`: agent ID number
Returns	Positive or negative acknowledgement
Example	`https://hansel.rokubun.cat/cps/api/unsubscribe_agent ?api-key={API-key}&_id={_id}&agent_id=1`

Table C.4: API description. Agent unsubscription.

Table C.5 shows the API's details.

/unsubscribe_all_agents	
Method	GET
Access	External
Uri	`unsubscribe_all_agents`
Params	`API-key`: hash code used for authentication
Returns	Positive or negative acknowledgement
Example	`https://hansel.rokubun.cat/cps/api/unsubscribe_all_agents ?api-key={API-key}`

Table C.5: API description. All agents unsubscription

Database Upkeep API

The API method `/db_upkeep` sets the expiration time of entries in the *raw measurements* collections. It is called bu FBS. Table C.6 shows the API's details.

Raw measurements and status

The sample output included in Listing C.1 shows a collection of data available at the CPS for a registered agent and obtained through the method `agent_fix()`, detailed in Table C.7. The sample reply includes the raw measurements obtained from a Xiaomi Mi 8 Pro registered to CPS along with other four agents (see `agent_subset` for IDs).

/db_upkeep	
Method	POST
Access	External
Uri	`db_upkeep`
Params	`API-key`: hash code used for authentication
Returns	Positive or negative acknowledgement
Example	`https://hansel.rokubun.cat/cps/api/db_upkeep ?api-key={API-key}`

Table C.6: API description. Database refresh time.

/agent_fix	
Action	
Method	GET
Access	External
Uri	`_agent_fix`
Params	`API-key`: hash code used for authentication `agent_id`: agent ID number
Returns	Agent corresponding to `agents_id`
Example	`https://hansel.rokubun.cat/cps/api/agent_fix ?api-key={API-key}&agent_id=1`

Table C.7: API description. Agent information.

Listing C.1: Example of data retrieved through agent_fix

```
1
2 {"_id": {"$oid": "5db03dcf7063d8c820d4271b"},
3  "agent_id": 1,
4  "type": "Xiaomi MI 8 Pro",
5  "status": true,
6  "all": true,
7  "visible_sat": [6, 9, 17, 19, 3, 22, 1],
8  "usable_sat": [6, 9, 17, 19, 3, 22, 1],
9  "ag_subset": [2],
10 "cov": ["[ 58.25393308534426, -15.894230180614427, -181.83995940323592,
       124.14915758809606]"]
11 "cov_coop": ["[15.538197348988968, 3.1395898401645805, 20.17710162861915,
       14.649688332314021]"]
12 "distance": [72.66270493290985],
13 "ecef_pos": [4472473.843235724, 601384.0767840956, 4492789.074489612],
14 "llh_coop_pos": [45.064866746105494, 7.658122128206029, -84.17707859631628],
15 "llh_pos": [45.065574955842465, 7.658251476759935, 410.46206387504935]
16 }
```

Visibility configuration

The method `/agents_visibility` offers the possibility to remotely limit the satellite visibility and the interactions between the agents which are registered to the CPS. The reply shown in Listing C.2 was obtained by means of the method `agent_visibility`. It can be noticed that the device was configured to observe 9 satellites and to collaborate with 3 agents (see `satellite_set` for and `agents_set` for respective details).

/agents_visibility	
Method	POST
Access	External
Uri	`agents_visibility`
Params	`API-key`: hash code used for authentication
	`agent_id`: agent ID number
Returns	Positive or negative acknowledgement
Example	`https://hansel.rokubun.cat/cps/api/agents_visibility`
	`?api-key={API-key}&agent_id=1`

Table C.8: API description. Agent entry update.

Listing C.2: Example of data retrieved through agent_visibility

```
{
  "satellite_set": [G12,G3,G8,G26,G9,E4,E12,E24,E31],
  "agents_set" : [2,3,5]
}
```

Registered agents

The list of agents reported in Listing C.3 was obtained through the method `agent_id`. It shows that 4 agents are registered to the CPS. The API method `/agents_id` gets the list of all agents registered to the CPS. Table C.9 shows the API's details.

/agents_id	
Method	GET
Access	External
Uri	`agents_id`
Params	`API-key`: hash code used for authentication
Returns	List of the registered agent IDs
Example	`https://hansel.rokubun.cat/cps/api/agents_id`
	`?api-key={API-key}`

Table C.9: API description. Agent listing.

Listing C.3: Example of data retrieved through agent_id

```
{
  "agents_id" :  [1,2,3,4]
}
```

Raw measurements upload

Listing C.4: Example of data downloaded uploaded to the CPS

```
{
"_id": {"$oid": "5d00ccf5a9d68ff97d571ef4"},
"epoch": "[2039,145838.5974929312]",
"agent_id": "2",
"type": "songRX",
"status": true,
```

```
"sat_subset": "[G28,G7,G8,G4,G12,G16,G3,G17,G27]",
"ag_subset": "[1,3,4,5,6,7,8]",
"sat_raw_range":[2.4542675427833732E7,2.1409056885831743E7,
                 2.2037492893273685E7,2.489673462934284E7,
                 2.0446292198035542E7,2.1941325488014203E7,
                 2.0608730854230978E7,2.4259760887495834E7,
                 2.4440507138588656E7,2.4487624892299775E7]",
"sat_doppler":"[-3573.4968717823663,1616.9385368783649,-3182.0119141144132,-4
    410.015313713629,-1986.8888771404663,1563.5353029840799,-801.495005544276
    ,-3148.0048037427523,-355.342887512213,-3434.848056537203]",
"llh_pos":"[45.06779498069527,7.597496188162584,202.97572307387836]", "
    llh_coop_pos":"[]",
"distance":"[266.754087287577,265.4448624662285,501.7596808566831,817.9027524
    47363,1001.0497137762819,819.9610150810086,267.05468965203715]",
"ecef_pos":"[4472823.012104692,596603.0691357873,4492849.1943269605]",
"cov": "[4.2,0.34,0.87,6.34,0.56,8]",
"cov_coop": "[4.2,0.34,0.87,6.34,0.56,8]",
"db_timestamp": 1560333552.84
}
```


Raw measurements download

The API method `/agent_measurement` get the most recent *raw measurements* collection entry corresponding to the params `agent_id`. It can be used to get the last calculated position, cooperative position, pseudoranges and covariances.
Table C.10 shows the API's details.

`/agent_measurement`	
Method	GET
Access	External
Uri	`agent_measurement`
Params	`API-key`: hash code used for authentication `agent_id`: agent ID number
Returns	It returns the data carried by the last CRM from agent `agent_id` stored in its *raw measurements* collection.
Example	`https://hansel.rokubun.cat/cps/api/agent_measurement ?api-key={API-key}&agent_id=1`

Table C.10: API description. Agent last measurements information.

Listing C.5: Example of data downloaded from the CPS


```
{
"epoch": "[2039,145838.5974929312]",
"agent_id": "2",
"ecef_pos":"[4472823.012104692,596603.0691357873,4492849.1943269605]",
"sat_subset": "[28,7,8,4,12,16,3,17,27]",
"sat_raw_range": [2.4542675427833732E7,2.1409056885831743E7,
                  2.2037492893273685E7,2.489673462934284E7,
                  2.0446292198035542E7,2.1941325488014203E7,
                  2.0608730854230978E7,2.4259760887495834E7,
                  2.4440507138588656E7,2.4487624892299775E7]",
}
```

Database Download API

The API method `/all_db` downloads the whole database hosted by the central server as a .txt file. This method can be helpful for the post processing of raw measurements data collected by the network of agents.

Table C.11 shows the API's details.

`/all_db`	
Method	GET
Access	External
Uri	`all_db`
Params	`API-key`: hash code used for authentication
Returns	File named "CPS_database.txt"
Example	`https://hansel.rokubun.cat/cps/api/all_db ?api-key={API-key}`

Table C.11: API description. Database download.

Appendix D

Android Location Services

D.1 Background software architecture: Positioning in Android OS

Dealing with time-constrained GNSS measurements requires to act at very low level in the system architecture but unfortunately this cannot be achieved with smartphones when we work at the application level. As shown in Figure D.1, the Android Application Framework works as an interface to access sensors measurements and this holds also for the GNSS receiver. Different APIs allow to the developers to exploit positioning and navigation capabilities in Android smartphones.

As an affordable solution within the roadmap of the project, CAPS.loc has been initially deployed at application level but potential implementations at lower system level (e.g. operating system background services) are surely of interest for further development.

D.1.1 Android Location Manager

Android gives to the applications the access to the location services supported by the device through classes in the `android.location` package. The central component of the location framework is the `LocationManager` system service, which provides APIs to determine location and bearing (if compass sensor is available) of the underlying device.

Once a given application is registered to the `LocationManager` service, it is able to perform three actions:

- Query for the list of all `LocationProviders` for the last known user location.
- Register/unregister for periodic updates of the user's current location from a location provider (specified either by criteria or name).
- Register/unregister for a given Intent to be fired if the device comes within a given proximity (specified by radius in meters) of a given latitude and longitude.

The `LocationProvider` class is the superclass of the different location providers which deliver the information about the current location. This information is stored in the Location class. The Android's location APIs use three different providers to get location

- `LocationManager.GPS_PROVIDER`: This provider determines location using satellites only. Depending on conditions (i.e. visibility, signal quality, demodulation of the navigation message), this provider may require a considerable time to return a location fix. The `GPS_PROVIDER` foreseen accurate, precise and reliable solutions according to the quality of the on-board GNSS receiver.

- `LocationManager.NETWORK_PROVIDER`: This provider determines location based on availability of cell tower and Wi-Fi access points by exploiting their geo-tags or RSS measurements. Results are retrieved by means of a network lookup so the responsiveness of the `NETWORK_PROVIDER` depends on network latencies.
- `LocationManager.PASSIVE_PROVIDER`: This provider will return locations generated by other providers. The location is updated when other applications or services request them without actually requesting the locations yourself.

Some challenging aspects must be taken into account in determining the location of a device, some sources of error in the user location indeed include:

- **Multitude of location sources** - GNSS, Cell-ID, and Wi-Fi can each provide a clue to users location. Determining which to use and trust is a matter of trade-offs in accuracy, speed, and battery-efficiency.
- **User movement** - Because the user location changes, you must account for movement by re-estimating user location every so often. To cope with such a typical issue for highly-portable devices, the integration of on-board inertial sensors has become very appealing to guarantee better accuracy and precision.
- **Varying accuracy** - Location estimates coming from each location source are not consistent in their accuracy. As an example, the location obtained at a given epoch from one source might be more accurate than the newest location from another or same source. This issue hold for all the location providers implemented in the Android location framework.

These problems can make it difficult to obtain a reliable user location.

The usual way to obtain the location in Android devices works by means of callbacks. An application can receive location updates from the `LocationManager` by calling `requestLocationUpdates()`, passing it a `LocationListener`. Your `LocationListener` must implement several callback methods that the `LocationManager` calls when the user location changes or when the status of the service changes.

The high-level localization options offered to the Android users reflect the potential of the location provider so that it can be forced the only use of GNSS and on-board inertial sensors (device only), Networks only (low power) and a combined solution (high accuracy) which guarantees the best performance in terms of accuracy, precision and availability of the positioning solution.

D.1.2 Raw GNSS measurements

Raw pseudorange and Doppler measurements are provided as an output by the *Raw GNSS Measurement* API. All the information related to the GNSS receiver are hence encapsulated in a Java public class named `GnssMeasurement`. Further details about method and constant provided by the object android.location.GnssMeasurement can be found at `https://developer.android.com/reference/android/location/GnssMeasurement.html`. The reference positioning solution is foreseen by the Google Fused Location Provider which integrates available sensors and networks to refine the positioning estimation provided by means of GNSS, as shown in the right scheme of Figure D.1.

For this reasons the development of the CAPS.loc framework has been pursued at this level by knowing potential limits imposed by the operating system itself w.r.t. the management of the applications.

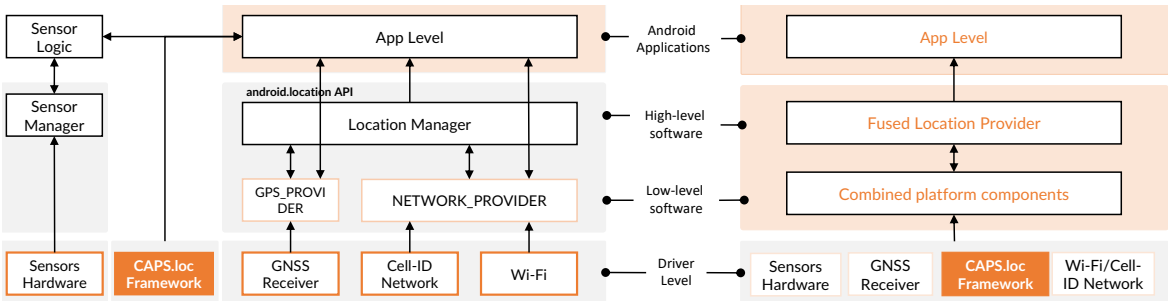

Figure D.1: Possible implementation of the CAPS.loc framework in Android systems.

Fused Location Provider API

As shown in the right portion of Figure D.1, the new paradigm aim at providing to the developer and to the users different layers. The Fused Location Provider is compatible with lower level sensors hubs which can be tightly-integrated prior to the application level. The Google Fused Location Provider has been used in the HANSEL project only to assess the improvement guaranteed by cooperative positioning w.r.t. the standalone GNSS solution.

Nevertheless, a natural extension of the CAPS.loc would act in synergy with other location providers, tightly related or augmenting to the capabilities of the GNSS receiver, as for the block scheme on the right of Figure D.1.

List of acronyms

A/D	Analog-to-Digital
ADC	Analog-to-Digital Converter
AGC	Automatic Gain Control
AoA	Angle of Arrival
AWGN	Additive White Gaussian Noise
APD	Absolute Position Distance
API	Application Programming Interface
AGNSS	Assisted GNSS
BOC	Binary Offset Carrier
BPSK	Binary Phase Shift Keying
BIC	Bayesian Information Criterion
CAF	Cross Ambiguity Function
CAPS.loc	Collaborative Android Positioning System for enhanced LOCalization
CBOC	Composite Binary Offset Carrier
CDF	Cumulative Distribution Function
CDMA	Code Division Multiple Access
C/N_0	Carrier-to-Noise density power ratio
CoO	Cell of Origin
CS	Commercial Service
CRM	Cooperative Raw Message
CP	Cooperative Positioning
CW	Continuous Wave
CWI	Continuous Wave Interference
CDOP	Cooperative Dilution of Precision
CRLB	Cramer-Rao Lower Bound
CRU	Collaborative Ranging Unit
COTS	Commercial Off-the-shelf
CPS	Cooperative Positiong Service
CPA	Cooperative Positioning Application
CPU	Control Processing Unit
CCD	Charge-Coupled Device

CMOS	complementary metal-oxide semiconductor
DAC	Digital-Analog Converter
DoD	Department of Defense
DARPA	Defense Advanced Research Projects Agency
DC	Deeply Coupled
DD	Double Difference
DDR	Double Difference Ranging
DCM	Direction Cosine Matrix
DLL	Delay Lock Loop
DSP	Digital Signal Processors
DOP	Dilution Of Precision
DGNSS	Differential GNSS
DGPS	Differential GPS
DSRC	Direct Short-Range Communication
DB	Database
ECEF	Earth-Centered Earth-Fixed
ENU	East-North-Up
ECI	Earth-Centered Inertial
EKF	Extended Kalman Filter
EPF	Extended Particle Filter
EOC	Early Operational Capability
ESA	European Space Agency
FLL	Frequency Lock Loop
FPGA	Field Programmable Gate Array
FIM	Fisher Information Matrix
FDMA	Frequency Division Multiple Access
GBPT	GNSS-Based Positioning Terminal
GLONASS	GLobal NAvigation Satellite System
GM	Gauss-Markov
GNSS	Global Navigation Satellite System
GPP	General Purpose Processor
GPS	Global Positioning System
GSA	Global Navigation Satellite Systems Agency
GDOP	Geometrical Dilution of Precision
GoF	Goodness of Fit
GEV	Generalized Extreme Value
GUI	Graphic User Interface
HOW	Hand-over word

HPE	Horizontal Positioning Error
HW	Hardware
H-LMS	Hybrid Least Mean Square
H-PVT	Hybrid PVT
H-WLMS	Hybrid Weighted Least Mean Square
H-EKF	Hybrid Extended Kalman Filter
H-PF	Hybrid Particle Filter
HMM	Hidden-state Markov Model
IAR	Inter-Agent Ranging
IF	Intermediate Frequency
IMU	Inertial Measurement Unit
ICD	Interface Control Document
IOC	Initial Operational Capability
IOV	In-Orbit Validation
INS	Inertial Navigation System
IVS	In-Vehicle Systems
ISMR	Ionospheric Scintillation Monitoring Receivers
ITS	Intelligent Transport System
IoT	Internet of Things
ILS	Instrument Landing System
KF	Kalman Filter
KPI	Key Performance Indicator
LC	Loosely Coupled
LLA	Latitude Longitude Altitude
LoS	Line-of-Sight
LDOP	Line Dilution Of Precision
LORAN	LOng-range Aid to Navigation
LiDAR	Light Detection and Ranging System
LNA	Low Noise Amplifier
LO	Local Oscillator
LMS	Least Mean Square
LS	Least Square
LTP	Local Tangent Plane
LBS	Location-Based Service
MBOC	Multiplexed BOC
MCS	Multilevel Coded Spreading Symbols
MEMS	Micro Electro-Mechanical System
ML	Maximum Likelihood

MLE	Maximum Likelihood Estimation
MSE	Mean Square Error
MMSE	Minimum Mean Square Error
MAP	Maximum A Posteriori
MEO	Medium Earth Orbit
NBI	Narrow Band Interference
NCO	Numerical Controlled Oscillator
NED	North-East-Down
NLOS	Non-Line-of-Sight
NNSS	Navy Navigation Satellite System
NAVSTAR	Navigation System with Time and Ranging
OS	Open Service
OCXO	Oven Controlled Xtal Oscillator
PC	Personal Computer
PPP	Precise Point Positioning
PLL	Phase Lock Loop
PND	Personal Navigation Device
PNT	Positioning and Navigation Technologies
PRN	Pseudo-Random Noise
PRS	Public Regulated Service
PSD	Power Spectral Density
PVT	Position, Velocity and Time
PDF	Probability Density Function
PR	Pseudorange Ranging
PF	Particle Filter
PCC	Pearson's Correlation Coefficients
PoC	Proof of Concept
RADAR	RAdio Detection And Ranging
RNSS	Radio Navigation Satellite Services
ROS	Robot Operating System
RIMS	Ranging and Integrity Monitoring Station
R&R	Record and Replay
RF	Radio Frequency
RFE	Radio Front-End
RFCS	Radio-Frequency Constellation Simulators
RFI	Radio-Frequency Interference
RMS	Root Mean Square
RSS	Receives Signal Straight

RTT	Round-trip Time
RSSI	Receives Signal Straight Indicator
RTMeS	Reference Trajectory Measurement System
RFCS	Radio Frequency Constellation Simulators
RTK	Real Time Kinematic
RTC	Real Time Clock
RMD	Raw Measurements Database
SAIA	Self-Adaptive Iterative Algorithm
SBAS	Satellite-based Augementation System
SDR	Software Defined Radio
SD	Single Difference
SiS	Signal-in-Space
SIS	Sequential Importance Sampling
SSE	Sum of Squared Error
SIFT	Scale Invariant Feature Transform
SLAM	Simultaneous Localization And Mapping
SONAR	Sound Navigation and Ranging
SNR	Signal-to-Noise Ratio
SoL	Safety-of-Life
SAR	Search-and-Rescue
SV	Satellite Vehicle
SW	Software
SPP	Single Point Positioning
SIR	Sampling Importance Resampling
STD	Standard Deviation
STL	Satellite Time and Location
s-PF	suboptimal PF
TC	Tightly Coupled
TLM	Telemetry word
TDoA	Time Difference of Arrival
ToA	Time of Arrival
DoA	Direction of Arrival
ToF	Time of Flight
TOW	Time of Week
TTF	Time-to-First-Fix
UKF	Unscented Kalman Filter
UAV	Unmanned Aerial Vehicle
USB	Universal Serial Bus

USRP	Universal Software Radio Peripheral
U-TC	Ultra-Tightly Coupled
UWB	Ultra Wide Band
UERE	User-equivalent Range Error
UDP	User Datagram Protocol
UHF	Ultra High Frequency
VDLL	Vector Delay Lock Loop
VERT	Vehicle for Experimental Research on Trajectories
VFLL	Vector Frequency Lock Loop
VO	Visual Odometry
VLC	Visual Light Communication
VSG	Vector Signal Generator
VHF	Very High Frequency
WB	Wide-Band
WBI	Wide-Band Interference
WLAN	Wireless Local Area Network
WLS	Weighted Least Square
W-DDR	Weighted Double Difference Ranging
W-DD	Weighted Double Difference
WSS	Wheel Speed Sensor
W-SAIA	Weighted SAIA
W-IAR	Weighted IAR
WGN	White Gaussian Noise

Bibliography

[1] Broadcom BCM47755. [Online]. Available: https://www.broadcom.com/products/wireless/gnss-gps-socs/bcm47755.

[2] P. Aggarwal, Z. Syed, and N. El-Sheimy. "Hybrid Extended Particle Filter (HEPF) for integrated civilian navigation system". In: *2008 IEEE/ION Position, Location and Navigation Symposium*. May 2008, pp. 984–992. DOI: 10.1109/PLANS.2008.4570072.

[3] N. Alam and A. G. Dempster. "Cooperative positioning for vehicular networks: Facts and future". In: *IEEE Transactions on Intelligent Transportation Systems* 14.4 (2013), pp. 1708–1717.

[4] N. Alam, A. Tabatabaei Balaei, and A. G. Dempster. "A DSRC Doppler-Based Cooperative Positioning Enhancement for Vehicular Networks With GPS Availability". In: *IEEE Transactions on Vehicular Technology* 60.9 (Nov. 2011), pp. 4462–4470. ISSN: 0018-9545. DOI: 10.1109/TVT.2011.2168249.

[5] N. Alam, A. Tabatabaei Balaei, and A. G. Dempster. "A DSRC Doppler-based cooperative positioning enhancement for vehicular networks with GPS availability". In: *IEEE Transactions on Vehicular Technology* 60.9 (2011), pp. 4462–4470.

[6] N. Alam, A. Tabatabaei Balaei, and A. G. Dempster. "Relative Positioning Enhancement in VANETs: A Tight Integration Approach". In: *IEEE Transactions on Intelligent Transportation Systems* 14.1 (Mar. 2013), pp. 47–55. ISSN: 1524-9050. DOI: 10.1109/TITS.2012.2205381.

[7] A. Angrisano. "GNSS/INS integration methods". In: *Dottorato di ricerca (PhD) in Scienze Geodetiche e Topografiche Thesis, Universita'degli Studi di Napoli Parthenope, Naple* 21 (2010).

[8] M. S. Arulampalam et al. "A tutorial on particle filters for online nonlinear/non-Gaussian Bayesian tracking". In: *IEEE Transactions on Signal Processing* 50.2 (Feb. 2002), pp. 174–188. ISSN: 1053-587X. DOI: 10.1109/78.978374.

[9] J. Avila-Rodriguez et al. "The MBOC modulation: the final touch to the Galileo frequency and signal plan". In: *Navigation* 55.1 (2008), pp. 15–28.

[10] S. Banville and F. Van Diggelen. "Precise positioning using raw GPS measurements from Android smartphones". In: *GPS World* 27.11 (2016), pp. 43–48.

[11] C. Basnayake, G. Lachapelle, and J. Bancroft. "Relative positioning for vehicle-to-vehicle communications-enabled vehicle safety applications". In: *18th ITS World Congress TransCore ITS America ERTICO-ITS Europe ITS Asia-Pacific*. 2011.

[12] A. Bhattacharyya. "On a measure of divergence between two multinomial populations". In: *Sankhyā: the indian journal of statistics* (1946), pp. 401–406.

[13] S. Bisnath and Y. Gao. "Current state of precise point positioning and future prospects and limitations". In: *Observing our changing earth*. Springer, 2009, pp. 615–623.

[14] S. Bityukov et al. “A method for statistical comparison of histograms”. In: *arXiv preprint arXiv:1302.2651* (2013).

[15] D. Borio. “A statistical theory for GNSS signal acquisition”. In: *Ph.D. Dissertation Politecnico di Torino* (2008).

[16] R. G. Brown and P. Y. C. Hwang. *Introduction to random signals and applied Kalman filtering: with MATLAB exercises*. John Wiley & Sons, Inc., 2012.

[17] R. Zekavat R. M. Buehrer. *Handbook of position location: Theory, practice and advances*. Vol. 27. John Wiley & Sons, 2011.

[18] M. A. Caceres et al. “Hybrid Cooperative Positioning Based on Distributed Belief Propagation”. In: *IEEE Journal on Selected Areas in Communications* 29.10 (Dec. 2011), pp. 1948–1958. ISSN: 0733-8716. DOI: 10.1109/JSAC.2011.111205.

[19] M. A. Caceres et al. “Hybrid GNSS-Terrestrial Cooperative Positioning via Distributed Belief Propagation”. In: *2010 IEEE Global Telecommunications Conference GLOBECOM 2010*. Dec. 2010, pp. 1–5. DOI: 10.1109/GLOCOM.2010.5683684.

[20] J. Chaffee and J. Abel. “GDOP and the Cramer-Rao bound”. In: *Proceedings of 1994 IEEE Position, Location and Navigation Symposium - PLANS’94*. Apr. 1994, pp. 663–668. DOI: 10.1109/PLANS.1994.303374.

[21] J. Chen et al. “Identification of a Moving Object’s Velocity and Range With a Static-Moving Camera System”. In: *IEEE Transactions on Automatic Control* 63.7 (July 2018), pp. 2168–2175. ISSN: 0018-9286. DOI: 10.1109/TAC.2017.2755988.

[22] M. L. Cherif, J. Leclère, et al. “Loosely coupled GPS/INS integration with snap to road for low-cost land vehicle navigation: EKF-STR for low-cost applications”. In: *2018 IEEE/ION Position, Location and Navigation Symposium (PLANS)*. IEEE. 2018, pp. 275–282.

[23] D. Chwa, A. P. Dani, and W. E. Dixon. “Range and Motion Estimation of a Monocular Camera Using Static and Moving Objects”. In: *IEEE Transactions on Control Systems Technology* 24.4 (July 2016), pp. 1174–1183. ISSN: 1063-6536. DOI: 10.1109/TCST.2015.2508001.

[24] D. Corrales et al. *HANSEL Testbed Design Document*. Tech. rep. Rokubun, HANSEL consortium, Oct. 2019.

[25] D. Corrales et al. *HANSEL Testbed Test and Validation Document*. Tech. rep. Rokubun, HANSEL consortium, Oct. 2019.

[26] C. Cristodaro. “Advanced Integration of GNSS and External Sensors for Autonomous Mobility Applications”. In: (2019).

[27] C. Cristodaro et al. “GNSS receiver performance in urban environment: Challenges and test approaches for automotive applications”. In: *2017 International Conference of Electrical and Electronic Technologies for Automotive*. June 2017, pp. 1–6. DOI: 10.23919/EETA.2017.7993222.

[28] S. B. Cruz et al. “Neighbor-Aided Localization in Vehicular Networks”. In: *IEEE Transactions on Intelligent Transportation Systems* 18.10 (Oct. 2017), pp. 2693–2702. ISSN: 1524-9050. DOI: 10.1109/TITS.2017.2655146.

[29] X. Cui et al. “Vehicle Positioning Using 5G Millimeter-Wave Systems”. In: *IEEE Access* 4 (2016), pp. 6964–6973. DOI: 10.1109/ACCESS.2016.2615425.

[30] P. Dabove and V. Di Pietra. "Towards high accuracy GNSS real-time positioning with smartphones". In: *Advances in Space Research* 63.1 (2019), pp. 94–102. ISSN: 0273-1177. DOI: https://doi.org/10.1016/j.asr.2018.08.025. URL: http://www.sciencedirect.com/science/article/pii/S0273117718306537.

[31] D. Dardari, E. Falletti, and M. Luise. *Satellite and terrestrial radio positioning techniques: a signal processing perspective*. Academic Press, 2012.

[32] K. Das and H. Wymeersch. "Censoring for Bayesian Cooperative Positioning in Dense Wireless Networks". In: *IEEE Journal on Selected Areas in Communications* 30.9 (Oct. 2012), pp. 1835–1842. ISSN: 0733-8716. DOI: 10.1109/JSAC.2012.121029.

[33] H. G. de Marina, B. Jayawardhana, and M. Cao. "Taming Mismatches in Inter-agent Distances for the Formation-Motion Control of Second-Order Agents". In: *IEEE Transactions on Automatic Control* 63.2 (Feb. 2018), pp. 449–462. ISSN: 0018-9286. DOI: 10.1109/TAC.2017.2715226.

[34] F. de Ponte Müller. "Survey on ranging sensors and cooperative techniques for relative positioning of vehicles". In: *Sensors* 17.2 (2017), p. 271.

[35] F. De Ponte Müller, A. Steingass, and T. Strang. "Zero-Baseline Measurements for Relative Positioning in Vehicular Environments". In: *6th European Workshop on GNSS Signals and Signal Processing*. Dec. 2013. URL: https://elib.dlr.de/86457/.

[36] F. de Ponte Müller, A. Steingass, and T. Strang. "Zero-baseline measurements for relative positioning in vehicular environments". In: *Sixth European Workshop on GNSS Signals and Signal Processing*. 2013.

[37] US Department of Defense. *DoD World Geodetic System 1984*. 2018. URL: https://earth-info.nga.mil/GandG/publications/tr8350.2/tr8350_2.html.

[38] X. Deng et al. "An iterative algorithm for solving ill-conditioned linear least squares problems". In: *Geodesy and Geodynamics* 6.6 (2015), pp. 453–459. ISSN: 1674-9847. DOI: http://dx.doi.org/10.1016/j.geog.2015.06.004.

[39] B. Denis, J. Pierrot, and C. Abou-Rjeily. "Joint distributed synchronization and positioning in UWB ad hoc networks using TOA". In: *IEEE Transactions on Microwave Theory and Techniques* 54.4 (June 2006), pp. 1896–1911. ISSN: 0018-9480. DOI: 10.1109/TMTT.2006.872082.

[40] A. Doucet, N. J. Gordon, and V. Krishnamurthy. "Particle filters for state estimation of jump Markov linear systems". In: *IEEE Transactions on Signal Processing* 49.3 (Mar. 2001), pp. 613–624. ISSN: 1053-587X. DOI: 10.1109/78.905890.

[41] F. Dovis, P. Mulassano, and F Dominici. "Overview of Global Navigation Satellite Systems". In: Sept. 2011, pp. 923–974.

[42] F. Dovis et al. "A Run-Time Method Based on Observable Data for the Quality Assessment of GNSS Positioning Solutions". In: *IEEE Journal on Selected Areas in Communications* 33.11 (Nov. 2015), pp. 2357–2365. ISSN: 0733-8716. DOI: 10.1109/JSAC.2015.2430513.

[43] F. Dovis et al. "A Run-Time Method Based on Observable Data for the Quality Assessment of GNSS Positioning Solutions". In: *IEEE Journal on Selected Areas in Communications* 33.11 (Nov. 2015), pp. 2357–2365. DOI: 10.1109/JSAC.2015.2430513.

[44] F. Dovis et al. "Analysis of the Signal Outage". In: *GPS World* (2019). URL: https://www.gpsworld.com/why-galileo-experienced-a-week-long-service-outage (visited on 2019).

[45] F. Dovis et al. “Anomalous GPS Signals from SVN49”. In: *GPS World* (2017). URL: http://digital.gpsworld.com/July2017/Default/4/0/3705752#&pageSet=7 (visited on 2019).

[46] F. Dovis et al. “Context-aware peer-to-peer and cooperative positioning”. In: *International Conference on Localization and GNSS 2014 (ICL-GNSS 2014)*. June 2014, pp. 1–6. DOI: 10.1109/ICL-GNSS.2014.6934166.

[47] Computer vision for dummies. *A geometric interpretation of the covariance matrix*. 2019. URL: https://www.visiondummy.com/2014/04/geometric-interpretation-covariance-matrix/#Covariance_matrix_as_a_linear_transformation.

[48] Computer vision for dummies. *How to draw a covariance error ellipse?* 2019. URL: visiondummy.com/2014/04/draw-error-ellipse-representing-covariance-matrix/.

[49] European Commission. *Implementing Decision (EU) 2017/224 of 8 February 2017 setting out the technical and operational specifications allowing the commercial service offered by the system established under the Galileo programme to fulfil the function referred to in Article 2(4)(c) of Regulation (EU) No 1285/2013 of the European Parliament and of the Council*. Available at: http://data.europa.eu/eli/dec_impl/2017/224/oj (accessed on May 2019). 2017.

[50] European Commission website. *Galileo goes live!, Press release, Brussels*. Available at: http://europa.eu/rapid/press-release_IP-16-4366_en.htm (accessed on May 2019). 2016.

[51] European Union. *European GNSS (Galileo) Open Service Signal-In-Space Interface Control Document, OS SIS ICD, Issue 1.3*. Available at: https://www.gsc-europa.eu/system/files/galileo_documents/Galileo-OS-SIS-ICD.pdf (accessed on May 2019). 2016.

[52] G. Falco, M. Pini, and G. Marucco. “Loose and Tight GNSS/INS Integrations: Comparison of Performance Assessed in Real Urban Scenarios”. In: *Sensors* 17.2 (2017). ISSN: 1424-8220. DOI: 10.3390/s17020255. URL: http://www.mdpi.com/1424-8220/17/2/255.

[53] G. Falco et al. “Performance analysis of constrained loosely coupled GPS/INS integration solutions”. In: *Sensors* 12.11 (2012), pp. 15983–16007.

[54] M. Falcone, J. Hahn, and T. Burger. “Galileo”. In: *Springer Handbook of Global Navigation Satellite Systems*. Springer, 2017, pp. 247–272.

[55] P. Fan, X. Cui, and M. Lu. “Space and frequency diversity characterization of mobile GNSS receivers in multipath fading channels”. In: *Tsinghua Science and Technology* 25.2 (Apr. 2020), pp. 294–301. DOI: 10.26599/TST.2019.9010016.

[56] Ronald Aylmer Fisher. *Statistical methods for research workers*. Genesis Publishing Pvt Ltd, 2006.

[57] J. Gabela et al. “Cramér Rao bound analysis for cooperative positioning in intelligent transportation systems”. In: *Proceedings of the 2018 Conference International Global Navigation Satellite Systems (IGNSS), Sydney, Australia*. 2018, pp. 7–9.

[58] ICD Galileo. *Galileo open service, signal in space interface control document (OS SIS ICD)*. 2008.

[59] G. E. Garcia et al. “On the Trade-Off Between Accuracy and Delay in Cooperative UWB Localization: Performance Bounds and Scaling Laws”. In: *IEEE Transactions on Wireless Communications* 13.8 (Aug. 2014), pp. 4574–4585. ISSN: 1536-1276. DOI: 10.1109/TWC.2014.2314662.

[60] M. Garcia. *HANSEL Testbed Concept Overview*. Tech. rep. Rokubun, HANSEL consortium, May 2019.

[61] L. Gauthier et al. "EGNOS: the first step in Europe's contribution to the global navigation satellite system". In: *ESA bulletin* 105 (2001), pp. 35–42.

[62] Global Positioning System Directorate, System Engineering and Integration. *Interface Specification, NAVSTAR GPS Space Segment / Navigation User Segment Interfaces, IS-GPS-200 Rev. H, IRN003*. Available at: http://www.gps.gov/technical/icwg/IRN-IS-200H-001+002+003_rollup.pdf (accessed on May 2019). 2016.

[63] Global Positioning System Directorate, System Engineering and Integration. *Interface Specification, NAVSTAR GPS Space Segment / User Segment L1C Interfaces, IS-GPS-800 Rev. D*. Available at: http://www.gps.gov/technical/icwg/IS-GPS-800D.pdf (accessed on May 2019). 2014.

[64] Global Positioning System Directorate, System Engineering and Integration. *Interface Specification, NAVSTAR GPS Space Segment / User Segment L5 Interfaces, IS-GPS-705 Rev. D*. Available at: http://www.gps.gov/technical/icwg/IS-GPS-705D.pdf (accessed on May 2019). 2014.

[65] Systems Engineering Global Positioning Systems Directorate and Integration. "Interface specification, Navstar GPS space segment/user segment L1C interfaces, IS-GPS-800." In: (2008).

[66] Salil Goel, Allison Kealy, and Bharat Lohani. "Posterior Cramér Rao Bounds for Cooperative Localization in Low-Cost UAV Swarms". In: *Journal of the Indian Society of Remote Sensing* 47.4 (Apr. 2019), pp. 671–684. ISSN: 0974-3006. DOI: 10.1007/s12524-018-0899-3. URL: https://doi.org/10.1007/s12524-018-0899-3.

[67] N. Gogoi, A. Minetto, and F. Dovisì. "On the Cooperative Ranging between Android Smartphones Sharing Raw GNSS Measurements". In: *Proceedings of VTC2019-Fall Honolulu Intelligent Connection and Transportation)*. Sept. 2019.

[68] N. Gogoi et al. "A Controlled-Environment Quality Assessment of Android GNSS Raw Measurements". In: *Electronics* 8.1 (Dec. 2018), p. 5. ISSN: 2079-9292. DOI: 10.3390/electronics8010005. URL: http://dx.doi.org/10.3390/electronics8010005.

[69] Google Developers. *GNSSMeasurement*. URL: https://developer.android.com/reference/android/location/GnssMeasurement. (accessed: 05.07.2019).

[70] N. Gordon. "A hybrid bootstrap filter for target tracking in clutter". In: *Proceedings of 1995 American Control Conference - ACC'95*. Vol. 1. June 1995, 628–632 vol.1. DOI: 10.1109/ACC.1995.529326.

[71] N. J. Gordon, D. J. Salmond, and A. F. M. Smith. "Novel approach to nonlinear/non-Gaussian Bayesian state estimation". In: *IEE proceedings F (radar and signal processing)*. Vol. 140. 2. IET. 1993, pp. 107–113.

[72] M. S. Grewal, L. R. Weill, and A. P. Andrews. *Global positioning systems, inertial navigation, and integration*. John Wiley & Sons, 2007.

[73] J. N. Gross, Y. Gu, and M. B. Rhudy. "Robust UAV Relative Navigation With DGPS, INS, and Peer-to-Peer Radio Ranging". In: *IEEE Transactions on Automation Science and Engineering* 12.3 (July 2015), pp. 935–944. ISSN: 1545-5955. DOI: 10.1109/TASE.2014.2383357.

[74] GSA working group. *Using GNSS Raw Measurements on Android Devices*. https://www.gsa.europa.eu/system/files/reports/gnss_raw_measurement_web_0.pdf. 2018.

[75] GNSS GSA. "Market Report Issue 6". In: *European Global Navigation Satellite Systems Agency* (Oct. 2019).

[76] F. Gustafsson. "Particle filter theory and practice with positioning applications". In: *IEEE Aerospace and Electronic Systems Magazine* 25.7 (July 2010), pp. 53–82. ISSN: 0885-8985. DOI: 10.1109/MAES.2010.5546308.

[77] F. Gustafsson et al. "Particle filters for positioning, navigation, and tracking". In: *IEEE Transactions on Signal Processing* 50.2 (Feb. 2002), pp. 425–437. ISSN: 1053-587X. DOI: 10.1109/78.978396.

[78] K. F. Hasan, Y. Feng, and Y. Tian. "GNSS Time Synchronization in Vehicular Ad-Hoc Networks: Benefits and Feasibility". In: *IEEE Transactions on Intelligent Transportation Systems* 19.12 (Dec. 2018), pp. 3915–3924. ISSN: 1524-9050. DOI: 10.1109/TITS.2017.2789291.

[79] S. S. Haykin and B. Widrow. *Least-mean-square adaptive filters*. Vol. 31. Wiley Online Library, 2003.

[80] G.W. Hein. "From GPS and GLONASS via EGNOS to Galileo – Positioning and Navigation in the Third Millennium". In: *GPS Solutions* 3.4 (Apr. 2000), pp. 39–47. ISSN: 1080-5370. DOI: 10.1007/PL00012814. URL: https://doi.org/10.1007/PL00012814.

[81] G. Hendeby and F. Gustafsson. *Fundamental filtering limitations in linear non-Gaussian systems*. Linköping University Electronic Press, 2004.

[82] G. M. Hoang et al. "Mitigating unbalanced GDoP effects in range-based vehicular Cooperative Localization". In: *2017 IEEE International Conference on Communications Workshops (ICC Workshops)*. May 2017, pp. 659–664. DOI: 10.1109/ICCW.2017.7962733.

[83] B. Hofmann-Wellenhof and J. Collins H. Lichtenegger. *Global positioning system: theory and practice*. Springer Science & Business Media, 2012.

[84] L. Hsu et al. "Urban Pedestrian Navigation Using Smartphone-Based Dead Reckoning and 3-D Map-Aided GNSS". In: *IEEE Sensors Journal* 16.5 (Mar. 2016), pp. 1281–1293. DOI: 10.1109/JSEN.2015.2496621.

[85] B. Huang et al. "Dilution of Precision Analysis for GNSS Collaborative Positioning". In: *IEEE Transactions on Vehicular Technology* 65.5 (May 2016), pp. 3401–3415. ISSN: 0018-9545. DOI: 10.1109/TVT.2015.2436700.

[86] J. Huang and H. Tan. "A Low-Order DGPS-Based Vehicle Positioning System Under Urban Environment". In: *IEEE/ASME Transactions on Mechatronics* 11.5 (Oct. 2006), pp. 567–575. ISSN: 1083-4435. DOI: 10.1109/TMECH.2006.882988.

[87] L. Huang et al. "Robust Inter-Vehicle Distance Estimation Method Based on Monocular Vision". In: *IEEE Access* 7 (2019), pp. 46059–46070. ISSN: 2169-3536. DOI: 10.1109/ACCESS.2019.2907984.

[88] C. Jekeli. *Inertial navigation systems with geodetic applications*. Walter de Gruyter, 2012.

[89] E. Kaplan and C. Hegarty. *Understanding GPS: Principles and Applications*. Artech house, 2005.

[90] E. Kaplan and C. Hegarty. *Understanding GPS/GNSS: principles and applications*. Artech House, 2017.

[91] N. Kassabian and L. Lo Presti. "Mean acquisition time of GNSS peer-to-peer networks". In: *2012 International Conference on Localization and GNSS*. June 2012, pp. 1–6. DOI: 10.1109/ICL-GNSS.2012.6253108.

[92] S. M. Kay. *Fundamentals of statistical signal processing, volume I: Estimation theory (v. 1)*. 1993.

[93] J. Khalife and Z. M. Kassas. "Navigation With Cellular CDMA Signals—Part II: Performance Analysis and Experimental Results". In: *IEEE Transactions on Signal Processing* 66.8 (Apr. 2018), pp. 2204–2218. ISSN: 1053-587X. DOI: 10.1109/TSP.2018.2799166.

[94] M. Khider. URL: https://github.com/google/gps-measurement-tools/releases/tag/2.0.0.1. (accessed: 05.07.2019).

[95] S. S. Kia, S. Rounds, and S. Martinez. "Cooperative Localization for Mobile Agents: A Recursive Decentralized Algorithm Based on Kalman-Filter Decoupling". In: *IEEE Control Systems Magazine* 36.2 (Apr. 2016), pp. 86–101. ISSN: 1066-033X. DOI: 10.1109/MCS.2015.2512033.

[96] K. Kidono et al. "Pedestrian recognition using high-definition LIDAR". In: *2011 IEEE Intelligent Vehicles Symposium (IV)*. June 2011, pp. 405–410. DOI: 10.1109/IVS.2011.5940433.

[97] H. Kim, S. W. Choi, and S. Kim. "Connectivity Information-Aided Belief Propagation for Cooperative Localization". In: *IEEE Wireless Communications Letters* 7.6 (Dec. 2018), pp. 1010–1013. ISSN: 2162-2337. DOI: 10.1109/LWC.2018.2844785.

[98] M. Kishimoto et al. "QZSS system design and its performance". In: *Proceedings of the 2007 National Technical Meeting of The Institute of Navigation*. 2001, pp. 405–410.

[99] J. KyoungHwan, L. Jihong, and K. JungBae. "Cooperative multi-robot localization using differential position data". In: *2007 IEEE/ASME international conference on advanced intelligent mechatronics*. Sept. 2007, pp. 1–6. DOI: 10.1109/AIM.2007.4412548.

[100] R. B. Langley. "The mathematics of GPS". In: *GPS world* 2.7 (1991), pp. 45–50.

[101] E. G. Larsson. "Cramer-Rao bound analysis of distributed positioning in sensor networks". In: *IEEE Signal Processing Letters* 11.3 (Mar. 2004), pp. 334–337. ISSN: 1070-9908. DOI: 10.1109/LSP.2003.822899.

[102] K. Lassoued, I. Fantoni, and P. Bonnifait. "Mutual Localization and Positioning of Vehicles Sharing GNSS Pseudoranges: Sequential Bayesian Approach and Experiments". In: *2015 IEEE 18th International Conference on Intelligent Transportation Systems*. Sept. 2015, pp. 1896–1901. DOI: 10.1109/ITSC.2015.307.

[103] Khaoula Lassoued and Philippe Bonnifait. *Cooperative Localization for Autonomous Vehicles Sharing GNSS Measurements*. 2019.

[104] D. Laurichesse et al. "Smartphone applications for precise point positioning". In: *Proceedings of the ION GNSS*. 2017, pp. 171–187.

[105] A. Lehner and A. Steingass. "A novel channel model for land mobile satellite navigation". In: *Institute of Navigation Conference ION GNSS*. 2005, pp. 13–16.

[106] T. Li, M. Bolic, and P. M. Djuric. "Resampling methods for particle filtering: classification, implementation, and strategies". In: *IEEE Signal Processing Magazine* 32.3 (2015), pp. 70–86.

[107] Y. Li et al. “Self-Contained Indoor Pedestrian Navigation Using Smartphone Sensors and Magnetic Features”. In: *IEEE Sensors Journal* 16.19 (Oct. 2016), pp. 7173–7182. DOI: 10.1109/JSEN.2016.2591824.

[108] X. Lin et al. “Positioning for the Internet of Things: A 3GPP Perspective”. In: *IEEE Communications Magazine* 55.12 (Dec. 2017), pp. 179–185. DOI: 10.1109/MCOM.2017.1700269.

[109] K. Liu et al. “Improving Positioning Accuracy Using GPS Pseudorange Measurements for Cooperative Vehicular Localization”. In: *IEEE Transactions on Vehicular Technology* 63.6 (July 2014), pp. 2544–2556. ISSN: 0018-9545. DOI: 10.1109/TVT.2013.2296071.

[110] L. Lo Presti, D. Margaria, and M. Rao. “Novel techniques for a cooperative positioning approach based on peer-to-peer networks”. In: *Proc. of the Int’l Conf. on Data Flow From Space to Earth*. 2011.

[111] L. Lo Presti, D. Margaria, and J. Samson. “A novel peer to peer aided acquisition strategy tailored to Galileo E1 receivers”. In: *Proceedings ELMAR-2010*. Sept. 2010, pp. 417–424.

[112] L. Lo Presti et al. “Software defined radio technology for GNSS receivers”. In: *2014 IEEE Metrology for Aerospace (MetroAeroSpace)*. IEEE. 2014, pp. 314–319.

[113] R. Loh et al. “The US Wide-Area Augmentation System (WAAS)”. In: *Navigation* 42.3 (1995), pp. 435–465.

[114] V. Lucas-Sabola et al. “Cloud GNSS receivers: New advanced applications made possible”. In: *2016 International Conference on Localization and GNSS (ICL-GNSS)*. June 2016, pp. 1–6. DOI: 10.1109/ICL-GNSS.2016.7533852.

[115] V. Lucas-Sabola et al. “Demonstration of Cloud GNSS Signal Processing”. In: *Proc. ION GNSS)*. 2016.

[116] I. Elshafiey M. D. A. Hossain and A. Al-Sanie. “Cooperative vehicular positioning with VANET in urban environments”. In: *2016 IEEE Asia-Pacific Conference on Applied Electromagnetics (APACE)*. IEEE. 2016, pp. 393–396.

[117] D. Gingras M. Rohani and D. Gruyer. “A novel approach for improved vehicular positioning using cooperative map matching and dynamic base station DGPS concept”. In: *IEEE Transactions on Intelligent Transportation Systems* 17.1 (2015), pp. 230–239.

[118] D. Margaria et al. “A new peer-to-peer aided acquisition approach exploiting C/N0 aiding”. In: *2010 5th ESA Workshop on Satellite Navigation Technologies and European Workshop on GNSS Signals and Signal Processing (NAVITEC)*. Dec. 2010, pp. 1–10. DOI: 10.1109/NAVITEC.2010.5708021.

[119] D. Margaria et al. “Contact! First Acquisition and Tracking of IOV Galileo Signals”. In: *Inside GNSS Magazine* (Jan. 2012), pp. 46–55. URL: http://bit.ly/1s9xjvH.

[120] M. Marron et al. “"XPFCP": an extended particle filter for tracking multiple and dynamic objects in complex environments”. In: *2005 IEEE/RSJ International Conference on Intelligent Robots and Systems*. Aug. 2005, pp. 2474–2479. DOI: 10.1109/IROS.2005.1544987.

[121] H. Martin and PNT Command Lead. “GPS status and modernization”. In: *Munich Satellite Navigation Summit, Munchen* (2008).

[122] S. Mazuelas, Y. Shen, and M. Z. Win. "Information Coupling in Cooperative Localization". In: *IEEE Communications Letters* 15.7 (July 2011), pp. 737–739. ISSN: 1089-7798. DOI: 10.1109/LCOMM.2011.060111.110402.

[123] A. Minetto. "A Theoretical Study on the Benefits of Integrating GNSS and Collaborative Relative Ranges". In: *Proceedings of the 33th International Technical Meeting of The Satellite Division of the Institute of Navigation (ION GNSS+ 2019)*. Sept. 2019.

[124] A. Minetto, C. Cristodaro, and F. Dovis. "A Collaborative Method for GNSS-based Inter-Agent Range Estimation and Hybrid Positioning Algorithm in Harsh Environment". In: *Proceedings of the 30th International Technical Meeting of The Satellite Division of the Institute of Navigation (ION GNSS+ 2017) September 25 - 29, 2017 Oregon Convention Center Portland, Oregon*. Institute of Navigation. 2017, pp. 3784–3795.

[125] A. Minetto, C. Cristodaro, and F. Dovis. "A collaborative method for positioning based on GNSS inter agent range estimation". In: *2017 25th European Signal Processing Conference (EUSIPCO)*. Aug. 2017, pp. 2714–2718. DOI: 10.23919/EUSIPCO.2017.8081704.

[126] A. Minetto and F. Dovis. "A theoretical framework for collaborative estimation of distances among GNSS users". In: *2018 IEEE/ION Position, Location and Navigation Symposium (PLANS)*. Apr. 2018, pp. 1492–1501. DOI: 10.1109/PLANS.2018.8373543.

[127] A. Minetto and F. Dovis. "On the Information Carried by Correlated Collaborative Ranging Measurements for Hybrid Positioning". In: *IEEE Transactions on Vehicular Technology* (2019), pp. 1–1. ISSN: 1939-9359. DOI: 10.1109/TVT.2019.2957015.

[128] A. Minetto, G. Falco, and F. Dovis. "On the Trade-Off between Computational Complexity and Collaborative GNSS Hybridization". In: *2019 IEEE 90th Vehicular Technology Conference (VTC2019-Fall)*. Sept. 2019, pp. 1–5. DOI: 10.1109/VTCFall.2019.8891571.

[129] A. Minetto, A. Nardin, and F. Dovis. "GNSS-only Collaborative Positioning Among Connected Vehicles". In: *Proceedings of the 1st ACM MobiHoc Workshop on Technologies, mOdels, and Protocols for Cooperative Connected Cars*. TOP-Cars '19. Catania, Italy: ACM, 2019, pp. 37–42. ISBN: 978-1-4503-6807-0. DOI: 10.1145/3331054.3331552. URL: http://doi.acm.org/10.1145/3331054.3331552.

[130] A. Minetto, A. Nardin, and F. Dovis. "Tight Integration of GNSS Measurements and GNSS-based Collaborative Virtual Ranging". In: *31st International Technical Meeting of the Satellite Division of The Institute of Navigation (ION GNSS+ 2018)*. Sept. 2018, pp. 2399–2413. DOI: 10.33012/2018.15955.

[131] P. Misra and P. Enge. *Global Positioning System: Signals, Measurements and Performance Second Edition*. Lincoln, MA: Ganga-Jamuna Press, 2006.

[132] MongoDB. *MS Windows NT Kernel Description*. 2019. URL: https://www.mongodb.com/ (visited on 10/10/2019).

[133] A. I. Mourikis and S. I. Roumeliotis. "Performance analysis of multirobot Cooperative localization". In: *IEEE Transactions on Robotics* 22.4 (Aug. 2006), pp. 666–681. ISSN: 1552-3098. DOI: 10.1109/TRO.2006.878957.

[134] A. I. Mourikis, S. I. Roumeliotis, and J. W. Burdick. "SC-KF Mobile Robot Localization: A Stochastic Cloning Kalman Filter for Processing Relative-State Measurements". In: *IEEE Transactions on Robotics* 23.4 (Aug. 2007), pp. 717–730. ISSN: 1552-3098. DOI: 10.1109/TRO.2007.900610.

[135] F. Dovis N. Linty A. Minetto and L. Spogli. "Effects of phase scintillation on the GNSS positioning error during the September 2017 storm at Svalbard". In: *Space Weather* 16.9 (2018), pp. 1317–1329.

[136] GPS Navstar. "ICD-GPS-200". In: *Revision C, Oct* 10 (1993).

[137] U. Niesen et al. "Intervehicle Range Estimation From Periodic Broadcasts". In: *IEEE Transactions on Vehicular Technology* 66.12 (Dec. 2017), pp. 10637–10646. ISSN: 0018-9545. DOI: 10.1109/TVT.2017.2762242.

[138] A. Noureldin, T. B. Karamat, and J. Georgy. *Fundamentals of inertial navigation, satellite-based positioning and their integration*. Springer Science & Business Media, 2012.

[139] K.K. Oh and H. S. Ahn. "Formation control of mobile agents based on inter-agent distance dynamics". In: *Automatica* 47.10 (2011), pp. 2306–2312.

[140] R. Ong and G. Lachapelle. "Use of GNSS for vehicle-pedestrian and vehicle-cyclist crash avoidance". In: *International journal of vehicle safety* 5.2 (2011), pp. 137–155.

[141] B. W. Parkinson, J. Spilker J, and P. Enge. *Global positioning system: theory and applications*. Vol. 109. American Institute of Aeronautics and Astronautics, 1996.

[142] F. Penna, M. A. Caceres, and H. Wymeersch. "Cramér-Rao Bound for Hybrid GNSS-Terrestrial Cooperative Positioning". In: *IEEE Communications Letters* 14.11 (Nov. 2010), pp. 1005–1007. ISSN: 1089-7798. DOI: 10.1109/LCOMM.2010.091310.101060.

[143] M. Pini, G. Falco, and L. Lo Presti. *Estimation of Satellite-User Ranges Through GNSS Code Phase Measurements*. IntechOpen, 2012.

[144] F. de Ponte Müller et al. "Bayesian cooperative relative vehicle positioning using pseudorange differences". In: *2014 IEEE/ION Position, Location and Navigation Symposium - PLANS 2014*. May 2014, pp. 434–444. DOI: 10.1109/PLANS.2014.6851401.

[145] R. Prasad and M. Ruggieri. *Applied satellite navigation using GPS, GALILEO, and augmentation systems*. Artech House, 2005.

[146] L. L. Presti et al. "Software Defined Radio technology for GNSS receivers". In: *2014 IEEE Metrology for Aerospace (MetroAeroSpace)*. May 2014, pp. 314–319. DOI: 10.1109/MetroAeroSpace.2014.6865941.

[147] A. Privat, M. Pascaud, and D. Laurichesse. "Innovative smartphone applications for Precise Point Positioning". In: *2018 SpaceOps Conference*. DOI: 10.2514/6.2018-2324. eprint: https://arc.aiaa.org/doi/pdf/10.2514/6.2018-2324. URL: https://arc.aiaa.org/doi/abs/10.2514/6.2018-2324.

[148] K. N. Rao. "GAGAN-The Indian satellite based augmentation system". In: *84.40. Ua* (2007).

[149] M. Rao, L. L. Presti, and J. Samson. "Peer to Peer Equation Augmentation for an Altitude Aided GNSS Receiver". In: *2010 IEEE 72nd Vehicular Technology Conference - Fall*. Sept. 2010, pp. 1–5. DOI: 10.1109/VETECF.2010.5594103.

[150] E. Realini et al. "Precise gnss positioning using smart devices". In: *Sensors* 17.10 (2017), p. 2434.

[151] K. A. Redmill, T. Kitajima, and U. Ozguner. "DGPS/INS integrated positioning for control of automated vehicle". In: *ITSC 2001. 2001 IEEE Intelligent Transportation Systems. Proceedings (Cat. No.01TH8585)*. Aug. 2001, pp. 172–178. DOI: 10.1109/ITSC.2001.948650.

[152] K. Reif et al. "Stochastic stability of the discrete-time extended Kalman filter". In: *IEEE Transactions on Automatic Control* 44.4 (Apr. 1999), pp. 714–728. ISSN: 0018-9286. DOI: 10.1109/9.754809.

[153] B. W. Remondi. "Using the Global Positioning System (GPS) Phase Observable for Relative Geodesy: Modeling, Processing, and Results (Satellite, Timing)." In: (1985).

[154] S. Rezaei and R. Sengupta. "Kalman Filter-Based Integration of DGPS and Vehicle Sensors for Localization". In: *IEEE Transactions on Control Systems Technology* 15.6 (Nov. 2007), pp. 1080–1088. ISSN: 1063-6536. DOI: 10.1109/TCST.2006.886439.

[155] N. Gordon B. Ristic and S. Arulampalam. "Beyond the kalman filter: Particle filters for tracking applications". In: *Artech House, London* 830 (2004), p. 5.

[156] U. Robustelli, V. Baiocchi, and G. Pugliano. "Assessment of Dual Frequency GNSS Observations from a Xiaomi Mi 8 Android Smartphone and Positioning Performance Analysis". In: *Electronics* 8.1 (Jan. 2019), p. 91. ISSN: 2079-9292. DOI: 10.3390/electronics8010091. URL: http://dx.doi.org/10.3390/electronics8010091.

[157] G. Rodriguez et al. "Robust Step Counting for Inertial Navigation with Mobile Phones". In: *Sensors* 18.9 (2018), p. 3157.

[158] M. Rohani, D. Gingras, and D. Gruyer. "Dynamic base station DGPS for cooperative vehicle localization". In: *2014 International Conference on Connected Vehicles and Expo (ICCVE)*. Nov. 2014, pp. 781–785. DOI: 10.1109/ICCVE.2014.7297658.

[159] E. Roper. *GPS Status and Modernization*. Tech. rep. Air Force Systems Command Space Systems DIV Los Angeles AFB CA Navstar GPS ..., 2010.

[160] ROS.org. *Robot Operating System (ROS)*. 2019. URL: https://www.ros.org/.

[161] S. I. Roumeliotis and G. A. Bekey. "Distributed multirobot localization". In: *IEEE Transactions on Robotics and Automation* 18.5 (Oct. 2002), pp. 781–795. ISSN: 1042-296X. DOI: 10.1109/TRA.2002.803461.

[162] B. Saikiran and V. Vikram. "IRNSS architecture and applications". In: *KIET Int. J. of Comm. & Electron* 1.3 (2013), pp. 21–27.

[163] A. A. A.A. Salih, N. L. A. C. A. Zaini, and A. Zhahir. "The suitability of GPS receivers update rates for navigation applications". In: *Proceedings of World Academy of Science, Engineering and Technology*. 78. World Academy of Science, Engineering and Technology (WASET). 2013, p. 192.

[164] J. Sanz Subirana, J.M. Juan Zornoza, and M. Hernández-Pajares. *Reference Frames in GNSS*. 2018. URL: https://gssc.esa.int/navipedia/index.php/Reference_Frames_in_GNSS.

[165] J. Sanz Subirana, J.M. Juan Zornoza, and M. Hernández-Pajares. *Reference Systems and frames*. 2018. URL: https://gssc.esa.int/navipedia/index.php/Reference_Systems_and_Frames.

[166] P. Schwarzbach et al. "V2X based Probabilistic Cooperative Position Estimation Applying GNSS Double Differences". In: *2019 International Conference on Localization and GNSS (ICL-GNSS)*. June 2019, pp. 1–6. DOI: 10.1109/ICL-GNSS.2019.8752742.

[167] K. Shamaei, J. Khalife, and Z. M. Kassas. "Exploiting LTE Signals for Navigation: Theory to Implementation". In: *IEEE Transactions on Wireless Communications* 17.4 (Apr. 2018), pp. 2173–2189. ISSN: 1536-1276. DOI: 10.1109/TWC.2018.2789882.

[168] I. Shames et al. "Cooperative Self-Localization of Mobile Agents". In: *IEEE Transactions on Aerospace and Electronic Systems* 47.3 (July 2011), pp. 1926–1947. ISSN: 0018-9251. DOI: 10.1109/TAES.2011.5937274.

[169] M. S. Sheijani et al. "Implementation and performance comparison of indirect Kalman filtering approaches for AUV integrated navigation system using low cost IMU". In: *2013 21st Iranian Conference on Electrical Engineering (ICEE)*. IEEE. 2013, pp. 1–6.

[170] F. Shen, J. W. Cheong, and A. G. Dempster. "A DSRC Doppler/IMU/GNSS tightly-coupled cooperative positioning method for relative positioning in VANETs". In: *The Journal of Navigation* 70.1 (2017), pp. 120–136.

[171] Y. Shen and M. Z. Win. "Fundamental Limits of Wideband Localization Part I: A General Framework". In: *IEEE Transactions on Information Theory* 56.10 (Oct. 2010), pp. 4956–4980. ISSN: 0018-9448. DOI: 10.1109/TIT.2010.2060110.

[172] Y. Shen, H. Wymeersch, and M. Z. Win. "Fundamental Limits of Wideband Localization Part II: Cooperative Networks". In: *IEEE Transactions on Information Theory* 56.10 (Oct. 2010), pp. 4981–5000. ISSN: 0018-9448. DOI: 10.1109/TIT.2010.2059720.

[173] A. Sheta et al. "Improved Localization for Android Smartphones Based on Integration of Raw GNSS Measurements and IMU Sensors". In: *2018 International Conference on Computer and Applications (ICCA)*. Aug. 2018, pp. 297–302. DOI: 10.1109/COMAPP.2018.8460352.

[174] I. Skog and P. Handel. "In-Car Positioning and Navigation Technologies—A Survey". In: *IEEE Transactions on Intelligent Transportation Systems* 10.1 (Mar. 2009), pp. 4–21. ISSN: 1524-9050. DOI: 10.1109/TITS.2008.2011712.

[175] A. Smith. *Sequential Monte Carlo methods in practice*. Springer Science & Business Media, 2013.

[176] D. Sobel. *Longitude: The true story of a lone genius who solved the greatest scientific problem of his time*. Macmillan, 2005.

[177] T. Soler and M. Chin. "On transformation of covariance matrices between local Cartesian coordinate systems and commutative diagrams". In: *ASP-ACSM Convention*. 1985, pp. 393–406.

[178] F. Sottile et al. "Hybrid GNSS-Terrestrial Cooperative Positioning Based on Particle Filter". In: *2011 IEEE Global Telecommunications Conference - GLOBECOM 2011*. Dec. 2011, pp. 1–5. DOI: 10.1109/GLOCOM.2011.6134002.

[179] H. Stark and J. W. Woods. *Probability, random processes, and estimation theory for engineers*. Prentice-Hall, Inc., 1986.

[180] E. Steinmetz et al. "Theoretical Limits on Cooperative Positioning in Mixed Traffic". In: *IEEE Access* 7 (2019), pp. 49712–49725. ISSN: 2169-3536. DOI: 10.1109/ACCESS.2019.2910658.

[181] A. Štern and A. Kos. "Positioning Performance Assessment of Geodetic, Automotive, and Smartphone GNSS Receivers in Standardized Road Scenarios". In: *IEEE Access* 6 (2018), pp. 41410–41428. DOI: 10.1109/ACCESS.2018.2856521.

[182] X. Sun, S. Zhang, and Q. Hu. "Particle Filter for Positioning Accuracy Improvement in GNSS Receiver". In: *3rd International Conference on Electric and Electronics*. Atlantis Press. 2013.

[183] M. Tahir et al. “On the Accuracy of Inter-Vehicular Range Measurements Using GNSS Observables in a Cooperative Framework”. In: *IEEE Transactions on Intelligent Transportation Systems* (2018), pp. 1–10. ISSN: 1524-9050. DOI: 10.1109/TITS.2018.2833438.

[184] K. Takagi et al. “Road Environment Recognition Using On-vehicle LIDAR”. In: *2006 IEEE Intelligent Vehicles Symposium*. June 2006, pp. 120–125. DOI: 10.1109/IVS.2006.1689615.

[185] J. H. Taylor. “The Cramer-Rao estimation error lower bound computation for deterministic nonlinear systems”. In: *1978 IEEE Conference on Decision and Control including the 17th Symposium on Adaptive Processes*. Jan. 1978, pp. 1178–1181. DOI: 10.1109/CDC.1978.268121.

[186] P. J. G. Teunissen. “The probability distribution of the GPS baseline for a class of integer ambiguity estimators”. In: *Journal of Geodesy* 73.5 (June 1999), pp. 275–284. ISSN: 1432-1394. DOI: 10.1007/s001900050244. URL: https://doi.org/10.1007/s001900050244.

[187] R. Toledo-Moreo et al. “Fusing GNSS, Dead-Reckoning, and Enhanced Maps for Road Vehicle Lane-Level Navigation”. In: *IEEE Journal of Selected Topics in Signal Processing* 3.5 (Oct. 2009), pp. 798–809. ISSN: 1932-4553. DOI: 10.1109/JSTSP.2009.2027803.

[188] *Trimble R10 GNSS Receiver User Guide*.

[189] *Trimble R2 GNSS Receiver User Guide*.

[190] C. Tzaras, B. G. Evans, and S. R. Saunders. “Physical-statistical analysis of land mobile-satellite channel”. In: *Electronics Letters* 34.13 (June 1998), pp. 1355–1357. ISSN: 0013-5194. DOI: 10.1049/el:19980937.

[191] S. Uluskan, T. Filik, and O. Gerek. “Circular Uncertainty method for range-only localization with imprecise sensor positions”. In: *Multidimensional Systems and Signal Processing* 29.4 (2018), pp. 1757–1780.

[192] F. Van Diggelen. *A-gps: Assisted gps, gnss, and sbas*. Artech house, 2009.

[193] F. Van Diggelen. “Innovation: Gps accuracy-lies, damn lies, and statistics”. In: *GPS WORLD* 9 (1998), pp. 41–45.

[194] J. Van Sickle. *GPS and GNSS for Geospatial Professionals: Differencing*. 2018. URL: https://www.e-education.psu.edu/geog862/node/1727#:~:targetText=For%20example%2C%20a%20single%20difference,r%E2%80%94%20observing%20the%20same%20satellite..

[195] S. Venkatraman and J. Caffery and. “A novel ToA location algorithm using LoS range estimation for NLoS environments”. In: *IEEE Transactions on Vehicular Technology* 53.5 (Sept. 2004), pp. 1515–1524. ISSN: 0018-9545. DOI: 10.1109/TVT.2004.832384.

[196] J. Wang, C. Satirapod, and C. Rizos. “Stochastic assessment of GPS carrier phase measurements for precise static relative positioning”. In: *Journal of Geodesy* 76.2 (Feb. 2002), pp. 95–104. ISSN: 1432-1394. DOI: 10.1007/s00190-001-0225-6. URL: https://doi.org/10.1007/s00190-001-0225-6.

[197] J. Wang, M. P. Stewart, and M. Tsakiri. “Stochastic Modeling for Static GPS Baseline Data Processing”. In: *Journal of Surveying Engineering* 124.4 (1998), pp. 171–181. DOI: 10.1061/(ASCE)0733-9453(1998)124:4(171). eprint: https://ascelibrary.org/doi/pdf/10.1061/%28ASCE%290733-9453%281998%29124%3A4%28171%29. URL: https://ascelibrary.org/doi/abs/10.1061/%28ASCE%290733-9453%281998%29124%3A4%28171%29.

[198] L. Wang and M. J. Zawodniok. "Bias and CRB Analysis of LoS-based and RSS-based Ranging Methods". In: *IEEE Transactions on Vehicular Technology* 65.11 (2016), pp. 9085–9097.

[199] J. Y. Wee. *Vehicular ranging system and method of operation*. US Patent 9,897,700. Feb. 2018.

[200] K. Wisiol, M. Wieser, and R. Lesjak. "GNSS-based vehicle state determination tailored to cooperative driving and collision avoidance". In: *2016 European Navigation Conference (ENC)*. May 2016, pp. 1–8. DOI: 10.1109/EURONAV.2016.7530562.

[201] J. Won, T. Pany, and G. W. Hein. "GNSS software defined radio". In: *Inside GNSS* 1.5 (2006), pp. 48–56.

[202] Z. Xiong. "Hybrid and Cooperative Positioning Solutions for Wireless Networks". PhD thesis. PhD Dissertation, Politecnico di Torino (Italy), 2014.

[203] D. Yang et al. "A GPS Pseudorange Based Cooperative Vehicular Distance Measurement Technique". In: *2012 IEEE 75th Vehicular Technology Conference (VTC Spring)*. May 2012, pp. 1–5. DOI: 10.1109/VETECS.2012.6240332.

[204] L. Yin, Q. Ni, and Z. Deng. "A GNSS/5G Integrated Positioning Methodology in D2D Communication Networks". In: *IEEE Journal on Selected Areas in Communications* 36.2 (Feb. 2018), pp. 351–362. DOI: 10.1109/JSAC.2018.2804223.

[205] D. Yoon et al. "Position Accuracy Improvement by Implementing the DGNSS-CP Algorithm in Smartphones". In: *Sensors* 16.6 (June 2016), p. 910. ISSN: 1424-8220. DOI: 10.3390/s16060910. URL: http://dx.doi.org/10.3390/s16060910.

[206] X. Zhang et al. "Quality assessment of GNSS observations from an Android N smartphone and positioning performance analysis using time-differenced filtering approach". In: *GPS Solutions* 22.3 (May 2018), p. 70. ISSN: 1521-1886. DOI: 10.1007/s10291-018-0736-8. URL: https://doi.org/10.1007/s10291-018-0736-8.

[207] Y. Zhou et al. "Indoor Elliptical Localization Based on Asynchronous UWB Range Measurement". In: *IEEE Transactions on Instrumentation and Measurement* 60.1 (Jan. 2011), pp. 248–257. ISSN: 0018-9456. DOI: 10.1109/TIM.2010.2049185.

[208] F. Zhu et al. "Walker: Continuous and Precise Navigation by Fusing GNSS and MEMS in Smartphone Chipsets for Pedestrians". In: *Remote Sensing* 11.2 (Jan. 2019), p. 139. ISSN: 2072-4292. DOI: 10.3390/rs11020139. URL: http://dx.doi.org/10.3390/rs11020139.

[209] M. Zhu et al. "Public Vehicles for Future Urban Transportation". In: *IEEE Transactions on Intelligent Transportation Systems* 17.12 (Dec. 2016), pp. 3344–3353. ISSN: 1524-9050. DOI: 10.1109/TITS.2016.2543263.

[210] N. Zhu et al. "GNSS Position Integrity in Urban Environments: A Review of Literature". In: *IEEE Transactions on Intelligent Transportation Systems* 19.9 (Sept. 2018), pp. 2762–2778. ISSN: 1524-9050. DOI: 10.1109/TITS.2017.2766768.

[211] Y. Zhuang and N. El-Sheimy. "Tightly-Coupled Integration of WiFi and MEMS Sensors on Handheld Devices for Indoor Pedestrian Navigation". In: *IEEE Sensors Journal* 16.1 (Jan. 2016), pp. 224–234. ISSN: 1530-437X. DOI: 10.1109/JSEN.2015.2477444.

This Ph.D. thesis has been typeset by means of the TEX-system facilities. The typesetting engine was pdfLATEX. The document class was `toptesi`, by Claudio Beccari, with option `tipotesi=scudo`. This class is available in every up-to-date and complete TEX-system installation.